FEDERAL UNIVERSITY OF SÃO CARLOS
CENTER FOR EXACT SCIENCES AND TECHNOLOGY
GRADUATE PROGRAM IN MATERIALS SCIENCE AND ENGINEERING

SURFACE FUNCTIONALIZATION OF THE AA2017 ALUMINUM ALLOY POWDER FOR USE IN ADDITIVE MANUFACTURING

Bruna Fernanda Batistão

São Carlos-SP
2026

FEDERAL UNIVERSITY OF SÃO CARLOS
CENTER FOR EXACT SCIENCES AND TECHNOLOGY
GRADUATE PROGRAM IN MATERIALS SCIENCE AND ENGINEERING

SURFACE FUNCTIONALIZATION OF THE AA2017 ALUMINUM ALLOY POWDER FOR USE IN ADDITIVE MANUFACTURING

Bruna Fernanda Batistão

Thesis presented to the Graduate Program in Materials Science and Engineering as a partial requirement to obtain the title of DOCTOR IN MATERIALS SCIENCE AND ENGINEERING

Supervisor: Prof. Dr.-Ing. Piter Gargarella
Cotutelle Supervisor: Univ.-Prof. Dr.-Ing. Sergio de Traglia Amancio-Filho
Funding Agency: FAPESP (Process n° 2020/09544-7) and FAPESP/BEPE (Process n° 2022/02760-1)

São Carlos-SP
2026

VITAE

Master in Materials Science and Engineering – Federal University of São Carlos (2021)

Bachelor in Materials Engineering – Federal University of São Carlos (2018)

UNIVERSIDADE FEDERAL DE SÃO CARLOS

Centro de Ciências Exatas e de Tecnologia
Programa de Pós-Graduação em Ciência e Engenharia de Materiais

Folha de Aprovação

Defesa de Tese de Doutorado da candidata Bruna Fernanda Batistão, realizada em 23/01/2026.

Comissão Julgadora:

Prof. Dr. Piter Gargarella (UFSCar)

Prof. Dr. Guilherme Yuuki Koga (UFSCar)

Prof. Dr. Claudemiro Bolfarini (UFSCar)

Prof. Dr. Witor Wolf (USP)

Prof. Dr. Sergio de Traglia Amancio Filho (TU Graz)

O Relatório de Defesa assinado pelos membros da Comissão Julgadora encontra-se arquivado junto ao Programa de Pós-Graduação em Ciência e Engenharia de Materiais.

ACKNOWLEDGEMENTS

I would first like to express my gratitude to Professor Piter Gargarella for his invaluable guidance, expertise, and all the insightful conversations, suggestions, and opportunities that made the development and improvement of this work possible. I am also deeply thankful to Professor Sergio de Traglia Amancio Filho from the Graz University of Technology (TU Graz) for his essential insights and contributions to this research, and for providing the opportunity to conduct this study under a cotutelle agreement.

I extend my appreciation to Professor Claudio Kiminami for his support over the last years.

I would like to thank the São Paulo Research Foundation (FAPESP) for the financial support that made this study possible, under the processes no. 2020/09544-7 and 2022/02760-1 (FAPESP/BEPE), and 2017/27031-4 (FAPESP/Young Researcher).

This study was financed in part by the Coordenação de Aperfeiçoamento de Pessoal de Nível Superior - Brasil (CAPES) - Finance Code 001.

I would also like to thank the Austrian aviation program ‘‘TAKE OFF” (PILOT, grant number 852796, 2018), and BMK - The Austrian Ministry for Climate Action, Environment, Energy, Mobility, Innovation and Technology.

I would also like to express my sincere appreciation to my colleagues, professors, laboratory technicians, and staff members at the Department of Materials Engineering/Federal University of São Carlos (DEMa/UFSCar) and the Institute of Materials Science, Joining and Forming (IMAT/TU Graz). I am also grateful to the Laboratory of Structural Characterization (LCE/UFSCar), the Center for Development and Characterization of Materials (CCDM/UFSCar), and the Institute for Technological Research (IPT) for providing excellent infrastructure, technological support, and a collaborative research environment.

Lastly, I am profoundly grateful to my family (Salete, Maria, and Francisco) and to my fiancé Matheus for their unwavering love, patience, and support, which have been fundamental throughout this journey. I would also like to extend my heartfelt thanks to Carla, Ge, and Sueli, Matheus’s family, for their kindness, encouragement, and for welcoming me as part of their own.

ABSTRACT

Additive manufacturing (AM) of high-strength aluminum alloys faces challenges due to their high reflectivity, high thermal conductivity, poor powder flowability, and susceptibility to solidification cracking during laser powder bed fusion (L-PBF). These issues hinder stable powder spreading, full densification, and microstructural control, thus limiting their industrial applicability. In this context, the objective of this work was to investigate the surface functionalization of gas-atomized AA2017 powder – an aircraft Al-Cu-Mg alloy from the 2xxx series (EN AW-2017, AlCu4MgSi) – as a viable strategy to improve flowability, laser absorption, and solidification behavior during L-PBF processing. Two approaches were explored: chemical etching using acidic (HNO_3) and basic (NaOH) solutions, and the addition of TiC particles with different sizes and concentrations. Chemical etching treatments improved powder flowability and laser energy absorption but promoted the formation of oxide layers on powder surface, which increased oxidation-related porosity in the as-built samples. Conversely, the addition of TiC effectively modified the alloy solidification, promoting strong microstructural refinement and a columnar-to-equiaxed transition, along with the formation of coherent Al_3Ti particles, resulting in dense and crack-free samples. A key and novel outcome of this work is that fine micrometer-sized TiC particles (<4 μm) outperformed nanoparticles in enhancing the microstructure and mechanical properties of the AA2017 alloy. Although nanoparticles can theoretically provide greater grain refinement and strengthening, their strong tendency to agglomerate limited their efficiency. Therefore, the addition of fine micrometer-sized TiC particles proved to be a practical and efficient route to improve the processability of high-strength aluminum alloys by L-PBF, while also being safer to handle than nanoparticles. Additionally, to the best of the author's knowledge, this work provides important and new insights into the mechanisms governing grain refinement, strengthening, and discontinuous yielding behavior in TiC-modified 2xxx series aluminum alloys in L-PBF for the first time in the literature.

Palavras-chave: Laser powder bed fusion; AA2017 aluminum alloy; Surface functionalization of the powder; Chemical Etching; Particle Addition.

RESUMO

FUNCIONALIZAÇÃO DA SUPERFÍCIE DO PÓ DA LIGA DE ALUMÍNIO AA2017 PARA USO EM MANUFATURA ADITIVA

A manufatura aditiva (AM) de ligas de alumínio de alta resistência enfrenta desafios devido à sua alta refletividade, elevada condutividade térmica, baixa fluidez do pó e suscetibilidade ao trincamento durante a fusão seletiva a laser em leito de pó (L-PBF). Esses fatores dificultam a deposição estável das camadas de pó, a completa densificação e o controle microestrutural, limitando assim sua aplicabilidade industrial. Nesse contexto, o objetivo deste trabalho foi investigar a funcionalização da superfície do pó atomizado a gás da liga AA2017 – uma liga aeronáutica Al-Cu-Mg da séried 2xxx (EM AW-2017, AlCu4MgSi) – como uma estratégia viável para melhorar a fluidez, a absorção do laser e o comportamento de solidificação durante o processamento por L-PBF. Duas abordagens foram exploradas: ataque químico com soluções ácida (HNO_3) e básica (NaOH), e adição de partículas de TiC com diferentes tamanhos e concentrações. Os tratamentos químicos melhoraram a fluidez e a absorção do laser dos pós, mas promoveram a formação de camadas de óxido na superfície das partículas, aumentando a porosidade relacionada à oxidação nas amostras impressas. Em contraste, a adição de TiC modificou de forma eficaz a solidificação da liga, promovendo forte refinamento microestrutural e transição de grãos colunares para equiaxiais, juntamente com a formação de partículas coerentes de Al_3Ti, resultando em amostras densas e livres de trincas. Um resultado chave e inovador deste trabalho é que as partículas de TiC de tamanho micrométrico fino (<4 μm) superaram as nanopartículas na melhoria da microestrutura e das propriedades mecânicas da liga AA2017. Embora teoricamente nanopartículas possam proporcionar maior refinamento e endurecimento, sua forte tendência à aglomeração limitou sua eficiência. Portanto, a adição de partículas micrométricas finas de TiC mostrou-se uma rota prática e eficiente para melhorar a processabilidade de ligas de alumínio de alta resistência por L-PBF, além de serem mais seguras de manusear do que nanopartículas. Além disso, até onde é de conhecimento da autora, este trabalho

fornece, pela primeira ver na literatura, contribuições importantes e inéditas sobre os mecanismos que governam o refino de grão, endurecimento, e o comportamento de escoamento descontínuo em ligas de alumínio da série 2xxx modificadas com TiC processadas por L-PBF.

Palavras-chave: Fusão seletiva a laser em leito de pó; Liga de alumínio AA2017; Funcionalização da superfície do pó; Ataque Químico; Adição de Partículas.

PUBLICATIONS

Scientific Papers:

– **BATISTÃO, B.F.**; PINOTTI, V.E.; LIMA, M.L.; RODRIGUES, A.G.; AMANCIO FILHO, S.T.; GARGARELLA, P. Wet chemical surface functionalization of AA2017 powders for additive manufacturing. **Powder Technology**, v. 443, 119938, 2024. DOI: doi.org/10.1016/j.powtec.2024.119938

– MATHIAS, L.E.T.; PINOTTI, V.E.; **BATISTÃO, B.F.**; ROJAS-ARIAS, N.; FIGUEIRA, G.; ANDREOLI, A.F.; GARGARELLA, P. Metal powder as feedstock for laser-based additive manufacturing: From production to powder modification. **Journal of Materials Research**, v. 39, p. 19-47, 2024. DOI: doi.org/10.1557/s43578-023-01271-8

– **BATISTÃO, B.F.**; AMANCIO-FILHO, S.T.; SILVA, L.V.M.; GARGARELLA, P. Tailoring ceramic particle size and fraction to optimize aluminum powders for additive manufacturing. Paper submitted to **Journal of Materials Research and Technology** in 21st October 2025, manuscript number JMRT-D-25-09533.

Conference Presentations:

– **BATISTÃO, B.F.**; RODRIGUES, A.G.; AMANCIO-FILHO, S.T.; GARGARELLA, P. Surface functionalization of metal powders for laser powder bed fusion. Poster presentation in the International Conference on Processing and Manufacturing of Advanced Materials (THERMEC'2023), Viena, Austria. July 2023.

– **BATISTÃO, B.F.**; AMANCIO-FILHO, S.T.; GARGARELLA, P. Laser powder bed fusion of surface functionalized AA2017 powders. Poster presentation in EUROMAT 2023, Frankfurt, Germany. September 2023.

– **BATISTÃO, B.F.**; AMANCIO-FILHO, S.T.; GARGARELLA, P. Microstructural characterization of the high strength AA2017 alloy produced by laser powder bed fusion. Poster presentation in the XXI B-MRS Meeting 2023, Maceio, Brazil. October 2023.

– **BATISTÃO, B.F.**; AMANCIO-FILHO, S.T.; GARGARELLA, P. Microstructural and mechanical characterization of the AA201 alloy produced by laser powder

bed fusion with the addition of TiC nanoparticles. Oral presentation in the XXII B-MRS Meeting 2024, Santos, Brazil. September/October 2024.

– **BATISTÃO, B.F.**; AMANCIO-FILHO, S.T.; GARGARELLA, P. Influence of TiC surface functionalization on physical and rheological properties of AA2017 powders for laser powder bed fusion. Poster presentation in the CBECiMat 25, Fortaleza, Brazil. November 2024.

– **BATISTÃO, B.F.**; AMANCIO-FILHO, S.T.; GARGARELLA, P. TiC surface functionalization of AA2017 powders for L-PBF: Influence of TiC particle size and concentration. Oral presentation in the The Materials Science & Technology (MS&T25) technical meeting, Columbus, USA. September/October 2025.

SUMMARY

TABLES INDEX

FIGURES INDEX

SYMBOLS AND ABBREVIATIONS

A	Hamaker constant
AA	Aluminum alloy
AE	Aeration energy
AM	Additive manufacturing
AMS	Additive manufacturing suitability
ANOVA	Analysis of variance
AR	Aeration rate
ASTM	American Standard for Testing Materials
b	Burgers vector
BD	Building direction
BF	Bright field
BFE	Basic flow energy
BSE	Backscattered electron
C_0	Solute concentration
c_j	Atomic concentration of solute element
CAD	Computer-aided design
CBD	Conditioned bulk density
CCL	Cumulative crack length
CET	Columnar-to-equiaxed transition
CI	Compressibility index
CNTs	Carbon nanotubes
D	Crystallite size
D	Host particle diameter
d	Guest particle diameter
D_{gb}	Average grain size
DED	Direct energy deposition
DEMa	Department of Materials Engineering
DF	Dark field
DRS	Diffuse reflectance spectroscopy
E2EM	Edge-to-edge matching model

E_v	Volumetric energy density
EDS	Energy-dispersive X-ray spectroscopy
EBSD	Electron backscatter diffraction
$F_{VdW,H-G}$	Van der Waals attraction force
FE	Flow energy
ffc	Flow factor
FFT	Fast Fourier Transforms
FIB	Focused ion beam
FRI	Flow rate index
G	Shear modulus
G	Temperature gradient
GxR	Cooling rate
GA	Gas atomization
h	Hatch distance
HAADF	High-angle annular dark-field
HRTEM	High-resolution transmission electron microscopy
IDR	Inter-decil range
IMAT	Institute of Materials Science, Joining and Forming
IPF	Inverse pole figure
K	Shape factor
k	Hall-Petch coefficient
k	Partition coefficient
k_B	Boltzmann constant
k_j	Solute strengthening coefficient
L	Powder bed length
L-PBF	Laser powder bed fusion
m	Atomic mass
m	Liquidus slope
MPB	Melt pool boundary
MPC	Melt pool center
OM	Optical microscopy
P	Laser power

PA	Plasma atomization
PD	Pressure drop
PF	Pole figure
PIPS	Precision ion polishing system
PREP	Plasma rotating electrode process
PSD	Particle size distribution
q	Airflow rate
Q	Growth restriction factor
R	Solidification rate
RSM	Response surface methodology
SAC	Surface area coverage
SAED	Selected area electron diffraction
SE	Specific energy
SEM	Scanning electron microscopy
SI	Stability index
S-OES	Spark optical emission spectrometry
STEM	Scanning transmission electron microscopy
t	Powder layer thickness
T	Melt temperature
TEM	Transmission electron microscopy
TUGraz	Graz University of Technology
UCS	Ultimate compressive strength
UTS	Ultimate tensile strength
UFSCar	Federal University of Sao Carlos
V_p	Volume fraction of particles
v	Scanning speed
WA	Water atomization
XRD	X-ray diffraction
z_0	Minimum contact distance
θ	Bragg angle
μ	Air viscosity
σ_c	Unconfined yield strength

σ_1	Consolidation stress
τ_0	Cohesion coefficient
μ	Dynamic viscosity
λ	Liquid surface tension
$(hkl)_m$	Crystallographic planes in matrix
$(hkl)_n$	Crystallographic planes in nucleant
$[uvw]_m$	Crystallographic directions in matrix
$[uvw]_n$	Crystallographic directions in nucleant
$d[uvw]_m$	Interatomic spacing along [uvw] in the matrix
δ	interplanar spacing mismatch
ΔT_{CS}	Constitutional undercooling
ΔT_{total}	Total undercooling
ΔT_{therm}	Thermal undercooling
ΔT_n	Critical nucleation undercooling
γ	Interfacial energy
ΔS_V	Entropy of fusion per unit volume
ρ	Dislocation density
ε	Microstrain
λ	Radiation wavelength
β	Full width at half maximum
$\Delta\sigma_g$	Grain-boundary strengthening
$\Delta\sigma_{SS}$	Solid-solution strengthening
$\Delta\sigma_{oro}$	Orowan strengthening
$\Delta\sigma_L$	Load-bearing strengthening
σ_0	Yield strength of the matrix

1 INTRODUCTION

Aluminum alloys combine excellent properties such as high specific mechanical strength, stiffness, and good thermal and electrical conductivity, making them increasingly attractive for aerospace and automotive applications that demand functional, lightweight, and cost-effective components. Currently, these components are commonly manufactured through casting, forging, extrusion, and powder metallurgy, which are traditional routes characterized by longer manufacturing times due to their multi-step processing [1].

Compared with these conventional techniques, laser powder bed fusion (L-PBF), an additive manufacturing (AM) process, offers advantages such as the ability to produce nearly fully dense components with complex geometries, reduced material waste, and minimal post-processing requirements [2]. In the L-PBF process, successive layers of powder are deposited and selectively melted by a moving laser beam following a defined scanning strategy, building the component layer by layer. At present, AlSi10Mg and Al12Si are the main aluminum alloys used in L-PBF because the presence of silicon narrows the solidification range, lowering volumetric shrinkage and tendency for solidification cracking (or hot cracking) in the final component [3].

However, processing aluminum alloys by AM remains challenging. Their high reflectivity and thermal conductivity demand elevated laser power to melt the material, while poor powder flowability can lead to melt pool instabilities and porosity. Additionally, steep thermal gradients during solidification promote microstructural anisotropy [4,5]. Increasing laser energy absorption through powder surface roughening has proven effective in addressing some of these issues, simultaneously improving flowability [6,7]. This type of surface modification, known as surface functionalization, involves adjusting surface morphology, roughness, chemical composition, or surface properties such as surface energy, wettability, biocompatibility, and reflectivity [8].

Surface functionalization can be achieved using physical methods (grinding, polishing, sandblasting, metallization) or chemical routes involving chemical reactions or electrochemical treatments to incorporate compounds or form surface films or coatings [7,9]. Other approaches include chemical etching

or particle deposition onto the metallic powder [8]. In the latter case, the added particles can also act as nucleating agents for new grains during solidification, resulting in a fine and equiaxed grain microstructure that promotes a more isotropic behavior of the component and reduces the occurrence of defects such as porosity and cracking [10].

Aluminum alloys of the 2xxx series (Al-Cu alloys) are widely used in the aerospace and automotive industries due to their high specific strength, good fatigue and corrosion resistance, and ductility. With the growing demand for components with complex geometries, the L-PBF processing of these alloys has gained increasing attention [11]. Among them, AA2017 aluminum alloy – an aircraft Al-Cu-Mg alloy from the 2xxx series (EN AW-2017, AlCu4MgSi) – is the oldest and best known of the Al-Cu system, benefiting from age-hardening through the formation of fine, coherent $Al_2Cu(Mg)$ precipitates uniformly dispersed in the matrix [12,13]. Nevertheless, its wide solidification range favors columnar grain growth, which increases susceptibility to solidification cracking and porosity, compromising the mechanical performance of the final component [10].

In this context, powder surface functionalization, by increasing roughness or modifying the chemical composition and properties (e.g., surface energy and reflectivity) of the surface, emerges as a promising strategy to increase laser energy absorption during AM, consequently reducing porosity and increasing densification and processing speed. In addition, the incorporation of particles for powder surface functionalization can provide heterogeneous nucleation sites during solidification. This promotes a fine and equiaxed microstructure and mitigates solidification-related issues of the AA2017 aluminum alloy, enabling its application in AM and improving the mechanical properties of the final part. Despite its potential, few studies have systematically investigated the influence of powder surface functionalization by chemical etching or addition of ceramic particles of different sizes on powder properties, L-PBF process, and final properties of aluminum alloy components produced by AM.

Therefore, **the motivation of this work was to investigate the influence of surface functionalization of AA2017 aluminum powder on the**

processability, microstructure, and mechanical properties of samples produced by AM via L-PBF processing. Three different powder surface functionalization strategies were evaluated:

a) **Chemical etching with an acidic HNO_3 solution;**
b) **Chemical etching with a basic NaOH solution;**
c) **Addition of TiC particles with different particle sizes (45 nm, <4 µm, and 44 µm) in three different concentrations (1, 2, and 4 wt.%).**

The physical, chemical, and rheological properties of the surface-functionalized and gas-atomized AA2017 powders were analyzed to allow a direct comparison and to understand the effects of each treatment on powder flowability, laser absorption, solidification behavior, and final performance of the L-PBF-manufactured parts.

To achieve **the general objective, the following specific goals were defined:**

i. **Powder preparation and characterization:** obtain gas-atomized powder, apply the aforementioned surface functionalization treatments, and characterize the powders' morphology, chemical composition, flowability, apparent density, laser absorption, and rheological properties;
ii. **Process parameter understanding and optimization:** investigate the influence of L-PBF processing parameters on sample porosity and crack density using Box-Behnken design of experiments and analysis of variance (ANOVA) methodologies;
iii. **Sample manufacturing via L-PBF and characterization:** manufacture samples using optimized L-PBF processing parameters and perform microstructural (grain morphology and size, phase formation, and crack susceptibility) and mechanical (microhardness, compression, and tensile tests) analyses;
iv. **Comparison of surface functionalization treatment:** evaluate and compare the effectiveness of the different surface functionalization routes (chemical etching and TiC addition), identifying which approach is more suitable for improving L-PBF processability of high-strength aluminum alloys.

2 LITERATURE REVIEW

2.1 Additive manufacturing

Additive manufacturing (AM), which consists of layer-by-layer fabrication processes, has gained prominence in recent years due to its flexibility in producing complex, customized, and tailored geometries within short timeframes, thereby reducing or even eliminating the need for assembly of multiple components and consequently lowering manufacturing costs [4].

Initially used for rapid prototyping, AM technology has recently advanced to enable the manufacturing of components and products with complex geometries that are difficult or even impossible to manufacture using conventional techniques. As a result, it has been increasingly adopted in medical implants, as well as in the aerospace and automotive industries, among other applications [14,15]. For example, porous metallic biomedical implants with customized surfaces can be produced through AM processes (Figure 2.1a), improving fixation and osseointegration compared to conventional porous coatings [15,16]. It also enables the manufacture of aircraft components with highly complex geometries (Figure 2.1b), contributing to significant lightweighting [17].

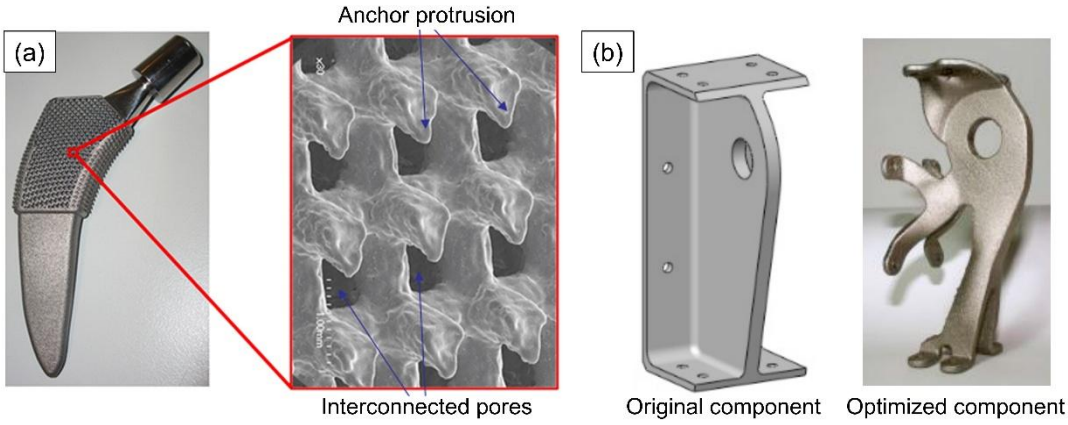

Figure 2.1 – (a) Implant produced by AM with micrometric surface features to enhance fixation. Reprinted and adapted from [16] with permission from Elsevier. (b) Original aircraft bracket and lightweight-optimized bracket manufactured by L-PBF. Reproduced from [17] under the terms of the CC BY NC ND license.

With the potential for application across various industries, the manufacturing of metallic objects is currently the fastest-growing sector of AM [14]. As highlighted by Debroy *et al.* [4], despite the significant advances in AM technologies in recent years, a better understanding of raw materials, processes, structures, properties, and performance is necessary to produce defect-free and safe AM parts.

In general, AM processes consist of the repetitive deposition of layers with thicknesses ranging from 20 μm to 1 mm and the localized melting of the material using an energy source [18]. The raw material can be in the form of powder, wire, or sheets, and the energy source can be a laser, electron beam, electric arc, or ultrasonic vibration [4].

Metallic materials are commonly used in powder form in AM due to their controlled melting and ease of feeding. The manufacturing of these powders is mainly carried out by gas atomization (GA), plasma atomization (PA), water atomization (WA), or plasma rotating electrode process (PREP) [4,18,19]. In the GA process, a high-pressure flow of nitrogen or argon is used to atomize the molten alloy, resulting in spherical powder particles with a relatively smooth surface, as shown in Figure 2.2a, although surface roughness increases in the presence of satellite particles, i.e., small particles attached to the surface of larger ones. Powder particles with irregular sizes and rough surfaces are obtained in the WA process, where a high-pressure water jet is used to atomize and solidify the molten metal, as shown in Figure 2.2b. In the PREP process, perfectly spherical powder particles with smooth surfaces (Figure 2.2c) are obtained by rotating a metallic rod along its longitudinal axis, with the tip melted by an electric arc or plasma. Highly spherical powders with narrow particle size distribution (PSD) can also be produced by PA, where a metal a metal wire is melted by plasma torches and atomized into fine droplets that solidify into uniform particles [4,18,19].

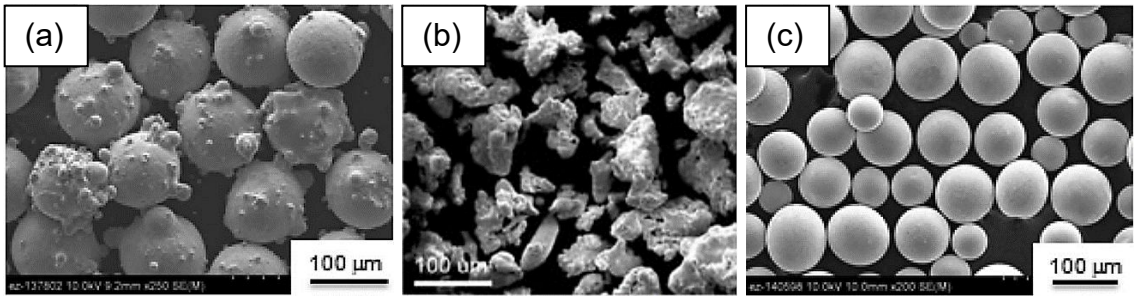

Figure 2.2 - Comparison of the powder particle shapes obtained by (a) GA [20], (b) WA [21], and (c) PREP [20]. (a,c) Reproduced from [20] with permission from John Wiley and Sons, and (b) Reproduced from [21] with permission from Springer Nature.

The morphology and surface texture of the powder will affect powder physical properties that are important for AM processes, such as powder flowability and apparent density (or packing) [22]. A more uniform particle size distribution promotes homogeneous metal melting, good surface finish, and mechanical properties. In contrast, powders with irregular shapes and rough surfaces, such as those produced by WA, result in lower powder flowability and higher surface roughness of the AM-produced component [4]. Additionally, small powder particles, although they may reduce flowability, fill the spaces between larger particles, improving apparent density, and reduce the size of satellite particles, also enhancing the surface finish of the metallic component produced by AM. The selection of powder particle size for the AM process will depend on a balance between cost and the desired surface finish, since finer powders, which improve surface finish, may be more expensive than coarser powders depending on the manufacturing process [22].

The main AM processes for metals such as steels, aluminum alloys, titanium and its alloys, and nickel-based alloys are laser powder bed fusion (L-PBF), and directed energy deposition (DED). In the first process, a thin layer of powder is spread and compacted on the build platform, and each powder layer is melted by a laser beam. Subsequent layers are added and fused until the part is fully built, after which the excess powder is removed. Unlike L-PBF, in the DED process, the material in the form of powder or wire is fed simultaneously with the application of the laser or electron beam onto a region of the substrate. In this

case, a powder layer is not used, and the raw material is melted before being deposited onto the substrate. In general, the DED process is characterized by high deposition rates and the possibility of producing large components, but it has lower precision and surface quality, and produces less complex components than those produced by L-PBF [5].

Due to these characteristics, DED is generally used for manufacturing large, low-complexity components and for the repair of large components, such as turbine blades, as well as for applications in the automotive and aerospace industries. In contrast, L-PBF is suitable for printing complex parts and is employed in various industries for advanced applications in aerospace and electronics, as well as for scaffolds (porous implants) in tissue engineering [5,23].

2.1.1 Laser powder bed fusion

L-PBF is a process that uses a high-intensity laser as an energy source to melt powder layer by layer according to a 3D CAD (Computer-Aided Design) model of the component, as schematically shown in Figure 2.3. After processing the 3D model, the build process begins with the deposition of a thin layer of metallic powder on the build platform inside a chamber. Once the powder is added, the high-density laser is used to melt selected areas according to the model. After the laser scanning is completed, the build platform is lowered, and a new powder layer is deposited, with selected areas again melted by the laser. This process is repeated until the complete construction of the component is finished. Due to the high temperatures required for material melting, an inert gas such as argon or nitrogen is used inside the chamber to prevent oxidation or other issues that could affect the mechanical properties of the component [24].

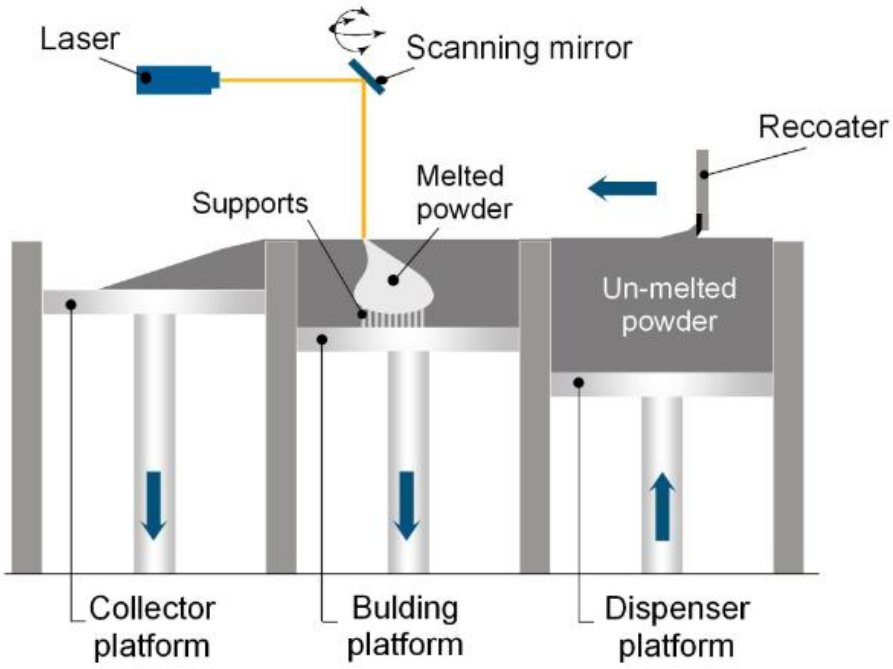

Figure 2.3 - Schematic illustration of the L-PBF process. © 2017 IEEE, reproduced with permission from [25].

The main parameters that can be adjusted to optimize the process are the laser power (P in W), the scanning speed (v in mm/s), the hatch distance (h in mm), and the powder layer thickness (t in mm). Figure 2.4 shows an illustration of these process parameters. These parameters affect the volumetric energy density (E_v in J/mm^3) available to heat and melt the powder, which is estimated by Equation 2.1 [26]:

$$E_v = \frac{P}{v.h.t}\left(\frac{J}{mm^3}\right) \tag{2.1}$$

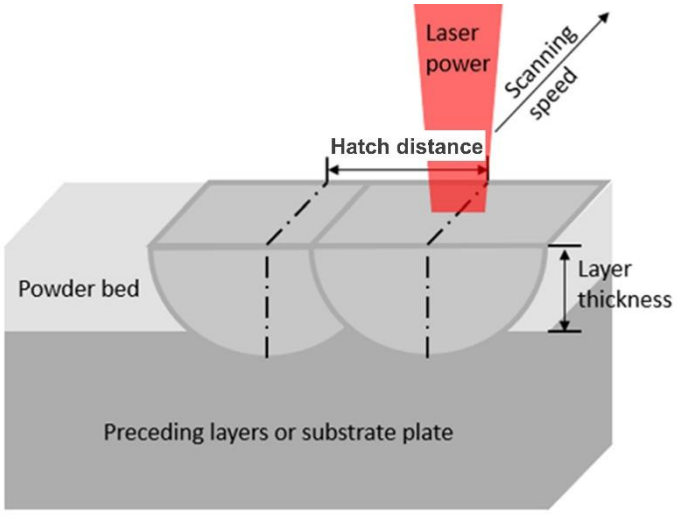

Figure 2.4 - Illustration of the L-PBF processing parameters (Reprinted and adapted from [24] with permission of AIP Publishing).

The combination of low laser power, high scanning speed, and large powder layer thickness results in insufficient energy and may lead to poor adhesion of the melt pool to the previous layer and the formation of coarse molten metal droplets (a phenomenon known as balling). This effect tends to generate porosity and cause delamination due to weak bonding between printed layers and thermal stresses [24,27]. Conversely, the combination of high laser power and low scanning speed can lead to material evaporation, which may condense on the laser window and compromise the processing [24]. Therefore, to obtain parts with high density and achieve the lowest porosity levels, an intermediate energy density should be used, with optimal energy density values also depending on the material and the AM equipment employed [23].

The hatch distance and the scanning strategy are two other parameters that can affect the relative density and microstructure of the part produced by L-PBF. The hatch distance should provide sufficient overlap between adjacent scan tracks to enable metallurgical bonding between them. Excessive overlap increases the manufacturing time, whereas insufficient overlap limits the maximum powder layer thickness, leading to longer build times due to the need for more layers, and gaps may form within the layers because of the lack of bonding between adjacent tracks [3,28].

Similarly, the scanning strategy defines the path followed by the laser in each layer and can be used to minimize defects and control the microstructure [3,29]. The most common scanning strategies are shown in Figure 2.5. Considering that the scanning strategy influences the thermal gradient, the main difference among the scanning patterns will be the degree of remelting, which makes the cooling rate and local heat treatment different. The unidirectional scanning strategy (Figure 2.5a) concentrates heat in consistent paths, generating higher directional thermal gradients and promoting columnar grain growth with stronger crystallographic texture. Conversely, the bidirectional scanning strategy (Figure 2.5b) distributes heat more evenly, typically producing less textured microstructures [30]. Together with the heat flow direction, the cooling rate and the thermal gradient affect the dislocation density, grain size, and texture [29].

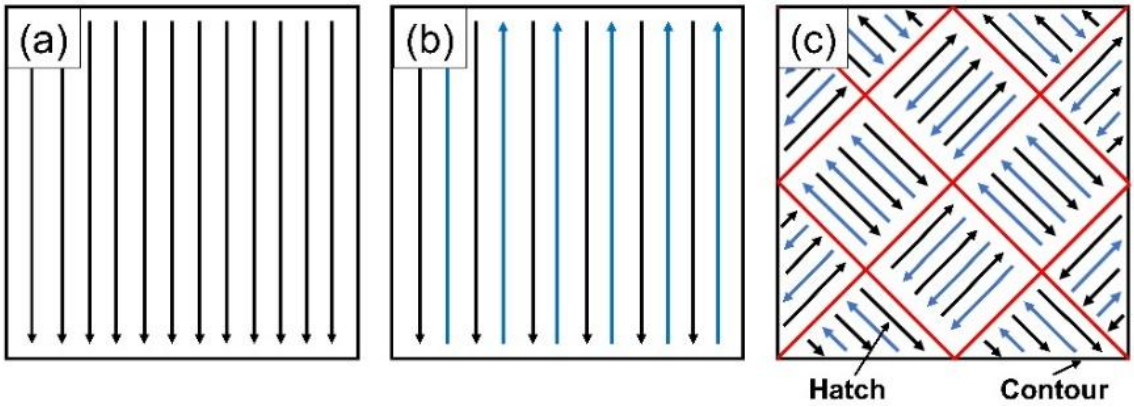

Figure 2.5 - Scanning strategy: (a) unidirectional, (b) bidirectional, and (c) island or chessboard pattern. Illustration created by the author based on [23,26,31].

The scanning direction can be kept constant or rotated between two successive layers [31]. Thijs *et al.* [32] showed that a 90° rotation of the scanning direction between layers using a bidirectional scanning strategy can significantly reduce the strong <100> fiber texture along the scanning direction in L-PBF-processed AlSi10Mg alloy. On the other hand, the use of a double scanning strategy with pre-sintering, in which the consolidation scan of the layer is preceded by a low-energy scan that levels the surface, proved effective in

reducing interlayer porosity, allowing the achievement of a relative density of 99.82% in AlSi10Mg alloy produced by L-PBF [33].

The quality of AM-produced parts can also be significantly influenced by the characteristics of the raw material, which include particle size distribution, surface morphology, composition, and powder flowability [4]. For example, powders with a narrow particle size range flow better and can produce parts with high strength and hardness, while powders with smaller particle sizes allow the fabrication of 3D parts using lower laser energy intensity and result in better surface finish [24].

In addition, the ability of the powder to absorb laser energy, which also depends on the laser wavelength, affects the energy efficiency of the L-PBF process. The laser systems used in L-PBF have evolved from CO_2 lasers (λ = 10600 nm) to Nd:YAG (λ = 1060 nm) and Yb:YAG fiber lasers, due to the higher absorption of metallic materials at the wavelengths of fiber lasers, which improves the energy efficiency of the L-PBF process [24]. Figure 2.6 shows the higher effectiveness of radiant energy absorption by different materials at shorter laser wavelengths. However, the absorption of laser energy by aluminum at a wavelength of 1064 nm (fiber laser) remains low, ranging between 5% and 15%. In this case, for wavelengths near 10000 nm (CO_2 laser), the laser energy is likely better absorbed by the naturally formed Al_2O_3 oxide layer on the surface of the powder particles. The absorption efficiency of CO_2 laser energy by aluminum increases with the thickness of the Al_2O_3 layer, following a sigmoidal curve, where it increases sharply after a threshold and approaches saturation at larger layer thicknesses [34,35].

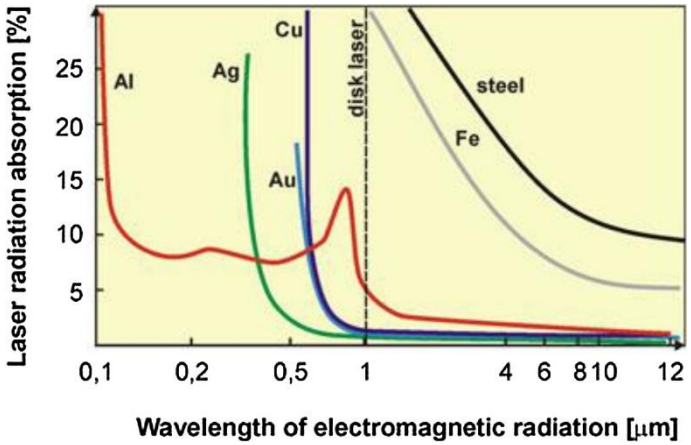

Figure 2.6 - Laser energy absorption by different materials as a function of wavelength. Reproduced and adapted from [36] with permission from Springer Nature.

Furthermore, since part of the laser energy is not absorbed, processing highly reflective metallic materials, such as aluminum alloys, requires higher laser power to ensure that the powder is fully melted and to prevent defects associated with insufficient melt pool consolidation during solidification, such as lack-of-fusion defects. However, higher laser power can lead to increased convective transport of liquid or vaporized metal out of the melt pool (spatter ejection) [3,22].

Despite the necessary care with the process parameters mentioned above to avoid the occurrence of defects, the main challenges in the manufacturing of metallic parts by AM are the presence of voids and the anisotropy of the microstructure and mechanical properties. Porosity may result from melt pool instability due to high laser energy density, the presence of trapped gas inside powder particles, or inadequate penetration of the upper layer's melt pool into the substrate or the previously deposited layer, and can cause delamination between layers after part manufacturing [4,5]. Microstructural anisotropy, on the other hand, occurs due to the thermal gradient during the addition of subsequent material layers and may be limited by the depth of heat penetration from the laser beam [5].

2.1.1.1 Solidification and metallurgy in L-PBF processing

Typical defects in parts produced by L-PBF, such as porosity, balling, cracks, and residual stress, originate from the interaction of the laser with the material, which is subjected to a complex thermal cycle during the L-PBF process. The brief interaction of the laser with the powder layer leads to rapid heating of the material above its melting temperature due to laser energy absorption. After the laser passes, the molten material undergoes rapid cooling, along with multiple cycles of remelting and cooling when subsequent layers are irradiated and the material is exposed to heat again [18,37]. As shown in Figure 2.7, the size and shape of the melt pool, as well as the cooling rate and phase transformations occurring during processing, are affected by heat transfer and material flow resulting from the laser-material interaction [37].

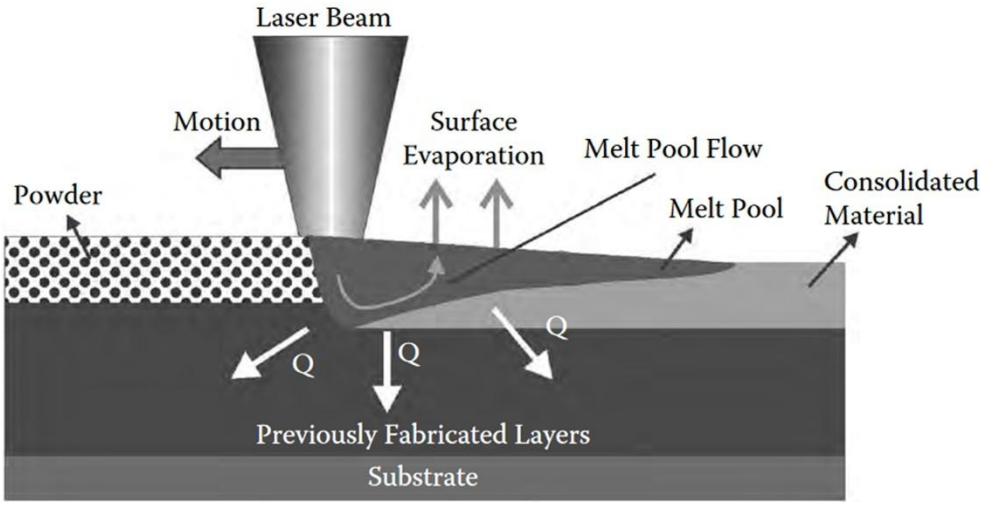

Figure 2.7 - Schematic illustration of the interaction between the laser and the metallic powder layer in the L-PBF process. Used with permission of Taylor and Francis Group LLC - Books, from [37]; permission conveyed through Copyright Clearance Center, Inc.

The high solidification rate in the L-PBF process, resulting from the high cooling rate (10^3-10^6 K/s), leads to the formation of non-equilibrium microstructures, such as refined microstructures and precipitates, as well as metastable phases. Rapid solidification also extends solute solubility and

increases chemical homogeneity, reducing segregation and producing a more uniform precipitate distribution [37,38].

The final microstructure, as well as the resulting mechanical properties, are affected by the ratio between the temperature gradient (G) and the solid-liquid interface velocity, or solidification rate (R), which in turn are influenced by the laser scanning speed and power [14,22]. Figure 2.8 presents a solidification map constructed using the combined forms G/R and GxR of the temperature gradient G and solidification rate R, and shows the effect of these variables on the solidification microstructure. The G/R ratio determines the solidification mode, which can result in planar, cellular, columnar dendritic, or equiaxed dendritic microstructures as the G/R ratio decreases. Meanwhile, the cooling rate, represented by the product GxR, governs the scale of the solidification microstructure, with an increase in cooling rate leading to refinement of the microstructure [4].

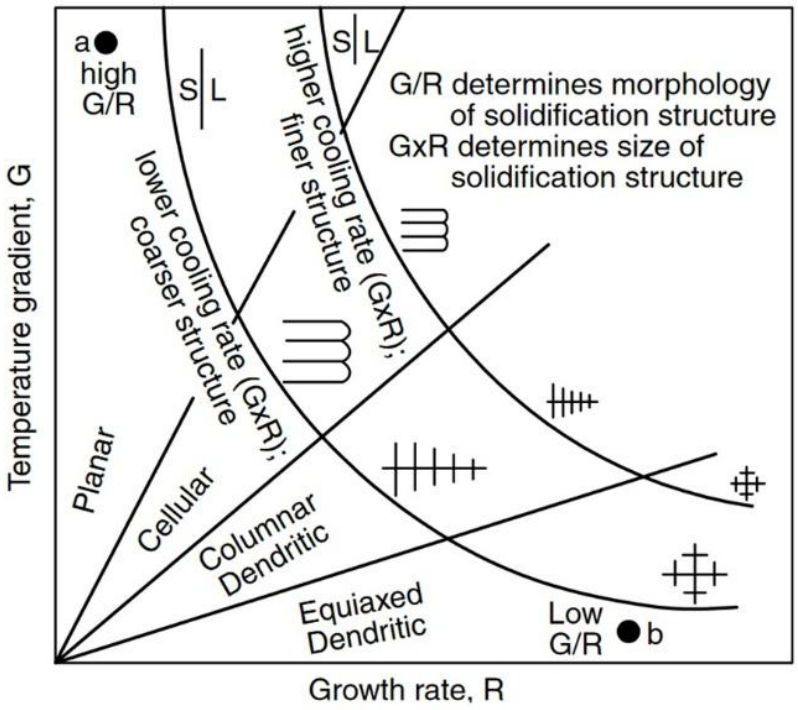

Figure 2.8 - Morphology and size of the solidification microstructure as a function of the temperature gradient G and the solidification rate R. Reproduced from [39] with permission from John Wiley and Sons.

The two most common solidification microstructures in AM are columnar and equiaxed grains [4]. During solidification, the first equilibrium phase to solidify has a different composition from the liquid, with lower solute solubility, resulting in solute enrichment in the liquid near the solidification interface. Consequently, the compositional difference at the solid/liquid interface causes a local variation in the liquidus temperature, leading to an unstable condition with supercooled liquid ahead of the solidification front and the formation of protrusions at the solid/liquid interface. This results in cellular or dendritic solidification structures, with solute-rich liquid retained between the solidifying columnar grains, which tend to grow along the direction of the maximum thermal gradient [10,37]. The columnar grain microstructure, as shown in Figure 2.9, is generally coarser and more heterogeneous, producing anisotropy in mechanical properties, which can be detrimental depending on the application [4,14].

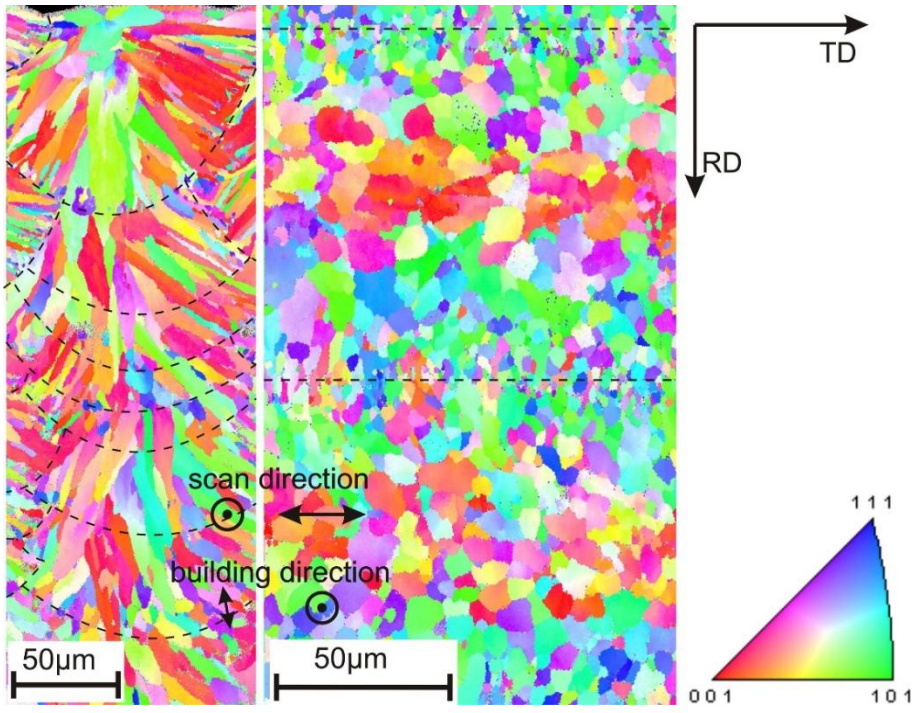

Figure 2.9 - Electron backscatter diffraction (EBSD) orientation maps of L-PBF-produced AlSi10Mg alloy: (a) frontal view and (b) top view. Reprinted from [32] with permission from Elsevier.

Furthermore, directional solidification also causes crystallographic texture, because the preferred growth directions of some grains will align with the direction of the maximum thermal gradient, and the rapid growth of these grains will result in crystallographic orientation. As shown in Figure 2.9, grains in the centerline of the melt pool of the L-PBF produced AlSi10Mg alloy tend to have <001> directions oriented parallel to the building direction, while between the center and the boundary of the melt pool, <110> and <111> directions of the grains are aligned along the building direction [32,37,38].

The transition from columnar to equiaxed grains occurs with the nucleation of numerous equiaxed dendrites in the constitutionally supercooled liquid near the dendritic columnar solidification front. Unlike columnar grains, equiaxed grains are generally smaller, do not exhibit a predominant crystallographic texture, and result in more uniform mechanical properties [3,4]. Despite the high thermal gradient in the L-PBF process, equiaxed grains can form due to constitutional supercooling near the solidification interface, heterogeneous nucleation on partially melted powders, or the addition of refractory particles, and are more likely to occur in alloys with a narrow solidification range through surface solidification [3,4].

The microstructure and texture can also be influenced by process parameters such as powder layer thickness and hatch distance. Because L-PBF involves epitaxial growth and partial remelting between adjacent melt tracks, decreasing the powder layer thickness and hatch distance increases the extent of remelting. This promotes the continued growth of grains already oriented along the building direction, thereby strengthening the morphological and crystallographic texture [32].

Similarly, the geometry of the melt pool influences grain growth, grain structure, and the crystallographic texture of the L-PBF-fabricated part. Each melt pool is composed of a fine-grained core, a coarser-grained boundary of the melt pool, and the heat-affected zone (HAZ) [3,32,33,37,40], as shown in Figure 2.10 for the L-PBF-produced AlSi10Mg alloy.

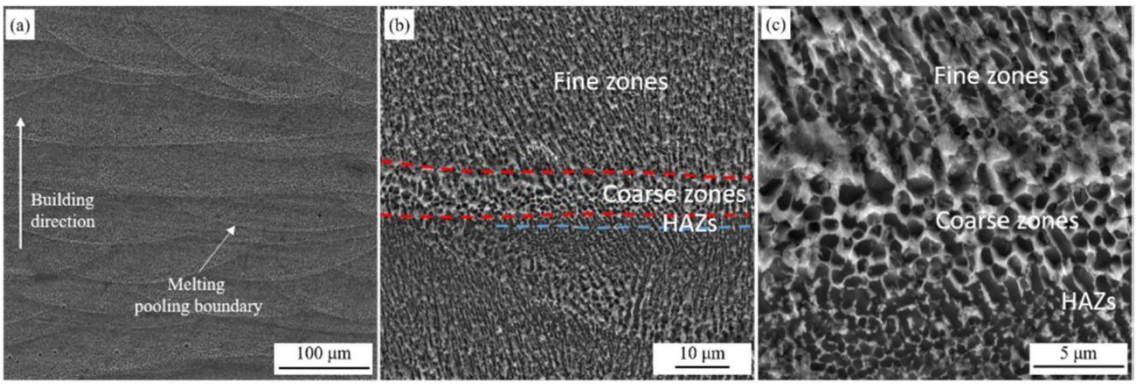

Figure 2.10 - Frontal view of the microstructure of L-PBF-produced AlSi10Mg alloy showing the different regions of the melt pool. Reprinted and adapted from [40] with permission from Elsevier.

The shape of the melt pool is influenced by process parameters and can be semicircular (conduction mode) or conical (keyhole mode) in the longitudinal section, as shown in Figure 2.11, depending on the energy input intensity and scanning speed [3,4]. Conduction mode occurs at low energy density, while keyhole mode occurs at high energy density, resulting in greater laser penetration into the solidified metal. During solidification, the solid-liquid interface tends to migrate in the build direction in conduction mode, and the curvature of the bottom of the melt pool is reduced, as shown in Figure 2.11a. In keyhole mode solidification (Figure 2.11b), lateral migration of the solid-liquid interface predominates at the bottom of the melt pool, and the curvature of the melt pool bottom increases as solidification progresses [41].

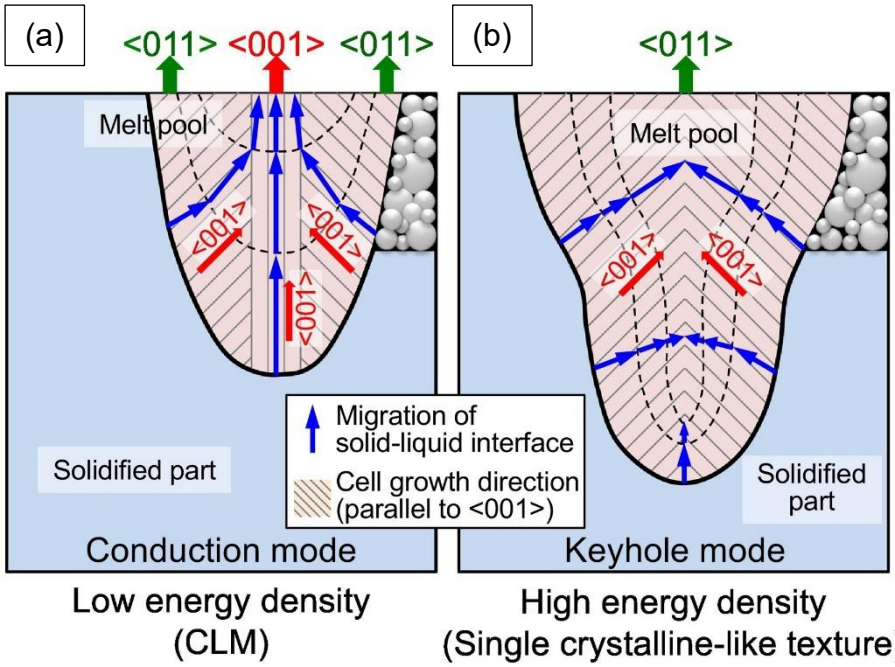

Figure 2.11 - Schematic illustration showing the migration direction of the solid–liquid interface during solidification in (a) conduction mode and (b) keyhole mode. Reproduced from [41] under the terms of the Creative Commons CC BY 4.0 license.

In conduction mode, grains are preferentially columnar, as the direction of the maximum thermal gradient and the migration of the solid-liquid interface tend to be parallel to the build direction, which additionally results in crystallographic texture, since grains with growth directions aligned with the maximum thermal gradient grow faster. In contrast, in keyhole mode (Figure 2.11b), grains are finer and exhibit high misorientation, because grains at the bottom of the melt pool rarely grow along the build direction, and the high depth-to-width ratio of the melt pool reduces remelting at the boundaries [3,41]. Furthermore, if fusion is not properly controlled in keyhole mode Trapped vapor during the process can also generate porosity, which in this case is nearly spherical due to the repeated formation and collapse of unstable keyholes, leaving voids inside the material known as keyhole porosity [4]. Keyhole forms when the laser locally vaporizes the material due to the extremely high energy input, creating a deep and narrow cavity, that becomes unstable and collapses, trapping vapor inside and resulting in keyhole porosity [42].

2.2 Aluminum alloys

Aluminum alloys exhibit good mechanical strength and low density, properties that, combined with high thermal and electrical conductivity, ease of manufacturing, and good corrosion resistance, make them suitable for use in various structures and components, for example, in the automotive and aerospace industries. In the automotive industry, the use of aluminum alloys in many parts as a substitute for steel has reduced vehicle weight, while in aircraft manufacturing, high-strength aluminum alloys meet the stringent requirements for materials with high strength and low density [43,44].

Aluminum alloys are classified into heat-treatable and non-heat-treatable alloys. The first group includes the non-heat-treatable alloys of the 1xxx series, which consist of essentially pure aluminum with only trace amounts of alloying elements, and the 3xxx, 5xxx, and 8xxx series, whose main alloying elements are manganese, magnesium, and iron and silicon, respectively. To increase tensile strength, alloys in these series must be strengthened by work hardening through cold working, usually combined with annealing treatments [44,45].

Among the heat-treatable alloys are the 2xxx, 4xxx, 6xxx, and 7xxx series, whose main alloying elements are copper, silicon, magnesium and silicon, and zinc and magnesium, respectively. In these aluminum alloys, the solubility of alloying elements in the solid solution decreases with decreasing temperature, as shown in Figure 2.12 for Al-Cu alloys (2xxx series), resulting in concentrations exceeding the equilibrium solid solubility at room temperature or slightly higher. Consequently, these alloys respond to solution treatment, quenching, and precipitation hardening [44–46].

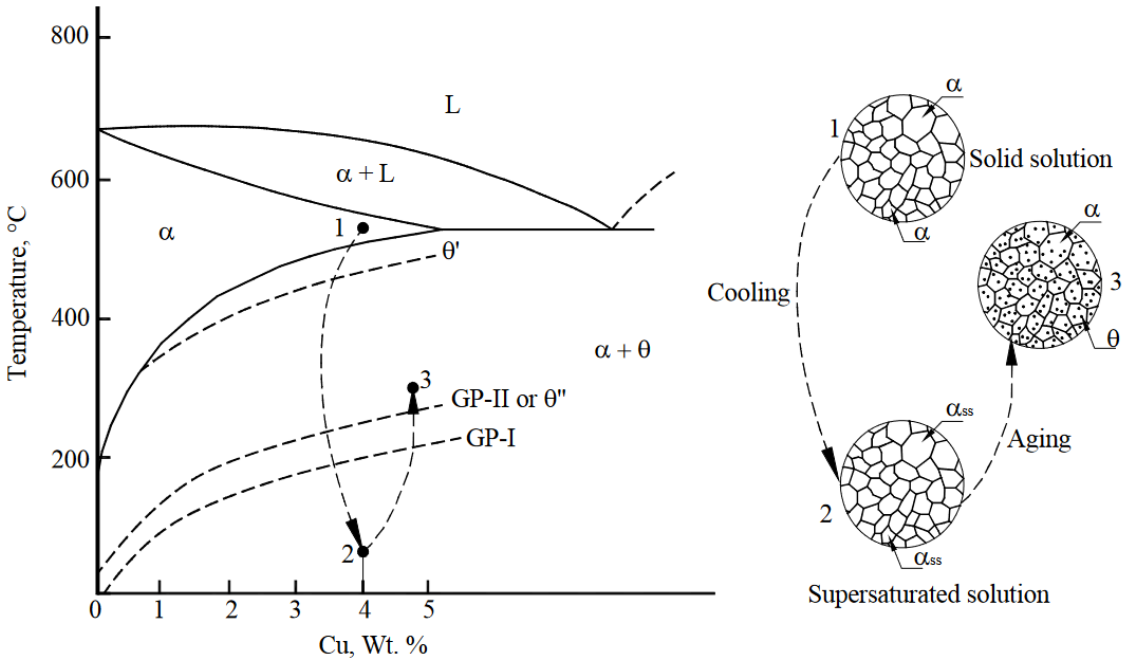

Figure 2.12 - Al-rich portion of the Al-Cu phase diagram showing the solution treatment and precipitation processes. Reproduced from [46], under the terms of the Creative Commons CC BY 3.0 license, and adapted from [47], © copyright 2013, reprinted by permission of Informa UK Limited, trading as Taylor and Francis Group.

Copper, as the primary alloying element, provides high mechanical strength and hardness at room or elevated temperatures in 2xxx-series Al-Cu aluminum alloys, because the addition of copper and magnesium to aluminum increases mechanical strength through solid-solution strengthening and precipitation hardening of the metastable phases θ''/θ' (Al_2Cu) and S''/S' (Al_2CuMg) with heat treatment [48].

As shown in Figure 2.12, for precipitation hardening to occur in Al-Cu alloys, the alloy must be heated above the solvus temperature to dissolve the θ phase, eliminate segregation in the alloy, and thereby obtain a homogeneous α-Al solid solution. Once solubilization occurs, the alloy is rapidly cooled to limit diffusion and prevent nucleation of the equilibrium θ phase, resulting in a supersaturated solid solution (SSS or α_{SS}). Precipitates are then formed during subsequent heating in the aging treatment of the supersaturated solid solution,

developing sequentially with increasing temperature or aging time according to the following sequence [45,46,49]:

$$SSS \rightarrow \text{GP Zones} \rightarrow \theta'' \rightarrow \theta' \rightarrow \theta\ (Al_2Cu)$$

The formation of GP zones and θ'' precipitates progressively increase the mechanical strength of Al-Cu alloys, while the formation of θ' and θ precipitates leads to a decrease in strength, as shown in Figure 2.13 for different binary alloys in the Al-Cu system. Starting from the supersaturated solid solution, the relatively low hardness is due to resistance to dislocation movement provided by solid-solution strengthening. As the aging time increases, coherent GP zones form within the α-Al matrix, and additional stress is required for dislocations to move through these coherent regions, resulting in increased hardness [50].

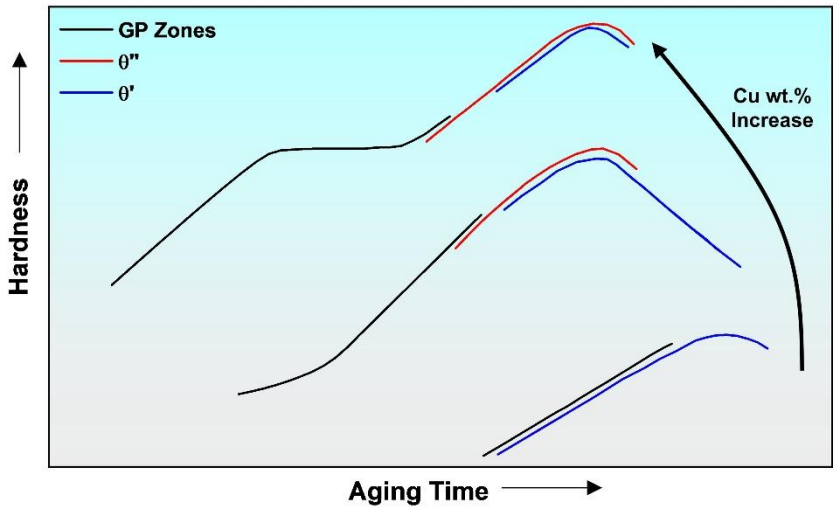

Figure 2.13 – Schematic representation of the precipitation hardening response of binary Al-Cu alloys with varying Cu contents, showing the evolution of hardness as a function of aging time. Illustration created by the author based on [50].

The θ'' precipitates are also coherent with the α-Al matrix, exhibiting atomic structures with (001) planes identical to the α-Al matrix and (010) and (100) planes very similar; however, there is slight distortion along the [001] direction perpendicular to the θ'' plates, requiring dislocations to be forced through the strained α-Al matrix, which continuously increases hardness. Continued aging leads to the formation of θ' and θ precipitates, which grow in size and become

more widely spaced as the heat treatment time increases, facilitating dislocation bowing and bypassing of the precipitates, and thus, hardness decreases with aging time. Therefore, the combination of θ'' and θ' precipitates results in maximum hardness, which depends on the alloy composition, as shown in Figure 2.13, and on the aging treatment temperature [50].

Among the 2xxx-series alloys, AA2017 – an aircraft Al-Cu-Mg alloy (EN AW-2017 or AlCu4SiMg) – was the first developed and one of the earliest to be used in the aerospace sector. Also known as duralumin, AA2017 exhibits good atmospheric corrosion resistance and processability, along with intermediate mechanical strength and ductility, with a service temperature below 100 °C. Today, the alloy is used in rivets for structural applications in construction and transportation, and in general engineering applications, although it has been replaced in aircraft wing skin applications by AA2024-T3, which has a higher yield strength after slight cold working and natural aging [45,51,52].

AA2017 is primarily composed of copper, magnesium, manganese, silicon, and iron, with the role of these alloying elements, particularly copper, being to increase mechanical strength through the formation of fine, dispersed precipitates of $Al_2Cu(Mg)$ coherent with the matrix after aging, as previously described [12,13]. The addition of magnesium and manganese can also contribute to increasing tensile strength and yield strength in Al-Cu alloys after solution treatment and quenching, with natural aging (at room temperature) of Al-Cu-Mg alloys potentially increasing mechanical strength while maintaining high ductility. However, manganese reduces ductility, so its concentration should be kept below 1 wt.% in commercial alloys. High mechanical strength and hardness at elevated temperatures can be achieved in Al-Cu-Mg alloys containing iron. However, these alloys must have sufficient silicon to allow iron to form FeSi intermetallic particles, preventing excess iron from forming Al_7Cu_2Fe constituents that reduce the copper available for precipitation strengthening. Silicon also contributes to strengthening through the formation of Mg_2Si precipitates [45].

The main heat treatments used for AA2017 are annealing (O) and natural aging (T4 or T451). In annealing, the alloy is heated to a high temperature to achieve complete recrystallization and remove the effects of prior treatments,

while the T451 temper involves a controlled plastic deformation of about 1-3% by stretching after natural aging to relieve residual stresses [13]. The mechanical properties of AA2017 after these treatments are shown in Table 2.1.

Table 2.1 - Typical mechanical properties of AA2017 alloy [13,51].

Temper	Ultimate Tensile Strength (MPa)	Yield Strength $\sigma_{0,2}$ (MPa)	Elongation in 50 mm (%)	Hardness (HV)*
AA2017-O	180	70	22	50
AA2017-T4, T451	427	275	22	123

* Converted from Brinell hardness according to the ASTM E-140 standard [53].

2.2.1 Additive manufacturing of aluminum alloys

The main aluminum alloys commonly used in AM are AlSi10Mg and Al12Si. This is because they can be easily melted, as they exhibit high fluidity due to the presence of silicon and low volumetric shrinkage due to the narrow solidification range and the large fraction of the eutectic Al-Si microconstituent [3]. Although much of the research on L-PBF focuses on these Al-Si alloys, the alloys widely used in the aerospace and automotive industries are high-strength alloys from the 2xxx, 5xxx, 6xxx, and 7xxx series, which exhibit greater ductility. Unlike AlSi10Mg, these alloys contain alloying elements (Cu, Mg, Zn, Si) that can form complex phases during subsequent heat treatment, effectively enhancing their mechanical properties [3,10,11]. However, some widely used precipitation-hardenable alloys, such as the 7xxx-series Al-Zn alloys, contain volatile elements such as zinc (Zn), which can cause turbulence in the melt pools and porosity, thus complicating their use in AM [18].

The 2xxx-series Al-Cu alloys exhibit high specific mechanical strength, good fatigue and corrosion resistance, and with the increasing demand for complex-shaped components, L-PBF of Al-Cu alloys has gained prominence [11]. L-PBF of high-strength Al-Cu alloys has been reported in several studies, for example, for the AA2219 [54,55], AA2618 [54,56,57], and Al-4.24Cu-1.97Mg-0.56Mn (AA2024) [58,59] alloys, showing that the mechanical properties of Al-Cu

alloys produced by L-PBF, without subsequent heat treatment, are comparable to those produced by conventional manufacturing methods [58]. Zhang *et al.* [58] demonstrated that the relative density of Al-Cu-Mg alloys is strongly dependent on the scanning speed, as shown in Figure 2.14. Lowering the scanning speed improves the wettability of the liquid metal and the metallurgical bonding between adjacent layers, which reduces the size of defects (voids) and microcracks, resulting in a high relative density (99.8%) in samples produced at a low scanning speed (5 m/min) [58].

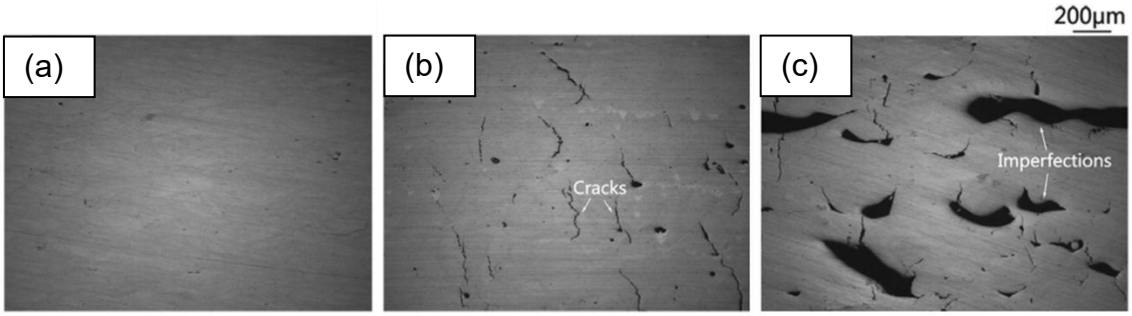

Figure 2.14 - Cross-sectional view of L-PBF-produced Al-Cu-Mg alloy samples at different scanning speeds: (a) 5 m/min, (b) 10 m/min, (c) 20 m/min. reprinted from [58] with permission from Elsevier.

Analysis of the L-PBF-produced Al-Cu-Mg alloy by Zhang *et al.* [58,59] revealed a very fine microstructure composed of a supersaturated primary α-Al phase and a copper-rich interdendritic eutectic microconstituent, as shown in Figure 2.15 in gray and white, respectively. The refined microstructure and supersaturated α-Al solid solution increased the tensile strength to 402.4 MPa, compared to 185 MPa for the cast AA2024-O alloy, but reduced the ductility from 12% to 6% [58].

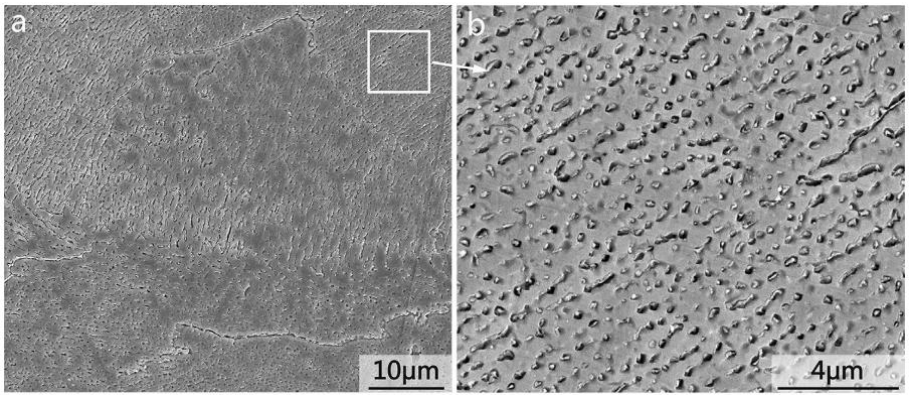

Figure 2.15 - SEM images of (a) the longitudinal section of L-PBF-produced Al-Cu-Mg alloy and (b) details of the selected area in (a). Reprinted from [58] with permission from Elsevier.

Among the Al-Cu alloys, despite being the oldest and most well-known in the system, studies on their processing by L-PBF remain scarce. This may be related to the alloy's wide solidification range, which promotes the formation of solidification cracks and porosity after solidification. During solidification, constitutional supercooling promotes the development of cellular or dendritic substructure within grains, while the high thermal gradient favors the growth of elongated columnar grains with long liquid channels trapped between the solidified regions. As the temperature and volume of liquid decrease, volumetric shrinkage and thermal contraction in these channels result in cavities and solidification cracking [10], as shown in Figure 2.14b. In this context, Dos Santos Bomfim *et al.* [60] investigated the influence of laser power and scanning speed on relative density, crack fraction, and crack length, revealing the high crack susceptibility of the L-PBF-processed AA2017 that remained with a crack fraction higher than 4% regardless of the L-PBF processing parameters.

Despite its application potential, L-PBF of aluminum alloys is also challenged by the high reflectivity of the powder at wavelengths commonly used in the process, as well as by its low flowability and high thermal conductivity. This requires high laser power to fully melt the material and overcome rapid heat dissipation [18,33].

2.3 Powder surface functionalization for additive manufacturing

The challenges previously mentioned in AM of aluminum alloys, such as high reflectivity and poor powder flowability, can be addressed through surface modification of the powder for AM, a treatment known as powder surface functionalization. Bergström, Powell, and Kaplan [6,61] demonstrated that for a laser beam incident normal to a surface, energy absorption by the metal increases with increasing surface roughness, especially for highly reflective metals such as copper and aluminum, due to enhanced energy absorption from multiple reflections on the rough surface. Figure 2.16 shows the increase in laser energy absorption (A_{rough}/A_{smooth}) with increasing surface roughness (σ/τ) for different materials, considering a laser beam incident normal to the surface (θ_0 = 0°). Increased roughness also reduces the contact area between particles, which decreases agglomeration and improves powder flowability [7].

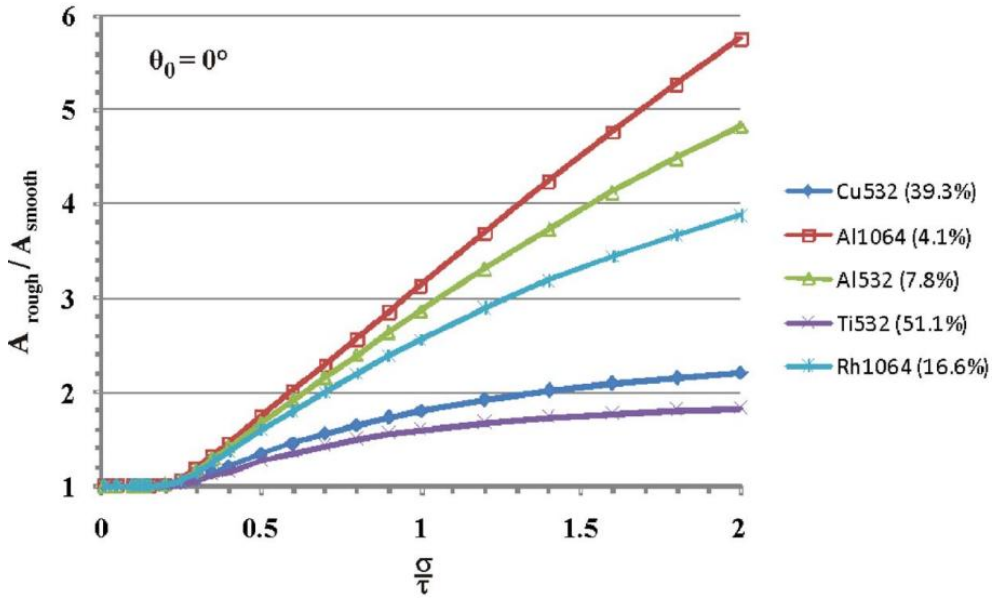

Figure 2.16 - Ratio of laser absorption on rough surfaces (A_{rough}) to smooth surfaces (A_{smooth}) as a function of roughness (σ/τ) for different materials. The absorption on the smooth surface is shown in paratheses in the legend. The numbers following the material symbols indicate the laser wavelength (in nm) analyzed, while σ and τ represent surface roughness amplitude and surface correlation length. Reprinted from [61], with the permission of AIP Publishing.

One way to obtain rough surfaces is through chemical etching. In this case, the increase in surface area in homogeneous materials occurs through different mechanisms, such as preferential material removal at grain boundaries, and electrochemical or kinetic effects due to ion bombardment of the surface [8]. Various chemical etching methods for aluminum alloys, such as using HCl solutions [62–64], NaOH [65–67], and H_3PO_4 and HNO_3 [68], have proven effective in creating rough surfaces.

Figure 2.17 shows the increase in surface roughness of an aluminum alloy after immersion in a 4 mol/L HCl solution for different durations. As discussed by Liu *et al.* [62], Sarkar, Farzaneh, and Paynter [63], and Wu *et al.* [64], the roughness obtained through chemical etching depends on the alloy's microstructure and the solution used, since regions with higher surface energy, such as grain boundaries and defects, are corroded more easily, and ions such as halides in the solution play an important role in pit formation on the surface.

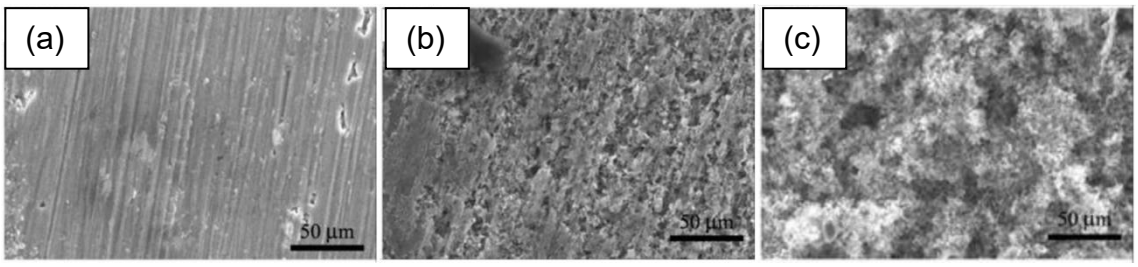

Figure 2.17 - Surface roughness of an aluminum alloy after immersion in a 4 mol/L HCl solution for (a) 0 min, (b) 15 min, and (c) 30 min. Reprinted from [62] with permission from Elsevier.

Although surface modification techniques have been widely explored for various materials, their application to powder surface functionalization in AM remains limited. Recent studies have begun to address this gap. Veron *et al.* [69] employed chemical etching of AlSi12 powders using NaOH solution to enable the fabrication of multi-material components combining metallic and dielectric (alumina) regions via laser fusion on a powder bed in air. Likewise, Lanoue *et al.* [70] demonstrated that similar structures could be produced using AlSi12 powders treated with pure hot water. Chemical and optical analyses revealed the

formation of hydroxide-rich surface layers whose thickness increased with NaOH concentration and exposure time to hot water, resulting in higher specific surface area and enhanced laser absorbance. These findings highlight the potential of chemical surface treatments for tailoring powder properties and encourage further studies on their influence on the physical behavior of powders and their influence on L-PBF processability of aluminum alloys.

Another way to increase laser energy absorption in aluminum alloys is through the addition of ceramic particles [71], such as TiN [71,72], TiC [73–76], TiB_2 [77–80], SiC [81–84], AlN [85,86], WC [87], TiO_2 [88], NbC [89], and CaB_6 [90,91], to the aluminum alloy powder, which exhibit high laser energy absorption [74]. Table 2.2 presents the laser absorption (λ = 1060 nm and 10600 nm) of some of these particles in comparison with alloys commonly used in L-PBF.

Table 2.2 - Laser absorption of some alloys and ceramic materials.

Material	Absorption		Reference
	λ = 1060 nm	λ = 10600 nm	
AlSi10Mg	0,38	NR*	[71]
Al_2O_3	0,03	0,96	[92]
Ti	0,77	0,59	[92]
TiC	0,82	0,46	[92]
TiN	0.87	NR*	[71]
TiB_2	0,80	NR*	[93]
SiC	0,78	0,66	[92]
WC	0,82	0,48	[92]

* NR = Not reported

For example, Gao *et al.* [71] reported a decrease in laser reflectivity from 62% to 25% during L-PBF of the AlSi10Mg aluminum alloy with the addition of 2 wt% TiN nanoparticles to the alloy powder, as shown in Figure 2.18, enabling L-PBF using a low laser power of 100 W. The increase in laser absorption with

the addition of ceramic particles to the aluminum alloy powder also occurs due to the greater number of laser reflections on the particle surfaces [71,94].

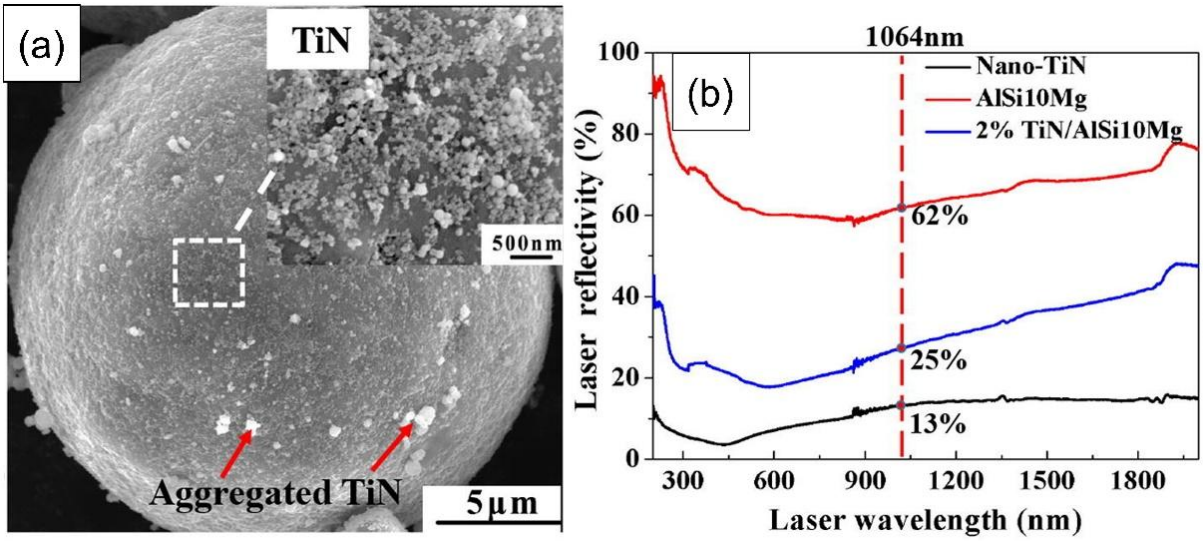

Figure 2.18 - (a) SEM image of the TiN/AlSi10Mg composite powder and (b) reflectivity of the different powders. Reprinted and adapted from [71] with permission from Elsevier.

Similarly, Lin *et al.* [74] reported a reduction in laser reflectivity to approximately 7.5%, and Zhou *et al.* [75] reported an increase in laser absorption of approximately 40% when TiC particles were added to aluminum powder and AlSi10Mg alloy powder, respectively, processed by L-PBF.

Apart from the laser wavelength, beam size, and material composition, laser reflectivity is strongly affected by the powder's physical attributes, such as particle size distribution, morphology, surface texture, porosity, and layer thickness [95,96]. Balbaa *et al.* [97] observed a slight rise in absorptivity when the average AlSi10Mg particle size decreased from 40 μm to 9 μm, consistent with Boley, Khairallah, and Rubenchik [96], who noted that finer particles enhance surface area and multiple light scattering within the powder bed, improving energy absorption. The influence of the size of the ceramic reinforcement was also investigated. For example, Xue *et al.* [98] found that reducing the SiC particle size from 50 μm to 6 μm in an AlSi10Mg/15 wt.% SiC powder mixture increased laser absorptivity by about 7%, due to a more uniform particle dispersion.

The addition of carbon or carbon-based particles has also proven effective in increasing the absorption of laser radiation by highly reflective metallic powders [99], for example, graphene [100,101] and carbon nanotubes (CNTs) [102,103] mixed with aluminum or aluminum alloy powders for L-PBF.

Besides the potential to increase laser absorption, ceramic particles added to aluminum alloy powder can act as heterogeneous nucleation sites for new grains during solidification, reducing the amount of undercooling required for equiaxed growth and thus enabling a fine equiaxed grain microstructure that accommodates stress and prevents cracking [10,79]. However, for this refinement to occur, the added particle must have a crystal structure similar to aluminum to minimize lattice distortions, with similar atomic packing along corresponding crystallographic planes, thermodynamic stability in the desired alloy, and availability [10]. ZrH_2 [10], TiN [71], TiC [73,104–106], TiB_2 [77–79,107], LaB_6 [108,109], CaB_6 [90,91] and AlN [86] particles added to aluminum powders have already proven effective in microstructure refinement in L-PBF, as shown in Figure 2.19. TiC is among the most commonly employed ceramic reinforcements in aluminum alloys for L-PBF, mainly due to its high hardness, stiffness, good wetting behavior, and thermodynamic stability in liquid aluminum [74,110,111].

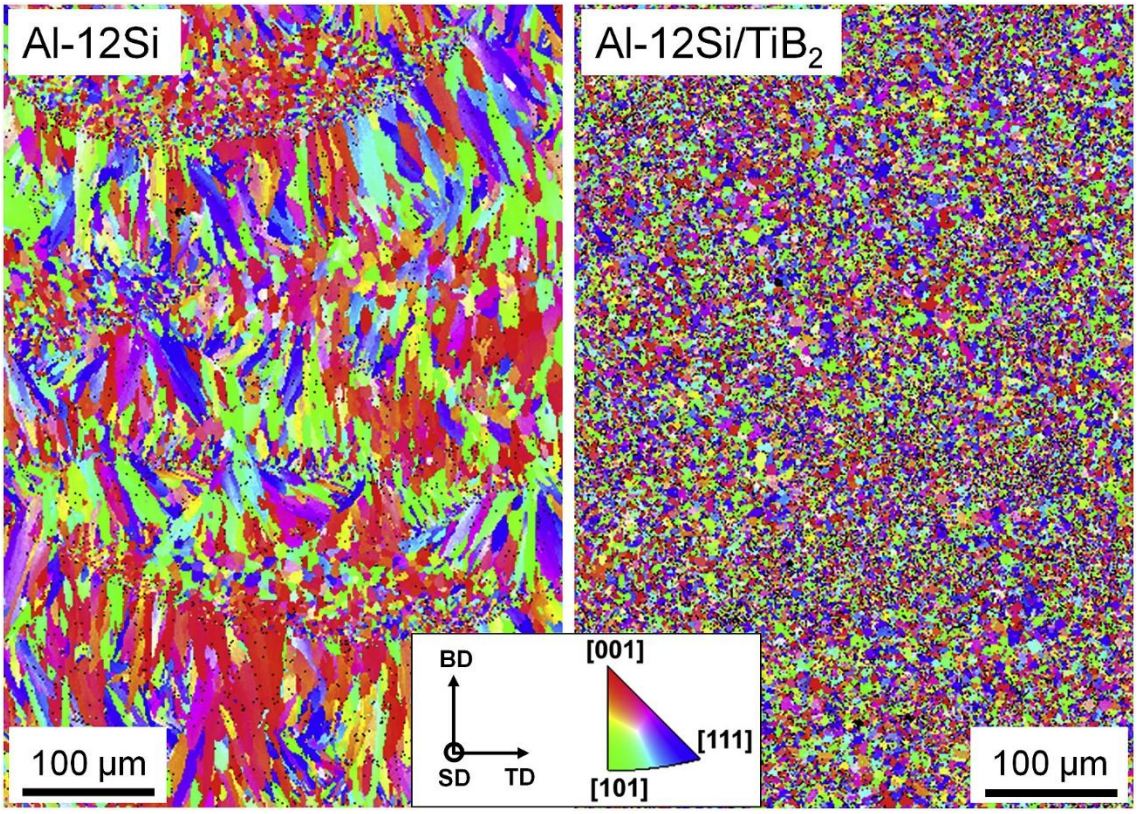

Figure 2.19 - Inverse pole figure (IPF) maps generated by EBSD of the Al-12Si alloy and the TiB_2-functionalized Al-12Si alloy (Al-12Si/TiB_2), measured from cross-sections parallel to the building direction (BD) in L-PBF (the SD and TD vectors indicate the scanning and transverse directions, and the colors indicate crystallographic orientation). Reprinted from [107] with permission from Elsevier.

Consequently, the addition of ceramic particles contributes to an increase in tensile strength while maintaining high ductility [76,78,83]. Grain refinement, which also occurs due to the restriction of α-Al matrix grain growth caused by the presence of ceramic particles, along with effective load transfer between the α-Al matrix and the ceramic particles during loading, results in the increase of tensile strength. Furthermore, similar to grain refinement strengthening is an effective mechanism for simultaneously improving ductility and tensile strength, the homogeneous distribution of ceramic particles along the grain boundaries of the α-Al matrix can also enhance ductility by restricting crack propagation during plastic deformation [73,74,77,79,80].

In general, nanoparticles are preferred because reducing the size of ceramic reinforcements is known to enhance the mechanical performance of aluminum metal matrix composites [110]. In addition to strengthening effects, nanoparticles can also improve powder flowability by increasing the surface roughness of micrometer-sized particles, thereby enlarging the interparticle spacing and decreasing van der Waals attraction forces [112]. Xi *et al.* [113] demonstrated that decreasing the TiB_2 particle size from the micrometer to the submicrometer range in AlSi10Mg alloys processed by L-PBF led to simultaneous improvements in ultimate tensile strength and ductility. This behavior is attributed to the limited interfacial wettability and mismatch in lattice coherence between metallic and ceramic phases, which render larger ceramic particles more prone to interfacial cracking under mechanical loading [110]. Similar enhancements in relative density, microhardness, wear resistance, and corrosion resistance have been reported when the size of ceramic reinforcements was reduced from the micrometer to the submicrometer scale in L-PBF-processed alloys [75,81,98,113].

However, to fully exploit the benefits of nanoscale inoculants, a homogeneous distribution of nanoparticles across both the powder surface and the resulting L-PBF microstructure is essential [110,112]. Achieving such dispersion is challenging because nanoparticles tend to agglomerate owing to their high surface energy and strong interparticle forces [112]. Beyond processing issues, nanoparticles also raise safety concerns due to their potential health risks, especially via inhalation, but also through dermal and ocular exposure [114–116]. Consequently, recent research [60,75,81,98,107,113,117,118] has begun exploring the use of larger ceramic particles for surface functionalization of metal powders in additive manufacturing as a safer and more manageable alternative. Nonetheless, the effectiveness of these larger particles, including the optimal particle size and concentration required to achieve desirable powder and microstructural and mechanical properties of the as-built L-PBF component, are not yet well established, highlighting a current gap in the literature.

3 MATERIALS AND METHODS

This work aimed to investigate the influence of surface functionalization of AA2017 aluminum powder - an aircraft Al-Cu-Mg alloy from the 2xxx series (EN AW-2017, AlCu4MgSi) - on the processability, microstructure, and mechanical properties of samples produced by additive manufacturing (AM) via laser powder bed fusion (L-PBF) processing. To achieve this objective, the powder was produced by gas atomization and surface-functionalized using chemical etchings (NaOH and HNO_3) and the addition of TiC particles with different sizes (45 nm, 4 µm, and 44 µm) and concentrations (1, 2, and 4 wt.%), followed by the characterization of the powders. To process these powders, the optimized L-PBF processing parameters were investigated with the support of the design of experiments and analysis of variance (ANOVA), enabling a deeper understanding of their influence on the process. Using the identified processing parameters, samples were produced by L-PBF for microstructural and mechanical characterization. This research was conducted in part at the Department of Materials Engineering (DEMa) at Federal University of São Carlos (UFSCar), Brazil, and in part at the Institute of Materials Science, Joining and Forming (IMAT) at Graz University of Technology (TU Graz), Austria. Figure 3.1 presents a flowchart summarizing the experimental procedure, which is discussed in detail in the next sections.

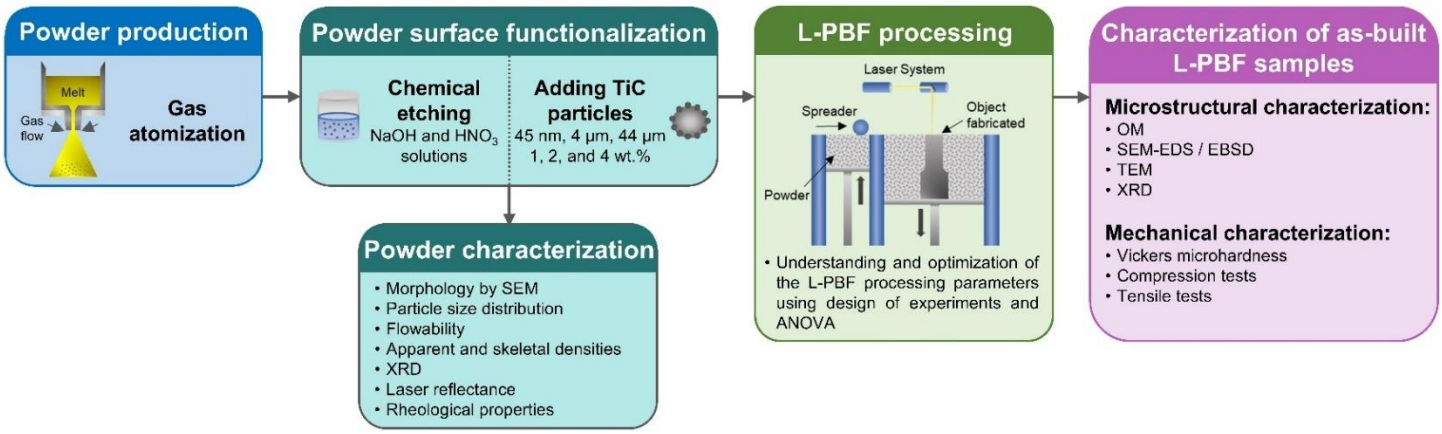

Figure 3.1 - Sequential workflow of powder preparation, powder surface functionalization, and L-PBF processing.

3.1 Powder manufacturing

The AA2017 alloy was produced by melting commercially pure metals (aluminum, copper, magnesium, silicon, iron, manganese, and titanium, each with a purity above 99.5%) in an Power-Trak 50-30 induction furnace (Inductotherm Corp. EUA). The resulting alloy ingot was analyzed by spark optical emission spectrometry (S-OES) (SPECTRO MAXx, SPECTRO Analytical Instruments GmbH, Germany) following the ASTM E1251-17a [119] standard to determine its chemical composition (wt.%). The measured composition is presented in Table 3.1, alongside the nominal composition specified for AA2017 in ASTM B211/B211M-23 [120], demonstrating that the measured composition is within the acceptable range specified by the standard.

Table 3.1 - Chemical composition (wt.%) of the AA2017 alloy determined by S-OES and compared with the standard composition specified in ASTM B211/B211M-23 [120].

	Chemical Composition (wt.%)									
	Si	**Fe**	**Cu**	**Mn**	**Mg**	**Cr**	**Zn**	**Ti**	**Others**	**Al**
ASTM B211/B211M	0.20-0.80	0.70*	3.5-4.5	0.4-1.0	0.4-0.8	0.1*	0.25*	0.15*	0.15*	Bal.
S-OES	0.5065	0.30	4.49	0.4783	0.4205	0.0195	0.0018	0.0510	0.0331	Bal.

* Maximum values for AA2017 alloy according to ASTM B211/B211M-23 [120].

The AA2017 alloy powder was produced via gas atomization (GA) using argon as the atomizing medium in a HERMIGA 75/5VI system (Phoenix Scientific Industries Ltd., formerly Powder Systems International Ltd., UK), which has a manufacturing capacity ranging from 3 to 10 kg of aluminum alloy powders. During atomization, the powders were collected in two separate containers, a primary collector and a cyclone separator. Only the material obtained from the primary collector was employed in this study, as the cyclone fraction predominantly contained ultrafine particles (<20 μm). The collected powder was subsequently sieved for 30 minutes using a EML 450 Digital Plus (Nexopart, formerly Haver & Boecker, Germany) mechanical vibrator equipped with sieves

of 20, 32, 45, 63, 75, 106, 150, and 250 μm opening diameters. The particle fraction between 20 and 63 μm was then homogenized in a shaker-mixer for 120 minutes at 35 rpm prior to the surface functionalization treatments and L-PBF processing.

3.1.1 Surface functionalization using chemical etchings

Two distinct chemical etching treatments were applied to modify the surface of the atomized AA2017 powders, based on the commonly used chemical solutions for modifying aluminum surfaces [65–68] and preliminary tests that indicated their effectiveness in altering the surface chemistry and morphology. In the first treatment, the powder was immersed in a nitric acid (HNO_3) solution with a concentration of 2.8 mol/L for 2 minutes, while in the second, it was immersed in a sodium hydroxide (NaOH) solution with a concentration of 0.25 mol/L for 5 minutes. The HNO_3-based surface functionalization was carried out in batches of 100 g of powder per 80 mL of solution, whereas the NaOH treatment was performed using 500 g of powder per 400 mL of solution. Maintaining the powder-to-solution ratio was essential to ensure reproducibility across batches.

After etching, both solutions were filtered using qualitative filter paper, and the treated powders were rinsed thoroughly with distilled water before being dried in a vacuum oven at 80 °C for 48 hours. Following drying, the powders were sieved again to eliminate agglomerates formed during treatment, and the fraction between 20 and 63 μm was selected for subsequent L-PBF processing. The recovery efficiency of the powders after drying was approximately 91% for the HNO_3-treated samples and 92% for those treated with NaOH. After the additional sieving step, the overall yield decreased to about 78% and 69% for the HNO_3 and NaOH treatments, respectively. The lower final yield was attributed to powder agglomeration during drying, which led to particle retention in the sieves.

3.1.2 Surface functionalization using TiC particles

TiC particles were selected due to their superior mechanical properties, including high hardness and elastic modulus, good wettability, and thermodynamic stability in molten aluminum [74,110,111], in addition to their well-

established effectiveness as grain refiners in aluminum alloys [105,106]. Three different TiC particle sizes were used as guest particles in this study: 35-55 nm (nanoparticles), <4 μm (fine micrometer-sized particles), and 44 μm (coarse micrometer-sized particles). The TiC nanopowder (35-55 nm, 99.5+% purity, nearly spherical morphology, product number NG04CO1902) and the coarse micrometer-sized TiC powder (44 μm, 99.9+% purity, 325 mesh, product number NG11EM0201) were purchased from Nanografi® (Nanografi Nano Technology, Turkey). The fine micrometer-sized TiC powder (<4 μm, ≥99% purity, product number 594849) was purchased from Sigma-Aldrich® (a brand of Merck KGaA, Germany).

Each TiC powder was mixed with gas-atomized AA2017 powder at concentrations of 1 wt.%, 2 wt.%, and 4 wt.% using a shaker mixer [121] operated at 15 rpm for 4 hours, resulting in nine distinct TiC surface-functionalized powders. The samples are denoted according to TiC size and concentration as follows, as shown in Table 3.2.

Table 3.2 - Samples designations according to TiC particle size and concentration.

TiC	**TiC Particle Size**		
Concentration	**35-55 nm**	**<4 μm**	**44 μm**
1 wt.%	1TiC45nm	1TiC4μm	1TiC44μm
2 wt.%	2TiC45nm	2TiC4μm	2TiC44μm
4 wt. %	4TiC45nm	4TiC4μm	4TiC44μm

3.2 Powder characterization

3.2.1 Physical Properties

The morphology and shape of the powder particles were examined by scanning electron microscopy (SEM) using a Quanta 400 (FEI Company, now part of Thermo Fisher Scientific, USA) microscope equipped with an Oxford Inca Energy 250 (Oxford Instruments, UK) energy-dispersive X-ray spectroscopy (EDS) system. Particle size distribution (PSD) was determined according to

ASTM B822-20 [122] via laser diffraction using a HORIBA LA-930 (HORIBA Scientific, Japan) instrument. Ethylene glycol and a vibration-feeding unit were employed to prevent particle agglomeration during the measurement. From the PSD curves, the characteristic diameters corresponding to 10%, 50%, and 90% of the cumulative volume frequency (d_{10}, d_{50}, and d_{90}, respectively) were obtained. The surface roughness of the powder particles was analyzed using laser scanning confocal microscopy with an LEXT OLS 4000 (Olympus Corporation, Japan) microscope.

The apparent density of the powders was measured following ASTM B417-22 using a Carney funnel, while the skeletal density was determined by helium gas pycnometry according to ASTM B923-22 [123] with a AccuPyc 1330 (Micromeritics Instrument Corporation, USA) instrument. Each density measurement was repeated five times to ensure reproducibility. Additionally, the powders' laser reflectance over the 400-950 nm wavelength range was assessed by diffuse reflectance spectroscopy (DRS) using a UV 3600 UV-Vis-NIR (Shimadzu Corporation, Japan) spectrophotometer equipped with an integrating sphere.

3.2.2 Chemical and phase compositions

The powders were metallographically prepared for cross-sectional analysis through sequential grinding and polishing, and their microstructure and chemical composition were examined using SEM coupled with an EDS system. Oxygen content was quantified via the inert gas fusion method with infrared absorption detection using a ONH-836 (LECO Corporation, USA) oxygen/nitron/hydrogen analyzer. Phase identification of the powders was performed by X-ray diffraction (XRD) using a D8 Advance ECO (Bruker Corporation, Germany) diffractometer, operating with Cu-$K_{\alpha 1}$ radiation (λ = 1.54 Å) over a 2θ range of 10–90° at a scan rate of 0.02° per minute. The local surface chemical composition was further analyzed by micro-Raman spectroscopy using a HR800 Evolution (HORIBA Scientific, Japan) spectrometer with a 633 nm laser as the excitation source. Laser power was carefully controlled to prevent thermal

effects, and spectra were collected over the range of 0-1200 cm^{-1}, averaging three accumulations of 60 seconds each.

3.2.3 Rheological properties

The flow behavior of the gas-atomized and surface-functionalized powders was assessed using an FT4 powder rheometer (Freeman Technology, a Micromeritics company, UK) in accordance with ASTM D7891-24 [124]. Measurements were performed under various testing modes, including dynamic flow, aerated, packed, and shear conditions, as detailed by Langlais, Demers, and Brailovski [125]. Prior to testing, the powders were dried at 80 °C for 24 hours to minimize the influence of moisture on flowability. Additionally, powder flowability was evaluated using a Carney funnel following ASTM B964-23 [126], with ten measurements conducted per powder sample for comparison.

3.2.3.1 Dynamic flow condition

In the dynamic flow test, the powder is slightly agitated by a rotating blade performing descending and ascending helical movements. The initial cycle, known as the conditioning cycle, establishes the baseline, after which the powder volume and mass in the vessel (plain base) are measured to calculate the conditioned bulk density (CBD) using Equation 3.1 [125]:

$$\text{Conditioned bulk density (CBD)} = \frac{\text{Mass}}{\text{Volume}} \left(\frac{\text{g}}{\text{cm}^3}\right) \tag{3.1}$$

Following the conditioning cycle, seven additional cycles of constant blade speed (100 mm/s) and four cycles with variable blade speed (ranging from 100 mm/s to 10 mm/s) are performed. The flow energy required to move the blade during specific descent (FE_{D1}, FE_{D7}, FE_{D8}, FE_{D11}) and ascent (FE_{A6}, FE_{A7}) cycles is used to determine key powder flow metrics, including the specific energy (SE), stability index (SI), flow rate index (FRI), and basic flow energy (BFE), as calculated in Equation 3.2 to Equation 3.5 [125]:

$$\text{Specific energy (SE)} = \frac{(\text{FE}_{\text{A6}} + \text{FE}_{\text{A7}})}{2 * \text{Mass}} \left(\frac{mJ}{g}\right) \quad (3.2)$$

$$\text{Stability index (SI)} = \frac{\text{FE}_{\text{D7}}}{\text{FE}_{\text{D1}}} \quad (3.3)$$

$$\text{Flow rate index (FRI)} = \frac{\text{FE}_{\text{D11}}}{\text{FE}_{\text{D8}}} \quad (3.4)$$

$$\text{Basic flow energy (BFE)} = \text{FE}_{\text{D7}}\ (\text{mJ}) \quad (3.5)$$

3.2.3.2 Aerated condition

During the aeration test, nitrogen gas is introduced from the aerated base of the powder vessel while the blade performs descending and ascending helical movements at a constant speed of 100 mm/s. In each cycle, a different gas flow velocity, ranging from 0 to 10 mm/s, is applied, and the energy required for the blade to move through the powder under these conditions is recorded. The energies measured during the descent cycle without gas flow (AE_0) and at a gas flow velocity of 4 mm/s (AE_4) are then used to calculate the aeration rate (AR) as described in Equation 3.6 [125]:

$$\text{Aeration rate (AR)} = \frac{\text{AE}_0}{\text{AE}_4} \quad (3.6)$$

3.2.3.3 Packed condition

Under packed condition, the nitrogen gas flow is maintained at a constant velocity of 2 mm/s. In this mode, instead of the rotating blade, a vented piston is employed to compress the powder under progressively increasing normal stresses, ranging from 1 kPa to 15 kPa. The permeability of the powder bed during compression is determined from the measured air pressure drop (PD), which represents the resistance to airflow through the powder, and can be calculated according to Equation 3.7 [125]:

$$\text{Permeability} = \frac{\text{q}\mu\text{L}}{\Delta\text{P}}\ (\text{cm}^2) \quad (3.7)$$

where q is the airflow rate (0.02 cm/s), μ is the air viscosity (1.74×10^{-7} mbar.s at sea level), L is the powder bed length (cm), and ΔP is the pressure drop (PD, mbar).

Additionally, the test performed under packed conditions provides data on the powder compressibility, expressed as the percentage change in volume after compression (Equation 3.8). The compressibility index (CI), defined by the ratio of the compressed powder density to the CBD, is calculated according to Equation 3.9) [125]. In this case, a plain base is used rather than an aerated one, and no gas flow is applied to the sample.

$$\text{Compressibility} = \frac{V_{\text{conditioned}} - V_{\text{compressed}}}{V_{\text{compressed}}} * 100\ (\%) \tag{3.8}$$

$$\text{Compressibility index (CI)} = \frac{\text{Compressed powder density}}{\text{Conditioned bulk density (CBD)}} \tag{3.9}$$

3.2.3.4 Shear condition

Under shear condition, following the previous compression cycle at 9 kPa using the plain base, the vented piston is replaced by a shear head. The shear head rotates at a constant speed while a compressive stress is applied, inducing powder flow. This shear procedure is repeated five times under varying normal stresses, ranging from 9 kPa to 3 kPa, in order to determine the shear yield stress as a function of the applied normal stress. From these measurements, the unconfined yield strength (σ_c) and consolidation stress (σ_1) are obtained using Mohr's circle analysis. The cohesion coefficient (τ_0) is determined by extrapolating the linear fit of the shear yield stresses to the ordinate axis, while the flow factor (ff_c) is calculated as the ratio between σ_1 and σ_c [125].

3.3 Investigation on laser powder bed fusion processing window using design of experiments and analysis of variance

The gas-atomized and surface-functionalized AA2017 powders were processed by L-PBF using an ORLAS Creator RA system (Coherent Inc., USA). The machine is equipped with a Yb-fiber laser (λ = 1070 nm) with a Gaussian energy distribution and a maximum output power of 250 W. The L-PBF parameters adopted in this work are derived from optimized processing conditions previously established by the research group [60,121,127,128], in alignment with parameter windows widely applied for Al-Cu alloys in L-PBF processing [129–133]. During fabrication, a laser spot diameter of 80 μm and a constant powder layer thickness of 30 μm were employed. All builds were conducted under an argon atmosphere containing less than 1000 ppm of oxygen to minimize oxidation. A zig-zag scanning strategy with a 67° rotation between consecutive layers was applied, and no preheating of the build platform was used in this work.

Laser power (P), scanning speed (v), and hatch distance (h) were selected as the primary process variables for the investigation and subsequent statistical analysis, as these are the most extensively studied parameters in L-PBF [58,129–131,134–136]. Response Surface Methodology (RSM) coupled with ANOVA was employed to evaluate the combined effects of these parameters on the responses. RSM is a statistical technique used to model and analyze the relationship between input variables and output responses through first-order (linear), second-order (quadratic), or higher-order polynomial functions. The second-order polynomial model is expressed by Equation 3.10, where Y represents the response variable, x the input factors, β the regression coefficients determined from experimental data, and ε the random error associated with experimental uncertainty [137].

$$Y = \beta_0 + \sum_{i=1}^{k} \beta_i x_i + \sum_{i=1}^{k} \beta_{ii} x_i^2 + \sum\sum_{i<j} \beta_{ij} x_i x_j + \varepsilon \qquad (3.10)$$

A Box-Behnken design (BBD) of experiments was selected as the experimental framework for the second-order RSM. This design enables efficient experimental planning with a reduced number of samples while maintaining statistical robustness and has been successfully applied in previous studies for optimizing L-PBF process parameters [138,139]. In the present work, three input variables (laser power, scanning speed, and hatch distance) were considered. For three factors, the Box-Behnken design can be represented as a cube whose design points correspond to the center and the midpoints of the edges, as illustrated in Figure 3.2a. Consequently, each factor is evaluated at three coded levels: -1, 0, and +1.

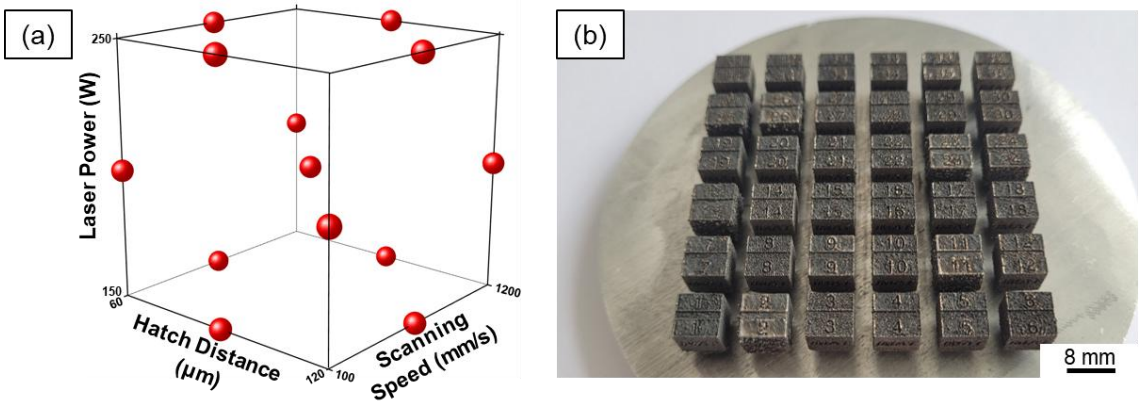

Figure 3.2 - (a) Schematic representation of the Box–Behnken experimental design employed in this study and (b) appearance of as-built cubic samples produced by L-PBF.

The specific input factors and their corresponding levels adopted in this study are summarized in Table 3.3. Following the Box-Behnken design, a total of 13 experimental conditions were fabricated by L-PBF, including ten replicates of the central point, as detailed in Table A1 (Appendix A). Furthermore, additional specimens were produced using random combinations of the input parameters to validate the predictive accuracy of the statistical models. All experimental planning, RSM modeling, and ANOVA calculations were conducted in Minitab statistical software (Minitab LLC., USA), using a 95% confidence level for the statistical analysis.

Table 3.3 - L-PBF process parameters and corresponding levels adopted in the Box-Behnken design of experiments.

Parameters		Levels		
		-1	**0**	**+1**
X1	**Laser Power (W)**	150	200	250
X2	**Scanning Speed (mm/s)**	100	650	1200
X3	**Hatch Distance (µm)**	60	90	120

For process parameter understanding and optimization, four different powders were processed by L-PBF using the experimental conditions from the Box-Behnken design: the gas-atomized AA2017 powder (Section 4.2), the HNO_3 and NaOH surface-functionalized powders (Section 4.3), and the 2TiC45nm surface-functionalized powder (Section 4.2). Among the nine different TiC-modified powder combinations, the process parameter optimization was performed using the powder containing 2 wt.% of TiC nanoparticles, as this composition and particle size are widely adopted in the literature and represent the most commonly investigated approach when reinforcing aluminum alloys with ceramic particles [90,91,104,140]. Therefore, the 2TiC45nm powder was selected within the TiC-modified powders as a reference condition to evaluate the process parameters and establish a basis for comparison with the alloys produced using the chemically surface-functionalized and gas-atomized powders. Porosity and cumulative crack length in the as-built samples were selected as the response variables. The smaller-the-better approach was applied to determine the optimal L-PBF parameter combinations resulting in lower porosity and cumulative crack length.

Cubic samples with dimensions of 8 x 8 x 8 mm^3 (Figure 3.2b) were fabricated by L-PBF, sectioned into three planes parallel to the build direction, and subsequently cold-mounted in phenolic resin. The metallographic preparation involved sequential grinding using SiC abrasive papers (240, 400, 600, and 1200 grit), followed by polishing with 3 µm and 1 µm diamond suspensions and a final 0.05 µm colloidal silica finish.

The microstructure of the samples was examined using a Axio Observer (Carl Zeiss Microscopy GmbH, Germany) light optical microscope. To quantify porosity and crack length, eighteen micrographs per sample were captured at 100x magnification and analyzed with ImageJ software (Fiji plugin) [141]. The ridge detection function in ImageJ was applied to determine the cumulative crack length per unit area (mm/mm^2), while porosity was measured using threshold-based image segmentation. Both porosity and crack length were correlated with the volumetric energy density (E_v), calculated as a function of the process parameters using Equation 2.1.

3.4 Laser powder bed fusion using optimized processing parameters

The optimized L-PBF processing parameters obtained for the as-built AA2017 alloy (P = 190 W, v = 100 mm/s, h = 120 µm, described in Section 4.2) were applied to produce samples for microstructural and mechanical characterization using the gas-atomized and TiC surface-functionalized powders. The same nomenclature used for the TiC surface-functionalized powders will be applied for the as-built L-PBF samples using the TiC surface-functionalized powders (Table 3.2).

Due to the high porosity and crack density in the as-built samples using the HNO_3 and NaOH surface-functionalized powders, the further microstructure and mechanical characterization of these alloys were not conducted, but the analysis of the defects on these alloys will be shown separately in Section 4.3.

Using the gas-atomized and TiC surface-functionalized powders and the optimized L-PBF processing parameters, cubic specimens with dimensions of 8 x 8 x 8 mm^3 (Figure 3.2b) were produced by L-PBF for microstructural characterization. Additionally, cylindrical samples with a diameter of 5 mm and a length of 10 mm were fabricated for compression testing in three different build orientations, 0°, 45°, and 90° relative to the building platform (Figure 3.3a). For tensile testing, cylindrical specimens measuring 8 mm in diameter and 50 mm in length were manufactured horizontally (0° orientation), with the loading axis parallel to the build plate (Figure 3.3b). An overview of the machined samples used for compression and tensile testing is presented in Figure 3.3c.

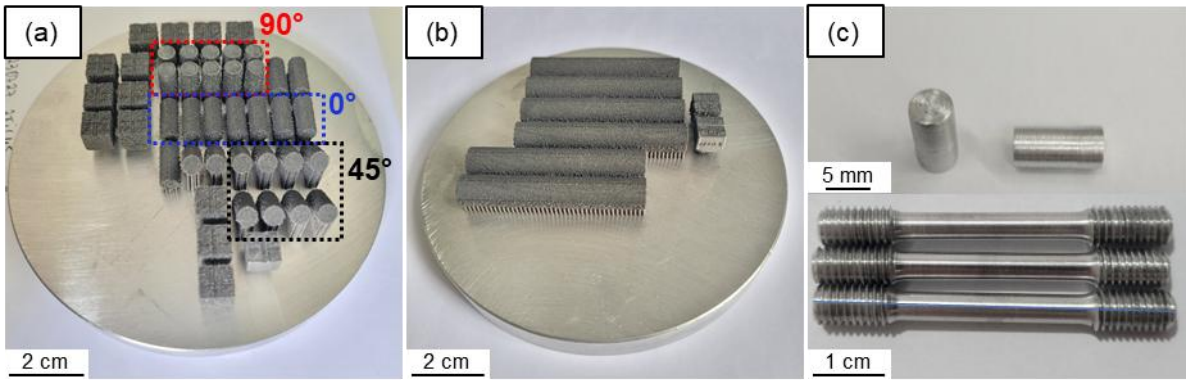

Figure 3.3 - L-PBF processing of samples from (a) compression and (b) tensile tests, and (c) machined specimens for compression and tensile tests.

3.4.1 Microstructural characterization

The cubic specimens were sectioned parallel to the building direction (BD), cold-mounted in phenolic resin, and metallographically prepared through sequential grinding with SiC papers (240, 400, 600, and 1200 grit), followed by polishing with diamond suspensions (3 μm and 1 μm) and a final polish with colloidal silica (0.05 μm). The microstructural features of the polished as-built samples were characterized by SEM using a TESCAN Mira3 (TESCAN, Czech Republic) microscope and a Quanta 400 (FEI Company, now part of Thermo Fisher Scientific, USA) microscope equipped with an Oxford Inca Energy 250 (Oxford Instruments, UK) EDS system. Grain size, aspect ratio, and crystallographic texture were evaluated by electron backscatter diffraction (EBSD) using a TESCAN Mira3 (TESCAN, Czech Republic) SEM microscope fitted with an EDAX EBSD detector (EDAX Inc., USA), employing varying magnifications and step sizes to accommodate differences in microstructural refinement among samples. Phase identification was performed by XRD on a D8 Advance ECO (Bruker AXS GmbH, Germany) diffractometer with Cu-$K_{\alpha 1}$ radiation (λ = 1.54 Å), scanning from 10° to 90° (2θ) at a rate of 0.02°/min.

Precipitate characterization was carried out using transmission electron microscopy (TEM) on Tecnai G^2 F20 (FEI Company, now part of Thermo Fisher Scientific, USA) and Talos F200X (Thermo Fisher Scientific, USA) microscopes. Imaging modes included bright-field (BF), dark-field (DF), and scanning transmission electron microscopy (STEM) with a high-angle annular dark-field

(HAADF) detector. Elemental mapping and composition were determined by EDS, while crystallographic structures were analyzed using selected area electron diffraction (SAED) high-resolution transmission electron microscopy (HRTEM). TEM lamellae were prepared on a Gatan 691 precision ion polishing system (PIPS) (Gatan Inc., USA) and via focused ion beam (FIB) technique using a Scios 2 DualBeam FIB-SEM (Thermo Fisher Scientific, USA).

3.4.2 Mechanical characterization

Mechanical characterization was conducted through hardness, quasi-static tensile, and compression testing. The microhardness was measured using a Shimadzu Vickers hardness tester (Shimadzu Corporation, Japan) under a load of 200 gf and a loading time of 15 s.

Compression tests were also conducted at room temperature on an Instron 5900R/5569 50 kN (Instron, USA) universal testing machine at a constant crosshead speed of 1 mm/min, using a INSTRON 2663-821 (Instron, USA) video extensometer to record strain. The L-PBF cylindrical specimens, with dimensions and geometry according to ASTM E9-19 [142], were tested with the loading axis oriented at 0°, 45°, and 90° relative to the building platform to evaluate anisotropy in mechanical behavior.

The tensile properties were evaluated at room temperature using an Instron 5500R 250 kN (Instron, USA) universal testing machine equipped with the video extensometer. The tests were performed at a constant crosshead speed of 1 mm/min. The as-built L-PBF samples were machined into small-size cylindrical specimens with dimensions and geometry compliant with ASTM E8M-25 [143] (specimen 4 for round tensile test), ensuring that the loading axis was parallel to the L-PBF building platform. The dimensions of the compression and tensile specimens are presented in Figure A1 in the Appendix.

4 RESULTS AND DISCUSSION

4.1 Powder characterization

4.1.1 Surface-functionalized powders using chemical etchings

4.1.1.1 Physical and chemical properties

Figure 1 presents the morphology and particle size distribution (PSD) of the gas-atomized and surface-functionalized powders. The gas-atomized powder (Figure 4.1a) shows spherical particles with smooth surfaces and occasional satellites (yellow arrows, Figure 4.1), typical of this process. After surface functionalization with acidic HNO_3 solution (Figure 4.1b), the particles became rougher and more irregular, whereas surface functionalization with basic NaOH solution (Figure 4.1c) preserved the smooth morphology of the as-atomized powder.

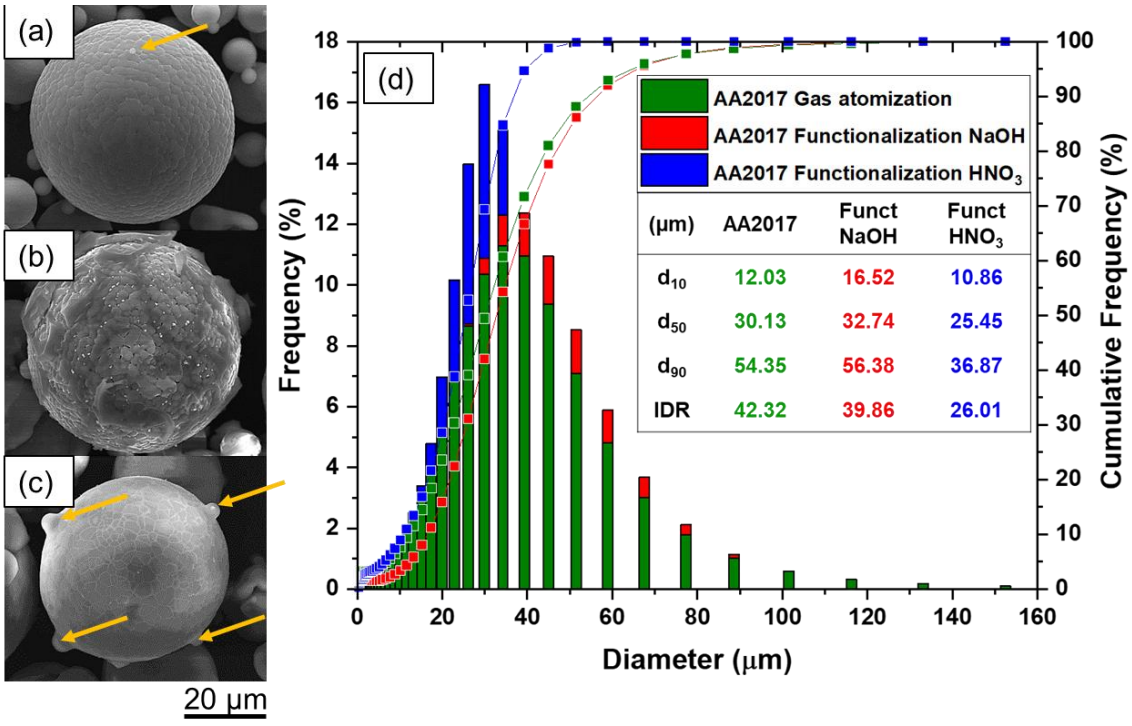

Figure 4.1 – Scanning electron microscopy (SEM) images of (a) gas-atomized and surface-functionalized powders with (b) acidic HNO_3 and (c) basic NaOH solutions, along with their (d) PSD. Yellow arrows highlight the presence of satellite particles.

As shown in Figure 4.1d, the gas-atomized and NaOH-treated powders exhibit similar PSDs, with d_{50} values of 30.13 and 32.74 µm and inter-decil range (IDR = d_{90}-d_{10}) of 42.32 and 39.86 µm, respectively. The HNO_3-treated powder presented smaller particles (d_{50} = 25.45 µm) and a narrower size range (IDR = 26.01 µm). Confocal microscopy revealed a decrease in surface roughness after NaOH treatment (Ra = 0.03 ± 0.01 µm) compared to the gas-atomized powder (Ra = 0.032 ± 0.008 µm), while HNO_3 treatment increased it to Ra = 0.04 ± 0.01 µm. Therefore, the NaOH surface functionalization had little influence on PSD or surface texture, whereas HNO_3 surface functionalization led to higher roughness, irregular morphology, and smaller average particle size. Despite sieving, small fractions of particles below 20 µm and above 63 µm remained due to agglomeration effects.

The PSD span ((d_{90}-d_{10})/d_{50}) indicates powder flowability. As noted by Tan, Wong, and Dalgarno [144], values ≥ 1.5 suggest poor flow due to fine particles (≤10 µm). All powders here show good flowability, improving from the gas-atomized (span = 1.40) to the NaOH (span = 1.22) and HNO_3 surface-functionalized (span = 1.02) powders due to reduced d_{90}. A wider PSD improves packing but may reduce flowability when many fine particles are present [145]. The spherical shape of gas-atomized powders benefits both packing and flowability [144,145]. In the context of L-PBF, finer PSDs can further enhance density and surface quality of the as-built sample due to the higher powder packing density [146].

As shown in Table 4.1, the apparent density is similar for gas-atomized and NaOH surface-functionalized powder, but slightly lower for the HNO_3-treated one due to finer PSD, agglomeration, and irregular morphology. The skeletal density remains nearly constant for all powders. Table 4.1 also presents the flowability results of the gas-atomized and surface-functionalized powders measured by Caney's funnel. The gas-atomized powder showed no flow, while the HNO_3 and NaOH surface-functionalized powders exhibited flow times of 19.5 ± 0.5 s and 18.5 ± 1.1 s, respectively. The slightly lower flowability of the HNO_3-treated powder is attributed to its smaller particle size and narrower PSD. According to Jallo *et al*. [7], surface roughness and surface energy significantly

affect flowability. Compared to the gas-atomized powder, the increased roughness in the HNO_3-treated powder reduces interparticle adhesion, improving flow, whereas in the NaOH-treated powder, the reaction of powder with the chemical solution likely forms an oxide compound with lower surface energy, also enhancing flowability. Visser [147] reported that oxide layer formation on metal particles diminishes van der Waals attraction, reducing agglomeration and promoting flow. Overall, surface functionalization effectively improved powder flowability.

Table 4.1 - Apparent and skeletal densities and flowability of the gas-atomized and surface-functionalized powders.

AA2017 Powders	Apparent Density (g/cm^3)	Skeletal Density (g/cm^3)	Flowability (s/50g)
Gas-atomized	1.36 ± 0.02	2.809 ± 0.002	No Flow
Surface-functionalized using HNO_3	1.224 ± 0.006	2.817 ± 0.004	19.5 ± 0.5
Surface-functionalized using NaOH	1.386 ± 0.008	2.772 ± 0.001	18.5 ± 1.1

Additionally, the surface-functionalized powders showed lower laser reflectance compared to the gas-atomized powder due to changes in particle morphology, surface roughness, and chemical composition, as illustrated in Figure 4.2. Although the spectrum in Figure 4.2 is restricted from 400 to 950 nm due to equipment limitations, similar trends are expected at 950 nm and 1070 nm (the Yb-fiber laser wavelength used in L-PBF). Therefore, the HNO_3-treated powder exhibited an 8.7% reduction in laser reflectance, while the NaOH-treated powder showed a 13.3% decrease compared to the gas-atomized powder, despite having similar morphology and roughness.

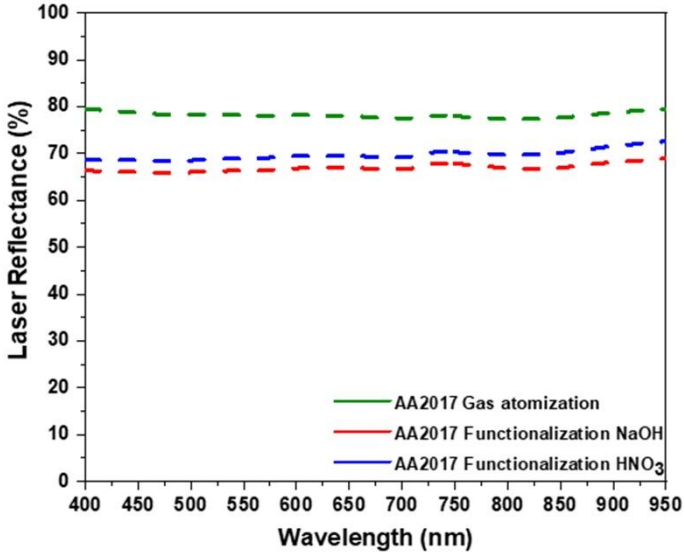

Figure 4.2 - Laser reflectance of the gas-atomized and surface-functionalized powders.

These differences in laser reflectance arise not only from particle morphology and roughness but also from PSD and surface chemistry. Fine particles filling gaps between larger particles enhance energy absorption by promoting multiple reflections of the laser beam. These repeated internal reflections increase the effective interaction between the laser and the powder bed, allowing more energy to be absorbed and thereby increasing laser absorptivity [96]. Consequently, powders with wider PSD and higher apparent density, such as the NaOH-treated powder, would tend to absorb more laser energy. In contrast, powders with finer PSD and lower apparent density, such as the HNO_3 surface-functionalized powder, have higher surface-area-to-volume ratios, facilitating light penetration and interaction with particle surfaces, reducing reflectance [97]. The differences between gas-atomized and NaOH surface-functionalized powders, despite similar PSD, suggest surface chemistry plays a key role in laser absorptivity. Overall, surface functionalization reduces laser reflectance, suggesting that powder modification can enhance L-PBF by lowering the energy needed for melting.

The cross-sectional microstructure and elemental distribution by energy-dispersive X-ray spectroscopy (EDS) of the gas-atomized and surface-functionalized powders are presented in Figure 4.3. All powders exhibit a similar

microstructure, with an α-Al matrix and Cu-rich phase at the cell boundaries. Copper segregation at the cell boundaries is evident, while magnesium, silicon, and iron are uniformly distributed. No new elements besides oxygen appear in the functionalized powders. In the HNO_3-treated powder, slight material removal at cell boundaries and lower copper concentration near the surface suggest a reaction with copper (Figure 4.3b). Additionally, while the gas-atomized powder shows negligible surface oxygen, the functionalized powders display an oxygen-rich surface layer, consistent with oxygen contents measured via inert gas fusion: 0.166 ± 0.003%, 3.69 ± 0.13%, and 3.65 ± 0.33% for the gas-atomized, HNO_3, and NaOH surface-functionalized powders, respectively.

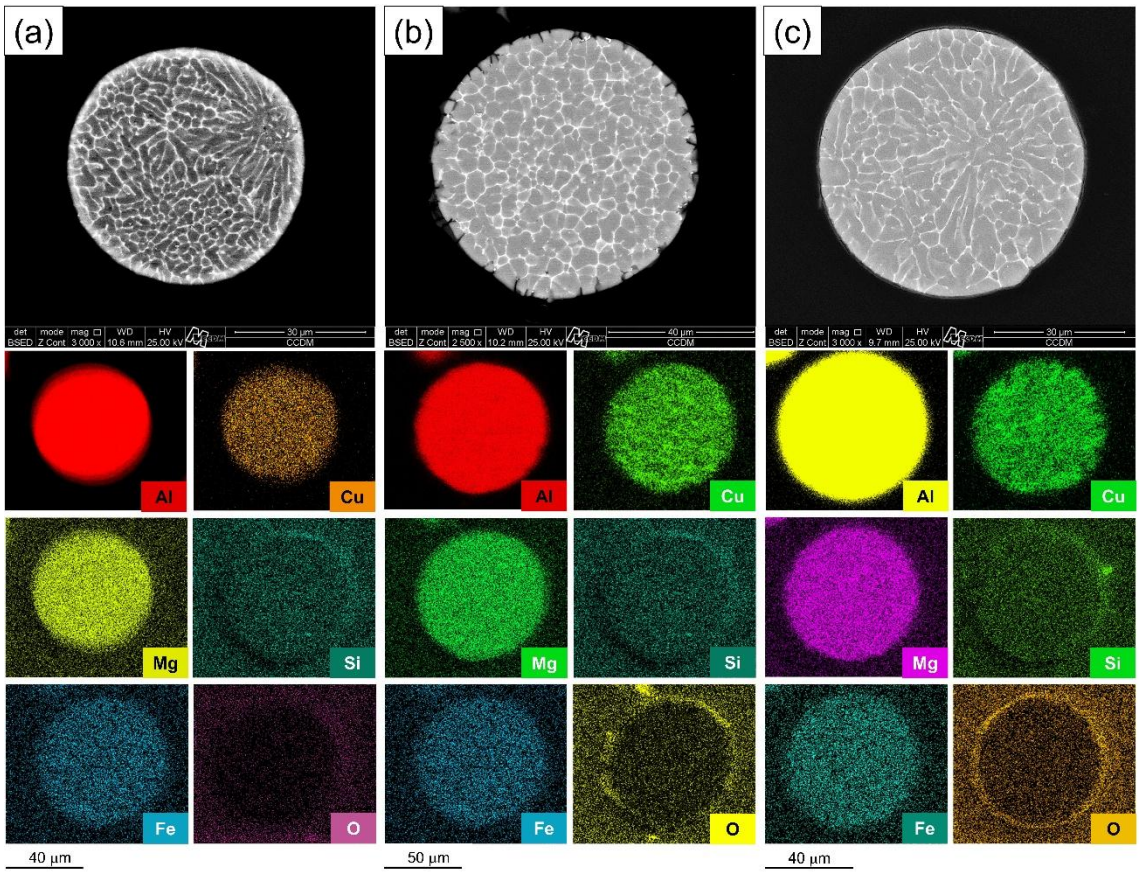

Figure 4.3 - SEM images and EDS elemental distribution maps of (a) the gas-atomized powder and surface-functionalized powders with (b) acidic HNO_3 and (c) basic NaOH solutions.

X-ray diffraction (XRD) and Raman spectroscopy were used to analyze the phases and surface composition of the powders, as shown in Figure 4.4. All powders mainly contain α-Al and Al_2Cu phases (Figure 4.4a), typical of Al-Cu alloys. Minor unidentified peaks around 2θ = 35° and 43° likely correspond to trace constituents of the AA2017 alloy and are not caused by surface functionalization.

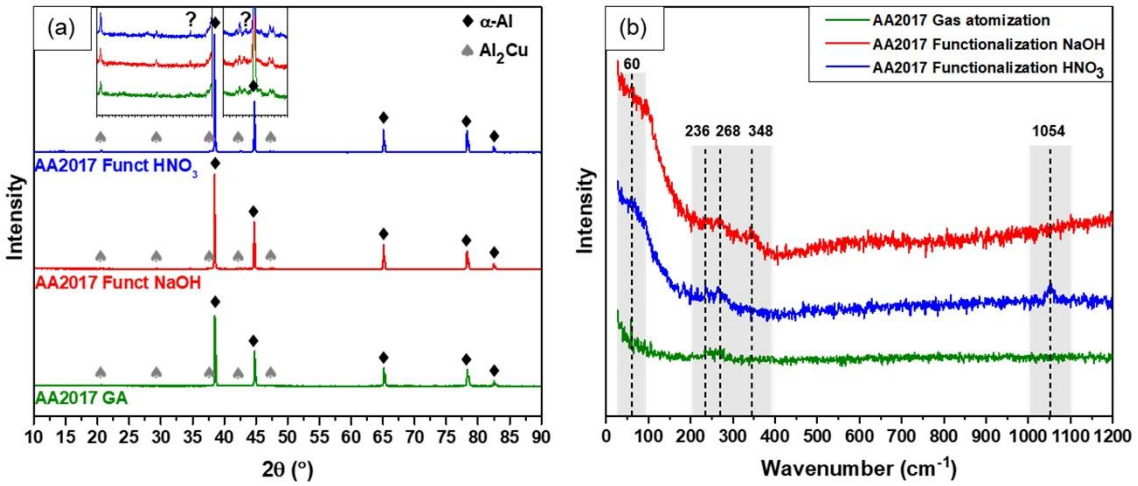

Figure 4.4 - (a) XRD diffractograms and (b) Raman spectra of the gas-atomized and surface-functionalized powders.

Raman spectra (Figure 4.4b) show two components at ~236 cm^{-1} and ~268 cm^{-1} on the gas-atomized powder, attributed to phonon modes of Al_2Cu or surface oxides [148]. These peaks are also present in the surface-functionalized powders, confirming the preservation of the Al_2Cu phase after treatment. For the HNO_3-treated powder, an additional peak at ~1054 cm^{-1} appears, likely due to the C–O stretch in cellulose from partial contamination with fibers from the filter paper used during treatment [149]. The NaOH-treated powder shows a new peak at ~348 cm^{-1}, which may correspond to an oxide such as SiO_2 [150,151], consistent with the detected surface silicon (Figure 4.3c). A peak around 60 cm^{-1}, associated with Al_2O_3, could also be present in the surface-functionalized powders [150].

The reactions involved in aluminum surface etching with NaOH and HNO_3 solutions are summarized in Equation 4.1 to 4.5. In the NaOH treatment,

aluminum reacts to form soluble sodium aluminate salt and hydrogen (Equation 4.1), which then hydrolyzes to produce aluminum hydroxide and regenerate NaOH (Equation 4.2). Upon drying, aluminum hydroxide dehydrates to form Al_2O_3 (Equation 4.3) [67].

$$2Al_{(s)} + 2NaOH_{(aq)} + 2H_2O_{(l)} \rightarrow 2\ NaAlO_{2(aq)} + 3H_{2(g)} \quad (4.1)$$

$$NaAlO_{2(aq)} + H_2O_{(l)} \rightarrow Al(OH)_{3(aq)} + NaOH_{(aq)} \quad (4.2)$$

$$2Al(OH)_{3(aq)} \rightarrow Al_2O_{3(s)} + 3H_2O_{(l)} \quad (4.3)$$

For HNO_3, the reaction depends on its concentration. At low concentrations, the acidic behavior dominates, corroding aluminum (Equation 4.4) [152] and copper (Equation 4.5) [153]. Higher concentrations (>40–50%) favor the formation of a metal oxide with minimal aluminum dissolution [152]. In this study, the 2.8 mol/L HNO_3 solution primarily caused aluminum dissolution, but copper on the powder surface could also react with the HNO_3.

$$Al_{(s)} + 4HNO_{3(aq)} \rightarrow NO_{(g)} + Al(NO_3)_{3(aq)} + 2H_2O_{(l)} \quad (4.4)$$

$$3Cu_{(s)} + 8HNO_{3(aq)} \rightarrow 2NO_{(g)} + 3Cu(NO_3)_{2(aq)} + 4H_2O_{(l)} \quad (4.5)$$

As a result, surface functionalization with NaOH produced an Al_2O_3 layer on the powder surface and maintained smooth particle morphology, whereas HNO_3 treatment led to smaller particle sizes and partial removal of copper from cell boundaries due to the reaction of aluminum and copper with HNO_3. Rubenchik *et al.* [154] reported that the presence of an Al_2O_3 film on the aluminum surface enhances laser absorption up to a certain critical oxide thickness, beyond which the absorption starts to decline as the oxide layer continues to grow. Therefore, the Al_2O_3 layers on both powders likely contributed to the observed decrease in laser reflectance (Figure 4.2). Any remaining reaction products were

likely removed during filtration and rinsing, as EDS and Raman analyses showed no nitrogen or sodium on the powder surfaces.

4.1.1.2 Rheological Properties

Hall and Carney funnels are commonly used to assess powder flowability for L-PBF. However, the FT4 powder rheometer provides a more sensitive evaluation for cohesive powders and better represents powder behavior under the low-stress conditions experienced during dynamic spreading in the L-PBF process [97,155]. Table 4.2 summarizes the dynamic flow properties of the gas-atomized and surface-functionalized powders. A higher conditioned bulk density (CBD) indicates less air trapped between particles and better powder packing [145]. CBD is lowest for the NaOH-treated (CBD = 1.20 g/cm^3) due to slightly wider PSD and more wall particle voids, highest for the gas-atomized powder, and intermediate for the HNO_3-treated (CBD = 1.32 g/cm^3) because of finer and narrower PSD, and irregular particles, which hampers powder packing.

Table 4.2 - CBD, SE, SI, FRI, and BFE of the gas-atomized and surface-functionalized powders under dynamic flow condition.

AA2017 Powders	CBD (g/cm^3)	SE (mJ/g)	SI (-)	FRI (-)	BFE (mJ)
Gas-atomized	1.47	2.88	0.98 ± 0.06	1.38 ± 0.03	166 ± 4
Surface-functionalized using HNO_3 solution	1.32	3.85	1.11 ± 0.14	1.25 ± 0.04	316 ± 12
Surface-functionalized using NaOH solution	1.20	2.57	1.04 ± 0.03	1.23 ± 0.04	180 ± 4

Specific energy (SE) and basic flow energy (BFE), indicating resistance to flow due to particles cohesiveness, are highest for the HNO_3-treated powder due to increased particle cohesion and agglomeration, while the NaOH-treated powder exhibits the lowest SE, showing easier flow. SE reflects the powder's flowability under low-stress conditions, where its behavior is primarily governed by interparticle interactions, similar to the powder spreading stage in the L-PBF

process [97,125]. This suggests that the NaOH-treated powder requires less energy to initiate flow and achieve uniform dispersion compared to the other powders.

Stability index (SI) reflects how the powder flow behavior changes during repeated measurements at constant blade speed, while flow rate index (FRI) quantifies how the powder responds to changes in blade speed. Powders are considered stable when the flow energy remains similar across repeated cycles, resulting in SI values close to 1. In contrast, values above 1 indicate agglomeration, segregation, or de-aeration, and values below 1 suggest agglomeration during the test [125]. In this context, the gas-atomized and NaOH-treated powders exhibit SI values closest to1, confirming their higher stability under constant blade speeds. The HNO_3-treated powder shows slightly lower stability (SI = 1.11 ± 0.14), which can be attributed to particle rearrangement during the test. Additionally, lower FRI values (FRI ≈ 1-3) correspond to improved powder flowability because the powder flow resistance does not significantly increase when the blade moves faster Conversely, FRI values above 3 indicate highly cohesive powders that exhibit a strong rise in flow resistance as speed increases, whereas a FRI ≤ 1 can be achieved for flow-enhanced powders [125]. Overall, all powders display flow properties consistent with coarse or surface-treated aluminum powders (FRI ≈ 1), with surface treatments enhancing dynamic flow behavior.

Figure 4.5 shows that the gas-atomized and surface-functionalized powders behave similarly under aerated condition, with the energy required to move the blade dropping sharply even at low nitrogen flow (2 mm/s), reaching fluidization. Among the powders, the gas-atomized powder is least sensitive to aeration (AR = 19 ± 3), while the HNO_3-treated powder is most sensitive (AR = 72 ± 7), likely due to its finer particles. At high gas velocities, very little energy (<10 mJ) is needed to move the powders. For the aeration energy (AE), lower values indicate a reduced tendency to agglomerate [145]. Without gas flow, the HNO_3-treated powder shows the highest agglomeration tendency (AE_0 = 219.50 mJ) due to fine irregular particles, whereas the NaOH-treated powder shows the lowest (AE_0 = 155.75 mJ). At 4 mm/s gas flow, the trend reverses, and the HNO_3-

treated powder exhibits the lowest agglomeration tendency (AE_4 = 3 ± 1 mJ). This behavior is likely associated with its finer PSD and lower apparent density, which allow gas to penetrate the powder bed more easily, thereby reducing interparticle cohesion under gas flow. Higher AE indicates more gas entrapped between powder layers, causing uneven layer thickness [155], suggesting that the gas-atomized powder may form less uniform layers under gas pressure.

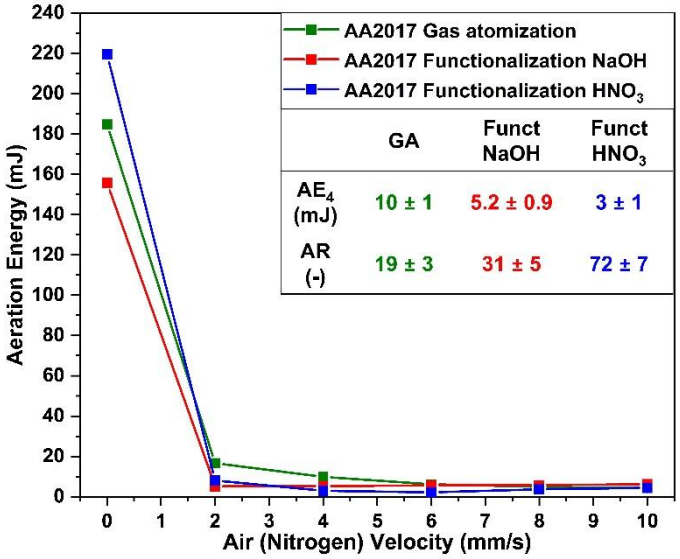

Figure 4.5 - Aerated flow energy as a function of the nitrogen flow velocity of the gas-atomized and surface-functionalized powders under aerated condition.

Under packed condition, high permeability (low pressure drop) indicates easier gas flow through the powder [145]. As shown in Figure 4.6a, the HNO_3-treated powder exhibits the highest permeability due to its intermediate CBD (more voids and air entrapped between the particles) and fine, irregular particles that facilitate gas flow. Conversely, the larger particles and wider PSD of the NaOH-treated powder hinder gas flow. The studied surface-functionalized powders are also less sensitive to applied normal stress than the gas-atomized powder, in which compression rearranges its particles, reducing voids and channels, and consequently lowering permeability.

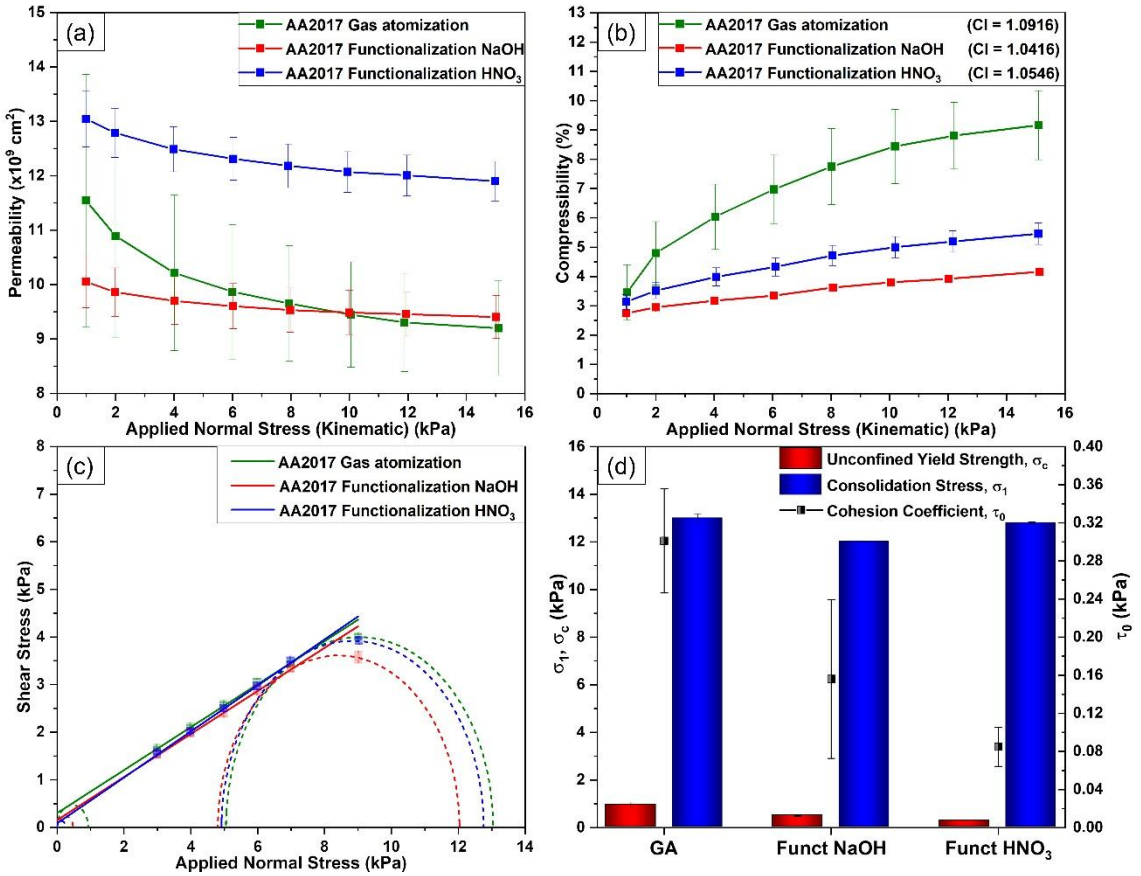

Figure 4.6 - (a) Permeability and (b) compressibility as a function of the applied normal stress under packed condition; (c) shear stress as a function of the applied normal stress, and (d) consolidation stress, unconfined yield strength, and cohesion coefficient under shear condition of the gas-atomized and surface-functionalized powders.

Compressibility and the compressibility index (CI) under packed conditions are shown in Figure 4.6b. Lower compressibility indicates better flowability [125], thus the NaOH-treated powder shows improved flowability compared to the gas-atomized powder, consistent with its low SE under dynamic flow condition. A low CI also reflects good packing and minimal entrapped air [145,155]. Therefore, the NaOH-treated powder (CI = 1.0416) demonstrates the best packing, while the gas-atomized powder (CI = 1.0916) shows the worst.

Under shear condition, after compression at 9 kPa, the powders were tested for flow under rotating shear at different stresses to determine unconfined yield strength (σ_c), consolidation stress (σ_1), cohesion (τ_0), and flow factor (ff_c =

σ_1/σ_c) (Figure 4.6c). The gas-atomized powder has the lowest ff_c (ff_c = 14 ± 2), while the acidic HNO_3-treated powder has the highest (ff_c = 47 ± 9). Higher ff_c indicates lower cohesiveness and better flowability [156,157], then all powders are categorized as free-flowing (ff_c > 10). Figure 4.6d shows σ_1, σ_c, and τ_0, where lower τ_0 indicates lower cohesion and easier transition from static to flowing states [145,155]. The HNO_3-treated powder shows the lowest τ_0 (τ_0 = 0.08 ± 0.02 kPa), NaOH-treated powder is intermediate (τ_0 = 0.16 ± 0.08 kPa), and the gas-atomized powder the highest (τ_0 = 0.30 ± 0.05 kPa), confirming the improved flowability of the surface-functionalized powders.

The rheological analysis of the powders indicated that flowability depends on the stress state. To summarize their suitability for L-PBF, Brika *et al.* [145] proposed the AM suitability (AMS) factor, Equation 4.6, where each index is normalized based on the maximum value among the powders: CBD, CI, inverse permeability (used instead of pressure drop), SE, AE_4, BFE, and τ_0.

$$\mathrm{AMS} = \left(\frac{1}{\mathrm{CBD}} + \mathrm{CI} + \mathrm{PD} + \mathrm{SE} + \mathrm{AE}_4 + \mathrm{BFE} + \tau_0\right)/7 \tag{4.6}$$

According to Brika *et al.* [145], lower AMS values indicate better L-PBF suitability. This is consistent with the fact that higher CBD, lower CI, and higher permeability improve powder bed density, while lower AE, SE, and τ_0 enhance powder bed uniformity. Minimizing SE and BFE reduces disturbances during spreading and L-PBF. In practice, powders that exhibit this flow and spreading characteristics correspond to lower AMS values, justifying why a lower AMS reflects better L-PBF suitability. Figure 4.7 shows the normalized radar diagram, and the AMS factors for the gas-atomized, NaOH, and HNO_3 surface-functionalized powders are 0.870 ± 0.06, 0.75 ± 0.03, and 0.744 ± 0.06, respectively. In Figure 4a, the gas-atomized powder shows a larger area, indicating a higher AMS factor and poorer L-PBF suitability. In contrast, the HNO_3-treated powder exhibits a smaller area, reflecting a lower AMS factor and improved suitability for L-PBF. Figure 4.4b highlights that τ_0, AE_4, and BFE contribute most to the differences in AMS. In general, the surface-functionalized

powders show improved suitability compared to the gas-atomized powder, demonstrating that surface treatment effectively enhanced rheological behavior and, together with reduced laser reflectance, supports better L-PBF processability.

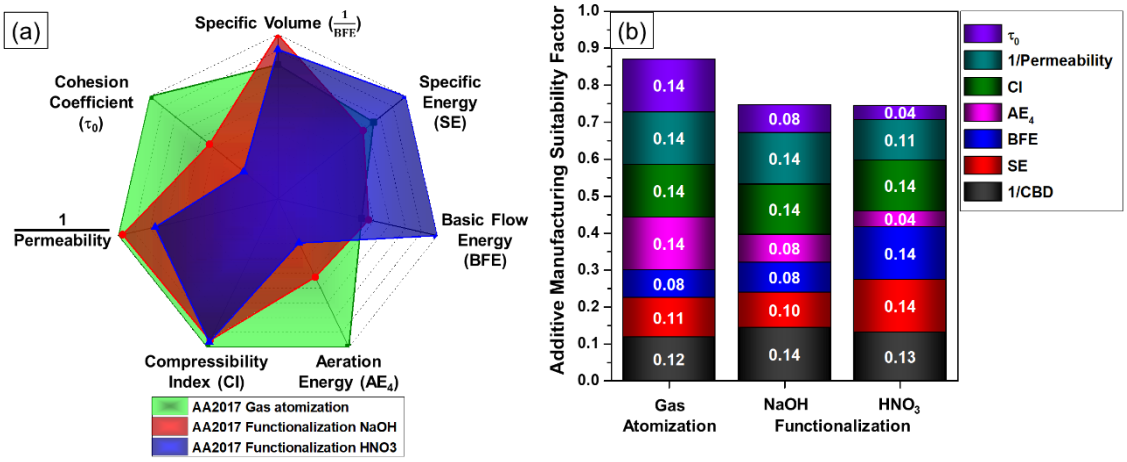

Figure 4.7 - (a) Radar chart showing the normalized rheological properties of the gas-atomized and surface-functionalized powders, and (b) the contribution of each rheological property to the AMS factor for these powders.

4.1.2 Surface-functionalized powders using TiC particles

4.1.2.1 Physical and chemical properties

Figure 4.8 shows the morphology of the TiC-functionalized powders. Nanosized TiC particles seems to be more uniformly attached to the AA2017 powder surface (Figure 4.8a-c), although higher TiC concentrations promote nanoparticle agglomeration, as highlighted by the yellow circles in Figure 4.8c. Similar aggregate formation was reported by Gärtner *et al.* [112], resulting from insufficient deagglomeration and interparticle interactions, which increases effective particle size and reduces surface coverage, affecting the powder's cohesiveness. When TiC particle size increases to fine micrometer-sized (<4 µm), the particles appear to be less uniformly distributed (Figure 4.8d-f). Coarse micrometer-sized TiC particles (44 µm) show a more heterogeneous distribution, with only some small particles remaining attached, often between satellites (blue

arrows) and host particles (Figure 4.8g-i). A lower-magnification overview of the powders is provided in Figure A2 in Appendix.

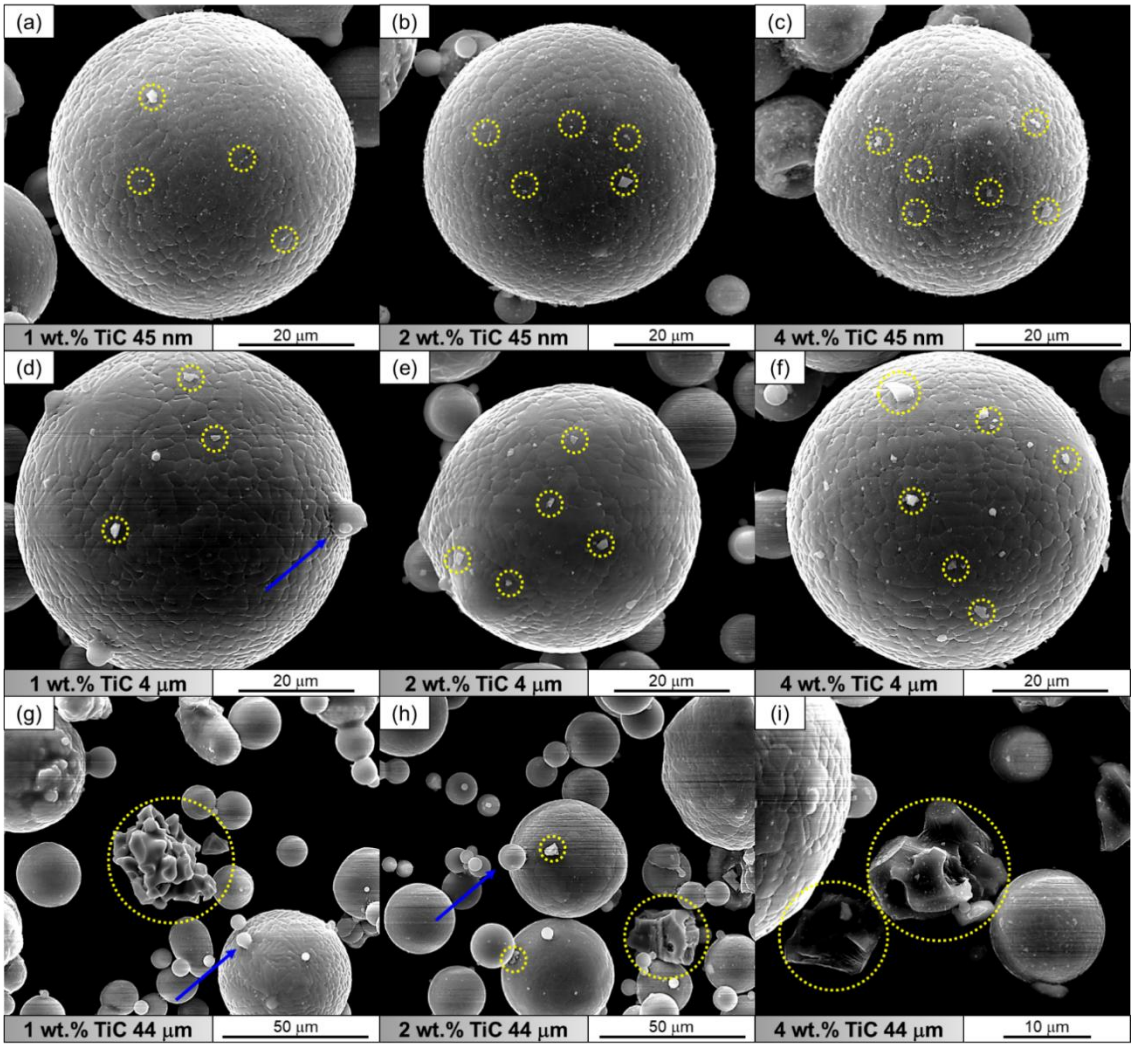

Figure 4.8 - SEM images showing the morphology of AA2017 powders surface-functionalized with TiC: (a–c) 1, 2, and 4 wt.% TiC with 45 nm particle size; (d–f) 1, 2, and 4 wt.% TiC with <4 µm particle size; and (g–i) 1, 2, and 4 wt.% TiC with 44 µm particle size. TiC particles and satellite particles are highlighted by yellow circles and blue arrows, respectively.

The PSD curves, along with the d_{10}, d_{50}, and d_{90} metrics of the gas-atomized and TiC surface-functionalized powders, are shown in Figure 4.9. Overall, the powders exhibit similar PSDs with slight variations. Compared to the gas-atomized powder, the surface-functionalized 1TiC45nm, 2TiC44µm, and

4TiC44µm powders display broader PSDs, whereas the 4TiC4µm powder exhibits a finer and narrower PSD, as seen in Figure 4.9a-b. These trends are clarified by analyzing d_{10}, d_{50}, d_{90}, and IDR values (Figure 4.9c). For the gas-atomized powder, d_{10}, d_{50}, and d_{90} are 14.33 µm, 29.13 µm, and 43.93 µm, respectively, with an IDR of 29.6 µm. The TiC-functionalized powders exhibited slightly larger average values, with d_{10} = 15 ± 1 µm, d_{50} = 32 ± 2 µm, d_{90} = 49 ± 5 µm, and IDR = 34 ± 4 µm, most likely due to the TiC particles attached to the powder surface, which increased the effective particle size.

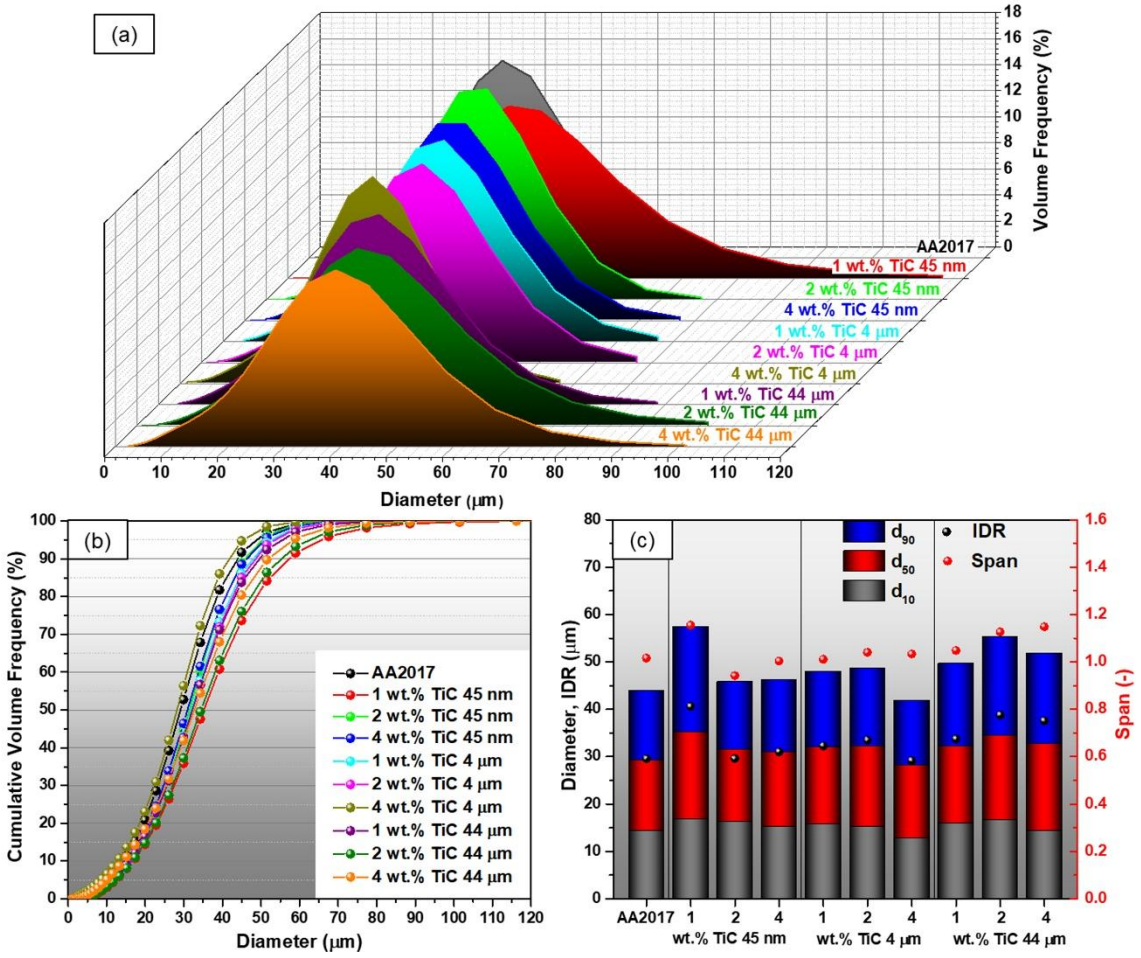

Figure 4.9 - PSD of the gas-atomized and TiC surface-functionalized AA2017 powders: (a) volume frequency, (b) cumulative volume frequency, and (c) characteristic PSD parameters including d_{10}, d_{50}, d_{90}, and IDR.

The finer and narrower PSD of the 4TiC4µm powder is attributed to many small TiC particles that were not all attached to the metal powder surface, resulting in decreased d_{10}, d_{50}, d_{90}, and IDR values of 12.67 µm, 28.21 µm, 41.83 µm, and 29.16 µm, respectively. In contrast, the broader PSD of the 2TiC44µm and 4TiC44µm powders is due to larger TiC particles dispersed among the metal particles, yielding higher d_{10}, d_{50}, d_{90}, and IDR values (d_{10} = 16.59 µm, d_{50} = 34.42 µm, d_{90} = 55.36 µm, IDR = 38.77 µm for 2TiC44µm powder, and d_{10} = 14.25 µm, d_{50} = 32.70 µm, d_{90} = 51.80 µm, IDR = 37.55 µm for 4TiC44µm powder). The wider PSD of the 1TiC45nm powder (IDR = 40.60 µm) likely arises from agglomeration during mixing. Since the TiC content is low, the mixing time may have been insufficient for deagglomeration or, conversely, may have caused reagglomeration or partial decoating. As reported by Gärtner *et al.* [112], exceeding the optimal mixing time increases particle collisions and agglomerate size, reducing powder flowability. Hence, shorter mixing times are more effective for low nanoparticle concentrations.

The PSD span, presented in Figure 4.9c, provides another quantitative measure of size distribution. The gas-atomized AA2017 powder and TiC-functionalized powders have spans of 1.05 ± 0.07, indicating generally good flowability (span < 1.5) [144]. However, powders with wider PSDs, such as 1TiC45nm, 2TiC44µm, and 4TiC44µm powders, show higher spans (span = 1.15, 1.13, and 1.15, respectively), as fine particles fill voids between larger particles, increasing interparticle contact, friction, and reducing flowability.

The skeletal and apparent densities, together with the flowability results of the gas-atomized and TiC surface-functionalized powders, are presented in Figure 4.10. All powders exhibited similar skeletal densities of approximately 2.74 ± 0.02 g/cm^3. Small deviations may result from minor porosity or structural imperfections within the TiC particles. In contrast, notable variations were observed in apparent density. The gas-atomized powder exhibits an apparent density of 1.45 ± 0.01 g/cm^3, which increases after the addition of 1 wt.% of TiC particles. However, with higher TiC concentrations, the apparent density gradually decreases for powders containing nanosized and fine micrometer-sized TiC particles. Conversely, in powders incorporating coarse micrometer-sized TiC

particles, the apparent density remained nearly constant regardless of particle concentration. A comparable trend was reported by Gärtner *et al.* [112], who observed an initial increase in apparent density at low nanoparticle concentrations, followed by negligible changes as the concentration of nanoparticles increased.

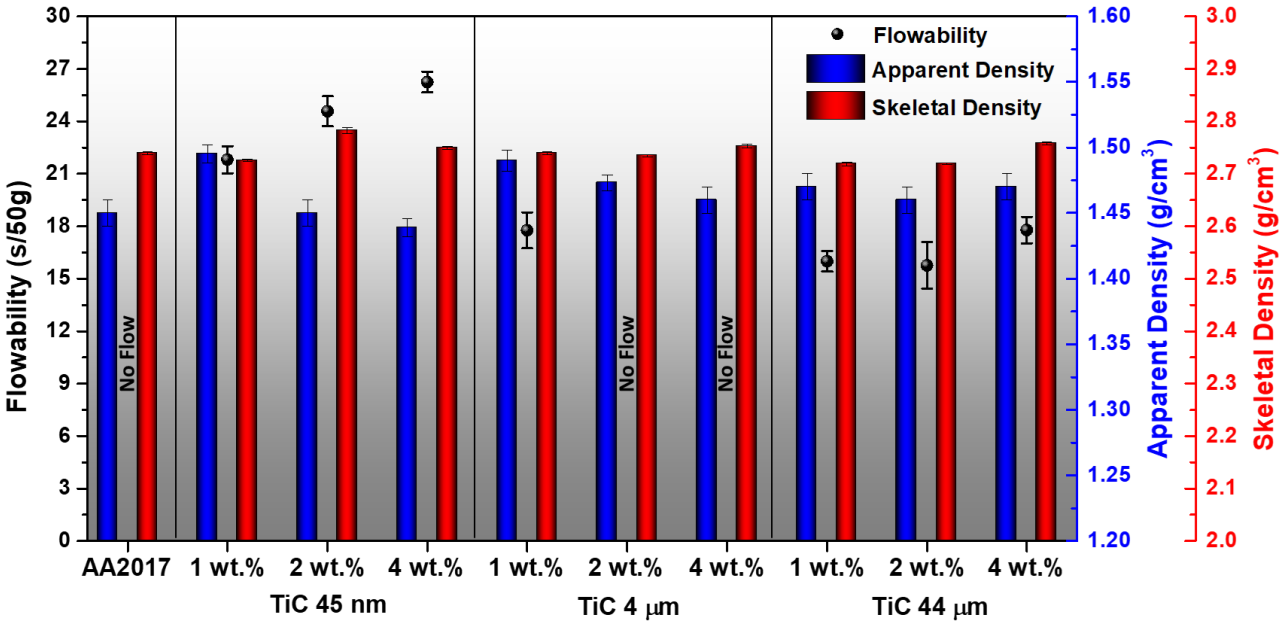

Figure 4.10 - Apparent and skeletal densities, and flowability of the gas-atomized and TiC surface-functionalized AA2017 powders.

The influence of TiC particle size and concentration on powder flowability, measured using Carney's funnel, is also shown in Figure 4.10. Powder flowability is a critical property for achieving homogeneous powder layers and consistent part density during the L-PBF process [144,145]. The gas-atomized AA2017 powder, as well as the 2TiC4μm and 4TiC4μm powders, did not exhibit measurable flow. This behavior is typical of aluminum alloy powders, whose low density enhances the effect of adhesion and contact forces compared to gravitational forces, thereby hindering free flow [158]. Notably, the addition of 1 wt.% of TiC particles, independent of their size, significantly improved the flow behavior, with measured flow times of 21.8 ± 0.8 s, 18 ± 1 s, and 16.0 ± 0.6 s for 50 g of the 1TiC45nm, 1TiC4μm, and 1TiC44μm powders, respectively.

Surface roughness and surface energy are key powder characteristics that most strongly affect flowability and interparticle forces [7,159]. These parameters can be modified by coating metallic powders with ceramic particles. In the absence of capillary and electrostatic forces, the dominant interaction between particles is the Van der Waals force, expressed for two uniformly coated host particles by Equation 4.7, where $F_{VdW,H\text{-}G}$ is the attraction force, A is the Hamaker constant (material-dependent constant that quantifies the magnitude of the Van der Waals attraction between particles), z_0 is the minimum contact distance between host particles, d and D are the diameters of the guest and host particles, respectively, and SAC is the surface area coverage (i.e., the projected area of guest particles on the host surface) [112,160]:

$$F_{VdW,H-G} = \frac{Ad}{4z_0^2} + \frac{A}{24\left(\sqrt{\left(1+\frac{d}{D}\right)^2 - \frac{1.21}{SAC}\left(\frac{d}{D}\right)^2} - 1\right)^2 D} \tag{4.7}$$

According to this relationship, the attraction force depends on the particle diameters and surface coverage of guest particles. At low SAC, the guest particle concentration is insufficient to separate host particles, maintaining high attraction. As SAC increases and reaches a critical value, host particles become spaced apart, leading to a sharp decrease in attraction that remains nearly constant at higher SAC. Moreover, the attraction force ($F_{VdW,H\text{-}G}$) follows a parabolic trend with the guest particle diameter, reaching a minimum at a critical particle size and increasing for smaller or larger diameters. This behavior may occur because very small guest particles have a minimal interaction area with the host, so the host-host attraction remains strong, resulting in a high attraction force. As the guest size increases, the host particles are more effectively separated, reducing host-host interaction and lowering the overall attraction to a minimum. Beyond this point, further increasing the guest particle size leads to a larger host-guest contact area and, eventually, to guest-guest interactions or bridging between host particles, both of which increase the total attraction force again. Likewise, larger host particles increase the overall attraction force [112,160].

The nanosized TiC particles uniformly distributed on the surface of AA2017 powder increased interparticle spacing, reduced attraction forces, and introduced additional surface roughness, enhancing the flowability of the 1TiC45 nm powder (Figure 4.10). As predicted by Equation 4.7 and literature [112,160], the Van der Waals force decreases with increasing TiC particle size up to an optimal point, beyond which coarsening increases attraction again. Thus, the formation of agglomerates at higher TiC nanoparticle concentrations likely prevented effective separation between particles, diminishing flowability. Similarly, fine micrometer-sized TiC particles improved the surface roughness and interparticle spacing, enhancing flow in the 1TiC4μm powder. However, increasing their concentration probably intensified cohesive and adhesive forces, leading to poor flowability in the 2TiC4μm and 4TiC4μm powders. Additionally, free fine TiC particles (<10 μm) not bonded to the metal surface may have further degraded the flow behavior. Conversely, the coarse micrometer-sized TiC particles exhibited a lower surface-area-to-volume ratio, which reduced the influence of interparticle forces relative to gravity, resulting in the best flowability for the 1TiC44μm, 2TiC44μm, and 4TiC44μm powders.

Overall, adding 1 wt.% TiC particles, regardless of size, appears to achieve the critical SAC predicted by Equation 4.7, substantially reducing Van der Waals forces and improving both flowability and apparent density compared to the gas-atomized AA2017 powder. Increasing TiC concentration, however, had contrasting effects depending on particle size. For nanosized TiC particle, agglomeration strengthened attraction forces and reduced flowability, while for fine micrometer-sized TiC particle, loose small particles and narrower PSD decreased apparent density. In contrast, powders with coarse micrometer-sized TiC particles benefited from their broader PSD, which favored higher apparent density and improved flow behavior.

The TiC surface functionalization of AA2017 powders modified surface characteristics, including surface roughness and chemistry, PSD, and apparent density, resulting in reduced laser reflectance compared to the gas-atomized powder (Figure 4.11). As shown in Figure 4.11, laser reflectance decreases with decreasing TiC particle size. For an equivalent TiC concentration, finer TiC

particles provide a higher particle count and greater TiC surface exposure to the laser, thereby enhancing absorption and lowering laser reflectance. Coarse micrometer-sized TiC particles are mostly heterogeneously distributed among AA2017 particles, allowing significant reflection from the aluminum surface, resulting in laser reflectance values similar to the unmodified powder. The most pronounced reduction occurs with nanosized TiC particles, which form a uniform coating layer over the AA2017 surface, maximizing TiC exposure to the laser beam. A similar particle-size-dependent increase in laser absorptivity was reported by Xue *et al.* [98] for AlSi10Mg mixed with SiC particles, where reducing SiC size from 50 µm to 6 µm significantly enhanced absorption. Regardless of TiC particle size, increasing concentration further decreases laser reflectance, reaching a minimum 54.4 % at λ = 950 nm for the 4TiC45nm powder, representing a 14.3% reduction compared to the gas-atomized powder (63.5%).

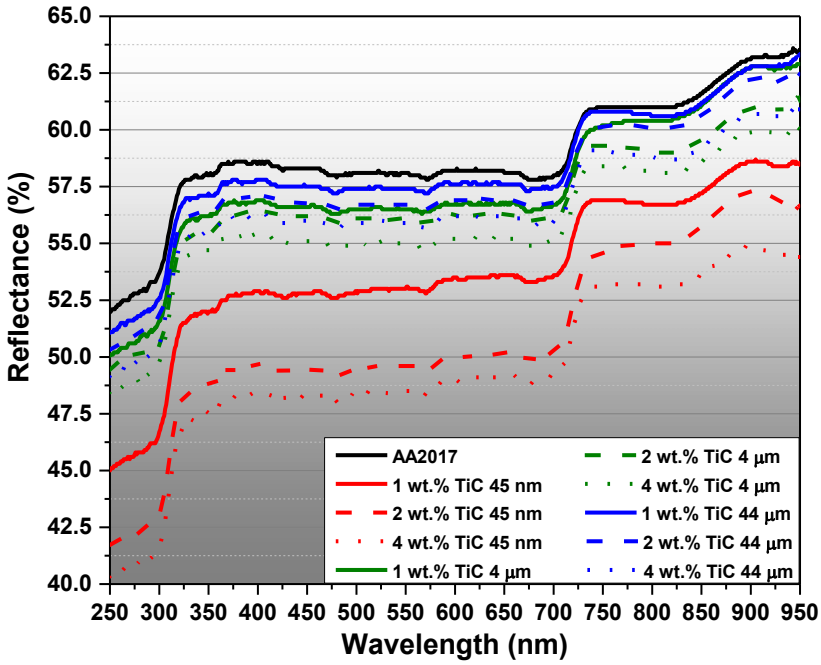

Figure 4.11 - Laser reflectance of the gas-atomized and TiC surface-functionalized AA2017 powders.

Figure 4.12 shows the phase composition of the gas-atomized and TiC surface-functionalized powders. The gas-atomized powder microstructure

consists of α-Al matrix and Al_2Cu phase at the cell boundaries, as previously illustrated in Figure 4.3a. The TiC phase is observed in the diffractograms of the surface-functionalized powders (Figure 4.12). The same unidentified peaks around 2θ = 35° and 2θ = 43° observed in Figure 4.4 can be also seen in Figure 4.12, reinforcing that their presence in the gas-atomized powder is due to minor components of the AA2017 alloy rather than products of surface functionalization. No new phases resulting from reactions between aluminum and TiC were detected, indicating that TiC remained chemically stable during mechanical mixing.

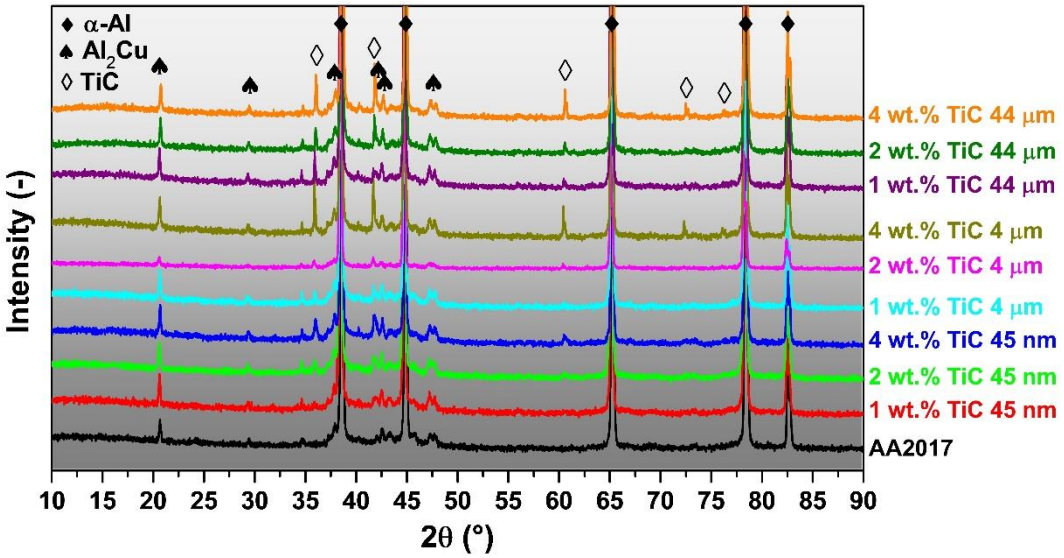

Figure 4.12 - XRD diffractograms of the gas-atomized and TiC surface-functionalized AA2017 powders.

4.1.2.2 Rheological Properties

Table 4.3 presents the CBD of the gas-atomized and TiC surface-functionalized AA2017 powders under dynamic flow condition. The gas-atomized powder exhibits the highest CBD, suggesting an improved packing efficiency of the powder and less air trapped between particles [145], while TiC surface-functionalized powders show lower CBD and greater air entrapment. As previously discussed, TiC particles attached to the powder surface increase artificial surface roughness and interparticle spacing, allowing more air to be trapped between particles and thereby reducing the CBD of powders with

nanosized and fine micrometer-sized TiC. In contrast, coarse micrometer-sized TiC particles, mainly distributed between the aluminum particles, have little impact on CBD. Chu *et al.* [155] similarly reported lower CBD values in coarse AlSi10Mg powders, attributed to increased voids from large particles (the “static wall effect”). Hence, the slightly larger particle size of the surface-functionalized powders compared to the gas-atomized may also contribute to their lower CBD.

Table 4.3 - CBD, SE, SI, FRI, and BFE of the gas-atomized and TiC surface-functionalized AA2017 powders under dynamic flow condition.

Powders	CBD (g/cm^3)	SE (mJ/g)	SI (-)	FRI (-)	BFE (mJ)
AA2017 Gas-atomized	1.55	3.37	1.01	1.39	248
AA2017 + 1 wt.% TiC 45 nm	1.55	3.43	1.08	1.20	304
AA2017 + 2 wt.% TiC 45 nm	1.06	5.14	1.03	1.22	312
AA2017 + 4 wt.% TiC 45 nm	1.49	3.84	1.08	1.20	347
AA2017 + 1 wt.% TiC 4 µm	1.53	3.12	0.99	1.32	241
AA2017 + 2 wt.% TiC 4 µm	1.49	3.59	1.04	1.33	265
AA2017 + 4 wt.% TiC 4 µm	1.01	5.97	1.05	1.36	306
AA2017 + 1 wt.% TiC 44 µm	1.50	3.84	1.04	1.28	327
AA2017 + 2 wt.% TiC 44 µm	1.50	3.35	1.06	1.34	242
AA2017 + 4 wt.% TiC 44 µm	1.49	3.68	1.10	1.30	302

The SE, SI, FRI, and BFE values of the gas-atomized and TiC-functionalized powders are also listed in Table 4.3. Generally, the higher SE and BFE of powders with nanosized and fine micrometer-sized TiC particles are attributed to increased surface roughness and mechanical interlocking caused by the attached TiC particles that increases flow resistance. The lowest SE = 3.12 mJ/g and BFE = 241 mJ values were recorded for the 1TiC4µm powder, likely due to its low TiC concentration providing sufficient interparticle spacing without substantially increasing surface roughness. As TiC concentration rises, roughness and interlocking intensify, increasing SE and BFE, particularly for

powders with fine micrometer-sized TiC. Since SE is closely related to flowability under low-stress conditions, such as during powder spreading in L-PBF [97,125], the 1TiC4 µm powder would require the least energy to flow and disperse among the TiC surface-functionalized powders. Overall, the CBD, SE, and BFE trends align with those observed for chemically surface-functionalized AA2017 powders (Table 4.2).

Additionally, the gas-atomized and TiC-functionalized powders display good stability, with SI values of approximately 1.01 and 1.05 ± 0.03, respectively. The highest stability occurs in the gas-atomized and 1TiC4µm powder, while the 4TiC44µm powder shows the lowest stability (SI = 1.10), likely due to the heterogeneous distribution of large irregular TiC particles altering its flow behavior during the test. Overall, FRI values of both gas-atomized and TiC-functionalized powders are similar to the chemically surface-functionalized powders, suggesting that they also present enhanced dynamic flow behavior.

Under aerated condition, as shown in Figure 4.13, the surface-functionalized 1TiC44µm powder is the least sensitive to aeration (AR = 69.97), followed by the gas-atomized powder (AR = 100.00), whereas the surface-functionalized 4TiC44µm powder exhibits the highest sensitivity (AR = 217.79), followed by the 1TiC4µm powder (AR = 204.62). Without gas flow, the 4TiC45nm powder presents the highest AE_0 and tendency to agglomeration due to its high concentration of nanosized TiC particles, while AE_0 decreases with lower TiC content and larger particle size. At a nitrogen flow velocity of 4 mm/s, the lowest tendency for agglomeration is observed for the 1TiC4µm powder (AE_4 = 2.38 mJ), likely resulting from reduced mechanical interlocking and interparticle forces. In contrast, the 1TiC44µm powder shows the highest AE_4, indicating the poorest flow under aeration condition. Such higher AE_4 suggests increased gas entrapment during powder spreading, which can produce non-uniform powder layers and higher cavity formation [155].

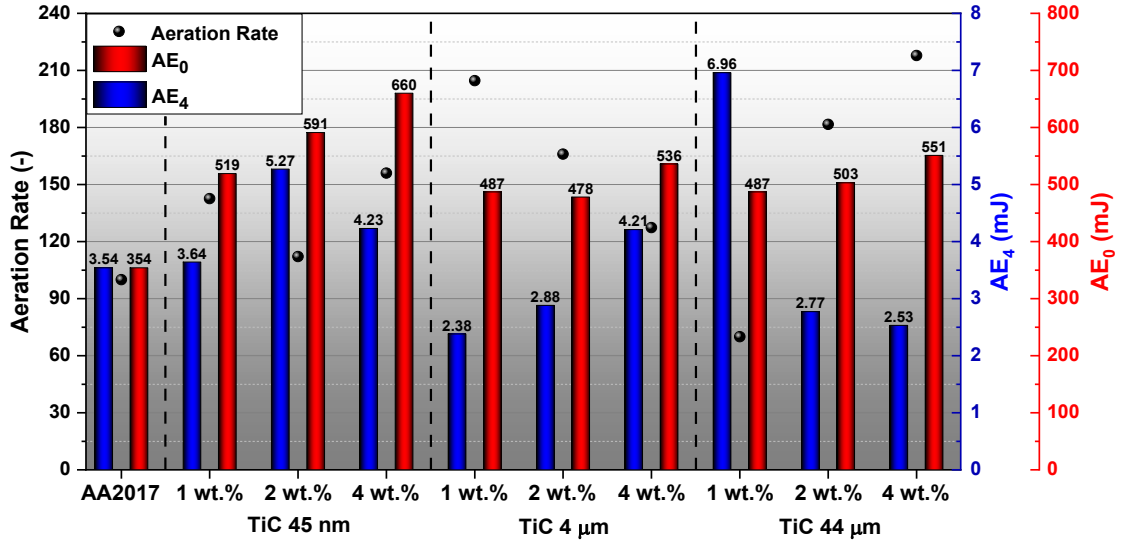

Figure 4.13 - AE_0, AE_4, and AR of the gas-atomized and TiC surface-functionalized AA2017 powders under aerated condition.

Under packed condition (Figure 4.14a), the gas-atomized powder and the surface-functionalized powders with coarse micrometer-sized TiC particles exhibit the highest permeability. Permeability decreases with finer TiC particles, likely due to particle agglomeration partially obstructing gas flow paths. Most powders show little sensitivity to applied normal stress, except for the 1TiC4µm powder, where compression reduces permeability through particle rearrangement. The best performance in the compressibility test (Figure 4.14b) is observed for the 2TiC45nm, 1TiC44µm, and 2TiC44µm powders, which display the lowest CI values and, consequently, the most efficient packing ability. In contrast, the 1TiC4µm powder shows the highest CI, indicating poor packing and higher entrapped air. Under shear conditions (Figure 4.14c), σ_c, σ_1, τ_0, and ff_c were measured. The 1TiC4µm powder exhibits the lowest ff_c (ff_c = 8.2), while the 1TiC44µm powder reaches the highest value (ff_c = 75.0). Based on ff_c classification [157], most powders are free-flowing (ff_c > 10), except the 1TiC4µm powder, which is categorized as easy flowing (4 < ff_c < 10). The cohesion coefficient τ_0 is generally lower for the surface-functionalized powders than for the gas-atomized powder, which suggests a reduced cohesion between the powder particles and better flowability, with the exception of the 1TiC4µm powder, which shows the highest τ_0 of 0.187. This pattern aligns with its poor

packing performance under compression and highlights that powder flow behavior varies with testing conditions.

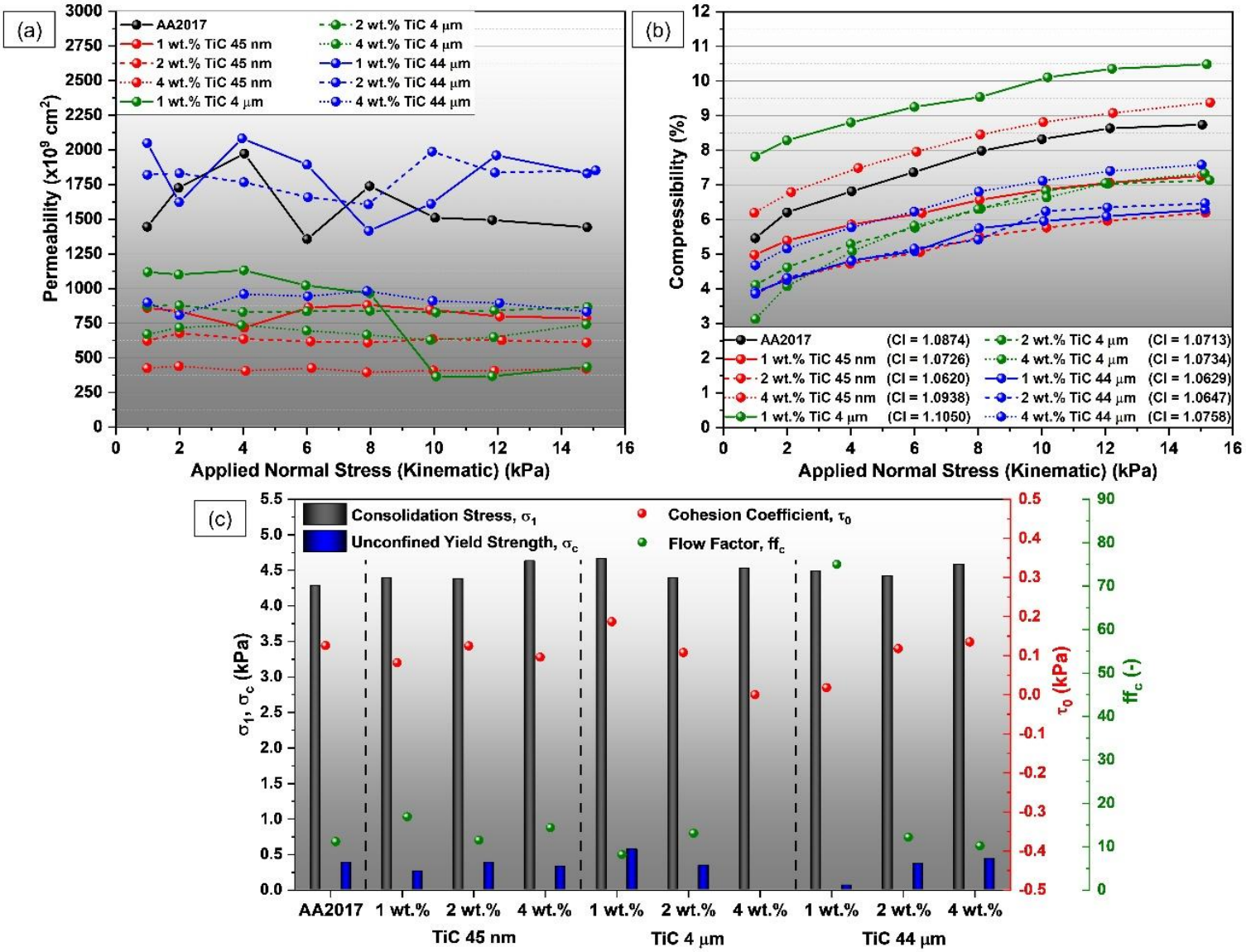

Figure 4.14 - (a) Permeability and (b) compressibility as a function of the applied normal stress; (c) consolidation stress, unconfined yield strength, cohesion coefficient, and flow factor of the gas-atomized and TiC surface-functionalized AA2017 powders under shear condition.

The summarized influence of the rheological properties of the gas-atomized and TiC surface-functionalized powders on their suitability for L-PBF (AMS factor) is shown in Figure 4.15, estimated using Equation 4.6. The TiC

surface-functionalized powders generally exhibit higher AMS factors (worse L-PBF suitability) than the gas-atomized powder. Among them, τ_0, permeability, and AE_4 contribute most to the differences, while CBD, CI, SE, and BFE are similar across powders. The 2TiC44µm powder shows the best L-PBF suitability (lowest AMS factor = 0.59), whereas the 1TiC4µm powder, despite good dynamic flow (low BFE and high CBD) and aerated (low AE_4) behavior, performs poorly under packed (low permeability) and shear (high τ_0) conditions, increasing its AMS factor (AMS factor = 0.74).

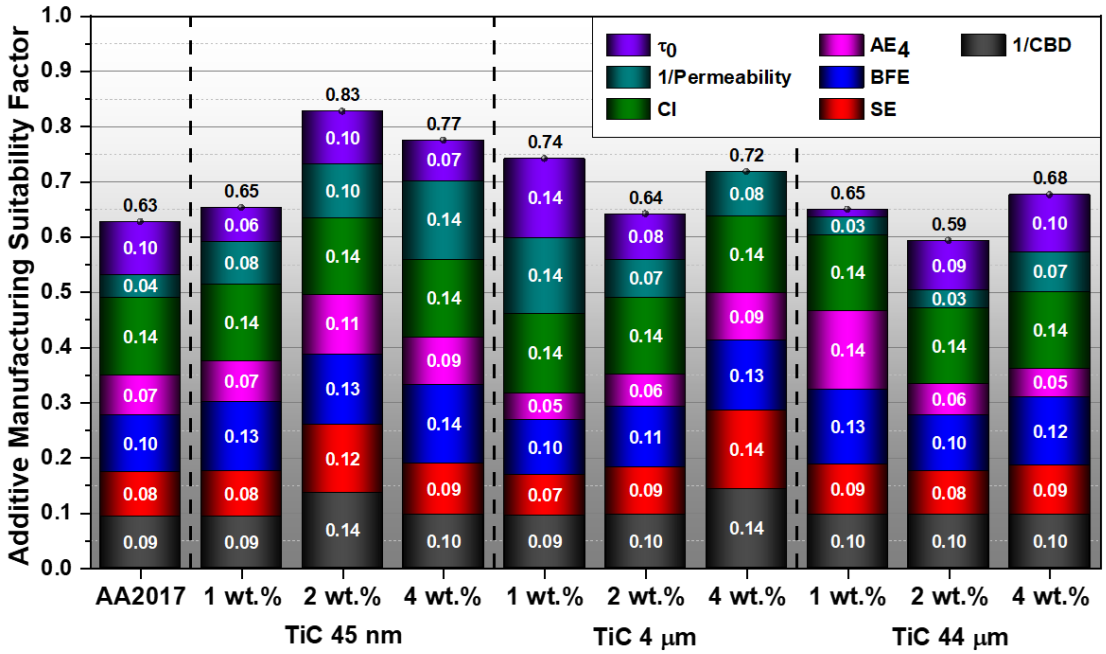

Figure 4.15 - AMS factors of the gas-atomized and TiC surface-functionalized AA2017 powders.

In general, 1 wt.% of TiC addition, regardless of particle size, markedly improves powder properties, including apparent density, flowability, and laser reflectance, making it favorable for L-PBF processing, even though the AMS factor is slightly increased. In contrast, higher TiC concentrations tend to reduce flow performance, except for the 2TiC44µm powder that exhibits the best L-PBF suitability (lowest AMS factor) according to its rheological properties.

4.2 Investigation on laser powder bed fusion processing window using design of experiments and analysis of variance

The influence of the processing parameters on the porosity and cumulative crack length of the as-built AA2017 and 2TiC45nm alloys was assessed using a Box-Behnken design combined with analysis of variance (ANOVA). Among the nine TiC-modified powder combinations, the process parameter understanding and optimization were carried out using the 2TiC45nm powder, as this composition and particle size are widely used and well-established in the literature (Section 3.3). Although the Box-Behnken design was initially also applied to the HNO_3 and NaOH surface-functionalized powders, these powders led to a higher defect formation and, in some parameter combinations, even failed to produce samples. This prevented a reliable optimization of the L-PBF processing parameters for chemically surface-functionalized powders. For this reason, only the optimization performed with the 2TiC45nm powder was compared to that of the gas-atomized AA2017 powder. The understanding of the influence of the L-PBF processing parameters on samples produced with chemically-treated powder will be presented separately in Section 4.3.

As shown in Figure 4.16, the as-built samples from the gas-atomized AA2017 powder display common defects such as lack-of-fusion porosity (blue arrows), gas pores, and solidification cracks (red arrows) oriented along the build direction. From a qualitative analysis of Figure 4.16, several general observations can be drawn. Firstly, large irregular voids appear mainly at low laser power (150 W) or high scanning speed (1200 mm/s) due to incomplete melting and weak interlayer bonding [129], as can be clearly seen in Figure 4.16l. Increasing the laser power and reducing the scanning speed mitigates lack-of-fusion porosity but makes existing solidification cracks more pronounced, a well-known issue in 2xxx aluminum alloys [10,90,131]. For instance, at a hatch distance of 90 μm, lack-of-fusion porosity significantly reduces when the scanning speed decreases from 1200 mm/s (Figure 4.16l) to 100 mm/s (Figure 4.16k) at low laser power (150 W), and appears to be completely eliminated when the laser power is increased to 250 W (Figure 4.16b and Figure 4.16c). Secondly, solidification cracking is highly dependent on laser parameters. As observed in Figure 4.16,

solidification crack density visually decreases with higher laser power (200 and 250 W) and lower scanning speed, particularly at the minimum of 100 mm/s, consistent with reports linking this behavior to lower cooling rates when the scanning speed is reduced, which favor liquid backfilling and reduce thermal stress [58,129,135]. Thirdly, however, the hatch distance, shows little effect on solidification crack formation. Hu *et al.* [134] showed that the influence of hatch distance on solidification crack susceptibility is weak compared to the laser power and scanning speed, but a small hatch distance is essential to ensure proper laser track and avoid cracking. Nevertheless, in the present study, the chosen parameters provided sufficient track overlap, so hatch distance did not significantly affect cracking or porosity. Instead, it appears that laser power and scanning speed play a more important role in determining defect formation.

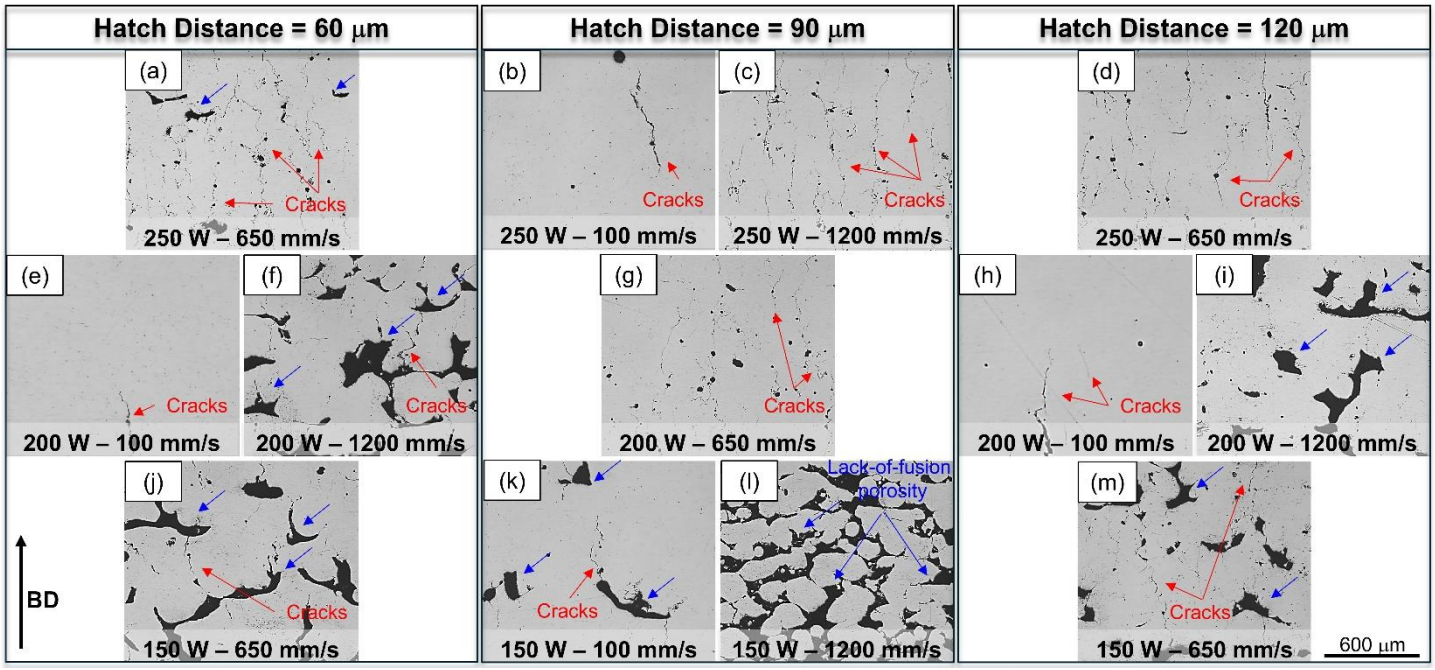

Figure 4.16 - Optical micrographs showing porosity and solidification cracks in L-PBF-processed AA2017 samples fabricated under different processing conditions. Blue arrows indicate lack-of-fusion pores, and red arrow marks solidification cracks.

Small spherical gas pores are observed in all samples, mainly originating from gas trapped during atomization, between powder layers, or from volatile

elements such as magnesium released during melting [34,129,161,162]. These fine pores are generally less harmful to the mechanical integrity of as-built components than lack-of-fusion porosity [34].

Figure 4.17 presents the microstructure of as-built L-PBF samples produced using the 2TiC45nm surface-functionalized powder. In a similar manner, general observations can be drawn from this figure. The TiC nanoparticles are uniformly dispersed throughout the 2TiC45nm samples, with a few minor agglomerations observed (green arrows in Figure 4.17). Both AA2017 and 2TiC45nm alloys exhibit lack-of-fusion porosity (blue arrows) and solidification cracks (red arrows). However, the overall defect content is notably lower in the 2TiC45nm specimens. When comparing Figures 4.16 and 4.17, for instance, at low laser power (150 W) and high scanning speed (1200 mm/s), the 2TiC45nm alloy qualitatively shows reduced porosity compared to the unmodified AA2017. Furthermore, for the 2TiC45nm alloy, lack-of-fusion defects seems to be eliminated (or strongly reduced) at intermediate scanning speed (650 mm/s) with high laser power (250 W) (Figure 4.17a and Figure 4.17d), or at low scanning speed (100 mm/s) with low laser power (150 W) (Figure 4.17k), whereas the AA2017 alloy required higher power levels (200-250 W) at low scanning speed (100 mm/s) to achieve similar densification. Solidification cracks were not detected in 2TiC45nm samples processed at 100 mm/s (Figure 4.17e and Figure 4.17h), while they persisted in the unmodified alloy under the same processing parameters (Figure 4.16e and Figure 4.17h). These results indicate that nano-TiC surface functionalization enhances the L-PBF processability of AA2017 alloy, consistent with previous findings on inoculant-modified 2xxx aluminum alloys [59,135,163,164].

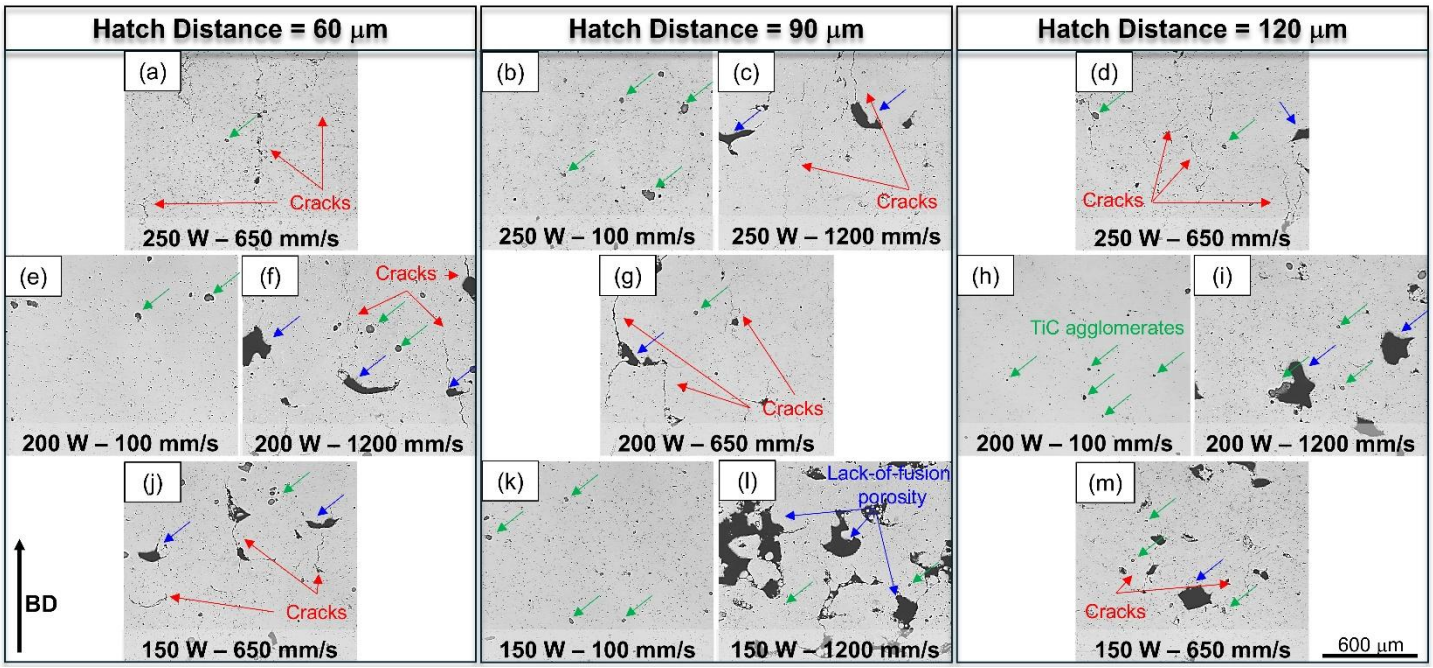

Figure 4.17 - Optical micrographs showing porosity and solidification cracks in L-PBF-processed 2TiC45nm samples fabricated under different processing conditions. Lack-of-fusion pores, solidification cracks, and TiC agglomerates indicated by blue, red, and green arrows, respectively.

Figure 4.18 and Table A1 (Appendix) present the porosity and cumulative crack length of the AA2017 and 2TiC45nm samples as a function of the E_v (Equation 2.1). For the AA2017 samples (Figure 4.18a), both responses follow a similar trend, decreasing as E_v increases. The minimum porosity and cumulative crack length of 0.21 ± 0.08 % and 0.01 ± 0.02 mm/mm^2, respectively, were obtained at E_v = 555.56 J/mm^3 (P = 200 W, v = 100 mm/s, h = 120 μm). This indicates that higher E_v values promote denser, nearly crack-free as-built samples in the studied parameters range. The observed reduction in porosity and solidification cracking with increasing E_v is primarily related to the combined effect of higher laser power and lower scanning speed, which enhances melting and interlayer bonding. Moreover, elevated E_v levels raise the melt pool temperature, which decreases residual stresses, thereby limiting solidification cracking [136]. The higher molten zone temperature also lowers the dynamic viscosity (μ) of the liquid metal, as expressed in Equation 4.8 by Gu *et al.* [165], where m is the atomic mass, λ the liquid surface tension, k_B the Boltzmann constant, and T the

melt temperature. According to Tan *et al.* [129], this viscosity reduction improves melt fluidity and facilitates an effective crack backfilling, leading to a lower overall solidification crack density.

$$\mu = \frac{16}{15}\sqrt{\frac{m}{k_B.T}\lambda}\left(\frac{kg}{m.s}\right) \quad (4.8)$$

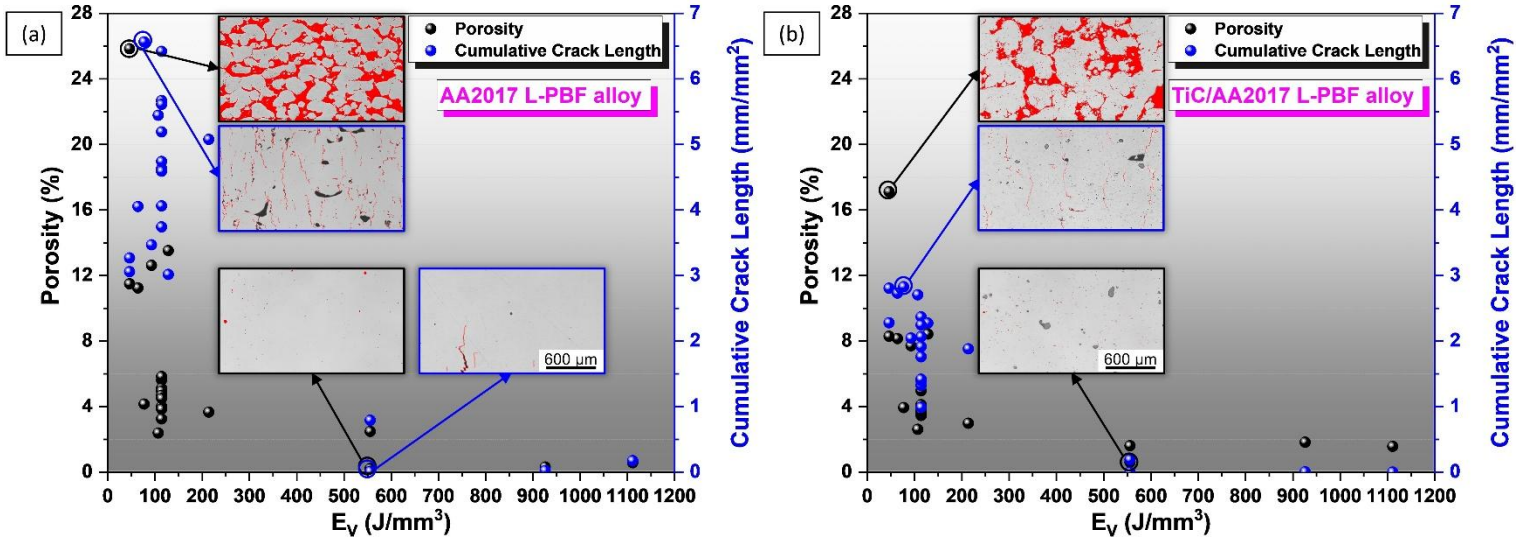

Figure 4.18 - Porosity and cumulative crack length of the as-built (a) AA2017 and (b) 2TiC45nm alloys produced by L-PBF as a function of the volumetric energy density (E_v).

The porosity and cumulative crack length of the 2TiC45nm samples (Figure 4.18b) exhibit a similar dependence on E_v as observed for the AA2017 alloy, both decreasing with increasing E_v. The minimum porosity of 0.6 ± 0.2 %, recorded at E_v = 555.56 J/mm^3 (P = 200 W, v = 100 mm/s, h = 120 µm), corresponded to a crack-free condition. Overall, the 2TiC45nm samples showed lower porosity and cumulative crack length than the unmodified AA2017 samples. The maximum porosity in the AA2017 alloy reached 25.8 ± 2.8 % at E_v = 46.30 J/mm^3 (P = 150 W, v = 1200 mm/s, h = 90 µm), whereas the 2TiC45nm counterpart exhibited a lower value of 17.1 ± 2.5 % under identical processing parameters. Similarly, the highest cumulative crack length in AA2017 was 6.6 ± 2.4 mm/mm^2 at Ev = 77.16 J/mm^3 (P = 250 W, v = 1200 mm/s, h = 90 µm),

compared to 2.8 ± 0.9 mm/mm^2 for the 2TiC45nm alloy under identical processing parameters. These results indicate that nano-TiC surface functionalization enhances the printability of AA2017 by mitigating porosity and solidification cracking under the same processing conditions. This trend aligns with previous reports where inoculant additions, such as AlTiB or Zr, improved the processability of high-strength Al alloys by reducing solidification cracking susceptibility and porosity during L-PBF processing [59,135,163,164].

To systematically assess the effect of L-PBF parameters on the porosity and cumulative crack length of AA2017 and 2TiC45nm alloys, an ANOVA was performed on the RSM models fitted to the experimental data. The ANOVA results, obtained at a 95% confidence level, are presented in Table A2 to Table A5 in Appendix. This statistical analysis quantifies the variance between measured and predicted data through F-values and p-values, which indicate the model's adequacy. Models are generally considered statistically significant when p-values are below 0.05 [166,167]. For the AA2017 alloy (Tables A2 and Table A3), the significant factors influencing porosity were identified as P, v, P^2, v^2, and the interaction P*v, while for cumulative crack length, the relevant terms were P, v, v^2, and P*v. The hatch distance showed no significant effect on either response and was thus excluded from the models, along with all terms having p-values above 0.05. After refitting, the resulting reduced quadratic models for porosity and cumulative crack length are given by Equation 4.9 and Equation 4.10, with R^2 values of 0.9757 and 0.8764, respectively, indicating good predictive accuracy.

$$\text{Porosity} = 39.64 - 0.4165 * \text{P} + 0.04190 * \text{v} + 0.001063 * \text{P}^2 + 0.000004 * \text{v}^2 - 0.000177 * \text{P} * \text{v} \quad (4.9)$$

$$\text{Cumulative Crack Length} = 0.68 - 0.0091 * \text{P} + 0.00730 * \text{v} - 0.000009 * \text{v}^2 + 0.000037 * \text{P} * \text{v} \quad (4.10)$$

For the 2TiC45nm alloy (Tables A4 and Table A5), porosity was governed by the same factors as in the unmodified alloy (i.e., P, v, P^2, v^2, and P*v), again

showing negligible influence of hatch distance. However, for cumulative crack length, the significant terms differed slightly, being P, v, P^2, and v^2. After excluding non-significant terms, the reduced quadratic models for porosity and cumulative crack length were expressed as Equation 4.11 and Equation 4.12, achieving R^2 values of 0.9815 and 0.8529, respectively, which confirm the strong fit and reliability of the models.

$$\text{Porosity} = 23.02 - 0.2482 * \text{P} + 0.02857 * \text{v} + 0.000669 * \text{P}^2 + 0.000002 * \text{v}^2 - 0.000122 * \text{P} * \text{v} \quad (4.11)$$

$$\text{Cumulative Crack Length} = 8.77 - 0.0938 * \text{P} + 0.005397 * \text{v} + 0.000231 * \text{P}^2 - 0.000002 * \text{v}^2 \quad (4.12)$$

The influence of both individual and interaction of L-PBF process parameters on the porosity and cumulative crack length of the AA2017 and 2TiC45nm alloys was evaluated using the reduced regression models (Equation 4.9 to Equation 4.12) and is presented in Figures 4.19 and Figure 4.20. For the AA2017 alloy, laser power and scanning speed were identified as the dominant parameters affecting both porosity and cumulative crack length. As shown in Figure 4.19a-c, increasing the laser power and reducing the scanning speed substantially decrease porosity, while the hatch distance exerts negligible influence. At high scanning speeds, increasing the laser power markedly lowers porosity, whereas at low scanning speeds, this effect becomes less pronounced or even slightly reversed, likely due to keyhole pores formed at high laser power as a consequence of the high melt pool temperature. Conversely, reducing scanning speed consistently decreases porosity, particularly at low laser power. Regarding cumulative crack length, laser power and scanning speed again play key roles, with complex interdependencies revealed in Figure 4.19d-f. The cumulative crack length increases with scanning speed up to a maximum (between 714 and 920 mm/s, depending on the laser power) before decreasing again, independently of hatch distance but influenced by laser power. At high scanning speeds (1200 mm/s), increasing laser power promotes solidification

crack formation, while at low scanning speeds (100 mm/s), the opposite trend occurs, and cumulative crack length slightly diminishes with increasing power. Overall, both porosity and solidification crack density can be minimized by employing high laser power and low scanning speed, confirming their critical interaction in determining build integrity.

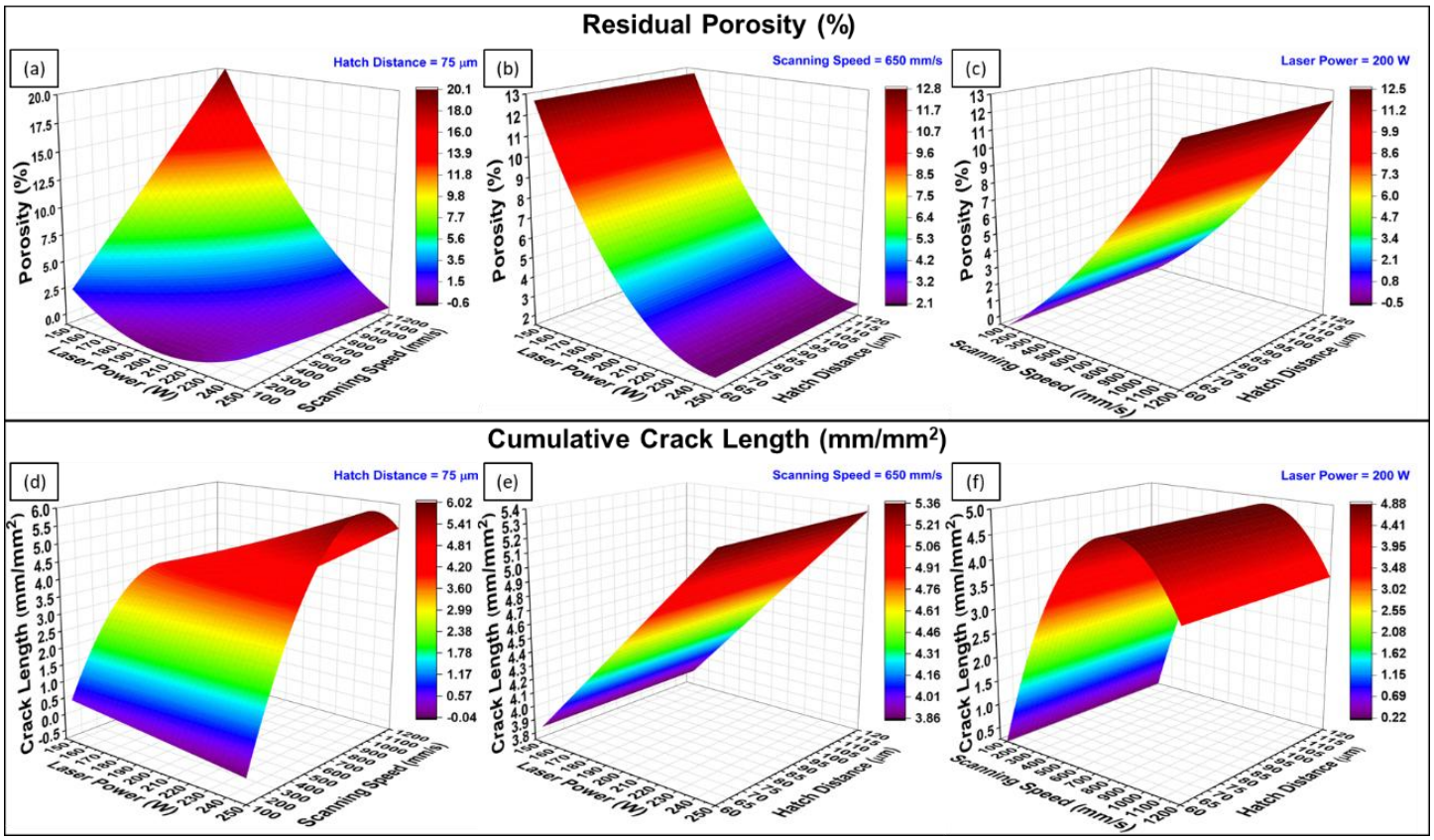

Figure 4.19 - Response surface plots from the reduced regression models showing the influence of L-PBF processing parameters on (a–c) porosity and (d–f) cumulative crack length of the as-built AA2017 alloy.

For the 2TiC45nm alloy, the effects of laser power, scanning speed, and hatch distance on porosity (Figure 4.20) follow similar general trends but exhibit notable differences in their influence on cumulative crack length. As shown in Figure 4.20a-c, porosity decreases with higher laser power and lower scanning speed, regardless of hatch distance, mirroring the unmodified alloy. However, the interaction effects on crack formation differ (Figure 4.20d-f). The cumulative crack

length initially decreases with increasing laser power up to an optimal point (around 200 W), beyond which it rises again, while increasing scanning speed consistently increases cumulative crack length. These effects are largely independent of hatch distance. The differing influence of laser power and scanning speed on the cumulative crack length of the as-built AA2017 and 2TiC45nm alloys may be related to the higher laser absorption of TiC-modified powder (Figure 4.11).

As previously discussed, lower scanning speed reduces solidification crack susceptibility due to slower cooling rates, while higher laser power, and consequently, higher E_v, reduces residual stress and melt viscosity, facilitating crack backfilling. This trend is observed in the as-built AA2017 alloy (Figure 4.19d), except at very low laser power (150 W) and high scanning speed (1200 mm/s), where cumulative crack length decreases due to very high porosity levels (i.e., lack-of-fusion defects) that limit solidification crack formation. In the as-built 2TiC45nm alloy, higher laser energy absorption improves melting and interlayer bonding, resulting in lower porosity (lower lack-of-fusion defects) compared to the as-built AA2017 alloy. Consequently, porosity does not limit solidification cracking at low laser power and high scanning speed, and an increase in cumulative crack length is observed under these conditions, as expected. However, unexpectedly, the cumulative crack length in the as-built 2TiC45nm alloy also increases at high laser power. A similar behavior was reported by Yao *et al.* [133] for L-PBF processing the AA2024 alloy, which attributed the increase in solidification cracking at low scanning speed and high laser power to excessive E_v. Excessive E_v can cause vaporization of moisture and low-melting-point metallic elements, leading to porosity and keyhole formation, which concentrates stress and promotes crack formation. Therefore, in the as-built 2TiC45nm alloy, the increase in cumulative crack length at high laser power is most likely due to excessive E_v. This leads to pore formation and, consequently, crack formation as a result of excessive laser energy absorption, due to the additional laser energy absorption occasioned by the TiC particles compared to gas-atomized AA2017 powder, as shown in Figure 4.11 (Section 4.1.2.1). In summary, both alloys benefit from increased laser power and reduced scanning speed (i.e., increased E_v), which

collectively minimize porosity and solidification cracking. However, the TiC-modified alloy exhibits a lower overall defect density and a more stable response to variations in processing parameters, indicating that nano-TiC surface functionalization enhances the processability and robustness of AA2017 alloy during L-PBF.

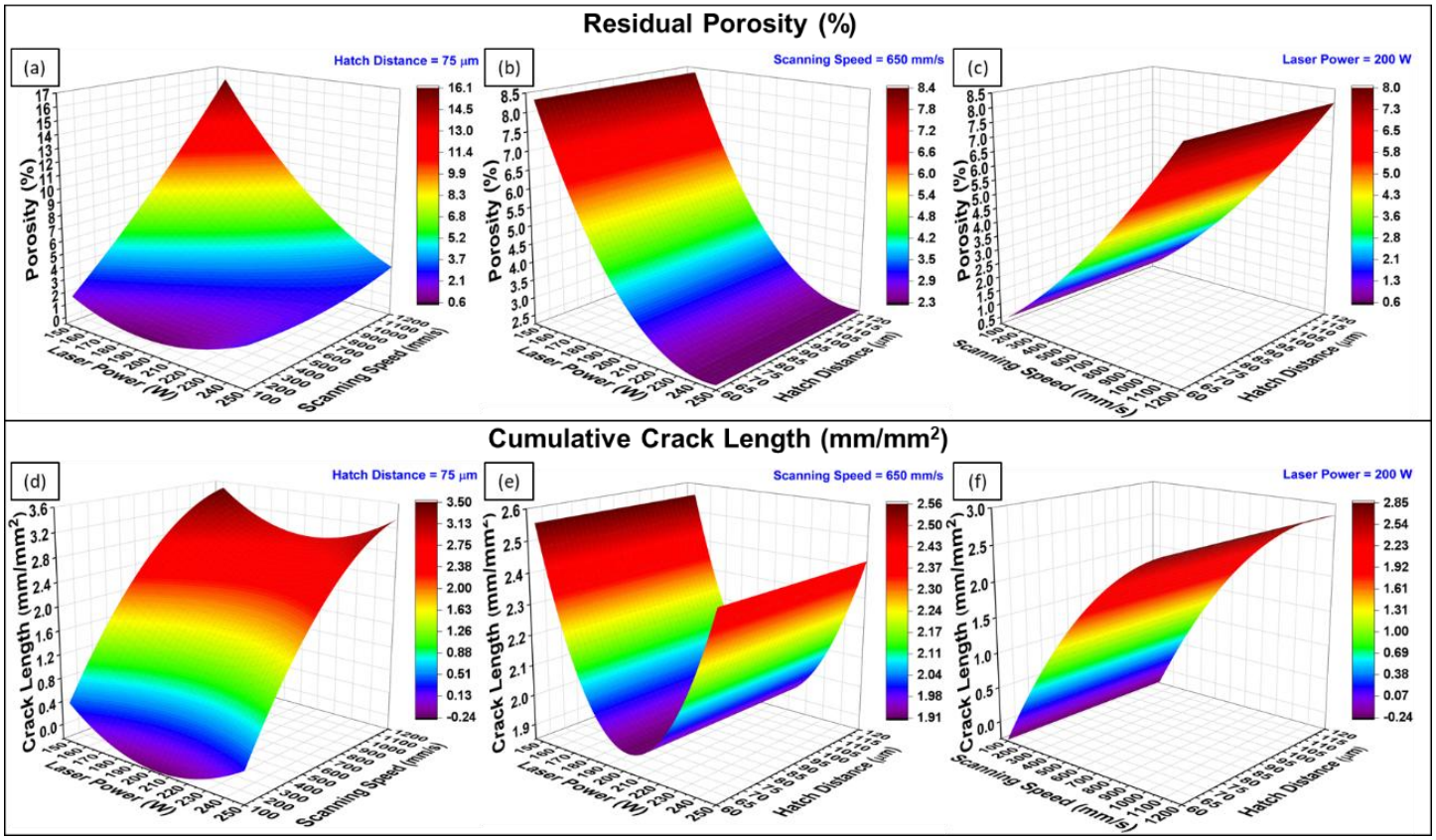

Figure 4.20 - Response surface plots from the reduced regression models showing the influence of L-PBF processing parameters on (a–c) porosity and (d–f) cumulative crack length of the as-built 2TiC45nm alloy.

The reduced regression models were validated by plotting predicted versus experimental values of porosity and cumulative crack length for both AA2017 and 2TiC45nm alloys, as shown in Figure 4.21. Additional samples produced using randomly selected process parameters (Table A1, Appendix) were also included. The data points cluster close to the 45° line and fall within the confidence and prediction intervals, with R^2 values exceeding 0.80, confirming

that the models reliably predict porosity and cumulative crack length in L-PBF-fabricated AA2017 and 2TiC45nm alloys.

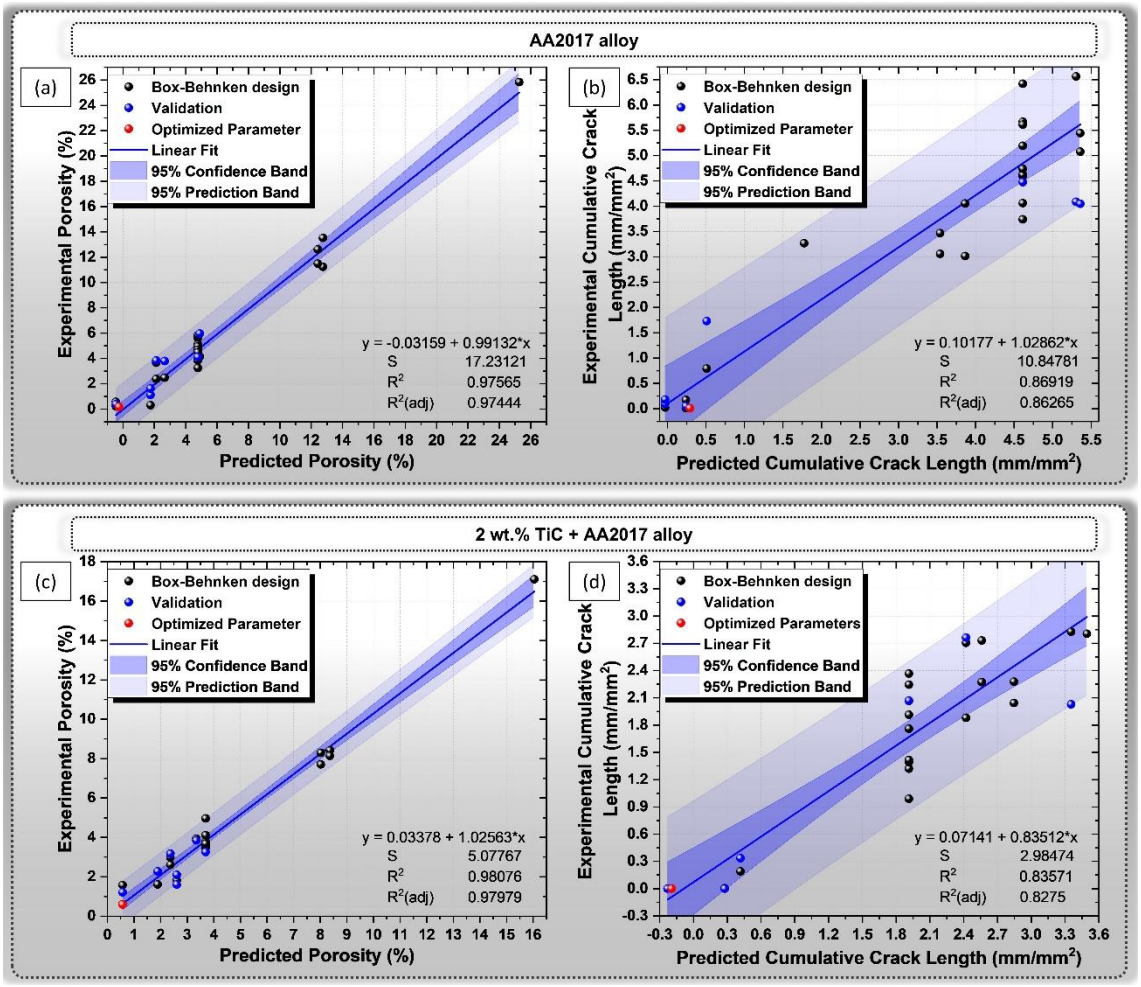

Figure 4.21 - Comparison of experimental and predicted values for porosity and cumulative crack length of the as-built (a–b) AA2017 and (c–d) 2TiC45nm samples, based on the experimental results and reduced regression models.

The contour plots in Figure 4.22 illustrate the combinations of processing parameters to obtain the AA2017 (blue region) and 2TiC45nm (green region) alloys with low porosity (<1%) and cumulative crack length (<1 mm/mm^2). The red region in Figure 4.22b indicates the processing parameter combinations that can produce a crack-free 2TiC45nm alloy. Comparing the alloys, a wider range of processing parameter combinations yields a low-porosity AA2017 alloy compared to the 2TiC45nm alloy (Figure 4.22a). Conversely, more processing

parameter combinations result in a lower cumulative crack length in the 2TiC45nm alloy than in the AA2017 alloy Figure 4.22b).

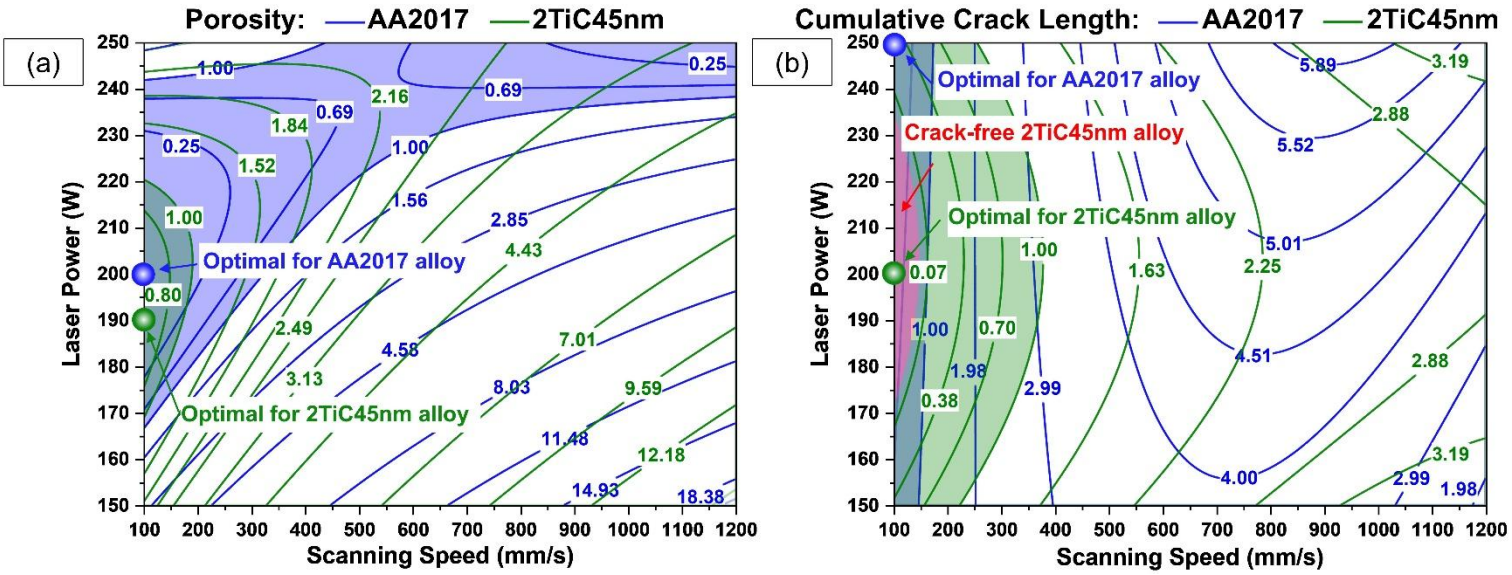

Figure 4.22 - Contour plots showing the influence of the laser power and scanning speed on the (a) porosity and (b) cumulative crack length of the as-built AA2017 and 2TiC45nm alloys.

To minimize porosity and cumulative crack length, the L-PBF process parameters were optimized using the validated reduced regression models (Equation 4.9 to Equation 4.12) (refer to Section 3.3). For this, the reduced regression models were used to predict responses across the entire design space, generating response graphs that show how porosity and cumulative crack length vary with each parameter (Figure A3 in the Appendix). A desirability function was then applied to identify the parameter combination that minimizes both responses. Table 4.4 presents the optimized L-PBF process parameters for both alloys. The optimized processing parameters for the AA2017 and 2TiC45nm alloys are also indicated in Figure 4.22. The laser power values obtained from the ANOVA optimization were slightly rounded down to practical setup processing values. These remained within the acceptable 95% confidence interval range.

Table 4.4 - Optimized L-PBF process parameters for the porosity and cumulative crack length of the AA2017 and TiC/AA2017 alloys.

Optimized Response	AA2017 alloy			TiC/AA2017 alloy		
	Laser Power (W)	Scanning Speed (mm/s)	Hatch Distance (μm)	Laser Power (W)	Scanning Speed (mm/s)	Hatch Distance (μm)
Porosity	200	100	-	190	100	-
Cumulative crack length	250	100	-	200	100	-

For both responses and alloys, the optimal scanning speed was consistently 100 mm/s, aligning with the reductions in porosity and cumulative crack length observed at lower scanning speeds (Figure 4.16 and Figure 4.17). Optimal laser power varied with the response and alloy: for porosity, 200 W for AA2017 and 190 W for 2TiC45nm alloy; for cumulative crack length, 250 W for AA2017 and 200 W for 2TiC45nm alloy. Firstly, these results indicate that lower laser power is sufficient to minimize porosity than to minimize cumulative crack length, when considering the individual alloys. Secondly, the 2TiC45nm alloy requires lower laser power than the AA2017 alloy for both responses, confirming that nano-TiC surface functionalization improved the L-PBF processing of the AA2017 alloy.

As hatch distance was not significant in the reduced regression models, an one-factor-at-a-time approach was employed to evaluate the influence of hatch distance on the porosity and cumulative crack length of AA2017 and 2TiC45nm samples (Figure 4.23, numerical values reported in Table A6 in the Appendix). Three hatch distances (60, 90, and 120 μm) were tested for each combination of optimal laser power and scanning speed. For both alloys, porosity and cumulative crack length generally decrease slightly with increasing hatch distance (Figure 4.23a). AA2017 samples produced at 200 W show slightly lower porosity and solidification crack density than those produced at 250 W, and the same trend is observed for 2TiC45nm samples at 200 W. Except for the sample produced at E_v = 925.93 J/mm^3 (P = 250 W, v = 100 mm/s, h = 90 μm), which

exhibited minor solidification cracks (0.005 ± 0.020 mm/mm^2), all remaining 2TiC45nm samples were crack-free.

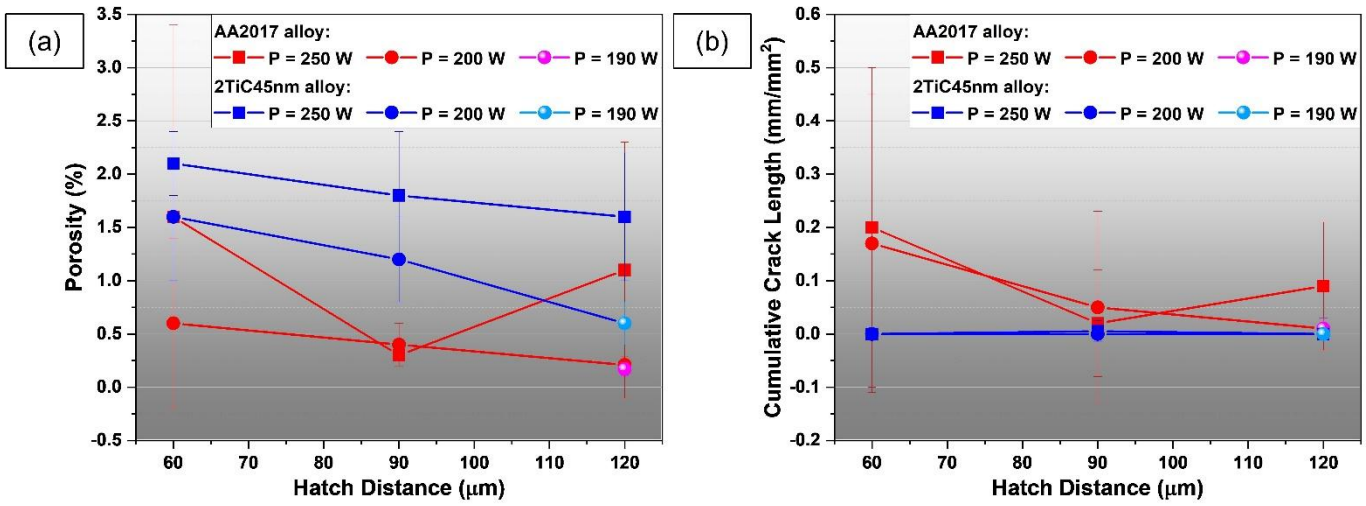

Figure 4.23 - Comparison of (a) porosity and (b) cumulative crack length of the AA2017 and 2TiC45nm samples produced using the optimized sets of L-PBF process parameters.

Based on the observations, an optimal hatch distance of 120 µm was selected to produce samples with a laser power of 190 W and scanning speed of 100 mm/s, resulting in the lowest porosity for both alloys and the lowest cumulative crack length for AA2017 alloy, with the 2TiC45nm samples remaining crack-free (Figure 4.23). Accordingly, a hatch distance of 120 µm was used to prepare contour plots overlaying the combined effect of laser power and scanning speed on porosity and cumulative crack length for each alloy (Figure 4.24). As shown in Figure 4.22, the regions meeting the criteria of low porosity (<1%) and low cumulative crack length (<1 mm/mm^2) for the AA2017 alloy, and low porosity and crack-free conditions for the 2TiC45nm alloy, were identified and highlighted as hatched areas in Figure 4.24, defining the optimal L-PBF processing windows. For the AA2017 alloy, low porosity and cumulative crack length can be obtained at laser powder between 178 and 231 W and scanning speeds between 100 and 165 mm/s, while low-porosity and crack-free 2TiC45nm samples can be produced using laser powder between 172 and 220 W and scanning speeds between 100 and 146 mm/s. If a small cumulative crack length (<1 mm/mm^2) is

acceptable for the 2TiC45nm alloy, the upper scanning speed limit extends to 190 mm/s. Notably, the selected combination of a laser power of 190 W and scanning speed of 100 mm/s lies well within these optimal processing windows, confirming its suitability for producing high-quality specimens with both alloys.

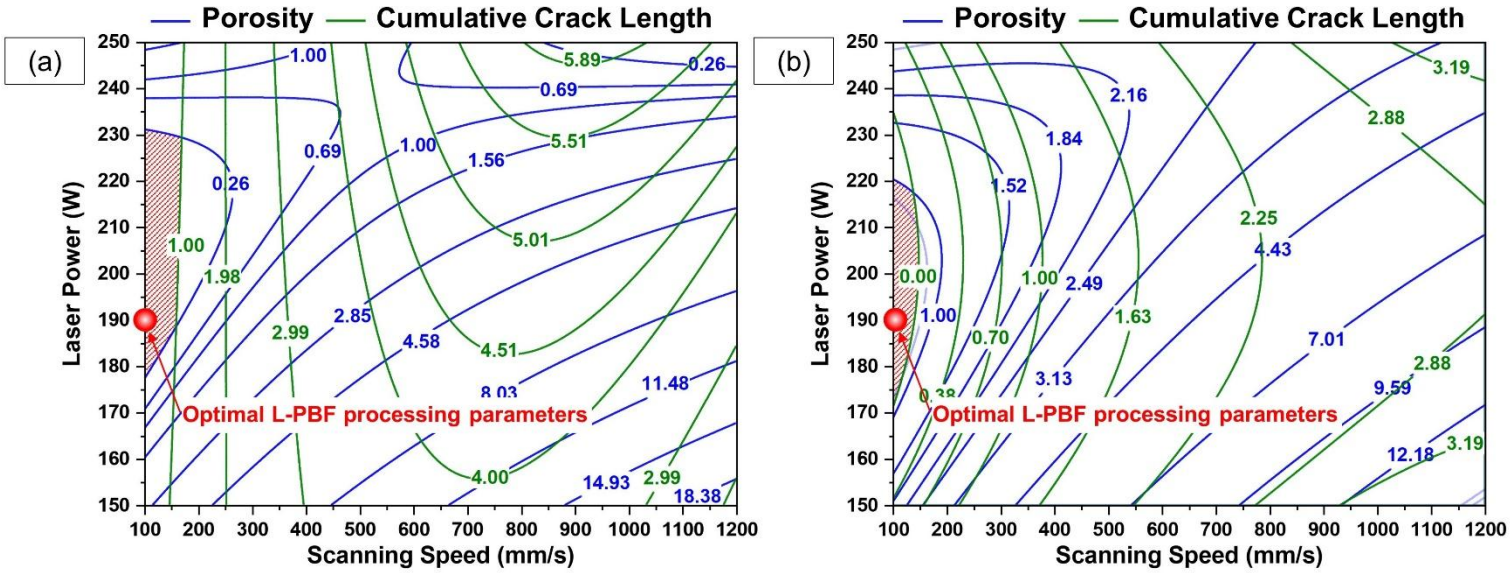

Figure 4.24 - Contour plots showing the influence of the laser power and scanning speed on the porosity and cumulative crack length of the as-built (a) AA2017 and (b) 2TiC45nm alloys.

Therefore, an optimized combination of processing parameters, with a laser power of 190 W, a scanning speed of 100 mm/s, and a hatch distance of 120 µm, can be established in this work, minimizing porosity and cumulative crack length in both alloys. These optimized L-PBF conditions resulted in a AA2017 alloy with a very reduced amount of porosity of 0.17 ± 0.06 % and a cumulative crack length of 0.01 ± 0.02 mm/mm^2, and a crack-free 2TiC45nm alloy with a porosity of 0.6 ± 0.2 %. Similar optimized parameters have been reported by Wang *et al.* [136] and Elambasseril *et al.* [135] for Al-Cu alloy and AA2139 alloy with AlTiB addition, respectively. Using the energy-based, optimized combination of process parameters allows E_v to be kept constant and decoupled from the effect of powder surface functionalization on L-PBF specimens. This combination of parameters was used for further characterization and mechanical testing.

4.3 Characterization of the as-built samples produced by laser powder bed fusion

4.3.1 L-PBF of surface-functionalized powders using chemical etchings

Figure 4.25a shows the porosity of as-printed samples from gas-atomized and surface-functionalized powders using chemical etchings as a function of E_v. For the unmodified alloy, increasing E_v reduced porosity, achieving very low porosity, as discussed in the previous section. Defects such as lack-of-fusion porosity (i.e., large irregular pores) and solidification cracks parallel to the building direction (BD) were observed, as previously seen in Figure 4.16. In contrast, samples from surface-functionalized powders using chemical etchings showed no clear correlation between porosity and E_v, exhibiting higher porosity than AA2017 samples. Minimum porosity was 20 ± 3% for samples produced using the NaOH surface-functionalized powder at E_v = 1111.11 J/mm³, and 4.6 ± 1.2% for samples produced using the HNO_3 surface-functionalized powder at E_v = 925.93 J/mm^3. The as-built samples using the surface-functionalized powders that presented the lowest porosities displayed large keyhole-like pores (Figure 4.25b), unlike the small spherical pores in as-built samples using gas-atomized powder. Keyhole pores result from local vaporization causing unstable melt pool depressions [42,168], while spherical pores arise from entrapped gas or vaporized low-melting elements [34,162]. The cross-section of all L-PBF samples produced using the HNO_3 and NaOH surface-functionalization for the Box-Behnken design of experiments is shown in Figure A4 in the Appendix.

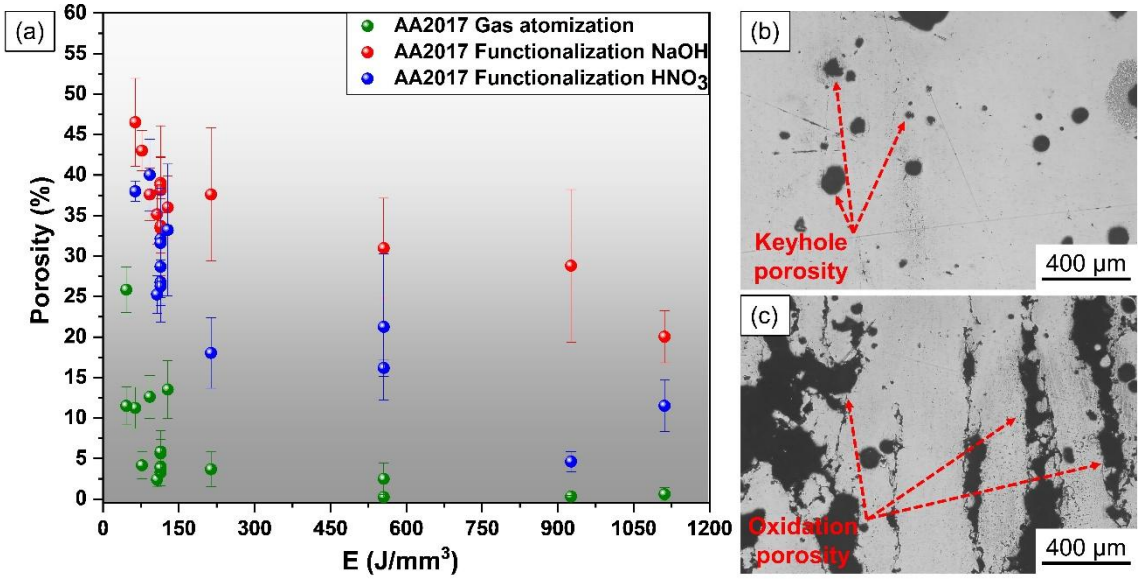

Figure 4.25 - (a) Porosity of L-PBF samples produced from gas-atomized and chemically surface-functionalized powders. Defects in surface-functionalized powder samples: (b) keyhole-like pores and (c) oxidation-related porosity.

The lower laser reflectance of the chemically surface-functionalized powders (Figure 4.2) increased laser energy absorption, raising the local melt temperature to levels that favored vapor depression instability and, consequently, a higher incidence of keyhole pores. Evaporation of organic impurities (cellulose from the partial contamination with fibers from the filter paper used during the surface functionalization treatments) and the thick oxide layer on powder surfaces (Figure 4.3) also contributed to porosity. Oxide layers resist melting, potentially causing melt pool instabilities, reduced wettability, and interconnected porosity, as observed in prior studies [69,70,169–172]. Thus, although surface functionalization using chemical etchings enhanced flowability and laser absorption, thick oxide layers negatively affected L-PBF sample density, resulting in porosity (Figure 4.25c). Because of that, and considering that some of the processing parameters from the Box-Behnken design, particularly those at high scanning speed (Figure A4), could not be manufactured due to insufficient melting during L-PBF, further investigations were not conducted. Future work should focus on surface functionalization methods that avoid oxide formation to enable processing under inert atmospheres. Nevertheless, these powders may be suitable for producing multi-material components with dielectric ceramic

(alumina) and metallic conductor regions via L-PBF, similar to the NaOH- and hot water-treated powders studied by Veron *et al.* [69] and Lanoue *et al.* [70], leveraging their improved laser absorption and rheological properties for uniform powder layers.

4.3.2 L-PBF of surface-functionalized powders using TiC particles

4.3.2.1 Microstructural characterization

To assess the effect of larger TiC particles on the solidification cracking behavior and microstructure of Al-Cu alloys produced by L-PBF, gas-atomized AA2017 powders containing different TiC particle sizes (45 nm, 4 µm, and 44 µm) and concentrations (1, 2, and 4 wt.%) were processed using the optimized L-PBF processing parameters (laser power of 190 W, scanning speed of 100 m/s, and hatch distance of 120 µm). Figure 4.26 and Figure 4.27 display the microstructure of the as-built AA2017 and TiC/AA2017 alloys parallel to the BD, showing the typical layer-wise morphology with overlapping, arc-shaped melt tracks. In the unmodified AA2017 alloy (Figure 4.26), large columnar α-Al grains extend across multiple layers along the BD, consistent with the solidification structures commonly observed in L-PBF aluminum alloys [173,174]. Most secondary phases are concentrated along grain boundaries, associated with the segregation of low-melting-point eutectic constituents during cellular or dendritic solidification, whereas fine granular precipitates are dispersed within grains due to the high cooling rates. These granular phases appear coarser at the melt pool boundaries (MPB) and finer at the melt pool center (MPC), likely resulting from local variations in the temperature gradient during solidification [32,136,175] and localized remelting during successive laser scans [58]. Cracks propagating along grain boundaries across successive melt pools, as highlighted in Figure 4.26b, indicate the occurrence of solidification cracking, a typical defect in high-strength Al alloys during L-PBF. Although the process parameters were optimized to minimize solidification cracking and porosity, residual cracks remained, as similarly reported for other Al-Cu alloys processed under optimized L-PBF conditions [60,104,129–131,140,163,176,177].

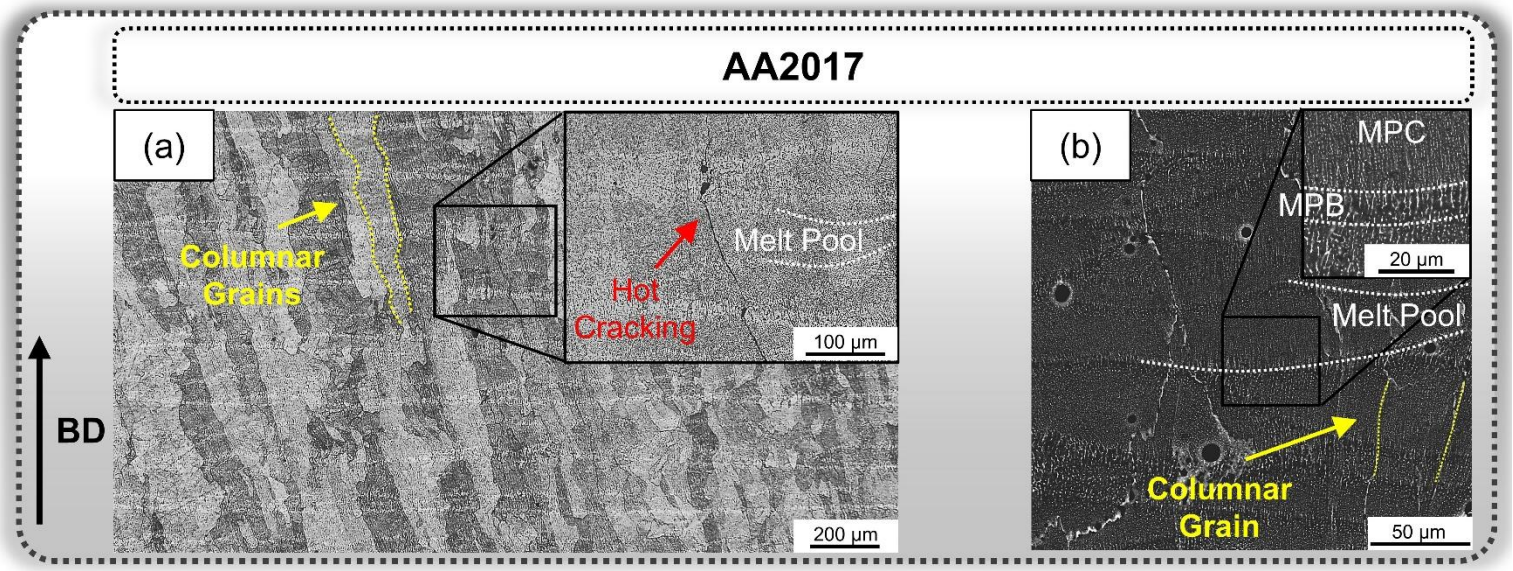

Figure 4.26 - (a) Optical micrograph and (b) image from SEM of a cross-section parallel to BD of the as-built AA2017 alloy produced by L-PBF.

In contrast, the incorporation of TiC particles successfully eliminated solidification cracking, as evidenced in Figure 4.27. However, the TiC-reinforced AA2017 samples containing 1 wt.% and 2 wt.% TiC displayed slightly higher residual porosity. Similar trends were reported by Liu *et al.* [104] for L-PBF-processed AA2024 alloys with TiC nanoparticles, where the relative density decreased at 2 wt.% of TiC and then increased again at higher concentrations (5 wt.%). The cross-sectional morphologies and corresponding residual porosity of the present samples are shown in Figures A3 and A4 in the Appendix A. As observed in Figure 4.27, the pores in the TiC/AA2017 samples with 1 wt.% and 2 wt.% of TiC are predominantly located along grain boundaries, coinciding with the presence of second phases. This indicates that, although TiC addition effectively suppressed solidification cracking, the solidification process still involved the formation of elongated liquid channels between growing grains. Upon cooling, these regions likely experienced shrinkage and thermal contraction, leaving behind residual porosity along the boundaries. Consequently, samples with 1 wt.% and 2 wt.% TiC exhibited slightly higher residual porosity levels (Figure A6). The as-built AA2017 alloy presents a residual porosity of 0.17 ± 0.06 %, while the as-built 1TiC45nm and 2TiC45nm alloys show increased porosity levels of 0.38 ± 0.11 % and 0.57 ± 0.12 %, respectively, the

highest values among the TiC-modified alloys. Increasing the TiC concentration to 4 wt.% markedly reduced this effect, resulting in a very low residual porosity of 0.024 ± 0.022 % in the as-built 4TiC4μm sample, which may be associated with the higher particle concentration promoting more heterogeneous nucleation events during solidification. This likely limited the extent of columnar grain growth and favored the formation of a more equiaxed grain structure, thereby reducing the persistence of liquid films at grain boundaries in the final stages of solidification and, consequently, the residual porosity.

The above interpretation is in agreement with the microstructural evidence. Beyond suppressing solidification cracking, the addition of TiC particles, regardless of size, also promoted grain refinement and a columnar-to-equiaxed transition (CET) of the microstructure. This transition is evidenced in Figure 4.27 by the reduction in columnar grain size and the emergence of equiaxed grains surrounded by a network of second phases. In samples with 1 wt.% of TiC addition (Figure 4.27a,d,g), the microstructure remains mostly columnar, though equiaxed grains begin to form near the melt pool boundaries, restricting columnar growth to the melt pool center. Increasing the TiC content to 2 wt.% (Figure 4.27b,e,h) further enhances this transition, leading to a predominance of fine equiaxed grains and only a few short columnar grains. At 4 wt.% TiC (Figure 4.27c,f,i), the microstructure becomes almost fully equiaxed with a uniform grain size. Additionally, intragranular cuboidal particles appear more frequently at higher TiC concentrations (Figure 4.27c,f,i), likely corresponding to Al_3Ti with the $L1_2$ structure, as commonly observed in TiC- or Ti-containing aluminum alloys processed by L-PBF [104–106,178].

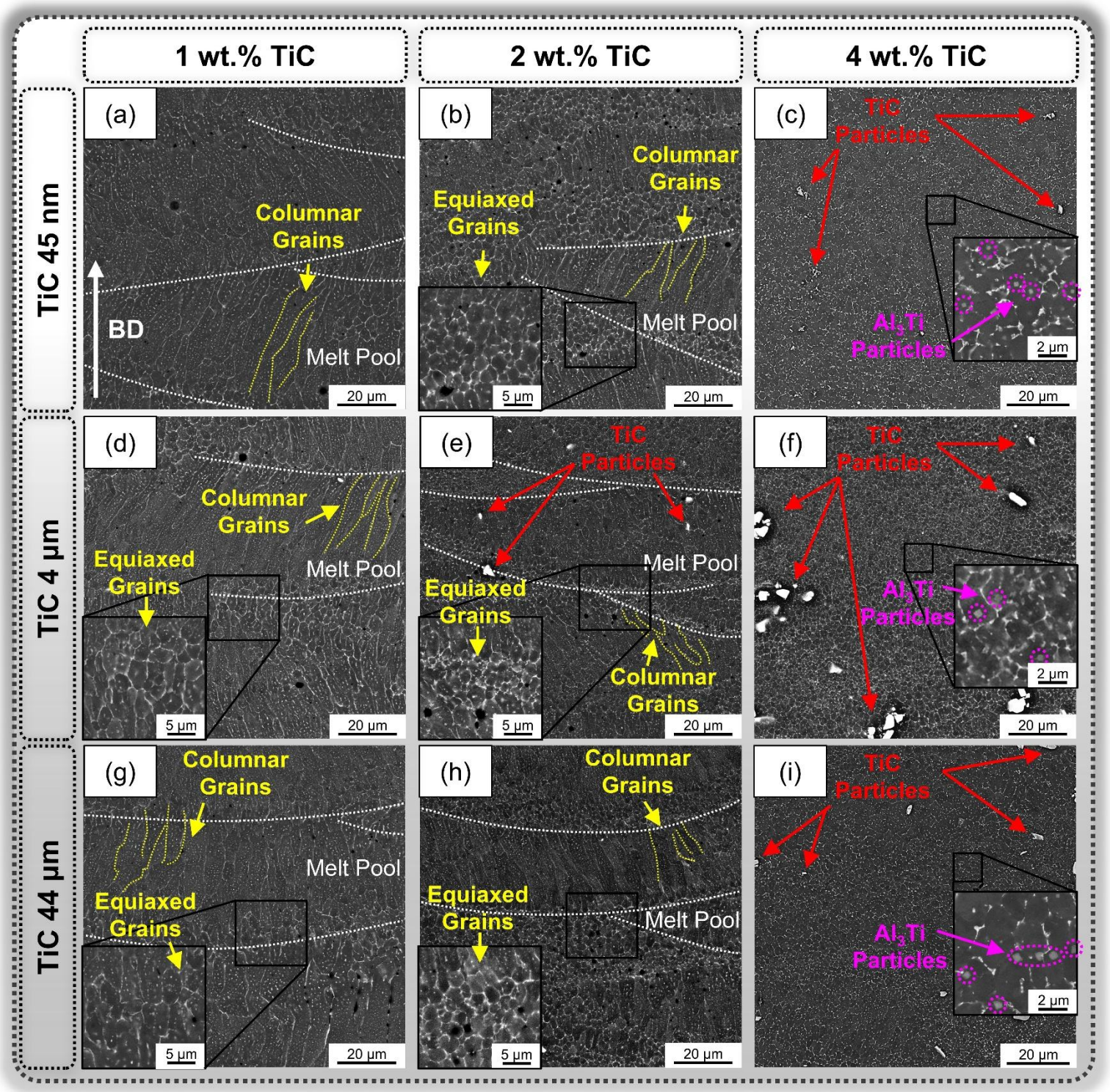

Figure 4.27 - SEM micrographs from the cross-sections parallel to the building direction (BD) of the as-built TiC/AA2017 alloys.

The TiC particle size also played a key role in promoting the CET. Fine micrometer-sized TiC particles (<4 µm) were more effective in stimulating

equiaxed grain formation and refining the columnar structure, even at low particle concentrations (Figure 4.27d-f). In contrast, coarser micrometer-sized TiC particles (average particle size of 44 μm) had a limited effect, as coarser grains persisted in the 4TiC44μm alloy (Figure 4.27i). TiC nanoparticles exhibited an intermediate effect, and although the 1TiC45nm alloy still showed a mainly columnar microstructure similar to that with coarse micrometer-sized TiC particles, increasing the TiC concentration to 4 wt.% resulted in an almost fully equiaxed microstructure (Figure 4.27c).

The spatial distribution, orientation, and stability of the reinforcing TiC particles in the as-printed samples, visible in Figure 4.27 and Figure A5, is governed by melt flow behavior during L-PBF. During L-PBF, the absorption of high-laser radiation generates a molten pool characterized by steep temperature gradients between its center and boundary. Such gradients induce surface tension variations along the liquid-gas interface, driving fluid motion known as the Marangoni effect. This results in strong Marangoni convection within the molten pool [73,179,180]. The direction and intensity of the Marangoni flow are governed by both thermal and solutal contributions. The thermal component typically drives a clockwise circulation, whereas concentration gradients at the solid-liquid interface can produce a counterclockwise solutal component, which often dominates [181]. This combined flow not only enhances liquid mixing but also creates local torque on nonspherical TiC particles due to the misalignment of their geometric center relative to the convective forces. Such torque facilitates particle rotation and redistribution, preventing preferential clustering and improving their overall dispersion within the melt [181]. Capillary forces generated by the Marangoni-driven flow further act on suspended particles, promoting their rearrangement in the liquid [73,179,182]. At the nanoscale, these forces are particularly effective in counteracting the strong van der Waals attraction between TiC nanoparticles, thereby mitigating agglomeration and fostering a more homogeneous dispersion in the solidified matrix.

However, the efficiency of this process strongly depends on the volumetric E_v. Insufficient E_v decreases the temperature gradient, reducing Marangoni intensity and limiting the capacity to redistribute TiC particles, resulting in the

deposition of the particles at the bottom of the melt pool due to the gravity force, and severe agglomeration [73,181,182]. Conversely, higher E_v amplifies the convective strength, accelerating nanoparticle rearrangement and contributing to the formation of distinctive patterns, such as ring-like distributions of reinforcement [73,110,179,181]. Nevertheless, excessive E_v can lead to prolonged thermal accumulation that reduces the steepness of temperature gradients, enhancing coarsening and, simultaneously, promoting local concentration of TiC particles [73,110,179,182]. Some studies [110,179,182] reported that even though the dispersion of TiC nanoparticles in the solidified aluminum matrix is improved with E_v increase, it may also cause coarsening of the effective TiC particle size. This coarsening may be attributed to the longer residence time of the TiC particles in the melt at elevated E_v, together with intensified Marangoni flow, which facilitates particle collision, partial dissolution-reprecipitation, and agglomeration.

Overall, the TiC particles in the AA2017 matrix were uniformly dispersed (Figure 4.27 and Figure A5), though nanoparticle-based alloys exhibited some agglomerates. The largest agglomerates observed in these samples reached about 35 μm (Figure 4.28a), comparable to the maximum TiC particle size (~32 μm) found in alloys containing coarse micrometer-sized TiC particles (Figure 4.28c). No significant agglomeration of particles was observed in the samples produced using the fine micrometer-sized TiC particles (as-built 1TiC4μm, 2TiC4μm, and 4TiC4μm alloys).

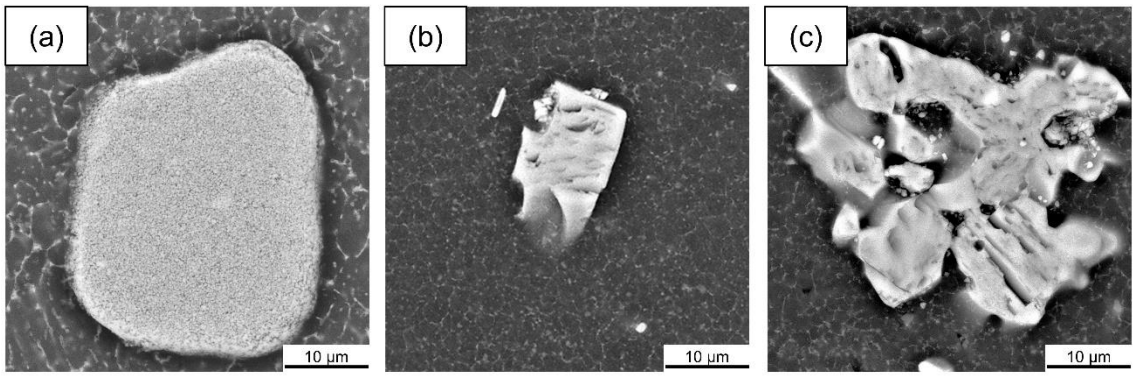

Figure 4.28 - Backscattered electron (BSE-SEM) images from TiC particles present in the as-built (a) 1TiC45nm, (b) 4TiC4µm, (c) 4TiC44µm alloys.

The microstructure of the as-built AA2017 and TiC/AA2017 alloys parallel to the BD was examined through electron backscatter diffraction (EBSD) inverse pole figure (IPF) maps, as shown in Figure 4.29. The AA2017 alloy exhibits large, elongated columnar grains aligned along the BD, while no strongly pronounced crystallographic orientation is evident (Figure 4.29a). In the as-printed TiC/AA2017 samples, the IPF maps in Figure 4.29b-j reveal the formation of equiaxed grains and general microstructural refinement. Similar to the unmodified AA2017 alloy, no strong crystallographic orientation is apparent in the IPF maps of the TiC-modified alloys.

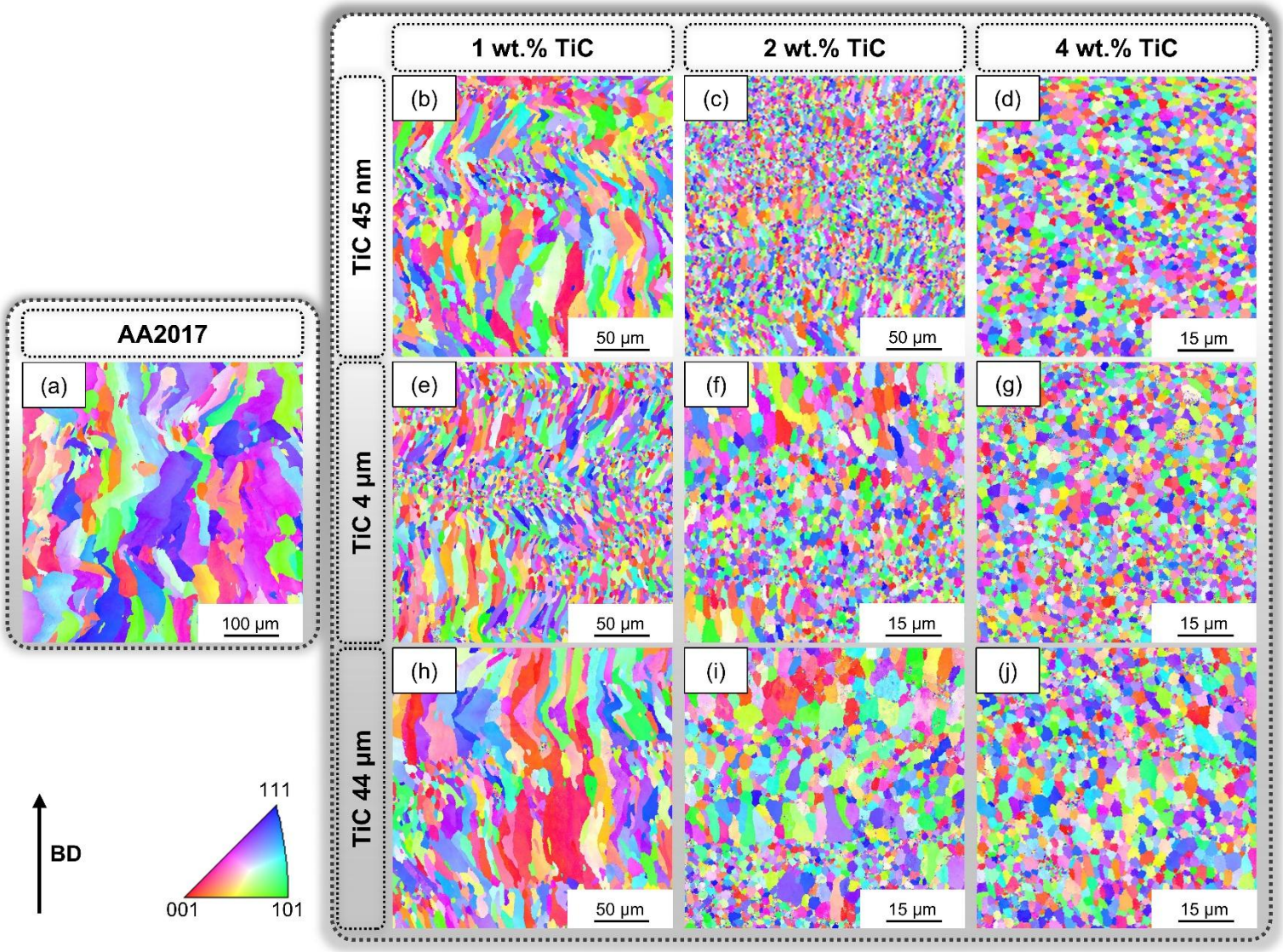

Figure 4.29 - EBSD IPF maps from the cross-section parallel to the building direction (BD) of the as-built L-PBF (a) AA2017 and (b-j) TiC/AA2017 alloys.

In aluminum alloys processed by L-PBF, a <001> fiber texture commonly develops due to epitaxial grain growth along the thermal gradient, reflecting the preferred solidification direction of face-centered cubic (fcc) metals, where <001> is the energetically favorable growth axis [32,104,173]. Such directional dendritic solidification, however, is often undesirable because it induces microstructural anisotropy and enhances solidification cracking susceptibility in high-strength Al alloys [104]. Although the IPF map does not display a dominant orientation, the corresponding pole figures (PF) in Figure 4.30a reveal a mild <001> texture near the BD, with a peak intensity of 9.96. The crystallographic texture in L-PBF

aluminum alloys is strongly governed by the process parameters and scan strategy. High scanning speeds favor the formation of a <001> texture due to teardrop-shaped melt pools with steep solidification angles relative to the surface plane, while lower scanning speeds or higher E_v promote weaker <110> or <111> textures [173]. A short hatch distance enhances vertical thermal gradients, supporting epitaxial <001> growth, whereas larger hatch distances lead to shallower melt pools and finer equiaxed grains, weakening the texture [173]. Additionally, bidirectional scanning with 55°, 67°, 90°, or 120° rotation between powder layers alters the thermal flux direction, limiting remelting of grains and encouraging competitive grain growth, which reduces texture intensity [173]. Therefore, the adopted combination of large hatch distance and bidirectional scanning with 67° rotation between layers may have weakened the <001> texture in the as-built AA2017 alloy that is favored by the combination of low scanning speed and high laser power (i.e., high E_v and deeper melt pools).

In the as-built TiC/AA2017 alloys, the maximum texture intensity decreases notably with TiC addition and tends to diminish further with increasing TiC concentration (Figure 4.30b-j), consistent with observations by Liu *et al.* [104] for AA2024 processed with varying TiC content. Overall, samples with TiC nanoparticles (Figure 4.30b-d) show the lowest texture intensity, while those with coarse micrometer-sized TiC particles (Figure 4.30h-j) tend to exhibit the highest texture intensity among the TiC/AA2017 alloys. This texture weakening has also been reported in Al-Cu alloys modified with Ti [183], TiC [104,106], CaB_6 [90,91], or TiB_2 [184] particles during L-PBF.

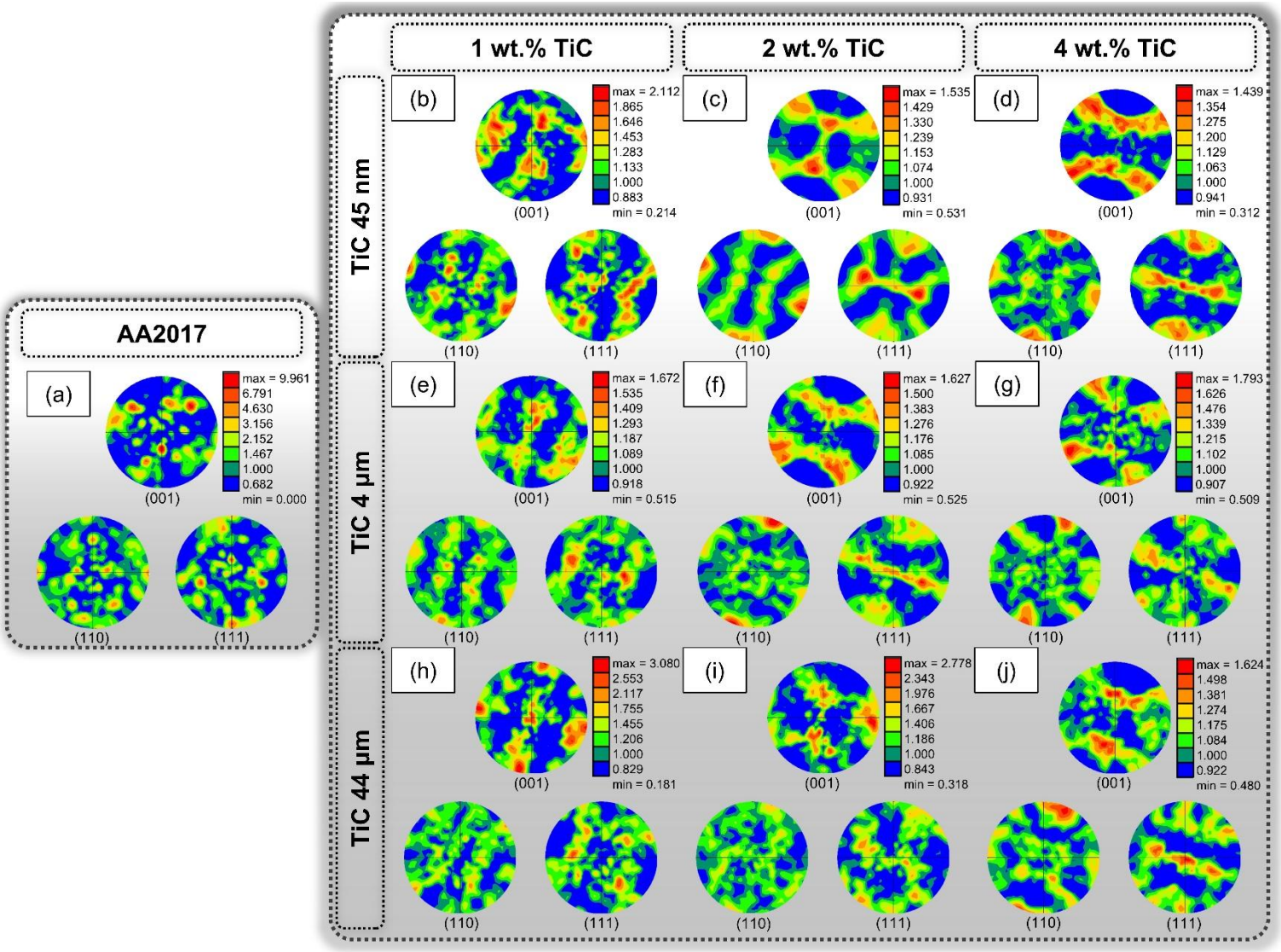

Figure 4.30 - EBSD (001), (110), and (111) PF images from the cross-section parallel to the building direction (BD) of the as-built L-PBF (a) AA2017 and (b-j) TiC/AA2017 alloys.

Moreover, Figure 4.29d,g highlights that the 4TiC45nm and 4TiC4µm samples predominantly consist of fine, equiaxed grains. The average grain size and fraction of equiaxed grains in the as-built AA2017 and TiC/AA2017 alloys were quantified from EBSD data, as shown in Figure 4.31. The as-built AA2017 alloy exhibits a relatively large average grain size of 71 ± 48 µm, which decreases sharply with the addition of 1 wt.% TiC, reaching 7 ± 4 µm in the 1TiC4µm sample. Increasing the TiC content further reduces grain size, with the finest grains observed in alloys processed with fine micrometer-sized TiC particles, achieving

a minimum of 2.0 ± 0.9 μm in the 4TiC4μm sample. This trend aligns with observations by Liu *et al.* [104], who reported a similar grain size of 1.6 ± 0.5 μm for AA2024 processed with 5 wt.% TiC nanoparticles. Additionally, the fraction of equiaxed grains was determined using the grain aspect ratio distribution from EBSD, with grains having an aspect ratio below 3 considered equiaxed [140]. The as-built AA2017 contains 30.7% of equiaxed grains, which increases with TiC addition (Figure 4.31b). Fine micrometer-sized TiC particles are particularly effective in promoting CET of microstructure, with 1TiC4μm alloy showing 56.6% of equiaxed grains. Higher TiC concentrations further enhance CET, resulting in nearly fully equiaxed microstructures, such as 97.7% of equiaxed grains in 4TiC45nm alloy. While coarse micrometer-sized TiC particles also contribute to microstructural refinement and CET, their effect is less pronounced compared to nano-sized and fine micrometer-sized TiC particles.

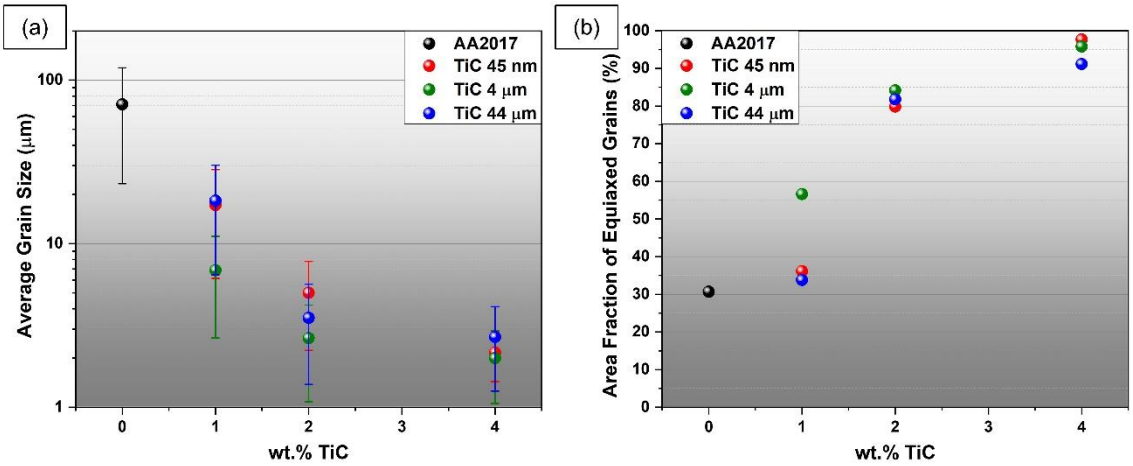

Figure 4.31 - (a) Average grain size and (b) area fraction of equiaxed grains of the as-built AA2017 and TiC/AA2017 alloys.

The phase composition of the as-built AA2017 and TiC/AA2017 alloys was examined by XRD, as shown in Figure 4.32a. Consistent with SEM observations, the alloys are primarily composed of α-Al solid solution and eutectic θ-Al_2Cu phases. Minor Al_2O_3 peaks are also present. In the TiC/AA2017 alloys, diffraction peaks corresponding to TiC are clearly detected. Although no distinct reaction product between Al and TiC was observed, a small peak near 2θ = 39.2° in samples with higher TiC content may indicate the formation of Al_3Ti, a phase

commonly reported in Ti- or TiC-containing Al alloys processed by L-PBF [104,106,140,178]; this will be further investigated by transmission electron microscopy (TEM). Moreover, the relative intensities of the α-Al (111) and (200) peaks changed with TiC addition (Figure 4.32b). The as-built AA2017 alloy shows a higher (200) intensity, consistent with a preferred <001> fiber texture along the build direction, as confirmed by EBSD pole figures (Figure 4.30a) [131]. Adding TiC particles increases the (111) peak intensity and reduces the (200) peak intensity, indicating a weakening of the <001> texture, in agreement with observations by Mair *et al.* [91] for AA2024 processed with CaB_6 particles.

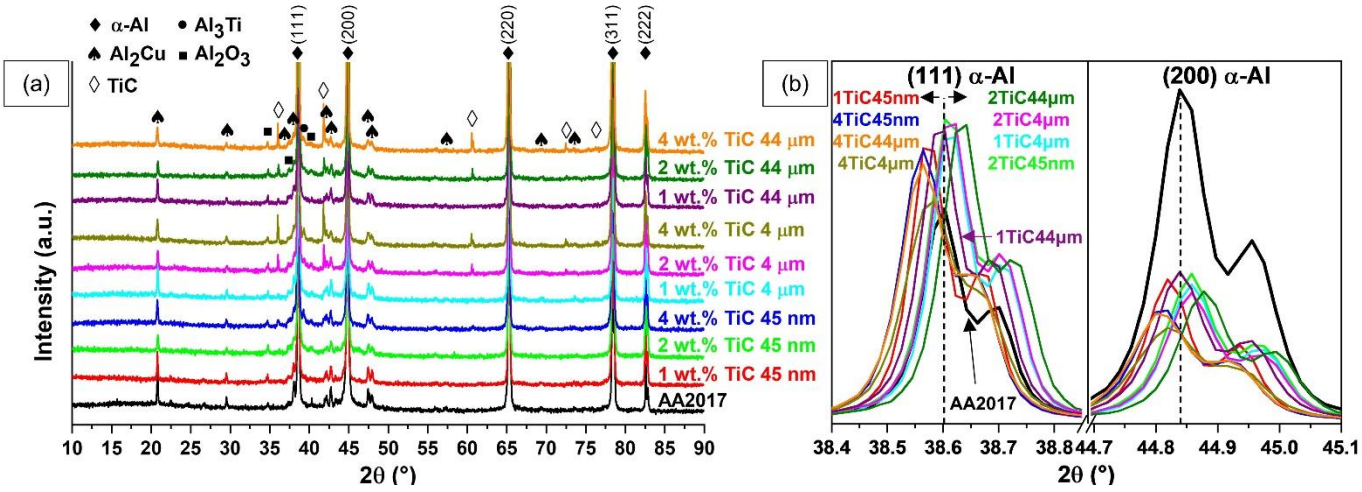

Figure 4.32 - XRD patterns of the as-built AA2017 and AA2017/TiC alloys from the surface parallel to the BD: (a) the complete XRD spectra of the samples and (b) the magnified spectra of the (111) and (200) peaks of the face-centered cubic α-Al phase.

A further observation from the XRD results is the shift of the α-Al diffraction peaks after TiC incorporation (Figure 4.32b), indicating variations in the lattice parameter likely caused by solute incorporation and residual stress effects. The exact position of the (111) and (200) peaks for each alloy can be checked in Table A7 in the Appendix. The presence of smaller solute atoms such as Ti tends to contract the aluminum lattice, shifting the peaks to higher 2θ angles, as observed for the as-built 1TiC4μm, 2TiC45nm, 2TiC4μm, and 2TiC44μm alloys. Beyond solute effects, residual stresses can also arise from the thermal expansion

mismatch between the TiC particles and the Al matrix [185,186]. According to the experimental–numerical analysis by Balokhonov *et al.* [185], cooling induces compressive stresses in the carbide particles and tensile stresses in the adjacent aluminum, particularly near interface convexities, which can manifest as peak shifts toward lower diffraction angles. In this study, such lower-angle shifts were evident in the 1TiC45nm, 4TiC45nm, 4TiC4µm, and 4TiC44µm alloys, suggesting the presence of tensile macrostresses, especially at higher TiC contents or in samples with larger particles and agglomerates (Figure 4.28). Therefore, the observed peak displacements result from the interplay between Ti-induced lattice contraction and tensile stress fields at the TiC particle-matrix interfaces during L-PBF processing.

The influence of TiC surface functionalization on the L-PBF-processed AA2017 alloy was further examined by TEM. Figure 4.33 presents the microstructural features of the as-built AA2017 sample. The high-angle annular dark-field scanning transmission electron microscopy (HAADF-STEM) image and corresponding EDS elemental maps (Figure 4.33a) reveal uniformly distributed fine Cu-rich and Fe-, Mn-, and Si-rich particles throughout the aluminum matrix. Due to the relatively large grain size of the alloy, the focused ion beam (FIB)-prepared lamella encompasses a single grain. The Cu-rich precipitates identified by selected area electron diffraction (SAED) (Figure 4.33c) and XRD correspond to the eutectic θ-Al_2Cu phase, while the Cu- and Mg-rich particles are confirmed as S-Al_2CuMg (Figure 4.33d), both typical of Al-Cu-Mg alloys [104,132,183]. Additionally, small Mg- and O-enriched precipitates were detected, indicating the presence of (Al,Mg) oxides, as also reported by Mair *et al.* [187] in TiB_2-modified Al-Cu alloys produced by L-PBF. The Fe-, Mn-, and Si-containing particles likely correspond to Al-Fe-Mn-Si intermetallics, such as $Al_{15}(Fe,Mn)_4Si_2$ (α-phase), consistent with observations by Del Guercio *et al.* [131] for L-PBF-processed AA2024.

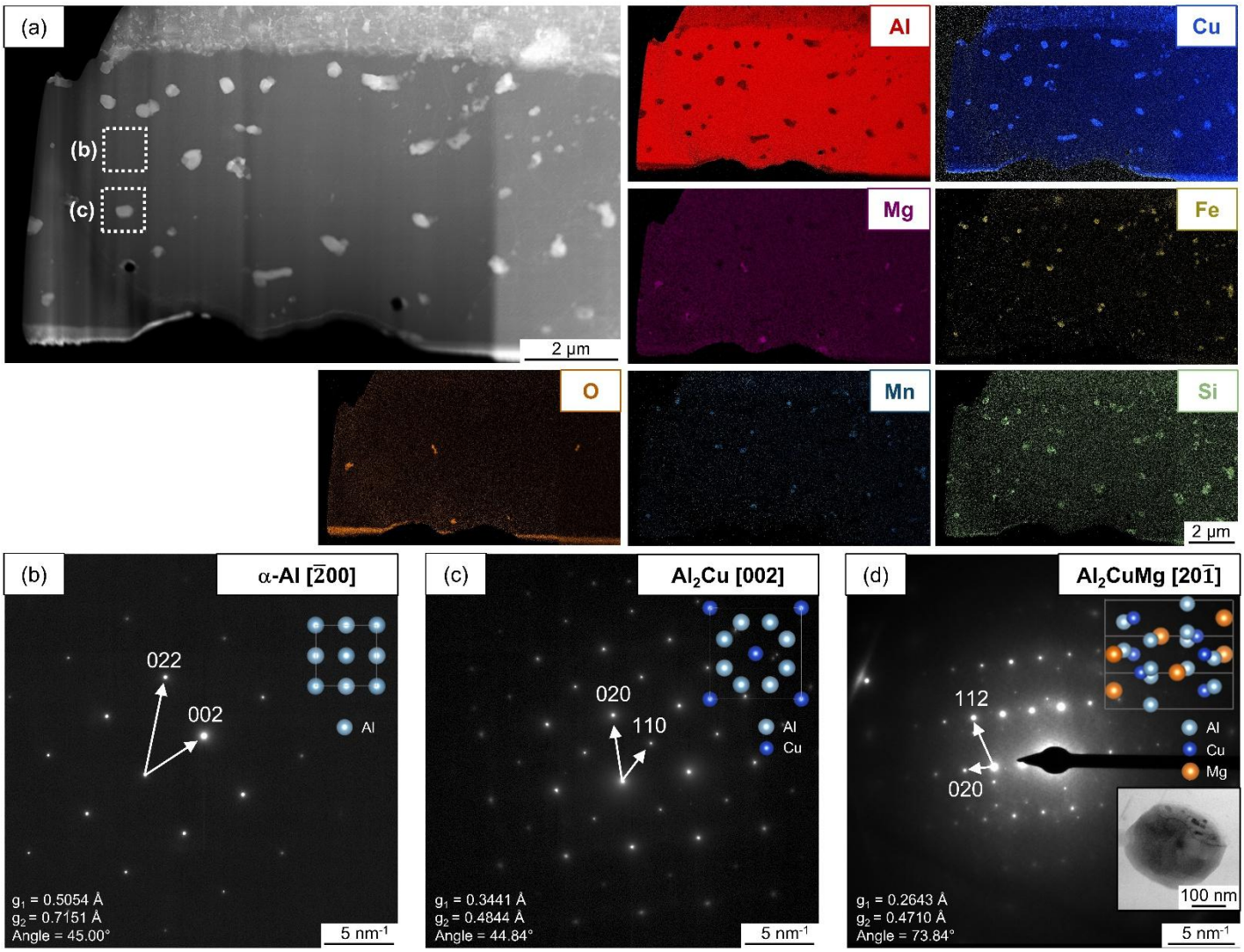

Figure 4.33 - (a) HAADF-STEM image and corresponding EDS elemental maps of Al, Cu, Mg, Fe, Mn, Si, and O in the as-built AA2017 alloy. (b–d) SAED patterns of (b) the aluminum matrix, (c) a Cu-rich particle, and (d) a Cu- and Mg-rich particle (highlighted in white boxes in (a)), with an inset showing a magnified bright-field (BF) image of an Al_2CuMg precipitate.

The microstructure and phase constituents of the as-built 2TiC45nm alloy are presented in Figure 4.34. The BF image and corresponding EDS elemental maps (Figure 4.34a) reveal a refined grain, with Cu, Mg, Fe, Si, and Ti segregated along the grain boundaries. In addition to the θ-Al_2Cu and S-Al_2CuMg precipitates identified in the unmodified alloy (Figure 4.33), the SAED pattern in Figure 4.34c confirms the presence of Fe-rich Al_6Fe particles. The overlapping distribution of Mn and Si with Fe in the EDS maps suggests either the nucleation of Mn- and Si-

bearing precipitates around Al_6Fe particles or their partial incorporation within them. Moreover, Ti enrichment at grain boundaries (Figure 4.34a) corresponds to TiC particles, as verified by the SAED pattern in Figure 4.34d. The localization of TiC nanoparticles at grain boundaries indicates that they did not work as primary nucleation sites for α-Al grains but rather contributed to microstructural refinement by hindering grain growth.

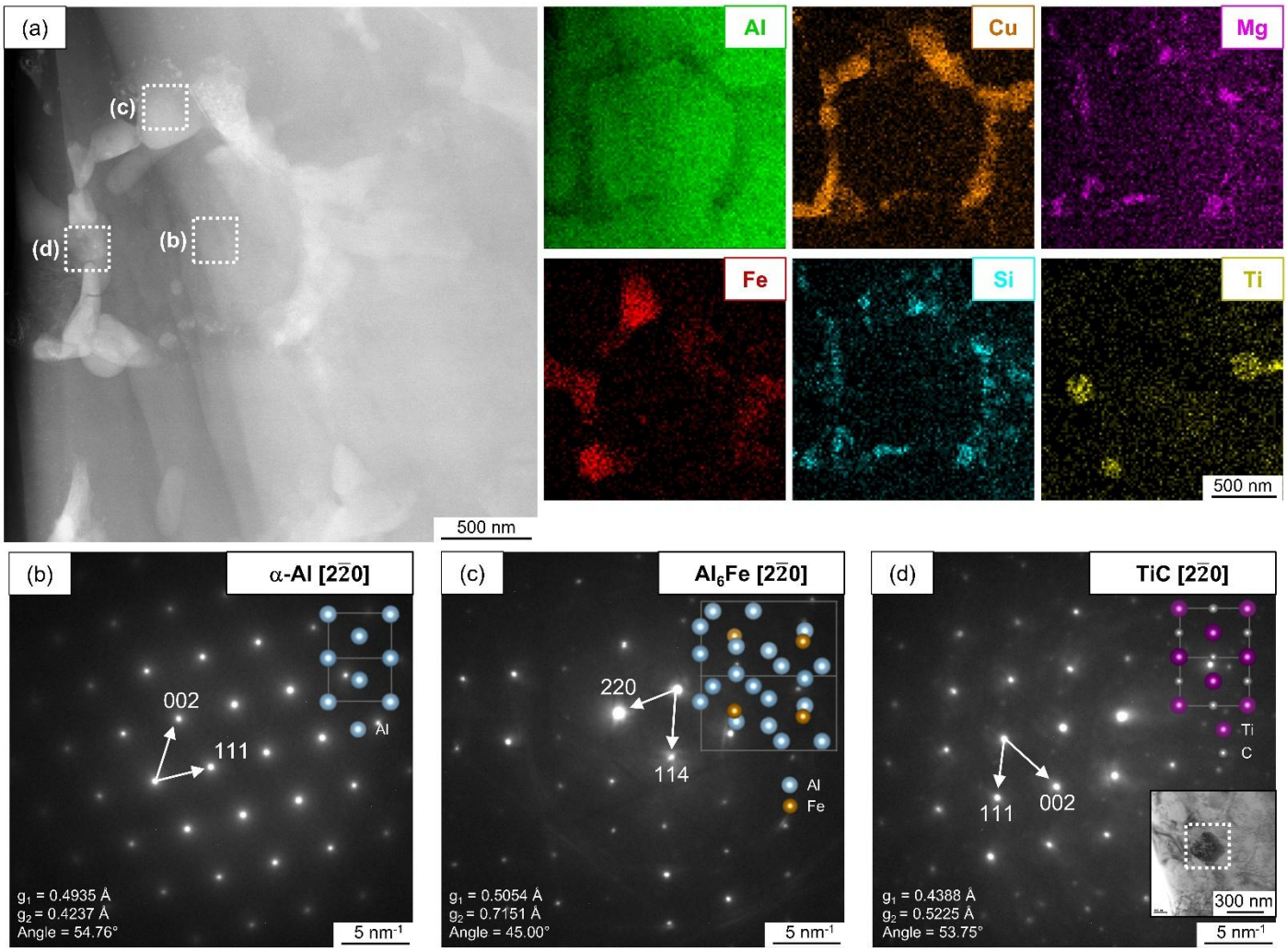

Figure 4.34 - HAADF-STEM image and corresponding EDS elemental maps showing the distribution of Al, Cu, Mg, Fe, Si, and Ti in the as-built 2TiC45nm alloy. SAED patterns of the (b) aluminum matrix, (c) Fe-rich particle, and (d) Ti-rich particle (highlighted in white boxes in (a)), with an enlarged BF image displaying the TiC particle.

Further TEM analysis was performed to identify the cuboidal particles previously observed in the SEM images (Figure 4.27c,f,i). Figure 4.35a-b presents the BF image of the as-built 4TiC45nm alloy and the corresponding EDS elemental maps for Cu, Fe, and Ti. Unlike the Cu- and Fe-rich particles concentrated along grain boundaries, Ti-enriched cuboidal particles are found within the grains. These were confirmed by the SAED pattern (Figure 4.35d) as Al_3Ti with an $L1_2$ crystal structure. The α-Al/Al_3Ti interface, examined by high-resolution transmission electron microscopy (HRTEM) and fast Fourier transforms (FFT) (Figure 4.35e), exhibits a highly coherent interface with parallel orientation relationships: directions $[001]_{Al}//[001]_{Al_3Ti}$ and $[110]_{Al}//[110]_{Al_3Ti}$ parallel to each other, and the orientation relationship of $(002)_{Al}//(002)_{Al_3Ti}$ and $(111)_{Al}//(111)_{Al_3Ti}$. This configuration, also reported for Ti- and TiC-modified Al-Cu-Mg alloys processed by L-PBF [104,132,176], results in an interplanar spacing mismatch of approximately 1.02 % between the (111) planes, calculated using Equation 4.13, where $(hkl)_m$ and $(hkl)_n$ are the planes in the matrix and nucleants, $[uvw]_m$ and $[uvw]_n$ are the directions in the planes, $d_{[uvw]m}$ is the interatomic spacing along $[uvw]_m$, and θ is the angle between $[uvw]_m$ and $[uvw]_n$ [188]. The formation of this coherent interface with minimal mismatch highlights the strong ability of Al_3Ti particles to act as heterogeneous nucleation sites for α-Al, promoting CET of the microstructure and grain refinement, as observed in Figures 4.27 and Figure 4.29.

$$\delta_{(hkl)_n}^{(hkl)_m} = \sum_{i=1}^{3} \frac{\frac{\left|\left(d_{[uvw]_m^i}\cos\theta\right) - d_{[uvw]_n^i}\right|}{d_{[uvw]_n^i}}}{3} \times 100\% \qquad (4.13)$$

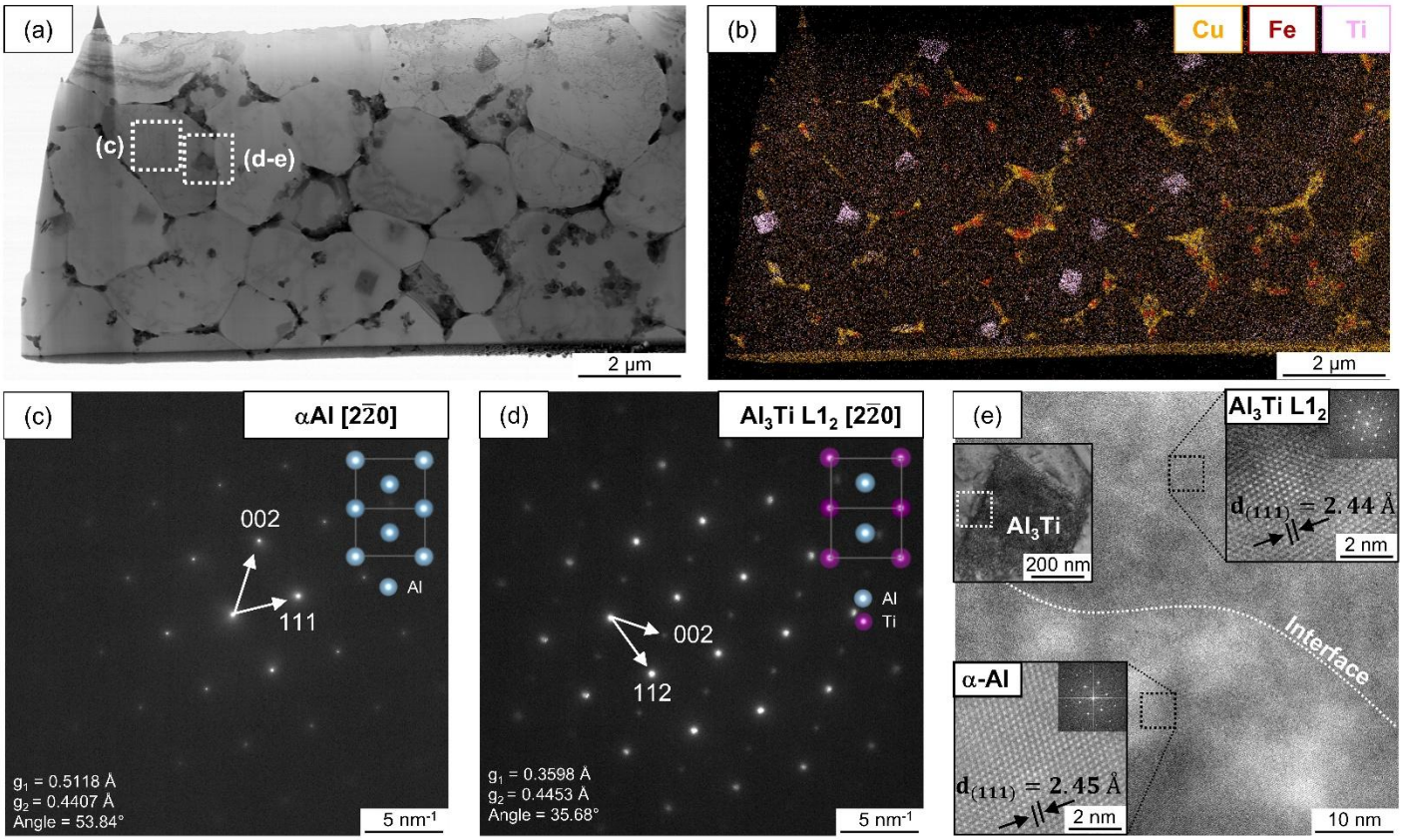

Figure 4.35 - (a) BF-STEM image and (b) EDS elemental maps of Cu, Fe, and Ti in the as-built 4TiC45nm alloy. (c) SAED pattern of the matrix and (d) SAED pattern of the cuboidal Ti-rich particle indicated in (a). (e) HRTEM image of the α-Al/Al_3Ti interface showing their corresponding FFT and a magnified BF image of the Al_3Ti particle.

4.3.2.1.1 TiC-induced columnar-to-equiaxed transition of microstructure, grain refinement, and solidification crack suppression

During L-PBF of high-strength aluminum alloys, the combination of rapid solidification and steep thermal gradients promotes the formation of columnar grains aligned with the build direction. The grain morphology is mainly controlled by the thermal gradient (G) and solidification rate (R): while G/R governs the solid-liquid interface stability and solidification mode, the product GxR determines the cooling rate and microstructural refinement [32,173]. The high G values typical of L-PBF favor epitaxial columnar growth [59,104,129,131,140,163,176–178], as shown in Figure 4.26 and Figure 4.29a for the as-built AA2017 alloy.

In Al-Cu alloys, solute rejection and limited diffusion during solidification lead to Cu enrichment ahead of the solid-liquid interface, inducing constitutional supercooling and dendritic growth. The segregation of Al_2Cu along dendrite arms and grain boundaries increases the likelihood of solidification crack formation, as these regions concentrate thermal and solidification stresses, especially in alloys with 3-5 wt.% of Cu and wide solidification intervals [140,189]. Consequently, coarse columnar grains are more susceptible to solidification cracking than fine equiaxed ones, due to their reduced capacity to accommodate strain in the semi-solid state [104], which facilitates the development of solidification cracking, as shown in Figure 4.26.

To mitigate solidification cracking, ceramic inoculants such as TiC [104–106], TiB_2 [77,79], LaB_6 [108,109], and CaB_6 [90,91] particles are often added, as they can cause the CET of the microstructure during solidification. These particles act as effective heterogeneous nucleation sites for α-Al grains due to their crystallographic compatibility and thermal stability, disrupting columnar grain growth [104]. In the as-built 1TiC4μm alloy, the addition of 1 wt.% TiC increased the fraction of equiaxed grains by 84% and reduced the average grain size by 91% compared to the as-built AA2017 alloy (Figure 4.31). Equiaxed grains are primarily located at the melt pool boundaries, where the growth rate is slower and the heat flow is mostly perpendicular to the scan direction. In contrast, the melt pool center experiences higher energy input and faster growth along the laser path. This spatial variation results in higher G, G/R, and cooling rates at the melt pool boundaries, while R dominates at the melt pool center [173,190]. Consequently, heterogeneous microstructures develop across the melt pool, with columnar dendrites forming at the melt pool center and finer equiaxed grains forming near the melt pool boundaries when heterogeneous nucleation sites are available.

While TiC particles serve as effective inoculants in aluminum alloys, their function as heterogeneous nucleation sites alone does not fully explain the extensive grain refinement and CET observed in the as-built TiC-reinforced samples. Large or agglomerated TiC particles (Figure 4.28) are insufficient to drive such refinement, and TiC nanoparticles are rarely found within the grains,

instead accumulating along grain boundaries (Figure 4.34). This distribution indicates that additional mechanisms contribute to CET in TiC-reinforced alloys. In this study, the observed grain refinement and CET in AA2017 during L-PBF appear to result from a combination of factors: (i) heterogeneous nucleation induced by TiC particles [105,106,140], (ii) enhanced constitutional supercooling and growth restriction from solute enrichment [178,187], (iii) heterogeneous nucleation facilitated by Al_3Ti particles [104–106,140], and (iv) grain growth restriction effects from nanoparticle incorporation [104–106,140,187].

Grain refinement during L-PBF is partly driven by the heterogeneous nucleation of α-Al grains on TiC particles. In high cooling rate conditions, native nucleants such as oxides or impurities are often insufficient due to poor lattice matching and low density, leading to coarse columnar grains [106]. The addition of TiC introduces thermally stable particles with low interfacial energy and favorable lattice alignment with molten aluminum. According to literature-based assessments using the edge-to-edge matching (E2EM) model [106,191], which predicts crystallographic compatibility between reinforcement and matrix phases, the interatomic mismatch along $[001]_{Al}//[001]_{TiC}$ is 6.9°, and the $(020)_{Al}$ plane deviates by only 0.52° from $(020)_{TiC}$. This small lattice misfit (<10%) reduces the critical undercooling (ΔT_n) required for heterogeneous nucleation, while the high melting point of TiC ensures particle survival in the melt [106]. Consequently, TiC particles act as numerous effective nucleation sites, promoting the formation of fine equiaxed grains. The presence of partially developed equiaxed grains on the surface of TiC particles and agglomerates, as shown in Figure 4.36, reinforces the occurrence of TiC-induced heterogeneous nucleation in the TiC/AA2017 alloys. Since TiC particles are randomly distributed, the nucleated Al grains also exhibit no preferred crystallographic orientation, as observed in Figure 4.29b-j and Figure 4.30b-j.

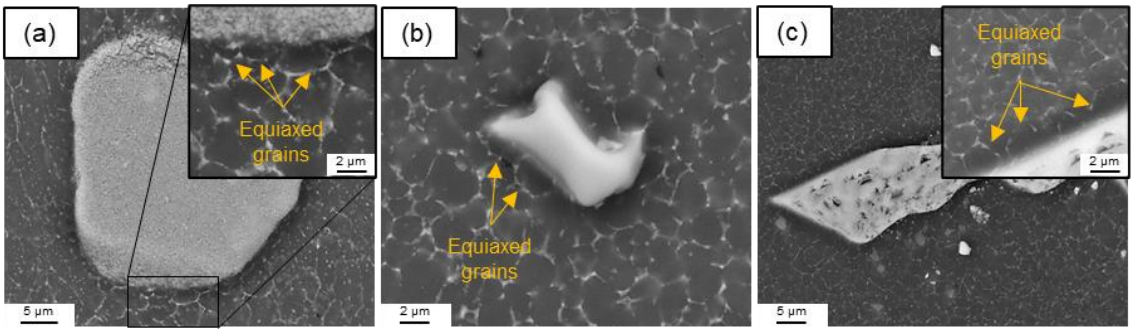

Figure 4.36 - SEM images showing the partial formation of equiaxed grains on the surface of TiC particles and agglomerates in the as-built (a) 1TiC45nm, (b) 1TiC4µm, and (c) 4TiC44µm alloys.

TiC has a high melting point (3157 °C [192]) and remains thermodynamically stable at elevated temperatures, coexisting with molten aluminum [105,110]. However, Banerji and Reif [193] reported that TiC can become unstable below 1177 °C in aluminum melts, reacting to form Al_4C_3 and releasing Ti into the melt. Supporting this, Liu *et al.* [104] observed that TiC particles near grain boundaries in L-PBF AA2024 alloys exhibited morphologies different from the original granular TiC, indicating partial dissolution and reprecipitation during processing. Figure 4.37 shows punctual EDS measurements of solute concentrations in the matrix of the as-built AA2017 and TiC/AA2017 alloys, revealing that Ti solute content increases with higher TiC additions, regardless of particle size, which can influence solidification. The total undercooling (ΔT_{total}) at the solid-liquid interface consists of thermal undercooling (ΔT_{therm}), due to latent heat lag, and constitutional supercooling (ΔT_{CS}), caused by solute accumulation ahead of the interface [106,178,194]. Constitutional supercooling is particularly important for heterogeneous nucleation and is quantified by the growth restriction factor (Q) in binary alloys, defined in Equation 4.14, where k is the partition coefficient, m the liquidus slope, and C_0 the solute concentration in the melt [194,195].

$$Q = m(k-1)C_0 \tag{4.14}$$

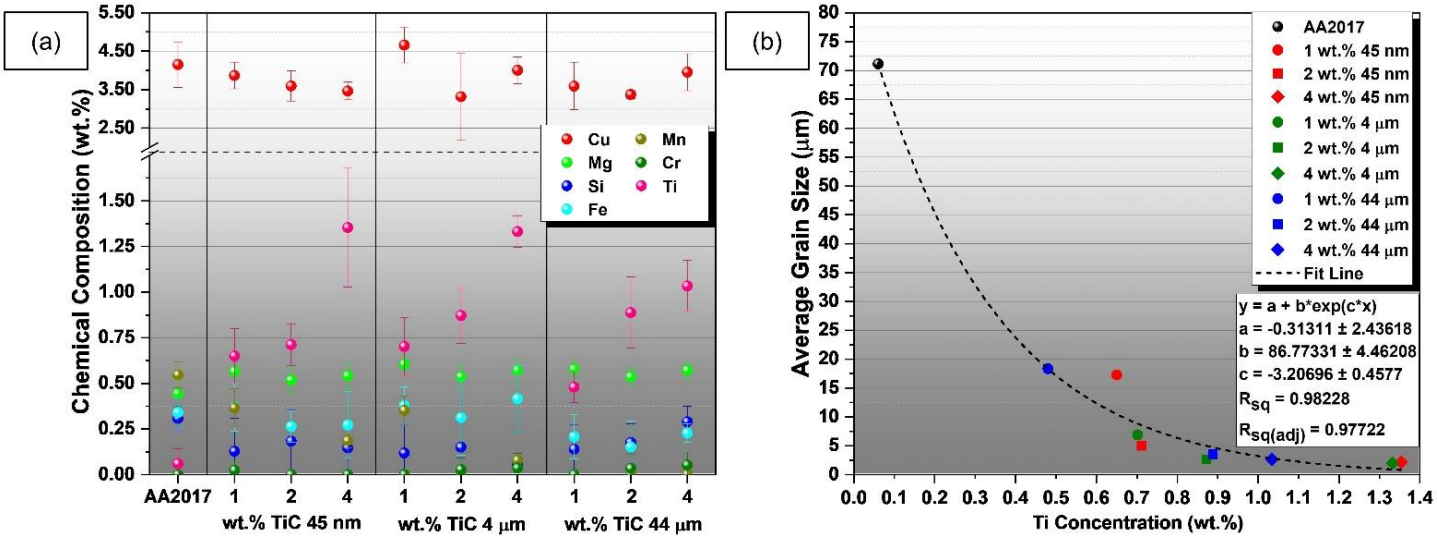

Figure 4.37 - (a) Punctual EDS chemical composition of the matrix and (b) average grain size as a function of the Ti concentration in the matrix of the as-built AA2017 and TiC/AA2017 alloys.

Solute elements with high Q factor accelerate the development of constitutional supercooling (ΔT_{CS}) ahead of the solid-liquid interface, promoting grain refinement [194]. Ti, with a high partition coefficient (k~9), is one of the most effective solutes in aluminum for enhancing ΔT_{CS} [187,195]. Zhang *et al.* [176] demonstrated that increasing Ti content in an Al-Cu-Mg alloy for L-PBF raises the Q value, accelerating ΔT_{CS} and refining grains. Unlike conventional casting, thermal undercooling (ΔT_{therm}) is significant in L-PBF due to extremely high cooling rates (10^3-10^6 K/s) [178,194]. High solute concentration at the interface causes a growth lag of α-Al grains relative to the theoretical interface, enlarging the region of ΔT_{therm} and restricting interface growth, which allows more time for nuclei to reach critical size [178,194]. Consequently, higher Ti concentrations from TiC additions enhance grain refinement through both rapid ΔT_{CS} development and larger ΔT_{therm} at the solid-liquid interface.

The elevated Ti solute concentration in the melt can react with aluminum to form Al_3Ti particles [140]. In L-PBF-processed TiC-modified aluminum alloys, in-situ Al_3Ti can adopt either the tetragonal $D0_{22}$ [105] or the face-centered cubic $L1_2$ [104,140] ordered structures. While conventional casting favors the equilibrium $D0_{22}$-Al_3Ti due to slow cooling, the high cooling rates in L-PBF

promote the metastable $L1_2$-Al_3Ti phase, which offers improved ductility through a higher number of independent slip systems [183,196,197]. HRTEM analyses and E2EM modeling show excellent lattice matching at the Al/$L1_2$-Al_3Ti interface, with an interatomic mismatch of only 0.24° along $[001]_{Al}//[001]_{Al3Ti}$ and $(020)_{Al}//(020)_{Al3Ti}$ [106,183,191], resulting in lower interfacial energy than TiC and more efficient heterogeneous nucleation. While TiC assists in refining the microstructure, Al_3Ti has been shown to play the primary role in promoting grain refinement and improving mechanical properties in TiC-modified L-PBF aluminum alloys [104,105,140]. The distribution of Al_3Ti particles within the refined grains (Figure 4.27) confirms their key contribution to forming fine equiaxed grains as TiC concentration increases in AA2017.

Nanoparticles also aid grain refinement in L-PBF aluminum alloys through a growth-restriction mechanism, where they physically impede the migration of high- and low-angle grain boundaries [79,106]. Their segregation along the grain boundaries, as observed in Figure 4.34, supports this effect. The efficiency of this mechanism depends on the particle density in the melt. Higher nanoparticle concentrations promote the formation of interfacial barrier layers, enhancing grain refinement and contributing to the progressive decrease in grain size with increasing TiC concentration [104].

In summary, grain refinement in TiC-modified aluminum alloys processed by L-PBF results from multiple synergistic mechanisms. TiC particles act as heterogeneous nucleation sites and restrict grain growth through interfacial pinning. Concurrently, Ti dissolution into the melt enhances constitutional supercooling, increasing the Q factor. The in-situ formation of Al_3Ti, particularly the metastable $L1_2$ ordered structure favored under rapid solidification, provides excellent lattice matching with α-Al and promotes nucleation at lower undercooling. These combined effects refine the microstructure, promoting equiaxed grain formation, which interrupts columnar dendrite growth, improves microstructural uniformity, and reduces solidification cracking. The nearly fully equiaxed grains introduced by TiC addition increase grain boundary density, enhancing stress relaxation during solidification and further limiting crack propagation [106].

4.3.2.1.2 Influence of TiC particle size on grain refinement

Grain refinement in L-PBF of aluminum alloys using TiC inoculants is controlled by heterogeneous nucleation, solute-driven growth restriction, and in-situ Al_3Ti precipitation, as discussed in the previous section. Particle size plays a critical role in determining the effectiveness of these mechanisms. Nanoparticles, due to their high surface area, provide abundant nucleation sites, but their tendency to agglomerate and segregate along grain boundaries can limit their efficiency [73,105,110,179,181,182]. Van der Waals forces are stronger for smaller particles [144,147], promoting clustering into micron-sized aggregates and leading to heterogeneous microstructures [73,110,179,181,182], as observed in Figure 4.27. In contrast, micrometer-sized TiC particles, being fewer and less prone to agglomeration, act as more stable nucleation substrates with better dispersion in the melt. Moreover, as shown by Greer *et al.* [198,199], the undercooling (ΔT_n) required for α-Al nucleation on a particle surface is inversely proportional to particle diameter, as shown in Equation 4.15, where γ is the interfacial energy between solid and liquid phase, ΔS_v is the entropy of fusion per unit volume of aluminum, and d is the particle diameter. Consequently, larger particles facilitate nucleation at lower undercooling, while smaller particles become active at higher undercooling, progressively contributing to grain refinement.

$$\Delta T_n = \frac{4\gamma}{d\Delta S_v} \tag{4.15}$$

Particles must exceed a critical radius to act as stable nuclei, enabling grain growth and reducing the system's free energy [190,198,199]. For L-PBF of TiB_2-modified Al-Cu alloys, Mair *et al.* [187] estimated this critical radius to be approximately 50-100 nm, reflecting the extreme processing conditions, where high cooling and solidification rates generate strong thermal undercooling, and solute accumulation at the solidification front enhances constitutional supercooling. Importantly, the relationship between grain size and inoculant diameter is not linear but exhibits a U-shaped trend. Grain refinement improves

as particle size decreases to an optimal range, beyond which finer particles reduce nucleation efficiency and lead to coarser grains [198,199].

Accordingly, nanoparticles offer the greatest potential for grain refinement via heterogeneous nucleation due to their size being close to the critical radius, which allows efficient nucleation under L-PBF conditions. However, their tendency to agglomerate can reduce this effectiveness. Additionally, nanoparticles contribute to grain refinement by pinning grain boundaries, as the pinned grain size is proportional to particle diameter at a given particle volume [187,200]. In contrast, coarser particles require lower undercooling (ΔT_n) to nucleate and exhibit more stable dispersion in the melt, but their inherent ability to refine the microstructure is limited compared to well-dispersed nanoparticles.

Simultaneously, smaller TiC particles have a higher surface area-to-volume ratio, which facilitates their dissolution or reaction with molten aluminum, enhancing constitutional supercooling and growth restriction due to solute concentration, and heterogeneous nucleation via Al_3Ti formation. In contrast, alloys containing coarse micrometer-sized TiC particles exhibit lower Ti solute concentrations due to their smaller reactive surface area (Figure 4.37a). Interestingly, as shown in Figure 4.37a, alloys with 1-2 wt.% of fine micrometer-sized TiC particles display higher Ti solute levels than those with the same concentration of nano-sized TiC particles, likely due to nanoparticle agglomeration. As discussed in Figure 4.28, agglomerated nanoparticles increase the effective particle size and reduce the surface area available for dissolution, limiting the release of Ti into the melt and reducing their grain-refining effectiveness. Fine micrometer-sized TiC particles provide a better balance between surface area and dispersion, yielding higher Ti solute content and more efficient grain refinement. Figure 4.37b shows a clear correlation between Ti solute concentration and average grain size, where higher Ti content leads to smaller grains until a plateau is reached, after which further Ti increase has little effect. The figure also indicates that coarse micrometer-sized particles can still produce refined microstructures, but higher particle concentrations are required to achieve sufficient Ti solute in the matrix.

Higher Ti solute concentrations in the aluminum matrix can enhance the formation of Al_3Ti particles, which promote grain refinement through heterogeneous nucleation. Although nanoparticles provide a larger surface area for dissolution and would be expected to favor Al_3Ti formation, the Ti solute concentration is actually higher in alloys produced with fine micrometer-sized TiC particles (Figure 4.37a). Consequently, the contribution of Al_3Ti-mediated nucleation to grain refinement is likely more pronounced in these alloys. Overall, grain refinement in TiC-modified AA2017 alloys during L-PBF appears to be dominated by solute-driven effects (enhanced constitutional supercooling, growth restriction, and Al_3Ti nucleation) rather than by direct TiC-induced heterogeneous nucleation. While nanoparticles offer additional refinement through direct heterogeneous nucleation and grain boundary pinning, their tendency to agglomerate reduces their effectiveness, resulting in less refinement than that achieved with fine micrometer-sized TiC particles.

4.3.2.2 Mechanical properties

Microhardness measurements, along with uniaxial compression and tensile tests, were conducted on the as-built AA2017 and TiC/AA2017 alloys to evaluate the influence of TiC particle size and concentration on local mechanical properties. Figure 4.38 shows that microhardness slightly increases with higher TiC content. Due to the noticeable variability in hardness within each alloy, microhardness data were evaluated using one-way ANOVA, which indicated a statistically significant difference between the groups (p-value < 0.05), as shown in Table A8 in the Appendix. A post-hoc Tukey test was subsequently conducted to identify which compositions differed from each other (Table A9 in the Appendix). According to this, the as-built AA2017 and 1TiC44µm alloys exhibited the lowest microhardness (Group D). As-built 1TiC4µm, 2TiC45nm, and 2TiC44µm alloys presented transitional hardness levels (Group B-C), while the as-built 1TiC45nm and 2TiC4µm alloys formed an intermediate group (Group B). The as-built 4TiC45nm, 4TiC4µm, and 4TiC44µm alloys showed the highest microhardness values (Group A). Therefore, for alloys containing 1 wt.% of TiC particles, nanoparticles yield the highest microhardness of 90 ± 7 HV. However,

at higher TiC concentrations, no significant influence of the TiC particle size could be observed. The as-built AA2017 alloy exhibits a microhardness of 86 ± 9 HV, whereas the as-built 4TiC4µm alloy reached a maximum microhardness of 96 ± 8 HV, which demonstrates the potential of the fine micrometer-sized TiC particles to improve the global mechanical properties of the L-PBF-processed AA2017 alloy.

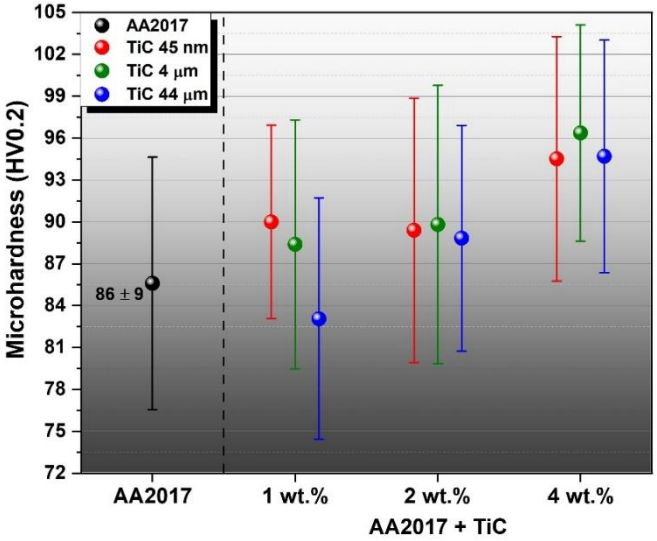

Figure 4.38 - Average microhardness of the as-built AA2017 and TiC/AA2017 alloys along the cross-section parallel to the building direction (BD).

The effect of the BD on the quasi-static mechanical behavior of the as-built AA2017 and TiC/AA2017 alloys was investigated through compression tests performed on specimens produced by L-PBF with loading axes oriented at 0°, 45°, and 90° relative to the build platform, as shown in Figure 4.39. Although previous studies report that BD can significantly affect mechanical anisotropy in L-PBF alloys due to melt pool morphology and layer-wise solidification, this influence was not clearly observed in the present work (Figure 4.39a). Oliveira de Menezes, Castrodeza, and Casati [201] observed higher superior mechanical properties in specimens produced by L-PBF horizontally (0° in relation to the build platform), which are mainly related to the differences in thermal condition and solidification behavior caused by the change in building direction. When the orientation shifts from vertical to horizontal, the heat dissipation paths and thermal boundaries are modified, altering the cooling rate and temperature gradient. These variations promote a CET and cause a tilt of the <001> crystallographic

orientation away from the build direction [202]. The resulting equiaxed and refined grain structure improves microstructural isotropy and contributes to the enhanced strength observed in the horizontally built samples (i.e., 0°-specimens). Although not all samples exhibit this behavior, a tendency toward enhanced properties in horizontally built specimens can be noted in the 4TiC45nm, 1TiC4µm, 2TiC4µm, 2TiC44µm, and 4TiC44µm alloys (Table A10 in the Appendix).

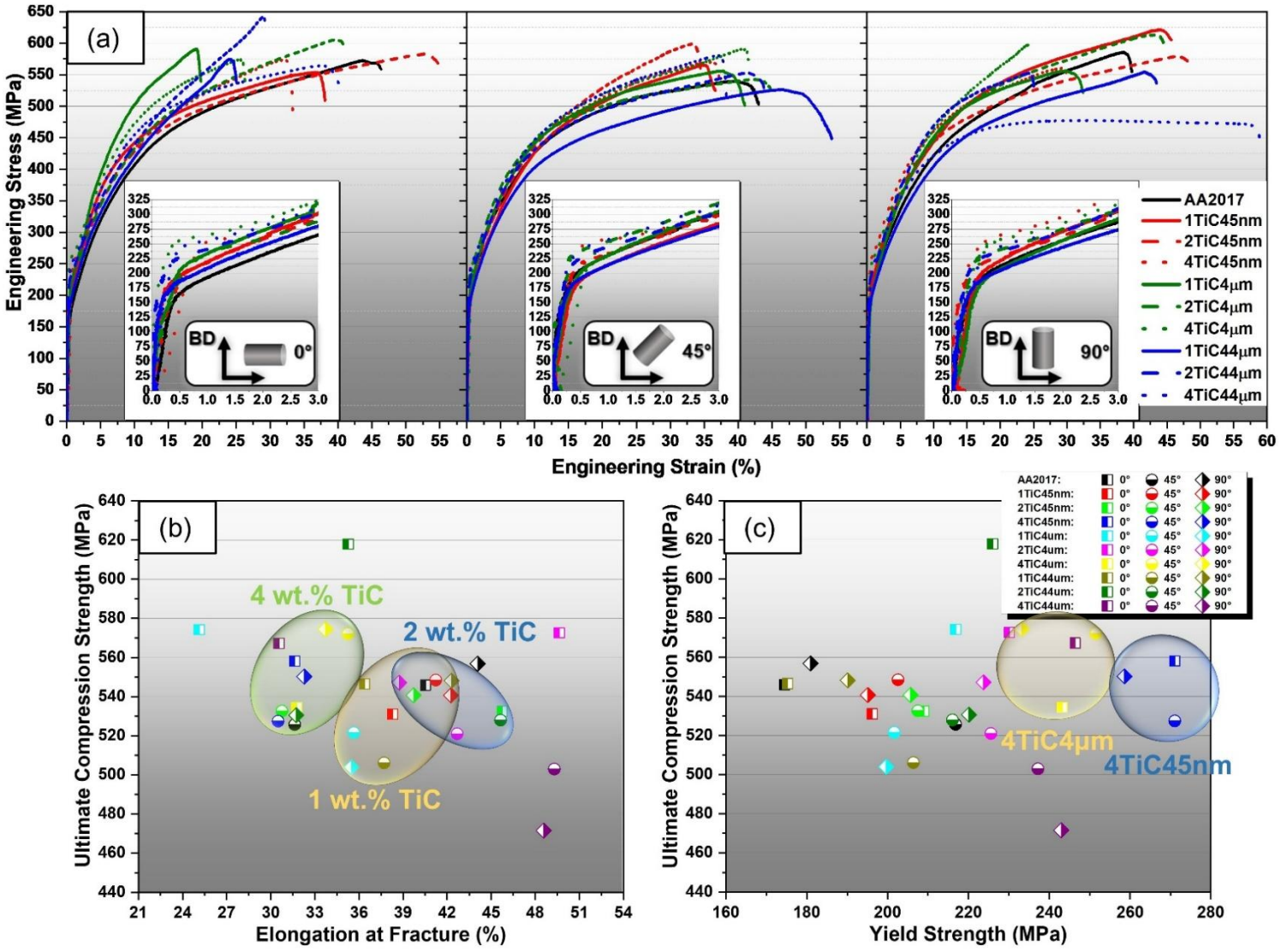

Figure 4.39 - (a) Compressive engineering stress versus engineering strength of the as-built AA2017 and TiC/AA2017 alloys produced by L-PBF with the loading axis at 0, 45, and 90° in relation to the build platform, and their respective UCS as a function of the (b) elongation at fracture, and (c) yield strength.

As seen in Figure 4.39b, specimens with 4 wt.% of TiC tend to present higher ultimate compressive strength (UCS) amongst the TiC/AA2017 alloys but lower elongation at fracture, while the specimens with 2 wt.% of TiC exhibit a better combination of UCS and elongation at fracture. The yield strength also tends to increase with the TiC concentration (Figure 4.39c). At 1 wt.% and 2 wt.% of TiC, the as-built specimens with fine micrometer-sized TiC particles exhibit a UCS and yield strength higher than those specimens with nano-sized and coarse micrometer-sized particles. To improve clarity in Figure 4.39b-c, the standard deviation bars were omitted, but the corresponding values are provided in Table A10 in the Appendix. In general, the UCS, yield strength, and elongation at fracture demonstrate that increasing TiC content leads to a consistent improvement in compressive strength, with the TiC/AA2017 alloys presenting a significantly higher yield strength than the AA2017 alloy. The highest UCS and elongation at fracture achieved by the AA2017 alloy was 557 ± 25 MPa and 44 ± 14 % in the specimen produced by L-PBF in the vertical direction (i.e., 90°-specimens), while the highest yield strength of 217 ± 6 MPa was obtained by the 45°-specimen. In the TiC/AA2017 alloys, the highest UCS of 618 ± 28 MPa was achieved by the 2TiC44µm alloy produced in the horizontal direction (i.e., 0°-specimens), and the highest yield strength was obtained by the 4TiC45nm alloy produced at 45° in relation to the build platform.

Tensile specimens of the as-built AA2017 and TiC/AA2017 alloys were fabricated by L-PBF with the loading axis oriented at 0° relative to the build platform to assess the influence of TiC particle size and concentration on the tensile properties. The corresponding results are presented in Figure 4.40. As shown in Figure 4.40a, the incorporation of TiC significantly enhanced the mechanical performance of the AA2017 alloy. Most TiC-reinforced samples exhibited higher ultimate tensile strength (UTS), yield strength, Young's modulus, and elongation at fracture than the unmodified alloy (Figure 4.40a). The as-built AA2017 alloy reached UTS, yield strength, Young's modulus, and elongation at fracture values of 314 ± 47 MPa, 184 ± 5 MPa, and 8 ± 6 %, respectively, aligning with mechanical properties reported for L-PBF-processed Al-Cu alloys in the literature (Figure 4.40c).

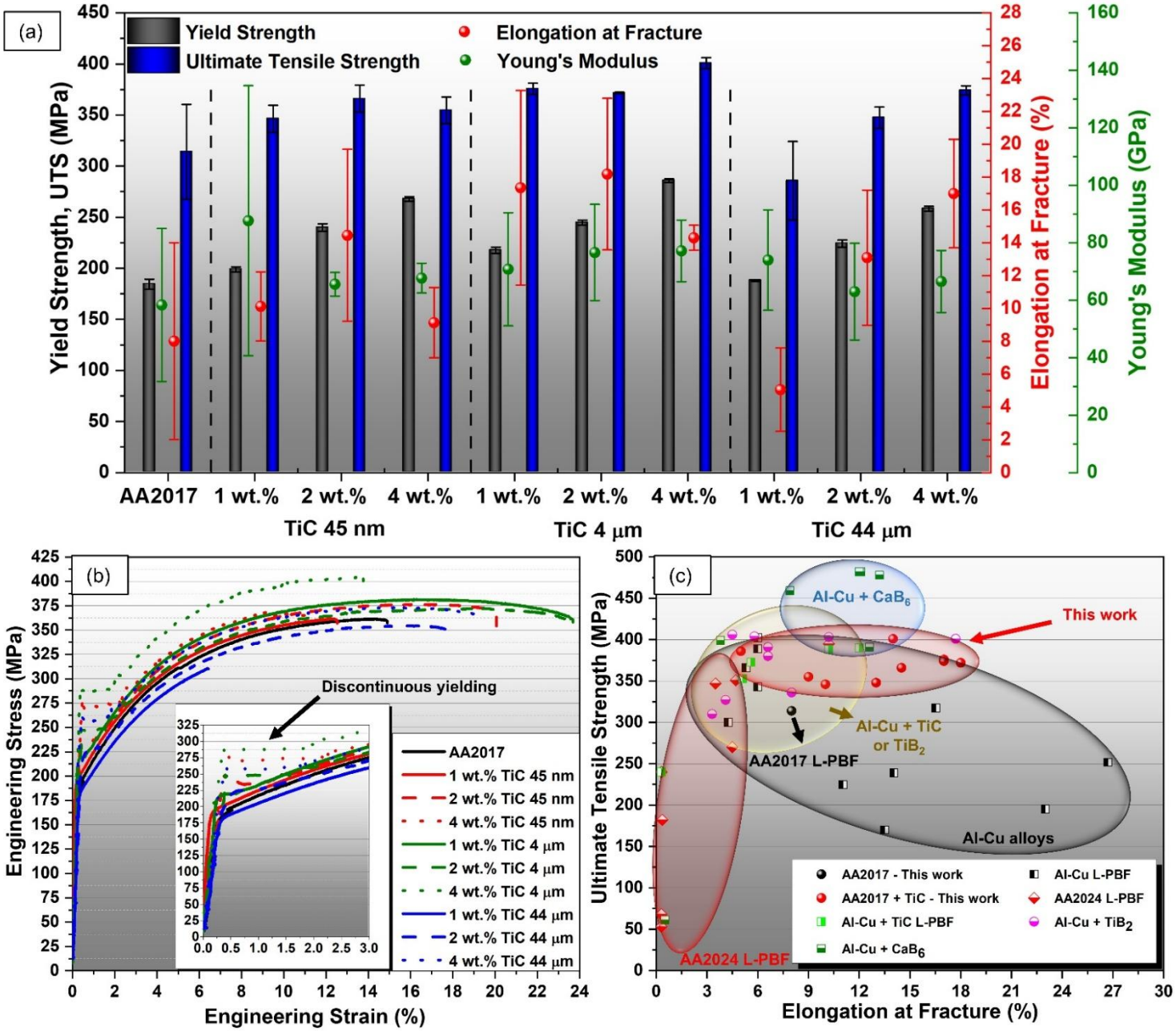

Figure 4.40 - (a) UTS, yield strength, Young's modulus, elongation at fracture, and (b) tensile engineering stress versus engineering strength of the as-built AA2017 and TiC/AA2017 alloys produced by L-PBF. (c) Comparison of UTS and elongation at fracture with Al-Cu [11,55,58,130,135,136,203–205], AA2024 [91,104,132,140,184,206], TiC/Al-Cu [104,140], TiB_2/Al-Cu [184,187,206–208], and CaB_6/Al-Cu [90,91] alloys produced by L-PBF previously reported in the literature.

In Figure 4.40a, the addition of 1 wt.% TiC, either as nanoparticles or fine micrometer-sized particles, resulted in noticeable improvements in UTS (19.6%), yield strength (18.0%), Young's modulus (50.2%), and elongation at fracture (116.8%) compared to the unmodified alloy. For the samples reinforced with TiC nanoparticles, increasing the particle concentration led to a rise in yield strength but a reduction in Young's modulus. Both UTS and elongation at fracture increased up to 2 wt.% of nano-sized TiC, reaching maximum values of 366 ± 13 MPa and 14 ± 5%, respectively, before decreasing at higher TiC concentrations. Although the as-built 1TiC44μm specimen exhibited slightly lower UTS and elongation at fracture than the as-built AA2017 alloy, a clear strengthening trend was observed with increasing the concentration of the coarse micrometer-sized TiC particles, achieving a maximum UTS of 374 ± 5 MPa, yield strength of 258 ± 2 MPa, and elongation at fracture of 17 ± 3% in the as-built 4TiC44μm alloy.

The highest overall tensile performance, however, was obtained for the alloys reinforced with fine micrometer-sized TiC particles. In these samples, UTS and yield strength increased steadily with particle concentration, while Young's modulus remained nearly constant, and elongation at fracture peaked at 2 wt.% of TiC before decreasing at higher contents. The optimal balance between strength and ductility was achieved in the 2TiC4μm alloy, with UTS, yield strength, Young's modulus, and elongation at fracture of 372 ± 1 MPa, 245 ± 3 MPa, 77 ± 17 GPa, and 18 ± 5%, respectively. The strengthening mechanisms involved in yield strength enhancement with TiC addition will be discussed in Section 4.3.2.2.2. Additionally, in the engineering stress-strain curves (Figure 4.40b), the discontinuous yielding behavior can be identified, which seems more significant as the TiC concentration increases. Discontinuous yielding behavior is commonly observed in low carbon steel and will be discussed in Section 4.3.2.2.1.

Figure 4.40c compares the tensile results of the as-built AA2017 and TiC/AA2017 alloys with those reported for other Al-Cu and reinforced-Al-Cu alloys produced by L-PBF in the literature. The unmodified AA2017 alloy achieved higher elongation than the AA2024 alloy and higher UTS than most of the Al-Cu alloys reported in the literature, probably due to the very low

concentration of defects (porosity and solidification cracks) obtained with the L-PBF process optimization through the systematic evaluation of the influence of the L-PBF processing parameters on defect formation (Section 4.2). The as-built TiC/AA2017 alloys also presented higher elongation and similar UTS of TiC- and TiB_2-modified Al-Cu alloys reported in the literature. This indicates that the mechanical performance of the as-built TiC/AA2017 alloys arises not only from the reinforcing effect of the TiC particles but also from exceptionally low defect content achieved in this work, which enhances the effectiveness of the strengthening mechanisms.

The fracture morphology of the as-built AA2017 and TiC/AA2017 alloys is shown in Figure 4.41. Figure 4.41 presents the fracture morphology of the TiC/AA2017 tensile specimens exhibiting the best mechanical performance for each TiC particle size, in comparison with the unreinforced AA2017 alloy. The fracture morphologies of the remaining alloys are provided in Figure A8 in the Appendix. The tested tensile specimens exhibited a combination of ductile and brittle fracture mechanisms for all alloys. A nonuniform and rough region on the fracture surface of the as-built AA2017 alloy, without any dimples (Figure 4.41a), suggests a brittle fracture mode, likely resulting from the rapid propagation of cracks along the grain boundaries during testing loading. Such fracture behavior could be associated with the presence of solidification cracking at grain boundaries in the as-built AA2017 alloy, as seen in Figure 4.26. Additionally, cracks and pores were also observed on the fracture surfaces, as highlighted in Figure 4.41. Conversely, a large number of dimples were observed in other regions of the as-built AA2017 alloy fracture surface (Figure 4.41b-c), indicating ductile fracture by microvoid coalescence. These dimples demonstrate that, in crack-free regions of the microstructure, the material was able to sustain significant plastic deformation prior to fracture. In the as-built TiC/AA2017 alloys (Figure 4.41d-f), TiC particles of different sizes were observed embedded in the aluminum matrix and surrounded by numerous dimples, suggesting good interfacial bonding and effective load transfer between the TiC particle and the matrix, indicating a predominant ductile fracture mode. However, the presence of voids and cracks around the TiC particles indicates that localized decohesion or

particle-matrix debonding occurred during fracture. This likely initiated at the particle-matrix interface due to stress concentration and mismatch in elastic modulus and thermal expansion between TiC and aluminum that favors the nucleation of microvoids. Overall, the coexistence of brittle and ductile features indicates a mixed fracture mechanism, influenced by both the microstructural defects inherent to L-PBF processing and the distribution and bonding quality of TiC particles.

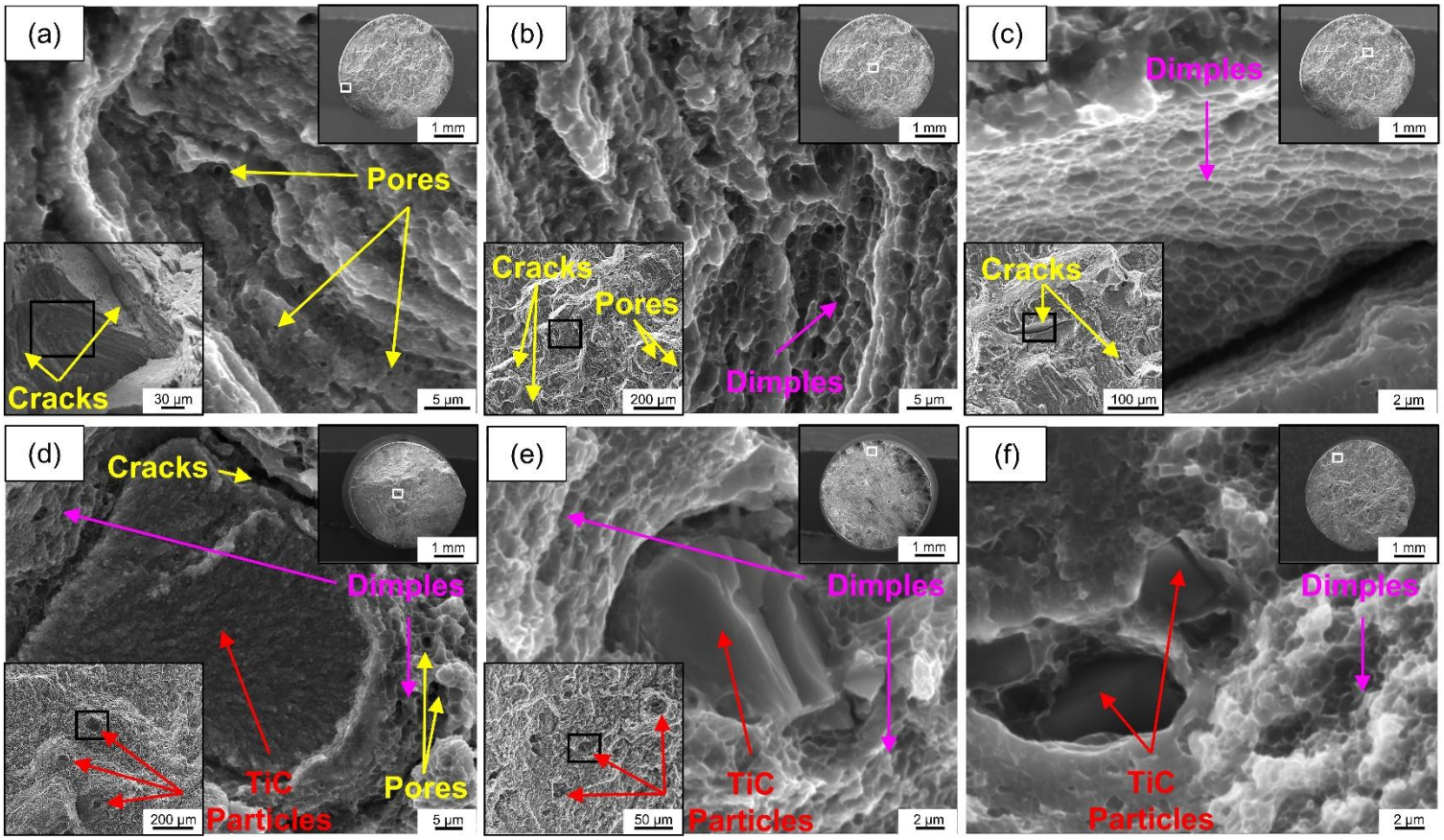

Figure 4.41 - SEM images of the fracture surface of the as-built (a-c) AA2017, (d) 2TiC45nm, (e) 2TiC4µm, and (f) 4TiC44µm alloys.

4.3.2.2.1 Discontinuous yielding behavior

Discontinuous yielding, often identified by a sharp yield drop followed by a stress plateau, represents a form of plastic instability commonly observed in metals [209]. It typically arises from an insufficient density of mobile dislocations available at the onset of plastic deformation. Two main factors contribute to this

lack of mobile dislocations: the pinning of dislocations by solute atoms, forming so-called Cottrell atmospheres, and the scarcity of active dislocation sources caused by grain refinement or prior annealing. While substitutional solute atoms such as Mg can influence yield point behavior in aluminum alloys, their effect is generally weaker than that of interstitial solutes in steels [210]. Consequently, in ultrafine-grained or fine-grained aluminum alloys, discontinuous yielding is often attributed primarily to microstructural factors rather than solute pinning effects [211].

In L-PBF of aluminum alloys, few studies reported [132,210–214] the occurrence of discontinuous yielding behavior in tensile tests, and the discussion on its origin and fundamental mechanisms in L-PBF remains very scarce. Nevertheless, the fine-grained regions formed during rapid solidification seem to play a dominant role in triggering discontinuous yielding [209,211]. The grain boundaries of these refined regions act as strong sinks for dislocations, absorbing pre-existing dislocations and limiting their mobility, further requiring elevated tensile stress to yield the material. As plastic deformation advances, new dislocation sources are activated, but the frequent interaction and annihilation of dislocations at closely spaced grain boundaries hinder their effective accumulation [211]. This behavior manifests macroscopically as the formation and propagation of Lüders bands, localized regions of higher strain that sweep through the material as deformation progresses [209,210]. Microscopic observations confirm that dislocations tend to accumulate in coarse-grained regions, while fine-grained areas remain relatively dislocation-free until they are swept by these bands [210].

However, it is well-established that the addition of reinforcements to aluminum alloys increases dislocation density in aluminum matrix composites due to thermal and elastic misfits [215,216]. Figure 4.42a shows a high concentration of dislocations in the as-built 4TiC45nm alloy near an Al_3Ti particle (red arrow) and the grain boundary. Compared to the as-built 4TiC45nm alloy, the as-built 1TiC45nm (Figure 4.42b) and AA2017 (Figure 4.42c) seem to present a lower dislocation density, which is related to the lower/absent TiC particle concentration.

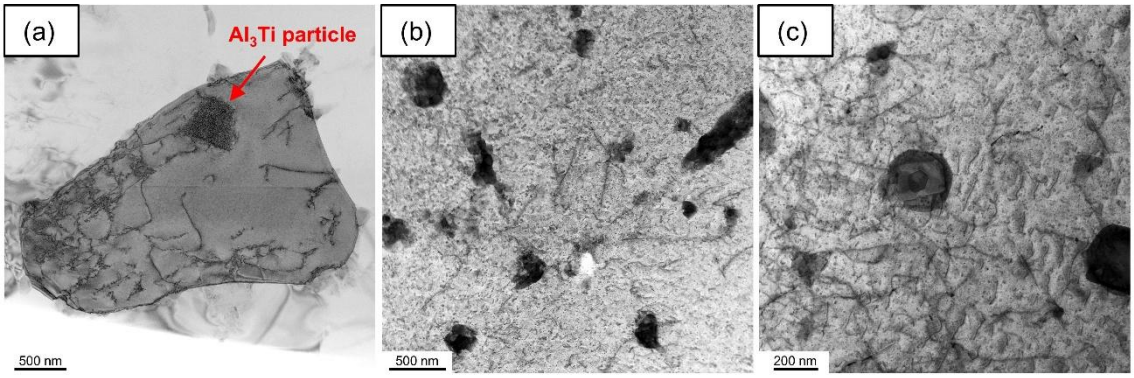

Figure 4.42 - BF-STEM images showing dislocation configurations in the as-built (a) 4TiC45nm, (b) 1TiC45nm, and (c) AA2017 alloys produced by L-PBF.

Dislocations are one of the main microstructural features responsible for XRD peak broadening, because their strain fields distort the periodicity of the crystal lattice [217–220]. When dislocations are present, the atomic planes are no longer perfectly spaced, and local variations in interplanar spacing introduce lattice microstrain. This microstrain causes a distribution of diffraction angles rather than a single sharp reflection, resulting in broader peak shapes. Therefore, the analysis of XRD peak broadening using line-profile methods, such as the Williamson-Hall method, enables the quantitative estimation of dislocation-related microstrain and dislocation density in polycrystalline materials [217–222]. Considering the XRD patterns in Figure 4.32, the dislocation density of the as-built AA2017 and TiC/AA2017 alloys can be estimated through the Williamson-Hall method using the following equations [221–224]:

$$\rho = \frac{2\sqrt{3}\,\varepsilon}{Db} \tag{4.16}$$

$$\beta \cos\theta = \frac{K\lambda}{D} + 4\varepsilon \sin\theta \tag{4.17}$$

where ρ is the dislocation density, b is the Burgers vector (b = 0.286 for Al [223]), D is the crystallite size, ε is the microstrain, θ is the Bragg angle, λ is the wavelength of Cu-$K_{\alpha 1}$ radiation (λ = 1.54 Å), β is the full width at half maximum

(FWHM) of the diffraction peak, and K is the shape factor (typically K = 0.9 [221]). D and ε can be extracted from the intercept and slope of the linear fit obtained from the Williamson-Hall plots (Figure A7 in the Appendix). After obtaining D and ε, the dislocation density (ρ) can be estimated using Equation 4.16, with results presented in Figure 4.43. Although instrumental broadening was not subtracted in this analysis, the estimated dislocation densities remain valid for comparative purposes, since all samples were measured under identical diffraction conditions. Thus, the relative differences in peak broadening can be directly attributed to differences in microstrain and crystallite size among the as-built alloys.

Figure 4.43a shows the effect of TiC particle size and concentration on the dislocation density of the as-built AA2017 alloy. Overall, an increase in TiC particle concentration leads to a higher dislocation density, indicating that the presence of ceramic particles contributes to lattice distortion during solidification. The TiC particle size also influences this behavior. At low TiC concentration, coarse micrometer-sized particles appear to induce more dislocation accumulation, while at higher TiC concentration, fine micrometer-sized particles have a more pronounced effect. In contrast, the nanoparticle additions show the smallest impact on dislocation density across all compositions.

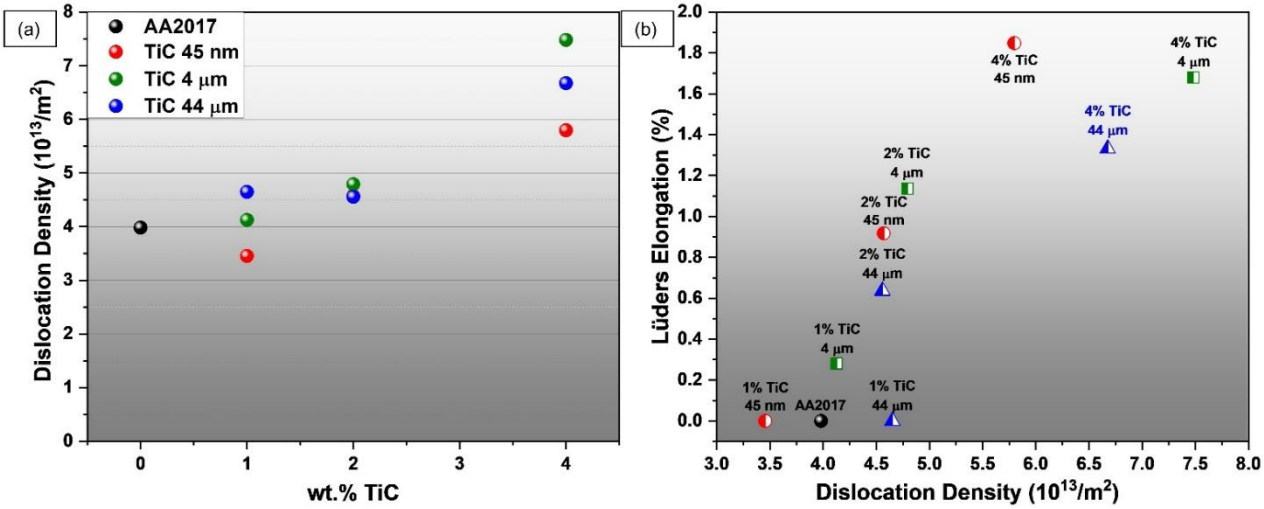

Figure 4.43 - (a) Dislocation density of the as-built AA2017 and TiC/AA2017 alloys obtained through the Williamson-Hall method, and (b) experimental Lüders elongation as a function of the dislocation density.

Although the as-built TiC/AA2017 alloys with higher TiC concentration present a higher dislocation density, it also displays higher Lüders elongation (Figure 4.43b), as quantified from the length of the yield plateaus in Figure 4.40b. Figure 4.43b shows that the Lüders elongation is increased with increasing TiC particle concentration. The rise in the dislocation density due to the TiC particle concentration increase might result in dislocation entanglement, hindering their movement and contributing to the discontinuous yielding due to the lack of movable dislocations. Similarly, Wang *et al.* [213] also observed discontinuous yielding in L-PBF-fabricated TiB_2/AlMgScZr composite, even though the alloy presented a large number of dislocations. They pointed out that the limited dislocation mobility, caused by the formation of a forest of intersecting dislocations, dislocation clustering at grain boundaries, and pinning by second-phase particles, lead to the observed yield behavior.

In addition, the fraction of fine-grained regions in heterogeneous structures strongly influences the mechanical response. Alloys with more fine-grained regions show a notable yield decrease and Lüders elongation due to the limited availability of mobile dislocations within those grains [211]. Conversely, when the fine-grained fraction decreases, dislocation sources spread more evenly through the microstructure, promoting a more homogeneous plastic flow and shifting the material from discontinuous to continuous yielding behavior [211]. Figure 4.44 shows this for as-built AA2017 and TiC/AA2017 alloys. Higher TiC concentration makes the microstructure finer, which sharply increases Lüders elongation (Figure 4.44a). As the TiC concentration rises, dislocation density is expected to increase, which leads to more dislocation entanglement, intensifying discontinuous yielding behavior due to fewer movable dislocation. Formation of Al_3Ti particles and increased Ti solute concentration in the matrix may also contribute to impede the dislocation movement. Figure 4.44b demonstrates that the yield strength follows a similar relation to the grain size, but while the fine micrometer-sized TiC particles appear to enhance yield strength most, the highest Lüders elongation is achieved by the as-built 4TiC45nm alloy. This interplay between grain size distribution and dislocation dynamics governs the

discontinuous yielding behaviors seen in additively manufactured aluminum alloys.

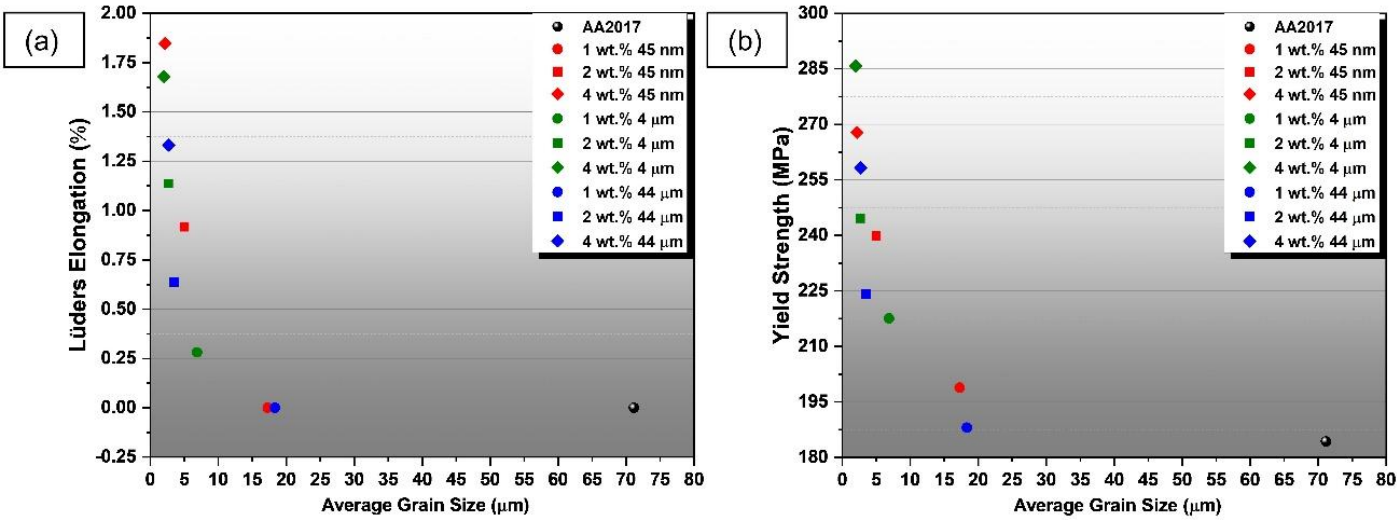

Figure 4.44 - (a) Lüders elongation and (b) yield strength of the as-built AA2017 and TiC/AA2017 alloy as a function of the average grain size.

4.3.2.2.2 Strengthening mechanisms

The mechanical behavior of TiC-modified AA2017 alloys fabricated by L-PBF is governed by a complex interplay of microstructural factors. The as-built 4TiC4μm alloy reaches a yield strength of 286 ± 2 MPa (Figure 4.40a), significantly higher than that of the unreinforced counterpart (184 ± 5 MPa). In the base alloy, the presence of coarse columnar grains facilitates intergranular delamination under tensile loading, while pre-existing microcracks act as preferential sites for crack initiation and rapid propagation. The introduction of TiC particles mitigates these issues by promoting the formation of equiaxed grains and reducing solidification cracking, thereby improving the mechanical performance.

Beyond the elimination of defects, the enhanced strength of the TiC/AA2017 alloys is attributed to several key microstructural factors, including grain refinement, solute enrichment of the aluminum matrix, and the presence of reinforcing phases such as TiC and Al_3Ti. Grain refinement plays a dominant role, as the increased grain boundary density impedes dislocation motion in

accordance with the Hall-Petch relationship [140,208]. Additionally, the dispersed TiC particles strengthen the alloy through Orowan strengthening, with the magnitude of this effect depending on their size and volume fraction [140,208]. These particles also enhance load transfer between the aluminum matrix and the reinforcement, while generating additional dislocations and locally modifying the grain boundary structure, further enhancing both strength and ductility [208].

Moreover, the partial dissolution or reaction of TiC during processing increases Ti solute content in the aluminum matrix, contributing to additional solid-solution strengthening. Collectively, these mechanisms act synergistically to refine the microstructure and improve the overall strength of the L-PBF-processed AA2017 alloy. To quantify these contributions, the yield strength of the TiC-modified alloys can be expressed as the sum of grain boundary strengthening ($\Delta\sigma_g$) , solid-solution strengthening ($\Delta\sigma_{SS}$), Orowan strengthening ($\Delta\sigma_{oro}$), and load-bearing strengthening ($\Delta\sigma_L$), as given by Equation 4.18 [208], where the yield strength of the as-built AA2017 alloy (σ_0) is 184 ± 5 MPa (Figure 4.40).

$$\sigma_{YS} = \sigma_0 + \Delta\sigma_g + \Delta\sigma_{SS} + \Delta\sigma_L + \Delta\sigma_{oro} \quad (4.18)$$

According to the Hall-Petch relationship, grain refinement enhances strength and toughness by increasing the density of grain boundaries, which serve as effective barriers to dislocation motion [140]. The strengthening contribution from grain boundaries ($\Delta\sigma_g$) can be quantified using the modified Hall-Petch equation [208,225]:

$$\Delta\sigma_g = k\, D_{gb}^{-\frac{1}{2}} \quad (4.19)$$

where k is the Hall-Petch coefficient, representing the relative strengthening contribution from grain boundaries (50 MPa.μm$^{1/2}$ for aluminum alloys [77,208]), and D_{gb} is the average grain size of the as-built TiC/AA2017 alloys (Figure 4.29a). Based on this relationship, the grain boundary strengthening contribution ($\Delta\sigma_g$)

ranges from 11.7 MPa for the as-built 1TiC44μm alloy to 35.4 MPa for the as-built 4TiC4μm alloy, as shown in Figure 4.45.

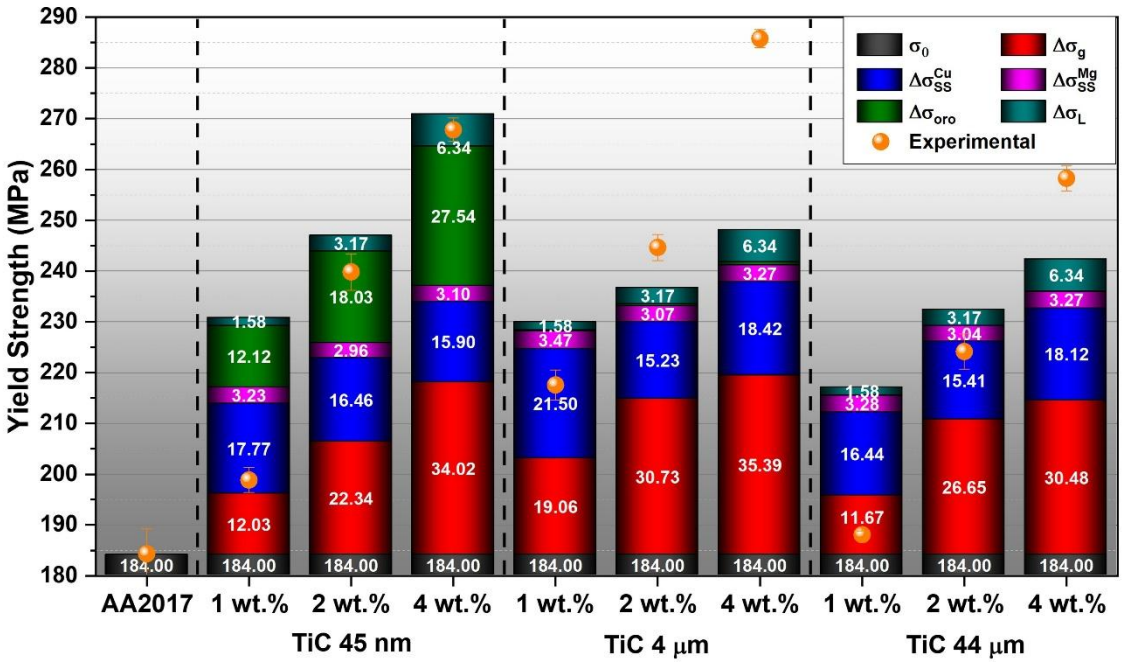

Figure 4.45 - Contribution of the grain boundary, solid solution, load-bearing, and Orowan strengthening mechanisms to the yield strength of the as-built TiC/AA2017 alloys produced by L-PBF.

Solid-solution strengthening arises from the interaction between moving dislocations and the local strain fields generated by solute atoms. According to the literature [208,226], the corresponding strengthening contribution ($\Delta\sigma_{SS}$) can be estimated using Equation 4.20:

$$\Delta\sigma_{SS} = \sum k_j c_j^n \tag{4.20}$$

where k_j represents the strengthening coefficient of each solute element, c_j is the atomic concentration, and n is a constant (n = 1 [208]). Given the low Ti solute content, only Cu and Mg were considered in the calculations, with k_{Cu} = 10.5 MPa/at% and k_{Mg} = 5 MPa/at% [208,226]. Based on these parameters, the solid-solution strengthening contribution of Cu varies from 15.2 MPa in the as-built

2TiC4μm alloy to 21.5 MPa in the as-built 1TiC4μm alloy, while Mg provides a smaller, nearly constant contribution of approximately 3.2 MPa.

The strong atomic-scale interfacial bonding between the aluminum matrix and the TiC particles promotes efficient load transfer during tensile deformation, allowing stress to be transmitted from the ductile aluminum matrix to the rigid ceramic reinforcements [208]. The corresponding contribution to the overall strengthening, referred to as load-bearing strengthening ($\Delta\sigma_L$), can be estimated using Equation 4.21 [77,208,227], where V_p represents the volume fraction of TiC particles. Based on these estimations, $\Delta\sigma_L$ ranges from 1.6 MPa in alloys containing 1 wt.% of TiC to 6.3 MPa in those reinforced with 4 wt.% of TiC particles, regardless of particle size.

$$\Delta\sigma_L = 1.5V_p\sigma_0 \tag{4.21}$$

Additionally, the uniformly distributed fine TiC particles impede dislocation motion, thereby enhancing the yield strength through dispersion strengthening. For non-deformable particles, this effect originates from dislocations bypassing the obstacles, with the corresponding increase in yield strength ($\Delta\sigma_{oro}$) described by the Orowan mechanism [140]. The contribution of Orowan strengthening to the overall yield strength can be estimated according to Equation 4.22 [208,228]:

$$\Delta\sigma_{oro} = \frac{0.13Gb}{d_p\left(\frac{1}{2V_p}^{1/3}-1\right)}\ln\frac{d_p}{2b} \tag{4.22}$$

where G is the shear modulus of aluminum (G = 28 GPa [207]), b is the Burgers vector of the Al matrix (b = 0.286 nm [77]), and d_p is the average TiC particle size. Based on the initial TiC particle size and concentration, the Orowan strengthening contribution ($\Delta\sigma_{oro}$) to the yield strength ranges from approximately 12.1 MPa in the as-built 1TiC45nm alloy to 27.5 MPa in the as-built 4TiC45nm alloy. This mechanism becomes negligible in alloys containing larger TiC particles (i.e., TiC4μm and TiC44μm) due to the reduced particle-dislocation interaction. Although nanometric Al_3Ti particles may also provide an additional strengthening

effect through the Orowan mechanism, their contribution was not quantified owing to the difficulty in accurately estimating their volume fraction within the as-built microstructure.

As shown in Figure 4.45, the overall strengthening of the as-built TiC-modified AA2017 alloys increases with decreasing particle size and higher TiC concentration. In general, grain boundary strengthening and solid-solution strengthening due to Cu solute are the most important mechanisms for strengthening in the TiC/AA2017 alloys, but the yield strength in the nano-TiC reinforced alloys is further improved due to Orowan strengthening. Besides that, a good agreement is observed between the predicted and experimental yield strengths for the 2TiC45nm, 4TiC45nm, 1TiC4μm, 2TiC4μm, and 2TiC44μm alloys. In contrast, the experimental yield strength of the 1TiC45nm and 1TiC44μm alloys is lower than predicted, likely due to higher residual porosity, coarser grain size, and a larger fraction of columnar grains that facilitate delamination along grain boundaries during tensile loading. Conversely, the 4TiC4μm and 4TiC44μm alloys exhibit experimental yield strengths exceeding the predicted values, highlighting the effectiveness of fine micrometer-sized TiC particles in enhancing the mechanical properties of the as-built AA2017 alloy. Although the 4TiC45nm alloy presents similar porosity, average grain size, and fraction of equiaxed grains as the 4TiC4μm alloy, its higher tendency to agglomerate likely limited mechanical improvement and affected elongation at fracture (Figure 4.40).

Moreover, the formation of equiaxed grains promotes isotropic mechanical performance and reduces residual stresses in the printed parts. Overall, the addition of TiC inoculants in AA2017 powders during L-PBF refines the microstructure, induces a columnar-to-equiaxed transition, and mitigates solidification cracking, thereby enhancing both printability and mechanical properties. Fine micrometer-sized TiC particles provide the most effective balance between dispersion and particle size, outperforming both nanoparticles and coarse micrometer-sized particles in improving the alloy’s performance. Therefore, these findings highlight that fine micrometer-sized TiC particles provide an effective strategy to refine the microstructure and enhance the

mechanical response of L-PBF-processed AA2017 alloy, while mitigating the processing and safety challenges associated with nanoparticle handling.

5 CONCLUSIONS

5.1 Surface functionalization of powders

Aiming to analyze the influence of the surface functionalization on the physical, chemical, and rheological properties of powders for additive manufacturing (AM), gas-atomized AA2017 powder was modified using chemical etchings and TiC particle deposition. Two distinct chemical etching treatments were applied to alter the particle surface, using an acidic HNO_3 solution and a basic NaOH solution. For the TiC surface functionalization, TiC particles of three different sizes (45 nm, <4 μm, and 44 μm) were incorporated as guest particles at concentrations of 1, 2, and 4 wt.%, resulting in nine TiC surface-functionalized powder variations. The following sections present and discuss the main outcomes obtained from the characterization of these powders.

5.1.1 Surface functionalization of powders using chemical etchings

Physical, chemical, and rheological properties of gas-atomized and NaOH and HNO_3 surface-functionalized powders were analyzed, and the following conclusions were drawn:

- Surface functionalization using acidic HNO_3 solution led to a refinement of the particle size, an increase in surface roughness and morphological irregularities, while surface functionalization using basic NaOH solution resulted in a smoother surface, with no significant influence on the particle size distribution compared to the gas-atomized powder.
- The NaOH- and HNO_3-treated powders exhibited a reduction of 13.3% and 8.7% in laser reflectance at a wavelength of 950 nm compared to the gas-atomized powder, but developed a thicker oxide layer on their surface due to the chemical etching and drying process.
- Surface functionalization of powders using chemical etchings enhanced the rheological behavior and flowability of the powders, achieving a maximum flowability of 18.5 ± 1.1 s/50g in the NaOH-treated powder, resulting in a reduction of the additive manufacturing suitability (AMS) factor and, therefore, improved L-PBF processability.

5.1.2 Surface functionalization of powders using TiC particles

Physical and rheological properties of gas-atomized and surface-functionalized powders with different TiC particle sizes (45nm, < 4 μm, and 44 μm) and concentrations (1, 2, and 4 wt.%) were analyzed, and the following conclusions were drawn:

- The addition of 1 wt.% of TiC, regardless of particle size, enhanced flowability and apparent density by reducing interparticle adhesion. However, higher concentrations of nano- and fine micrometer-sized TiC particles increased agglomeration, leading to poorer flow. Coarse TiC (44 μm) provided the highest flowability, with a value of 16.0 ± 0.6 s for 50g.
- Laser reflectance decreased with both smaller TiC particle size and higher TiC content, reaching the minimum of 54.4% for the 4 wt.% TiC (45 nm) powder compared to 63.5% of the gas-atomized powder at a wavelength of 950 nm.
- Rheological analyses revealed that under dynamic flow, TiC-functionalized powders entrapped more air and showed lower packing efficiency compared to the gas-atomized powder, while under shear, TiC addition reduced cohesion and facilitated easier flow initiation.
- The 1 wt.% TiC (<4 μm) powder required the least energy for powder spreading in L-PBF and exhibited minimal agglomeration under gas pressure. Under packed condition, 2 wt.% TiC (45 nm and 44 μm) and 1 wt.% TiC (44 μm) powders achieved the lowest compressibility index (CI), indicating the best packing performance.
- Overall, 1 wt.% TiC addition, regardless of particle size, was identified as the optimal composition for improving flowability, packing density, and laser absorption, while maintaining a good L-PBF processability. Higher TiC concentration led to general flow behavior impairment.

5.2 Investigation on laser powder bed fusion processing window using design of experiments and analysis of variance

The effects of the laser powder bed fusion (L-PBF) processing parameters (laser power, scanning speed, and hatch distance) on the porosity and cumulative crack length of the AA2017 and 2 wt.% TiC (45 nm)/AA2017 alloys were comprehensively investigated with the support of Box-Behnken design of experiments and analysis of variance (ANOVA). The main conclusions are summarized below:

- Both porosity and cumulative crack length in AA2017 and 2 wt.% TiC (45 nm)/AA2017 alloys decreased with lower scanning speeds and higher laser power, while the hatch distance showed negligible influence.
- The TiC/AA2017 samples yielded lower porosity and shorter cumulative crack lengths across nearly all L-PBF conditions, reducing the maximum porosity and cumulative crack length levels from 25.8 ± 2.8 % and 6.6 ± 2.4 mm/mm^2 in the as-built AA2017 alloy to 17.1 ± 2.5 % and 2.8 ± 0.9 mm/mm^2 in the as-built 2 wt.% TiC (45 nm)/AA2017alloy.
- Nano-TiC surface functionalization significantly expanded the L-PBF processing window for minimizing solidification cracking. While no crack-free AA2017 samples were achieved under the tested processing conditions, crack-free 2 wt.% TiC (45 nm)/AA2017 specimens were successfully obtained using high laser power and low scanning speed.
- Reduced regression models derived from the Box-Behnken design and ANOVA analyses were successful in identifying optimized L-PBF processing parameters (P = 190 W, v = 100 mm/s, h = 120 μm) that enabled fabrication of AA2017 alloy with minimal porosity and cumulative crack length (0.17 ± 0.06 % and 0.01 ± 0.02 mm/mm^2, respectively) and crack-free 2 wt.% TiC (45 nm)/AA2017 alloy with low porosity (0.6 ± 0.2 %).

5.3 Characterization of the as-built samples produced by laser powder bed fusion

To evaluate the effects of powder surface functionalization the microstructural evolution and mechanical performance of the AA2017 alloy produced by L-PBF, samples were produced by L-PBF using the surface-functionalized powders through chemical etching and TiC particle addition. The subsequent sections summarize the main findings regarding defect formation, microstructural characteristics, and mechanical behavior of resulting alloys.

5.3.1 L-PBF of surface-functionalized powders using chemical etchings

Microstructure and defect formation of as-built L-PBF samples produced using the powders modified through chemical etching were analyzed, and the following conclusions were drawn:

- Samples from HNO_3- and NaOH-treated powders exhibited no clear correlation between porosity and volumetric energy density, showing higher porosity than those produced from the gas-atomized AA2017 powder. Their higher porosity was mainly attributed to keyhole porosity due to the higher laser energy absorption of the chemically-treated powders, and oxidation-related porosity.
- The minimum porosity achieved using the chemically surface-functionalized powder was 20 ± 3% for the NaOH-treated powder and 4.6 ± 1.2% for the HNO_3 powder, with the presence of large keyhole-like pores. This keyhole porosity indicates that chemical surface functionalization of the powder effectively reduced laser reflectance, increasing laser energy absorption and local melt temperatures, thereby promoting vapor depression instability and the formation of keyhole pores.
- The oxide formation during powder surface functionalization induced oxidation-related porosity, decreasing the specimens' density, and making them unfit for applications that require low porosity.

- Despite the drawbacks associated with dense specimen fabrication in this work, the improved flowability, laser energy absorption, and rheological properties could still hold potential for other multi-material L-PBF applications that combine metallic and dielectric regions.

5.3.2 L-PBF of surface-functionalized powders using TiC particles

Defect formation, microstructure, and mechanical properties of the as-built L-PBF alloys produced using the gas-atomized and TiC surface-functionalized powders under optimized L-PBF processing parameters (P = 190 W, v = 100 mm/s, h = 120 μm) were analyzed, and the following conclusions were drawn:

- While the as-built AA2017 still exhibited low cumulative crack length (0.01 ± 0.02 mm/mm^2), all TiC/AA2017 alloys were crack-free. The TiC particles were homogeneously distributed in the aluminum matrix, but the nanoparticles showed a strong tendency to agglomerate into micrometer-sized clusters.
- The incorporation of TiC significantly refined the microstructure and promoted a columnar-to-equiaxed transition (CET). The average grain size and fraction of equiaxed grains evolved from 71 ± 48 μm and 30.7% in the as-built AA2017 alloy to a minimum average grain size of 2.0 ± 0.9 μm in the 4 wt.% TiC (4 μm)/AA2017 alloy and a maximum fraction of equiaxed grain of 97.7% in the 4 wt.% TiC (45 nm)/AA2017 alloy. Grain refinement and CET intensified with higher TiC concentration, and were most effective when using fine micrometer-sized TiC particles (< 4 μm). This enhanced efficiency is attributed to stronger solute-driven mechanisms, namely, enhanced constitutional supercooling, greater growth restriction, and more effective Al_3Ti nucleation.
- In addition to the typical θ-Al_2Cu, S-Al_2CuMg, and Al_6Fe phases, the TiC/AA2017 alloys with higher TiC concentrations exhibited the formation of cuboidal $L1_2$-Al_3Ti particles. These particles displayed a very low interplanar mismatch of 1.02% between the $(111)_{Al_3Ti}$ and $(111)_{Al}$ planes, confirming a highly coherent interface with the α-Al matrix.

- The observed CET and grain refinement were driven by heterogeneous nucleation promoted by TiC and Al_3Ti particles, enhanced constitutional supercooling and growth restriction effects due to Ti solute concentration in the matrix, and nanoparticle-induced growth restriction effects. Despite the high potential of nanoparticles for grain refinement, their high tendency for agglomeration reduced their efficiency, leading to lower grain refinement than that obtained using fine micrometer-sized TiC particles (< 4 μm).
- As-built TiC/AA2017 alloys demonstrated superior quasi-static mechanical properties compared to the as-built AA2017 alloy. The 2 wt.% TiC (4 μm)/AA2017 alloy achieved the best balance between strength and ductility, with ultimate tensile strength (UTS), yield strength, and elongation at fracture of 372 ± 1 MPa, 245 ± 3 MPa, and 18 ± 5%, respectively.
- Strengthening was primarily governed by grain boundary and solid-solution mechanisms, while Orowan strengthening contributed further improvement in the nano-TiC reinforced samples. TiC nanoparticles exhibited the highest potential for yield strengthening, but their higher tendency to agglomerate likely limited their strengthening effect and reduced ductility.
- Discontinuous yielding behavior was enhanced with increasing TiC content and grain refinement. The boundaries of the fine equiaxed grains acted as dislocation sinks, and the increased dislocation density and dislocation entanglement with increasing TiC concentration led to more pronounced Lüders band formation due to the reduced number of mobile dislocations.
- Overall, TiC surface functionalization of the powder effectively improved the microstructure and mechanical properties of the AA2017 alloy. However, excessive nanoparticle agglomeration constrained their refinement potential, making fine micrometer-sized TiC particles (< 4 μm) the most effective in optimizing processability, grain structure, and mechanical performance.

6 RECOMMENDATIONS FOR FUTURE WORK

- Explore alternative surface functionalization routes that prevent oxide layer formation during chemical etching, such as plasma or electrochemical treatments, to improve laser absorptivity without compromising powder purity or sample density.
- Investigate other reinforcements (such as TiB_2, CaB_6, ZrH_2, and TiN) with micrometer-sized particles to compare their efficiency with TiC in promoting grain refinement and reducing solidification cracking in high-strength aluminum alloys.
- Perform aging heat treatments on the AA2017 and TiC/AA2017 alloys to improve microhardness and assess the influence of the TiC particle size and concentration on thermal response and precipitation behavior.
- Investigate the wear and corrosion resistance of the TiC/AA2017 alloys, analyzing how the TiC particle size and concentration affect surface degradation mechanisms and overall durability.
- Study fatigue and damage tolerance performances of the TiC/AA2017 alloys, and their correlation with microstructural refinement and particle distribution.

7 REFERENCES

[1] L. Wang, S. Wang, J. Wu, Experimental investigation on densification behavior and surface roughness of AlSi10Mg powders produced by selective laser melting, Optics & Laser Technology, v. 96, p. 88–96, 2017. https://doi.org/10.1016/j.optlastec.2017.05.006.

[2] R. Baitimerov, P. Lykov, D. Zherebtsov, L. Radionova, A. Shultc, K.G. Prashanth, Influence of Powder Characteristics on Processability of AlSi12 Alloy Fabricated by Selective Laser Melting, Materials, v. 11, p. 742, 2018. Doi: 10.3390/ma11050742.

[3] N.T. Aboulkhair, M. Simonelli, L. Parry, I. Ashcroft, C. Tuck, R. Hague, 3D printing of Aluminium alloys: Additive Manufacturing of Aluminium alloys using selective laser melting, Progress in Materials Science, v. 106, p. 100578, 2019. Doi: 10.1016/j.pmatsci.2019.100578.

[4] T. DebRoy, H.L. Wei, J.S. Zuback, T. Mukherjee, J.W. Elmer, J.O. Milewski, A.M. Beese, A. Wilson-Heid, A. De, W. Zhang, Additive manufacturing of metallic components – Process, structure and properties, Progress in Materials Science, v. 92, p. 112–224, 2018. Doi: 10.1016/j.pmatsci.2017.10.001.

[5] T.D. Ngo, A. Kashani, G. Imbalzano, K.T.Q. Nguyen, D. Hui, Additive manufacturing (3D printing): A review of materials, methods, applications and challenges, Composites Part B: Engineering, v. 143, p. 172–196, 2018. Doi: 10.1016/j.compositesb.2018.02.012.

[6] D. Bergström, J. Powell, A.F.H. Kaplan, A ray-tracing analysis of the absorption of light by smooth and rough metal surfaces, Journal of Applied Physics, v. 101, p. 113504, 2007. Doi: 10.1063/1.2738417.

[7] L.J. Jallo, M. Schoenitz, E.L. Dreizin, R.N. Dave, C.E. Johnson, The effect of surface modification of aluminum powder on its flowability, combustion and reactivity, Powder Technology, v. 204, p. 63–70, 2010. Doi: 10.1016/j.powtec.2010.07.017.

[8] M. Mozetič, Surface Modification to Improve Properties of Materials, Materials, v. 12, p. 441, 2019. Doi: 10.3390/ma12030441.

[9] M. Xiao, Y.M. Chen, M.N. Biao, X.D. Zhang, B.C. Yang, Bio-functionalization of biomedical metals, Materials Science and Engineering: C, v. 70, p. 1057–1070, 2017. Doi: 10.1016/j.msec.2016.06.067.

[10] J.H. Martin, B.D. Yahata, J.M. Hundley, J.A. Mayer, T.A. Schaedler, T.M. Pollock, 3D printing of high-strength aluminium alloys, Nature 549 (2017) 365–369. Doi: 10.1038/nature23894.

[11] Y. Qi, H. Zhang, J. Zhu, X. Nie, Z. Hu, H. Zhu, X. Zeng, Mechanical behavior and microstructure evolution of Al-Cu-Mg alloy produced by laser powder bed fusion: Effect of heat treatment, Materials Characterization, v. 165, p. 110364, 2020. Doi: 10.1016/j.matchar.2020.110364.

[12] A.A. Tiamiyu, A.Y. Badmos, A.G. Odeshi, Effects of temper condition on high strain-rate deformation of AA 2017 aluminum alloy in compression, Materials & Design, v. 89, p. 872–883, 2016. Doi: 10.1016/j.matdes.2015.10.047.

[13] J.G. Kaufman, Introduction to Aluminum Alloys and Tempers, ASM International, Materials Park, 2000.

[14] T. DebRoy, T. Mukherjee, J.O. Milewski, J.W. Elmer, B. Ribic, J.J. Blecher, W. Zhang, Scientific, technological and economic issues in metal printing and their solutions, Nat. Mater., v. 18, p. 1026–1032, 2019. Doi: 10.1038/s41563-019-0408-2.

[15] M.K. Thompson, G. Moroni, T. Vaneker, G. Fadel, R.I. Campbell, I. Gibson, A. Bernard, J. Schulz, P. Graf, B. Ahuja, F. Martina, Design for Additive Manufacturing: Trends, opportunities, considerations, and constraints, CIRP Annals, v. 65, 737–760, 2016. Doi: 10.1016/j.cirp.2016.05.004.

[16] N. Harrison, P.E. McHugh, W. Curtin, P. Mc Donnell, Micromotion and friction evaluation of a novel surface architecture for improved primary fixation of cementless orthopaedic implants, Journal of the Mechanical Behavior of Biomedical Materials, v. 21, p. 37–46, 2013. Doi: 10.1016/j.jmbbm.2013.01.017.

[17] M. Seabra, J. Azevedo, A. Araújo, L. Reis, E. Pinto, N. Alves, R. Santos, J. Pedro Mortágua, Selective laser melting (SLM) and topology optimization

for lighter aerospace componentes, Procedia Structural Integrity, v. 1, p. 289–296, 2016. Doi: 10.1016/j.prostr.2016.02.039.

[18] D. Herzog, V. Seyda, E. Wycisk, C. Emmelmann, Additive manufacturing of metals, Acta Materialia, v. 117, p. 371–392, 2016. Doi: 10.1016/j.actamat.2016.07.019.

[19] L.E.T. Mathias, V.E. Pinotti, B.F. Batistão, N. Rojas-Arias, G. Figueira, A.F. Andreoli, P. Gargarella, Metal powder as feedstock for laser-based additive manufacturing: From production to powder modification, Journal of Materials Research, v. 39, p. 19–47, 2024. Doi: 10.1557/s43578-023-01271-8.

[20] W.J. Sames, F. Medina, W.H. Peter, S.S. Babu, R.R. Dehoff, Effect of Process Control and Powder Quality on Inconel 718 Produced Using Electron Beam Melting, in: E. Ott, A. Banik, J. Andersson, I. Dempster, T. Gabb, J. Groh, K. Heck, R. Helmink, X. Liu, A. Wusatowska-Sarnek (Eds.), 8th International Symposium on Superalloy 718 and Derivatives, 1st ed., Wiley, p. 409–423, 2014. Doi: 10.1002/9781119016854.ch32.

[21] A.J. Pinkerton, L. Li, Direct additive laser manufacturing using gas- and water-atomised H13 tool steel powders, Int J Adv Manuf Technol, v. 25, p. 471–479, 2005. Doi: 10.1007/s00170-003-1844-2.

[22] W.J. Sames, F.A. List, S. Pannala, R.R. Dehoff, S.S. Babu, The metallurgy and processing science of metal additive manufacturing, International Materials Reviews, v. 61, p. 315–360, 2016. Doi: 10.1080/09506608.2015.1116649.

[23] S. Lathabai, Additive Manufacturing of Aluminium-Based Alloys and Composites, in: Fundamentals of Aluminium Metallurgy, Woodhead, p. 47–92, 2018. Doi: 10.1016/B978-0-08-102063-0.00002-3.

[24] C.Y. Yap, C.K. Chua, Z.L. Dong, Z.H. Liu, D.Q. Zhang, L.E. Loh, S.L. Sing, Review of selective laser melting: Materials and applications, Applied Physics Reviews, v. 2, p. 041101, 2015. Doi: 10.1063/1.4935926.

[25] F. Calignano, D. Manfredi, E.P. Ambrosio, S. Biamino, M. Lombardi, E. Atzeni, A. Salmi, P. Minetola, L. Iuliano, P. Fino, Overview on Additive

Manufacturing Technologies, Proc. IEEE, v. 105, p. 593–612, 2017. Doi: 10.1109/JPROC.2016.2625098.

[26] N. Read, W. Wang, K. Essa, M.M. Attallah, Selective laser melting of AlSi10Mg alloy: Process optimisation and mechanical properties development, Materials & Design (1980-2015), v. 65, p. 417–424, 2015. Doi: 10.1016/j.matdes.2014.09.044.

[27] D. Gu, Y. Shen, Balling phenomena during direct laser sintering of multi-component Cu-based metal powder, Journal of Alloys and Compounds, v. 432, p. 163–166, 2007. Doi: 10.1016/j.jallcom.2006.06.011.

[28] X. Su, Y. Yang, Research on track overlapping during Selective Laser Melting of powders, Journal of Materials Processing Technology, v. 212, p, 2074–2079, 2012. Doi: 10.1016/j.jmatprotec.2012.05.012.

[29] H. Jia, H. Sun, H. Wang, Y. Wu, H. Wang, Scanning strategy in selective laser melting (SLM): a review, Int J Adv Manuf Technol, v. 113, p. 2413–2435, 2021. Doi: 10.1007/s00170-021-06810-3.

[30] W.C. Batalha, R.L. Batalha, K. Kosiba, C.S. Kiminami, P. Gargarella, Effect of scanning strategy on microstructure and mechanical properties of a biocompatible Ti–35Nb–7Zr–5Ta alloy processed by laser-powder bed fusion, Journal of Materials Research, v. 38, p. 154–164, 2023. Doi: 10.1557/s43578-022-00735-7.

[31] A.I. Mertens, J. Delahaye, J. Lecomte-Beckers, Fusion-Based Additive Manufacturing for Processing Aluminum Alloys: State-of-the-Art and Challenges, Adv Eng Mater, v. 19, p. 1700003, 2017. Doi: 10.1002/adem.201700003.

[32] L. Thijs, K. Kempen, J.-P. Kruth, J. Van Humbeeck, Fine-structured aluminium products with controllable texture by selective laser melting of pre-alloyed AlSi10Mg powder, Acta Materialia, v. 61, p. 1809–1819, 2013. Doi: 10.1016/j.actamat.2012.11.052.

[33] N.T. Aboulkhair, N.M. Everitt, I. Ashcroft, C. Tuck, Reducing porosity in AlSi10Mg parts processed by selective laser melting, Additive Manufacturing, v. 1–4, p. 77–86, 2014. Doi: 10.1016/j.addma.2014.08.001.

[34] C. Galy, E. Le Guen, E. Lacoste, C. Arvieu, Main defects observed in aluminum alloy parts produced by SLM: From causes to consequences, Additive Manufacturing, v. 22, p. 165–175, 2018. Doi: 10.1016/j.addma.2018.05.005.

[35] M. Arata, Yoshiaki Isamu, Some Fundamental Properties of High Power CO2 Laser Beam as a Heat Source.pdf, Transactions of the Japan Welding Society, v. 3, p. 1–20, 1974. Doi: 10.18910/3813.

[36] L. Quintino, R. Miranda, U. Dilthey, D. Iordachescu, M. Banasik, S. Stano, Laser Welding of Structural Aluminium, in: P.M.G.P. Moreira, L.F.M. Da Silva, P.M.S.T. De Castro (Eds.), Structural Connections for Lightweight Metallic Structures, Springer Berlin Heidelberg, Berlin, Heidelberg, pp. 33–57, 2010. Doi: 10.1007/8611_2010_46.

[37] T.S. Srivatsan, T.S. Sudarshan, (Eds.), Additive Manufacturing: Innovations, Advances, and Applications, 1st ed., CRC Press, 2015. Doi: 10.1201/b19360.

[38] N.T. Aboulkhair, N.M. Everitt, I. Maskery, I. Ashcroft, C. Tuck, Selective laser melting of aluminum alloys, MRS Bull., v. 42, p. 311–319, 2017. Doi: 10.1557/mrs.2017.63.

[39] S. Kou, Welding metallurgy, 2nd ed, Wiley-Interscience, Hoboken, N.J, 2003. Doi: 10.1002/0471434027.

[40] X. Liu, C. Zhao, X. Zhou, Z. Shen, W. Liu, Microstructure of selective laser melted AlSi10Mg alloy, Materials & Design, v. 168, p. 107677, 2019. Doi: 10.1016/j.matdes.2019.107677.

[41] S.-H. Sun, T. Ishimoto, K. Hagihara, Y. Tsutsumi, T. Hanawa, T. Nakano, Excellent mechanical and corrosion properties of austenitic stainless steel with a unique crystallographic lamellar microstructure via selective laser melting, Scripta Materialia, v. 159, p. 89–93, 2019. Doi: 10.1016/j.scriptamat.2018.09.017.

[42] M. Qu, Q. Guo, L.I. Escano, S.J. Clark, K. Fezzaa, L. Chen, Mitigating keyhole pore formation by nanoparticles during laser powder bed fusion additive manufacturing, Additive Manufacturing Letters, v. 3, p. 100068, 2022. Doi: 10.1016/j.addlet.2022.100068.

[43] M. Okayasu, K. Sato, M. Mizuno, A new etching technique for revealing the plastic deformation zone in an Al–Cu–Mg alloy, J Mater Sci, v. 43, p. 2792–2798, 2008. Doi: 10.1007/s10853-008-2544-y.

[44] E.L. Rooy, Introduction to Aluminum and Aluminum Alloys, in: ASM Handbook Committee (Ed.), Properties and Selection: Nonferrous Alloys and Special-Purpose Materials, ASM International, p. 3–14, 1990. Doi: 10.31399/asm.hb.v02.a0001057.

[45] P. Rambabu, N. Eswara Prasad, V.V. Kutumbarao, R.J.H. Wanhill, Aluminium Alloys for Aerospace Applications, in: N.E. Prasad, R.J.H. Wanhill (Eds.), Aerospace Materials and Material Technologies, Springer Singapore, Singapore, p. 29–52, 2017. Doi: 10.1007/978-981-10-2134-3_2.

[46] R.R. Ambriz, D. Jaramillo, Mechanical Behavior of Precipitation Hardened Aluminum Alloys Welds, in: W.A. Monteiro (Ed.), Light Metal Alloys Applications, InTech, 2014. Doi: 10.5772/58418.

[47] T. Gladman, Precipitation hardening in metals, Materials Science and Technology, v. 15, p. 30–36, 1999. Doi: 10.1179/026708399773002782.

[48] M. Zamani, S. Toschi, A. Morri, L. Ceschini, S. Seifeddine, Optimisation of heat treatment of Al–Cu–(Mg–Ag) cast alloys, J Therm Anal Calorim, v. 139, p. 3427–3440, 2020. Doi: 10.1007/s10973-019-08702-x.

[49] D. Sun, X. Sun, D.O. Northwood, J.H. Sokolowski, Thermoelectric power characterization of a 2024 aluminum alloy during solution treatment and aging, Materials Characterization, v. 36, p. 83–92, 1996. Doi: 10.1016/1044-5803(96)00002-2.

[50] D.A. Porter, K.E. Easterling, M.Y. Sherif, Phase Transformations in Metals and Alloys, 4th ed., CRC Press, Boca Raton, 2021. Doi: 10.1201/9781003011804.

[51] ASM Handbook Committee, ed., Properties of Wrought Aluminum and Aluminum Alloys, in: Properties and Selection: Nonferrous Alloys and Special-Purpose Materials, ASM International, p. 62–122, 1990. Doi: 10.31399/asm.hb.v02.a0001060.

[52] I.J. Polmear, Aluminium Alloys – A Century of Age Hardening, Materials Forum, v. 28, p. 1–14, 2004.

[53] ASTM International, ASTM E140-12b - Hardness Conversion Tables for Metals Relationship Among Brinell Hardness, Vickers Hardness, Rockwell Hardness, Superficial Hardness, Knoop Hardness, Scleroscope Hardness, and Leeb Hardness, ASTM International, 2019. 10.1520/E0140-12BR19E01.

[54] B. Ahuja, M. Karg, K.Yu. Nagulin, M. Schmidt, Fabrication and Characterization of High Strength Al-Cu Alloys Processed Using Laser Beam Melting in Metal Powder Bed, Physics Procedia, v. 56, p. 135–146, 2014. Doi: 10.1016/j.phpro.2014.08.156.

[55] M. Karg, B. Ahuja, S. Wiesenmayer, S. Kuryntsev, M. Schmidt, Effects of Process Conditions on the Mechanical Behavior of Aluminium Wrought Alloy EN AW-2219 (AlCu6Mn) Additively Manufactured by Laser Beam Melting in Powder Bed, Micromachines, v. 8, p. 23, 2017. Doi: 10.3390/mi8010023.

[56] R. Casati, J.N. Lemke, A.Z. Alarcon, M. Vedani, Aging Behavior of High-Strength Al Alloy 2618 Produced by Selective Laser Melting, Metall Mater Trans A, v. 48, p. 575–579, 2017. Doi: 10.1007/s11661-016-3883-y.

[57] D. Koutny, D. Palousek, L. Pantelejev, C. Hoeller, R. Pichler, L. Tesicky, J. Kaiser, Influence of Scanning Strategies on Processing of Aluminum Alloy EN AW 2618 Using Selective Laser Melting, Materials, v. 11, p. 298, 2018. Doi: 10.3390/ma11020298.

[58] H. Zhang, H. Zhu, T. Qi, Z. Hu, X. Zeng, Selective laser melting of high strength Al–Cu–Mg alloys: Processing, microstructure and mechanical properties, Materials Science and Engineering: A, v. 656, p. 47–54, 2016. Doi: 10.1016/j.msea.2015.12.101.

[59] H. Zhang, H. Zhu, X. Nie, J. Yin, Z. Hu, X. Zeng, Effect of Zirconium addition on crack, microstructure and mechanical behavior of selective laser melted Al-Cu-Mg alloy, Scripta Materialia, v. 134, p. 6–10, 2017. Doi: 10.1016/j.scriptamat.2017.02.036.

[60] P.K. Dos Santos Bomfim, B.F. Batistão, A.P.M. De Araújo, L.H. Pereira, R.H. Buzolin, S.T. Amancio-Filho, C.R.M. Afonso, C. Bolfarini, C.S. Kiminami, F.G. Coury, P. Gargarella, Influence of Al-5.0Nb-0.5B inoculant on the microstructure and mechanical properties of AA 2017 alloy fabricated using laser-based powder bed fusion, Journal of Alloys and Compounds, v. 1032, p. 180872, 2025. Doi: 10.1016/j.jallcom.2025.180872.

[61] D. Bergström, J. Powell, A.F.H. Kaplan, The absorption of light by rough metal surfaces—A three-dimensional ray-tracing analysis, Journal of Applied Physics, v. 103, p. 103515, 2008. Doi: 10.1063/1.2930808.

[62] W. Liu, L. Sun, Y. Luo, R. Wu, H. Jiang, Y. Chen, G. Zeng, Y. Liu, Facile transition from hydrophilicity to superhydrophilicity and superhydrophobicity on aluminum alloy surface by simple acid etching and polymer coating, Applied Surface Science, v. 280, p. 193–200, 2013. Doi: 10.1016/j.apsusc.2013.04.124.

[63] D.K. Sarkar, M. Farzaneh, R.W. Paynter, Superhydrophobic properties of ultrathin rf-sputtered Teflon films coated etched aluminum surfaces, Materials Letters, v. 62, p. 1226–1229, 2008. Doi: 10.1016/j.matlet.2007.08.051.

[64] R. Wu, S. Liang, A. Pan, Z. Yuan, Y. Tang, X. Tan, D. Guan, Y. Yu, Fabrication of nano-structured super-hydrophobic film on aluminum by controllable immersing method, Applied Surface Science, v. 258, p. 5933–5937, 2012. Doi: 10.1016/j.apsusc.2011.10.029.

[65] Y. Huang, D.K. Sarkar, X. Grant Chen, Superhydrophobic aluminum alloy surfaces prepared by chemical etching process and their corrosion resistance properties, Applied Surface Science, v. 356, p. 1012–1024, 2015. Doi: 10.1016/j.apsusc.2015.08.166.

[66] S.G. Prolongo, A. Ureña, Effect of surface pre-treatment on the adhesive strength of epoxy–aluminium joints, International Journal of Adhesion and Adhesives, v. 29, p. 23–31, 2009. Doi: 10.1016/j.ijadhadh.2008.01.001.

[67] N. Saleema, D.K. Sarkar, R.W. Paynter, D. Gallant, M. Eskandarian, A simple surface treatment and characterization of AA 6061 aluminum alloy

surface for adhesive bonding applications, Applied Surface Science, p. 261, p. 742–748, 2012. Doi: 10.1016/j.apsusc.2012.08.091.

[68] M. Kadlečková, A. Minařík, P. Smolka, A. Mráček, E. Wrzecionko, L. Novák, L. Musilová, R. Gajdošík, Preparation of Textured Surfaces on Aluminum-Alloy Substrates, Materials, v. 12, p. 109, 2018. Doi: 10.3390/ma12010109.

[69] F. Veron, F. Lanoue, V. Baco-Carles, K. Kiryukhina, O. Vendier, P. Tailhades, Selective laser powder bed fusion for manufacturing of 3D metal-ceramic multi-materials assemblies, Additive Manufacturing, v. 50, p. 102550, 2022. Doi: 10.1016/j.addma.2021.102550.

[70] F. Lanoue, F. Veron, I. Pasquet, K. Kiryukhina, V. Baco-Carles, O. Vendier, P. Tailhades, Treatment of AlSi12 feedstock with water to manufacture multi-material parts by laser powder bed fusion process: A potential route for the fabrication of inorganic 3D metamaterials, Journal of Materials Research and Technology, v. 27, p. 4772–4786, 2023. Doi: 10.1016/j.jmrt.2023.10.254.

[71] C. Gao, Z. Xiao, Z. Liu, Q. Zhu, W. Zhang, Selective laser melting of nano-TiN modified AlSi10Mg composite powder with low laser reflectivity, Materials Letters, v. 236, p. 362–365, 2019. Doi: 10.1016/j.matlet.2018.10.126.

[72] C. Gao, Z. Wang, Z. Xiao, D. You, K. Wong, A.H. Akbarzadeh, Selective laser melting of TiN nanoparticle-reinforced AlSi10Mg composite: Microstructural, interfacial, and mechanical properties, Journal of Materials Processing Technology, v. 281, p. 116618, 2020. Doi: 10.1016/j.jmatprotec.2020.116618.

[73] D. Gu, H. Wang, D. Dai, P. Yuan, W. Meiners, R. Poprawe, Rapid fabrication of Al-based bulk-form nanocomposites with novel reinforcement and enhanced performance by selective laser melting, Scripta Materialia, v. 96, p. 25–28, 2015. Doi: 10.1016/j.scriptamat.2014.10.011.

[74] T.-C. Lin, C. Cao, M. Sokoluk, L. Jiang, X. Wang, J.M. Schoenung, E.J. Lavernia, X. Li, Aluminum with dispersed nanoparticles by laser additive manufacturing, Nat Commun, v. 10, p. 4124, 2019. Doi: 10.1038/s41467-019-12047-2.

[75] S.Y. Zhou, Z.Y. Wang, Y. Su, H. Wang, G. Liu, T.T. Song, M. Yan, Effects of Micron/Submicron TiC on Additively Manufactured AlSi10Mg: A Comprehensive Study from Computer Simulation to Mechanical and Microstructural Analysis, JOM, v. 72, p. 3693–3704, 2020. Doi: 10.1007/s11837-019-03984-w.

[76] Y. Zhou, S. Wen, C. Wang, L. Duan, Q. Wei, Y. Shi, Effect of TiC content on the Al-15Si alloy processed by selective laser melting: Microstructure and mechanical properties, Optics & Laser Technology, v. 120, p. 105719, 2019. Doi: 10.1016/j.optlastec.2019.105719.

[77] X.P. Li, G. Ji, Z. Chen, A. Addad, Y. Wu, H.W. Wang, J. Vleugels, J. Van Humbeeck, J.P. Kruth, Selective laser melting of nano-TiB_2 decorated AlSi10Mg alloy with high fracture strength and ductility, Acta Materialia, v. 129, p. 183–193, 2017. Doi: 10.1016/j.actamat.2017.02.062.

[78] L. Xi, D. Gu, S. Guo, R. Wang, K. Ding, K.G. Prashanth, Grain refinement in laser manufactured Al-based composites with TiB_2 ceramic, Journal of Materials Research and Technology, v. 9, p. 2611–2622, 2020. Doi: 10.1016/j.jmrt.2020.04.059.

[79] Y.K. Xiao, Z.Y. Bian, Y. Wu, G. Ji, Y.Q. Li, M.J. Li, Q. Lian, Z. Chen, A. Addad, H.W. Wang, Effect of nano-TiB_2 particles on the anisotropy in an AlSi10Mg alloy processed by selective laser melting, Journal of Alloys and Compounds, v. 798, p. 644–655, 2019. Doi: 10.1016/j.jallcom.2019.05.279.

[80] Y. Li, D. Gu, H. Zhang, L. Xi, Effect of Trace Addition of Ceramic on Microstructure Development and Mechanical Properties of Selective Laser Melted AlSi10Mg Alloy, Chin. J. Mech. Eng., v. 33, p. 33, 2020. Doi: 10.1186/s10033-020-00448-0.

[81] F. Chang, D. Gu, D. Dai, P. Yuan, Selective laser melting of in-situ Al4SiC4 + SiC hybrid reinforced Al matrix composites: Influence of starting SiC particle size, Surface and Coatings Technology, v. 272, p. 15–24, 2015. Doi: 10.1016/j.surfcoat.2015.04.029.

[82] O.H. Famodimu, M. Stanford, C.F. Oduoza, L. Zhang, Effect of process parameters on the density and porosity of laser melted AlSi10Mg/SiC metal

matrix composite, Front. Mech. Eng., v. 13, p. 520–527, 2018. Doi: 10.1007/s11465-018-0521-y.

[83] M. Wang, B. Song, Q. Wei, Y. Shi, Improved mechanical properties of AlSi7Mg/nano-SiCp composites fabricated by selective laser melting, Journal of Alloys and Compounds, v. 810, p. 151926, 2019. Doi: 10.1016/j.jallcom.2019.151926.

[84] G. Xue, L. Ke, H. Zhu, H. Liao, J. Zhu, X. Zeng, Influence of processing parameters on selective laser melted SiCp/AlSi10Mg composites: Densification, microstructure and mechanical properties, Materials Science and Engineering: A, v. 764, p. 138155, 2019. Doi: 10.1016/j.msea.2019.138155.

[85] D. Dai, D. Gu, Influence of thermodynamics within molten pool on migration and distribution state of reinforcement during selective laser melting of AlN/AlSi10Mg composites, International Journal of Machine Tools and Manufacture, v. 100, p. 14–24, 2016. Doi: 10.1016/j.ijmachtools.2015.10.004.

[86] D. Dai, D. Gu, M. Xia, C. Ma, H. Chen, T. Zhao, C. Hong, A. Gasser, R. Poprawe, Melt spreading behavior, microstructure evolution and wear resistance of selective laser melting additive manufactured AlN/AlSi10Mg nanocomposite, Surface and Coatings Technology, v. 349, p. 279–288, 2018. Doi: 10.1016/j.surfcoat.2018.05.072.

[87] J.H. Martin, B.D. Yahata, E.C. Clough, J.A. Mayer, J.M. Hundley, T.A. Schaedler, Additive manufacturing of metal matrix composites via nanofunctionalization, MRS Communications, v. 8, p. 297–302, 2018. Doi: 10.1557/mrc.2018.95.

[88] G. Li, Y. Huang, X. Li, C. Guo, Q. Zhu, J. Lu, Laser powder bed fusion of nano-titania modified 2219 aluminium alloy with superior mechanical properties at both room and elevated temperatures: The significant impact of solute, Additive Manufacturing, v. 60, p. 103296, 2022. Doi: 10.1016/j.addma.2022.103296.

[89] R. Raj Mohan, R. Venkatraman, S. Raghuraman, Microstructure and Mechanical Properties of AlSi10Mg/NbC Composite Produced by Laser-

Based Powder Bed Fusion (L-PBF) Process, JOM, v. 75, p. 155–166, 2023. Doi: 10.1007/s11837-022-05428-4.

[90] P. Mair, V.S. Goettgens, T. Rainer, N. Weinberger, I. Letofsky-Papst, S. Mitsche, G. Leichtfried, Laser powder bed fusion of nano-CaB_6 decorated 2024 aluminum alloy, Journal of Alloys and Compounds, v. 863, p. 158714, 2021. Doi: 10.1016/j.jallcom.2021.158714.

[91] P. Mair, L. Kaserer, J. Braun, J. Stajkovic, C. Klein, D. Schimbäck, L. Perfler, E. Zhuravlev, O. Kessler, G. Leichtfried, Dependence of mechanical properties and microstructure on solidification onset temperature for Al2024–CaB_6 alloys processed using laser powder bed fusion, Materials Science and Engineering: A, v. 833, p. 142552, 2022. Doi: 10.1016/j.msea.2021.142552.

[92] N.K. Tolochko, Y.V. Khlopkov, S.E. Mozzharov, M.B. Ignatiev, T. Laoui, V.I. Titov, Absorptance of powder materials suitable for laser sintering, Rapid Prototyping Journal, v. 6, p. 155–161, 2000. Doi: 10.1108/13552540010337029.

[93] C. Chen, D. Gu, D. Dai, L. Du, R. Wang, C. Ma, M. Xia, Laser additive manufacturing of layered TiB_2/Ti6Al4V multi-material parts: Understanding thermal behavior evolution, Optics & Laser Technology, v. 119, p. 105666, 2019. Doi: 10.1016/j.optlastec.2019.105666.

[94] D. Gu, Y. Yang, L. Xi, J. Yang, M. Xia, Laser absorption behavior of randomly packed powder-bed during selective laser melting of SiC and TiB_2 reinforced Al matrix composites, Optics & Laser Technology, v. 119, p. 105600, 2019. Doi: 10.1016/j.optlastec.2019.105600.

[95] A. Rubenchik, S. Wu, S. Mitchell, I. Golosker, M. LeBlanc, N. Peterson, Direct measurements of temperature-dependent laser absorptivity of metal powders, Appl. Opt., v. 54, p. 7230, 2015. Doi: 10.1364/AO.54.007230.

[96] C.D. Boley, S.A. Khairallah, A.M. Rubenchik, Calculation of laser absorption by metal powders in additive manufacturing, Appl. Opt., v. 54, p. 2477, 2015. Doi: 10.1364/AO.54.002477.

[97] M.A. Balbaa, A. Ghasemi, E. Fereiduni, M.A. Elbestawi, S.D. Jadhav, J.-P. Kruth, Role of powder particle size on laser powder bed fusion

processability of AlSi10mg alloy, Additive Manufacturing, v. 37, p. 101630, 2021. Doi: 10.1016/j.addma.2020.101630.

[98] G. Xue, L. Ke, H. Liao, C. Chen, H. Zhu, Effect of SiC particle size on densification behavior and mechanical properties of SiCp/AlSi10Mg composites fabricated by laser powder bed fusion, Journal of Alloys and Compounds, v. 845, p. 156260, 2020. Doi: 10.1016/j.jallcom.2020.156260.

[99] S.D. Jadhav, S. Dadbakhsh, R. Chen, R. Shabadi, J.-P. Kruth, J. Van Humbeeck, K. Vanmeensel, Modification of Electrical and Mechanical Properties of Selective Laser-Melted CuCr0.3 Alloy Using Carbon Nanoparticles, Adv Eng Mater, v. 22, p. 1900946, 2020. Doi: 10.1002/adem.201900946.

[100] Z. Hu, F. Chen, J. Xu, Q. Nian, D. Lin, C. Chen, X. Zhu, Y. Chen, M. Zhang, 3D printing graphene-aluminum nanocomposites, Journal of Alloys and Compounds, v. 746, p. 269–276, 2018. Doi: 10.1016/j.jallcom.2018.02.272.

[101] Z. Zhao, P. Bai, R.D.K. Misra, M. Dong, R. Guan, Y. Li, J. Zhang, L. Tan, J. Gao, T. Ding, W. Du, Z. Guo, AlSi10Mg alloy nanocomposites reinforced with aluminum-coated graphene: Selective laser melting, interfacial microstructure and property analysis, Journal of Alloys and Compounds, v. 792, p. 203–214, 2019. Doi: 10.1016/j.jallcom.2019.04.007.

[102] D. Gu, X. Rao, D. Dai, C. Ma, L. Xi, K. Lin, Laser additive manufacturing of carbon nanotubes (CNTs) reinforced aluminum matrix nanocomposites: Processing optimization, microstructure evolution and mechanical properties, Additive Manufacturing, v. 29, p. 100801, 2019. Doi: 10.1016/j.addma.2019.100801.

[103] L.Y. Jiang, T.T. Liu, C.D. Zhang, K. Zhang, M.C. Li, T. Ma, W.H. Liao, Preparation and mechanical properties of CNTs-AlSi10Mg composite fabricated via selective laser melting, Materials Science and Engineering: A, v. 734, p. 171–177, 2018. Doi: 10.1016/j.msea.2018.07.092.

[104] X. Liu, Y. Liu, Z. Zhou, W. Luo, Z. Zeng, Enhanced printability and strength of unweldable AA2024-based nanocomposites fabricated by laser powder bed fusion via nano-TiC-induced grain refinement, Materials Science and

Engineering: A, v. 856, p. 144010, 2022. Doi: 10.1016/j.msea.2022.144010.

[105] Z. Fan, X. Yan, Z. Fu, B. Niu, J. Chen, Y. Hu, C. Chang, J. Yi, In situ formation of D022-Al_3Ti during selective laser melting of nano-TiC/AlSi10Mg alloy prepared by electrostatic self-assembly, Vacuum, v. 188, p. 110179, 2021. Doi: 10.1016/j.vacuum.2021.110179.

[106] Z. Fan, C. Li, H. Yang, Z. Liu, Effects of TiC nanoparticle inoculation on the hot-tearing cracks and grain refinement of additively-manufactured AA2024 Al alloys, Journal of Materials Research and Technology, v. 19, p. 194–207, 2022. Doi: 10.1016/j.jmrt.2022.05.039.

[107] L. Xi, P. Wang, K.G. Prashanth, H. Li, H.V. Prykhodko, S. Scudino, I. Kaban, Effect of TiB_2 particles on microstructure and crystallographic texture of Al-12Si fabricated by selective laser melting, Journal of Alloys and Compounds, v. 786, p. 551–556, 2019. Doi: 10.1016/j.jallcom.2019.01.327.

[108] Q. Tan, J. Zhang, N. Mo, Z. Fan, Y. Yin, M. Bermingham, Y. Liu, H. Huang, M.-X. Zhang, A novel method to 3D-print fine-grained AlSi10Mg alloy with isotropic properties via inoculation with LaB_6 nanoparticles, Additive Manufacturing, v. 32, p. 101034, 2020. Doi: 10.1016/j.addma.2019.101034.

[109] Q. Tan, Y. Yin, Z. Fan, J. Zhang, Y. Liu, M.-X. Zhang, Uncovering the roles of LaB6-nanoparticle inoculant in the AlSi10Mg alloy fabricated via selective laser melting, Materials Science and Engineering: A, v. 800, p. 140365, 2021. Doi: 10.1016/j.msea.2020.140365.

[110] D. Gu, H. Wang, D. Dai, F. Chang, W. Meiners, Y.-C. Hagedorn, K. Wissenbach, I. Kelbassa, R. Poprawe, Densification behavior, microstructure evolution, and wear property of TiC nanoparticle reinforced AlSi10Mg bulk-form nanocomposites prepared by selective laser melting, Journal of Laser Applications, v. 27, p. S17003, 2015. Doi: 10.2351/1.4870877.

[111] A. Albiter, A. Contreras, E. Bedolla, R. Perez, Structural and chemical characterization of precipitates in Al-2024/TiC composites, Composites

Part A: Applied Science and Manufacturing, v. 34, p. 17–24, 2003. Doi: 10.1016/S1359-835X(02)00259-2.

[112] E. Gärtner, H.Y. Jung, N.J. Peter, G. Dehm, E.A. Jägle, V. Uhlenwinkel, L. Mädler, Reducing cohesion of metal powders for additive manufacturing by nanoparticle dry-coating, Powder Technology, v. 379, p. 585–595, 2021. Doi: 10.1016/j.powtec.2020.10.065.

[113] L. Xi, D. Gu, K. Lin, S. Guo, Y. Liu, Y. Li, M. Guo, Effect of ceramic particle size on densification behavior, microstructure formation, and performance of TiB_2 -reinforced Al-based composites prepared by selective laser melting, J. Mater. Res., v. 35, p. 559–570, 2020. Doi: 10.1557/jmr.2019.392.

[114] R. Chen, H. Yin, I.S. Cole, S. Shen, X. Zhou, Y. Wang, S. Tang, Exposure, assessment and health hazards of particulate matter in metal additive manufacturing: A review, Chemosphere, v. 259, p. 127452, 2020. Doi: 10.1016/j.chemosphere.2020.127452.

[115] P. Oberbek, P. Kozikowski, K. Czarnecka, P. Sobiech, S. Jakubiak, T. Jankowski, Inhalation exposure to various nanoparticles in work environment—contextual information and results of measurements, J Nanopart Res, v. 21, p. 222, 2019. Doi: 10.1007/s11051-019-4651-x.

[116] M. Sousa, P. Arezes, F. Silva, Occupational Exposure to Ultrafine Particles in Metal Additive Manufacturing: A Qualitative and Quantitative Risk Assessment, IJERPH, v. 18, p. 9788, 2021. Doi: 10.3390/ijerph18189788.

[117] P. Wang, C. Gammer, F. Brenne, T. Niendorf, J. Eckert, S. Scudino, A heat treatable TiB2/Al-3.5Cu-1.5Mg-1Si composite fabricated by selective laser melting: Microstructure, heat treatment and mechanical properties, Composites Part B: Engineering, v. 147, p. 162–168, 2018. Doi: 10.1016/j.compositesb.2018.04.026.

[118] L.X. Xi, H. Zhang, P. Wang, H.C. Li, K.G. Prashanth, K.J. Lin, I. Kaban, D.D. Gu, Comparative investigation of microstructure, mechanical properties and strengthening mechanisms of Al-12Si/TiB_2 fabricated by selective laser melting and hot pressing, Ceramics International, v. 44, p. 17635–17642, 2018. Doi: 10.1016/j.ceramint.2018.06.225.

[119] ASTM International, ASTM E1251-25 - Standard Test Method for Analysis of Aluminum and Aluminum Alloys by Spark Atomic Emission Spectrometry, ASTM International, 2025. 10.1520/E1251-25.

[120] ASTM International, ASTM B211/B211M-23 - Specification for Aluminum and Aluminum-Alloy Rolled or Cold Finished Bar, Rod, and Wire, ASTM International, 2023. 10.1520/B0211_B0211M-19.

[121] L. Minkowitz, R.H. Buzolin, S. Arneitz, S.T. Amancio-Filho, Microstructure, tensile strength, and hardness of AA5024 modified with ZrH_4 additions produced by laser powder bed fusion, Materials Characterization, v. 212, p. 113963, 2024. Doi: 10.1016/j.matchar.2024.113963.

[122] ASTM International, ASTM B822-20 - Standard Test Method for Particle Size Distribution of Metal Powders and Related Compounds by Light Scattering, ASTM International, 2020. 10.1520/B0822-20.

[123] ASTM International, ASTM B923-22 - Standard Test Method for Metal Powder Skeletal Density by Helium or Nitrogen Pycnometry, ASTM International, 2022. 10.1520/B0923-22.

[124] ASTM International, ASTM D7891-24 - Standard Test Method for Shear Testing of Powders Using the Freeman Technology FT4 Powder Rheometer Shear Cell, ASTM International, 2024. 10.1520/D7891-24.

[125] D. Langlais, V. Demers, V. Brailovski, Rheology of dry powders and metal injection molding feedstocks formulated on their base, Powder Technology, v. 396, p. 13–26, 2022. Doi: 10.1016/j.powtec.2021.10.039.

[126] ASTM International, ASTM B964-23 - Standard Test Methods for Flow Rate of Metal Powders Using the Carney Funnel, ASTM International, 2023. 10.1520/B0964-23.

[127] N. Rojas-Arias, F.G. Coury, S.T. Amancio-Filho, P. Gargarella, A novel approach for tailoring aluminum alloys for additive manufacturing, Materials Science and Engineering: A, v. 931, p. 148179, 2025. Doi: 10.1016/j.msea.2025.148179.

[128] L. Minkowitz, S. Arneitz, P.S. Effertz, S.T. Amancio-Filho, Laser-powder bed fusion process optimisation of AlSi10Mg using extra trees regression,

Materials & Design, v. 227, p. 111718, 2023. Doi: 10.1016/j.matdes.2023.111718.

[129] Q. Tan, Y. Liu, Z. Fan, J. Zhang, Y. Yin, M.-X. Zhang, Effect of processing parameters on the densification of an additively manufactured 2024 Al alloy, Journal of Materials Science & Technology, v. 58, p. 34–45, 2020. Doi: 10.1016/j.jmst.2020.03.070.

[130] J. Deng, C. Chen, W. Zhang, Y. Li, R. Li, K. Zhou, Densification, Microstructure, and Mechanical Properties of Additively Manufactured 2124 Al–Cu Alloy by Selective Laser Melting, Materials, v. 13, p. 4423, 2020. Doi: 10.3390/ma13194423.

[131] G. Del Guercio, D.G. McCartney, N.T. Aboulkhair, S. Robertson, R. Maclachlan, C. Tuck, M. Simonelli, Cracking behaviour of high-strength AA2024 aluminium alloy produced by Laser Powder Bed Fusion, Additive Manufacturing, v. 54, p. 102776, 2022. Doi: 10.1016/j.addma.2022.102776.

[132] X. Liu, Y. Liu, Z. Zhou, H. Zhong, Q. Zhan, A combination strategy for additive manufacturing of AA2024 high-strength aluminium alloys fabricated by laser powder bed fusion: Role of hot isostatic pressing, Materials Science and Engineering: A, v. 850, p. 143597, 2022. Doi: 10.1016/j.msea.2022.143597.

[133] S. Yao, J. Wang, M. Li, Z. Chen, B. Lu, S. Shen, Y. Li, LPBF-Formed 2024Al Alloys: Process, Microstructure, Properties, and Thermal Cracking Behavior, Metals, v. 13, p. 268, 2023. Doi: 10.3390/met13020268.

[134] Z. Hu, X. Nie, Y. Qi, H. Zhang, H. Zhu, Cracking criterion for high strength Al–Cu alloys fabricated by selective laser melting, Additive Manufacturing, v. 37, p. 101709, 2021. Doi: 10.1016/j.addma.2020.101709.

[135] J. Elambasseril, M.J. Benoit, S. Zhu, M.A. Easton, E. Lui, C.A. Brice, M. Qian, M. Brandt, Effect of process parameters and grain refinement on hot tearing susceptibility of high strength aluminum alloy 2139 in laser powder bed fusion, Prog Addit Manuf, v. 7, p. 887–901, 2022. Doi: 10.1007/s40964-021-00259-2.

[136] P. Wang, C. Gammer, F. Brenne, K.G. Prashanth, R.G. Mendes, M.H. Rümmeli, T. Gemming, J. Eckert, S. Scudino, Microstructure and

mechanical properties of a heat-treatable Al-3.5Cu-1.5Mg-1Si alloy produced by selective laser melting, Materials Science and Engineering: A, v. 711, p. 562–570, 2018. Doi: 10.1016/j.msea.2017.11.063.

[137] D.C. Montgomery, ed., Design and analysis of experiments, 8th edition, John Wiley & Sons, Inc, Hoboken, NJ, 2013.

[138] B.J. Martins Freitas, G. Yuuki Koga, S. Arneitz, C. Bolfarini, S. De Traglia Amancio-Filho, Optimizing LPBF-parameters by Box-Behnken design for printing crack-free and dense high-boron alloyed stainless steel parts, Additive Manufacturing Letters, v. 9, p. 100206, 2024. Doi: 10.1016/j.addlet.2024.100206.

[139] A.P. Oliveira, G. Figueira, R.T. Coelho, C. Bolfarini, P. Gargarella, Application of the Box-Behnken Design in the Optimization of Laser Powder Bed Fusion of H13 Tool Steel, Mat. Res., v. 26, p. e20230250, 2023. Doi: 10.1590/1980-5373-mr-2023-0250.

[140] X. Liu, Y. Liu, Z. Zhou, K. Wang, Q. Zhan, X. Xiao, Grain refinement and crack inhibition of selective laser melted AA2024 aluminum alloy via inoculation with TiC–TiH_2, Materials Science and Engineering: A, v. 813, p. 141171, 2021. Doi: 10.1016/j.msea.2021.141171.

[141] C.A. Schneider, W.S. Rasband, K.W. Eliceiri, NIH Image to ImageJ: 25 years of image analysis, Nat Methods, v. 9, p. 671–675, 2012. Doi: 10.1038/nmeth.2089.

[142] ASTM International, ASTM E9-19 - Standard Test Methods of Compression Testing of Metallic Materials at Room Temperature, ASTM International, 2019. 10.1520/E0009-19R25E01.

[143] ASTM International, ASTM E8/E8M-25 - Test Methods for Tension Testing of Metallic Materials, ASTM International, 2025. 10.1520/E0008_E0008M-25.

[144] J.H. Tan, W.L.E. Wong, K.W. Dalgarno, An overview of powder granulometry on feedstock and part performance in the selective laser melting process, Additive Manufacturing 18 (2017) 228–255. Doi: 10.1016/j.addma.2017.10.011.

[145] S.E. Brika, M. Letenneur, C.A. Dion, V. Brailovski, Influence of particle morphology and size distribution on the powder flowability and laser powder bed fusion manufacturability of Ti-6Al-4V alloy, Additive Manufacturing, v. 31, p. 100929, 2020. Doi: 10.1016/j.addma.2019.100929.

[146] A.B. Spierings, N. Herres, G. Levy, Influence of the particle size distribution on surface quality and mechanical properties in AM steel parts, Rapid Prototyping Journal, v. 17, p. 195–202, 2011. Doi: 10.1108/13552541111124770.

[147] J. Visser, Van der Waals and other cohesive forces affecting powder fluidization, Powder Technology, v. 58, p. 1–10, 1989. Doi: 10.1016/0032-5910(89)80001-4.

[148] Y.I. Matvienko, A.D. Rud, N.D. Rud, O.M. Fesenko, A.D. Yaremkevich, V.V. Trachevski, Effect of copper concentration on the structure of intermetallics and graphite additives of Al–Cu/C powder composites, Appl Nanosci, v. 12, p. 1245–1255, 2022. Doi: 10.1007/s13204-021-01785-9.

[149] Y. Kim, D. Jeong, K.H. Park, J.-H. Yu, S. Jung, Efficient Adsorption on Benzoyl and Stearoyl Cellulose to Remove Phenanthrene and Pyrene from Aqueous Solution, Polymers, v. 10, p. 1042, 2018. Doi: 10.3390/polym10091042.

[150] A.S. Shinkaryov, D.Y. Ozherelkov, I.A. Pelevin, S.A. Eremin, V.N. Anikin, M.A. Burmistrov, S.V. Chernyshikhin, A.A. Gromov, A.Y. Nalivaiko, Laser Fusion of Aluminum Powder Coated with Diamond Particles via Selective Laser Melting: Powder Preparation and Synthesis Description, Coatings, v. 11, p. 1219, 2021. Doi: 10.3390/coatings11101219.

[151] V. Ranieri, D. Bourgogne, S. Darracq, M. Cambon, J. Haines, O. Cambon, R. Leparc, C. Levelut, A. Largeteau, G. Demazeau, Raman scattering study of α -quartz and $Si_{1-x}Ge_xO_2$ solid solutions, Phys. Rev. B, v. 79, p. 224304, 2009. Doi: 10.1103/PhysRevB.79.224304.

[152] D.D.N. Singh, R.S. Chaudhary, C.V. Agarwal, Corrosion Characteristics of Some Aluminum Alloys in Nitric Acid, J. Electrochem. Soc., v. 129, p. 1869–1874, 1982. Doi: 10.1149/1.2124317.

[153] J. Turnbull, R. Szukalo, D. Zagidulin, D. Shoesmith, Nitrite effects on copper corrosion in nitric acid solutions, Corrosion Science, v. 179, p. 109147, 2021. Doi: 10.1016/j.corsci.2020.109147.

[154] A.M. Rubenchik, S.S.Q. Wu, V.K. Kanz, M.M. LeBlanc, W.H. Lowdermilk, M.D. Rotter, J.R. Stanley, Temperature-dependent 780-nm laser absorption by engineering grade aluminum, titanium, and steel alloy surfaces, Opt. Eng, v. 53, p. 122506, 2014. Doi: 10.1117/1.OE.53.12.122506.

[155] F. Chu, K. Zhang, H. Shen, M. Liu, W. Huang, X. Zhang, E. Liang, Z. Zhou, L. Lei, J. Hou, A. Huang, Influence of satellite and agglomeration of powder on the processability of AlSi10Mg powder in Laser Powder Bed Fusion, Journal of Materials Research and Technology, v. 11, p. 2059–2073, 2021. Doi: 10.1016/j.jmrt.2021.02.015.

[156] G. Forte, P.J. Clark, Z. Yan, E.H. Stitt, M. Marigo, Using a Freeman FT4 rheometer and Electrical Capacitance Tomography to assess powder blending, Powder Technology, v. 337, p. 25–35, 2018. Doi: 10.1016/j.powtec.2017.12.020.

[157] J. Zegzulka, D. Gelnar, L. Jezerska, R. Prokes, J. Rozbroj, Characterization and flowability methods for metal powders, Sci Rep, v. 10, p. 21004, 2020. Doi: 10.1038/s41598-020-77974-3.

[158] S. Touzé, M. Rauch, J.-Y. Hascoët, Flowability characterization and enhancement of aluminium powders for additive manufacturing, Additive Manufacturing, v. 36, p. 101462, 2020. Doi: 10.1016/j.addma.2020.101462.

[159] Y. Chen, L. Jallo, M.A.S. Quintanilla, R. Dave, Characterization of particle and bulk level cohesion reduction of surface modified fine aluminum powders, Colloids and Surfaces A: Physicochemical and Engineering Aspects, v. 361, p. 66–80, 2010. Doi: 10.1016/j.colsurfa.2010.03.015.

[160] Y. Chen, J. Yang, R.N. Dave, R. Pfeffer, Fluidization of coated group C powders, AIChE Journal, v. 54, p. 104–121, 2008. Doi: 10.1002/aic.11368.

[161] B.F. Batistão, V.E. Pinotti, M.L.D. Lima, A.D.G. Rodrigues, S.D.T. Amancio-Filho, P. Gargarella, Wet chemical surface functionalization of AA2017

powders for additive manufacturing, Powder Technology, v. 443, p. 119938, 2024. Doi: 10.1016/j.powtec.2024.119938.

[162] M.S. Kenevisi, Y. Yu, F. Lin, A review on additive manufacturing of Al–Cu (2xxx) aluminium alloys, processes and defects, Materials Science and Technology, v. 37, p. 805–829, 2021. Doi: 10.1080/02670836.2021.1958487.

[163] G. Li, E. Brodu, J. Soete, H. Wei, T. Liu, T. Yang, W. Liao, K. Vanmeensel, Exploiting the rapid solidification potential of laser powder bed fusion in high strength and crack-free Al-Cu-Mg-Mn-Zr alloys, Additive Manufacturing, v. 47, p. 102210, 2021. Doi: 10.1016/j.addma.2021.102210.

[164] X. Nie, H. Zhang, H. Zhu, Z. Hu, L. Ke, X. Zeng, Effect of Zr content on formability, microstructure and mechanical properties of selective laser melted Zr modified Al-4.24Cu-1.97Mg-0.56Mn alloys, Journal of Alloys and Compounds, v. 764, p. 977–986, 2018. Doi: 10.1016/j.jallcom.2018.06.032.

[165] D. Gu, Y.-C. Hagedorn, W. Meiners, G. Meng, R.J.S. Batista, K. Wissenbach, R. Poprawe, Densification behavior, microstructure evolution, and wear performance of selective laser melting processed commercially pure titanium, Acta Materialia, v. 60, p. 3849–3860, 2012. Doi: 10.1016/j.actamat.2012.04.006.

[166] R. Palanivel, P. Koshy Mathews, Prediction and optimization of process parameter of friction stir welded AA5083-H111 aluminum alloy using response surface methodology, J. Cent. South Univ. Technol., v. 19, p. 1–8, 2012. Doi: 10.1007/s11771-012-0964-y.

[167] J.D. Kechagias, N. Vidakis, Parametric optimization of material extrusion 3D printing process: an assessment of Box-Behnken vs. full-factorial experimental approach, Int J Adv Manuf Technol, v. 121, p. 3163–3172, 2022. Doi: 10.1007/s00170-022-09532-2.

[168] W.E. King, H.D. Barth, V.M. Castillo, G.F. Gallegos, J.W. Gibbs, D.E. Hahn, C. Kamath, A.M. Rubenchik, Observation of keyhole-mode laser melting in laser powder-bed fusion additive manufacturing, Journal of Materials Processing Technology, v. 214, p. 2915–2925, 2014. Doi: 10.1016/j.jmatprotec.2014.06.005.

[169] N. Nudelis, P. Mayr, A Novel Classification Method for Pores in Laser Powder Bed Fusion, Metals, v. 11, p. 1912, 2021. Doi: 10.3390/met11121912.

[170] N. Nudelis, P. Mayr, Defect-based analysis of the laser powder bed fusion process using X-ray data, Int J Adv Manuf Technol, v. 123, p. 3223–3232, 2022. Doi: 10.1007/s00170-022-10407-9.

[171] D. Gu, D. Dai, Role of melt behavior in modifying oxidation distribution using an interface incorporated model in selective laser melting of aluminum-based material, Journal of Applied Physics, v. 120, p. 083104, 2016. Doi: 10.1063/1.4961410.

[172] E. Louvis, P. Fox, C.J. Sutcliffe, Selective laser melting of aluminium components, Journal of Materials Processing Technology, v. 211, p. 275–284, 2011. Doi: 10.1016/j.jmatprotec.2010.09.019.

[173] P.V. Cobbinah, S. Matsunaga, Y. Yamabe-Mitarai, Controlled Crystallographic Texture Orientation in Structural Materials Using the Laser Powder Bed Fusion Process—A Review, Adv Eng Mater, v. 25, p. 2300819, 2023. Doi: 10.1002/adem.202300819.

[174] Y. Lu, H. Zhang, P. Xue, L. Wu, F. Liu, L. Jia, D. Ni, B. Xiao, Z. Ma, Microstructural Evaluation and Tensile Properties of Al-Mg-Sc-Zr Alloys Prepared by LPBF, Crystals, v. 13, p. 913, 2023. Doi: 10.3390/cryst13060913.

[175] Y. Li, D. Gu, Parametric analysis of thermal behavior during selective laser melting additive manufacturing of aluminum alloy powder, Materials & Design, v. 63, p. 856–867, 2014. Doi: 10.1016/j.matdes.2014.07.006.

[176] J. Zhang, J. Gao, B. Song, L. Zhang, C. Han, C. Cai, K. Zhou, Y. Shi, A novel crack-free Ti-modified Al-Cu-Mg alloy designed for selective laser melting, Additive Manufacturing, v. 38, p. 101829, 2021. Doi: 10.1016/j.addma.2020.101829.

[177] Y. Wang, X. Lin, N. Kang, Z. Wang, Q. Wang, Y. Liu, W. Huang, Laser powder bed fusion of Zr-modified Al–Cu–Mg alloy: Crack-inhibiting, grain refinement, and mechanical properties, Materials Science and Engineering: A, v. 838, p. 142618, 2022. Doi: 10.1016/j.msea.2022.142618.

[178] P. Mair, J. Braun, L. Kaserer, L. March, D. Schimbäck, I. Letofsky-Papst, G. Leichtfried, Unique microstructure evolution of a novel Ti-modified Al-Cu alloy processed using laser powder bed fusion, Materials Today Communications, v. 31, p. 103353, 2022. Doi: 10.1016/j.mtcomm.2022.103353.

[179] D. Gu, H. Wang, F. Chang, D. Dai, P. Yuan, Y.-C. Hagedorn, W. Meiners, Selective Laser Melting Additive Manufacturing of TiC/AlSi10Mg Bulk-form Nanocomposites with Tailored Microstructures and Properties, Physics Procedia, v. 56, p. 108–116, 2014. Doi: 10.1016/j.phpro.2014.08.153.

[180] P. Yuan, D. Gu, Molten pool behaviour and its physical mechanism during selective laser melting of TiC/AlSi10Mg nanocomposites: simulation and experiments, J. Phys. D: Appl. Phys., v. 48, p. 035303, 2015. Doi: 10.1088/0022-3727/48/3/035303.

[181] D. Gu, H. Wang, D. Dai, Laser Additive Manufacturing of Novel Aluminum Based Nanocomposite Parts: Tailored Forming of Multiple Materials, Journal of Manufacturing Science and Engineering, v. 138, p. 021004, 2016. Doi: 10.1115/1.4030376.

[182] P. Yuan, D. Gu, D. Dai, Particulate migration behavior and its mechanism during selective laser melting of TiC reinforced Al matrix nanocomposites, Materials & Design, v. 82, p. 46–55, 2015. Doi: 10.1016/j.matdes.2015.05.041.

[183] Q. Tan, J. Zhang, Q. Sun, Z. Fan, G. Li, Y. Yin, Y. Liu, M.-X. Zhang, Inoculation treatment of an additively manufactured 2024 aluminium alloy with titanium nanoparticles, Acta Materialia, v. 196, p. 1–16, 2020. Doi: 10.1016/j.actamat.2020.06.026.

[184] T. Sun, H. Wang, Z. Gao, Y. Wu, M. Wang, X. Jin, C.L. Alex Leung, P.D. Lee, Y. Fu, H. Wang, The role of *in-situ* nano-TiB_2 particles in improving the printability of noncastable 2024Al alloy, Materials Research Letters, v. 10, p. 656–665, 2022. Doi: 10.1080/21663831.2022.2080514.

[185] R. Balokhonov, A. Zemlianov, D. Gatiyatullina, V. Romanova, Computational Analysis of the Influence of Residual Stress on the Strength

of Composites with Different Aluminum Matrices and Carbide Particles, Metals, v. 13, p. 724, 2023. Doi: 10.3390/met13040724.

[186] V. Luzin, P. Spiridonov, K. Spencer, T. Gnaupel-Herold, Neutron Diffraction Study of Macrostress and Microstress in Al-Al_2O_3-Based Corrosion Protection Coating Obtained by Cold Spray (Dynamic Metallization), J Therm Spray Tech, v. 29, p. 1437–1454, 2020. Doi: 10.1007/s11666-020-01077-8.

[187] P. Mair, L. Kaserer, J. Braun, N. Weinberger, I. Letofsky-Papst, G. Leichtfried, Microstructure and mechanical properties of a TiB_2-modified Al–Cu alloy processed by laser powder-bed fusion, Materials Science and Engineering: A, v. 799, p. 140209, 2021. Doi: 10.1016/j.msea.2020.140209.

[188] B.L. Bramfitt, The effect of carbide and nitride additions on the heterogeneous nucleation behavior of liquid iron, METALLURGICAL TRANSACTIONS, v.1, p. 1987-1995, 1970. Doi: 10.1007/BF02642799.

[189] J. Bi, Z. Lei, Y. Chen, X. Chen, Z. Tian, J. Liang, X. Qin, X. Zhang, Densification, microstructure and mechanical properties of an Al-14.1Mg-0.47Si-0.31Sc-0.17Zr alloy printed by selective laser melting, Materials Science and Engineering: A, v. 774, p. 138931, 2020. Doi: 10.1016/j.msea.2020.138931.

[190] P. Köhnen, M. Létang, M. Voshage, J.H. Schleifenbaum, C. Haase, Understanding the process-microstructure correlations for tailoring the mechanical properties of L-PBF produced austenitic advanced high strength steel, Additive Manufacturing, v. 30, p. 100914, 2019. Doi: 10.1016/j.addma.2019.100914.

[191] M. Zhang, P. Kelly, M. Easton, J. Taylor, Crystallographic study of grain refinement in aluminum alloys using the edge-to-edge matching model, Acta Materialia, v. 53, p. 1427–1438, 2005. Doi: 10.1016/j.actamat.2004.11.037.

[192] D. Dai, D. Gu, Tailoring surface quality through mass and momentum transfer modeling using a volume of fluid method in selective laser melting of TiC/AlSi10Mg powder, International Journal of Machine Tools and

Manufacture, v. 88, p. 95–107, 2015. Doi: 10.1016/j.ijmachtools.2014.09.010.

[193] A. Banerji, W. Reif, Development of Al-Ti-C grain refiners containing TiC, Metall Trans A, v. 17, p. 2127–2137, 1986. Doi: 10.1007/BF02645911.

[194] Q. Tan, Y. Yin, A. Prasad, G. Li, Q. Zhu, D.H. StJohn, M.-X. Zhang, Demonstrating the roles of solute and nucleant in grain refinement of additively manufactured aluminium alloys, Additive Manufacturing, v. 49, p. 102516, 2022. Doi: 10.1016/j.addma.2021.102516.

[195] M. Easton, D. StJohn, Grain refinement of aluminum alloys: Part I. the nucleant and solute paradigms—a review of the literature, Metall Mater Trans A, v. 30, p. 1613–1623, 1999. Doi: 10.1007/s11661-999-0098-5.

[196] A. Majumdar, B.C. Muddle, Microstructure in rapidly solidified Al-Ti alloys, Materials Science and Engineering: A 169 (1993) 135–147. Doi: 10.1016/0921-5093(93)90608-H.

[197] J.-Y. Park, I.-H. Kim, A.T. Motta, C.J. Ulmer, M.A. Kirk, E.A. Ryan, P.M. Baldo, Irradiation-induced disordering and amorphization of Al_3Ti-based intermetallic compounds, Journal of Nuclear Materials, v. 467, p. 601–606, 2015. Doi: 10.1016/j.jnucmat.2015.10.025.

[198] A.L. Greer, A.M. Bunn, A. Tronche, P.V. Evans, D.J. Bristow, Modelling of inoculation of metallic melts: application to grain refinement of aluminium by Al–Ti–B, Acta Materialia, v. 48, p. 2823–2835, 2000. Doi: 10.1016/S1359-6454(00)00094-X.

[199] A.L. Greer, P.S. Cooper, M.W. Meredith, W. Schneider, P. Schumacher, J.A. Spittle, A. Tronche, Grain Refinement of Aluminium Alloys by Inoculation, Adv Eng Mater, v. 5, p. 81–91, 2003. Doi: 10.1002/adem.200390013.

[200] D.C. Van Aken, P.E. Krajewski, G.M. Vyletel, J.E. Allison, J.W. Jones, Recrystallization and grain growth phenomena in a particle-reinforced aluminum composite, Metall Mater Trans A, v. 26, p. 1395–1405, 1995. Doi: 10.1007/BF02647590.

[201] J.T. Oliveira De Menezes, E.M. Castrodeza, R. Casati, Effect of build orientation on fracture and tensile behavior of A357 Al alloy processed by

Selective Laser Melting, Materials Science and Engineering: A, v. 766, p. 138392, 2019. Doi: 10.1016/j.msea.2019.138392.

[202] A. Hadadzadeh, B.S. Amirkhiz, J. Li, M. Mohammadi, Columnar to equiaxed transition during direct metal laser sintering of AlSi10Mg alloy: Effect of building direction, Additive Manufacturing, v. 23, p. 121–131, 2018. Doi: 10.1016/j.addma.2018.08.001.

[203] R. Lu, S. Zhang, X. Li, H. Yan, D. Yi, J. Wang, X. Yang, B. Liu, H. Xu, P. Bai, Composition design method of Al-Cu alloy for laser powder bed fusion, Journal of Alloys and Compounds, v. 914, p. 165298, 2022. Doi: 10.1016/j.jallcom.2022.165298.

[204] Z. Hu, Y. Qi, S. Gao, X. Nie, H. Zhang, H. Zhu, X. Zeng, Aging responses of an Al-Cu alloy fabricated by selective laser melting, Additive Manufacturing, v. 37, p. 101635, 2021. Doi: 10.1016/j.addma.2020.101635.

[205] P. Agrawal, S. Gupta, S. Thapliyal, S. Shukla, R.S. Haridas, R.S. Mishra, Additively manufactured novel Al-Cu-Sc-Zr alloy: Microstructure and mechanical properties, Additive Manufacturing, v. 37, p. 101623, 2021. Doi: 10.1016/j.addma.2020.101623.

[206] Q.Z. Wang, X. Lin, N. Kang, X.L. Wen, Y. Cao, J.L. Lu, D.J. Peng, J. Bai, Y.X. Zhou, M. El Mansori, W.D. Huang, Effect of laser additive manufacturing on the microstructure and mechanical properties of TiB_2 reinforced Al-Cu matrix composite, Materials Science and Engineering: A, v. 840, p. 142950, 2022. Doi: 10.1016/j.msea.2022.142950.

[207] S. Li, B. Cai, R. Duan, L. Tang, Z. Song, D. White, O.V. Magdysyuk, M.M. Attallah, Synchrotron Characterisation of Ultra-Fine Grain TiB_2/Al-Cu Composite Fabricated by Laser Powder Bed Fusion, Acta Metall. Sin. (Engl. Lett.), v. 35, p. 78–92, 2022. Doi: 10.1007/s40195-021-01317-y.

[208] T. Sun, J. Chen, Y. Wu, M. Wang, Y. Fu, H. Wang, H. Wang, Achieving excellent strength of the LPBF additively manufactured Al–Cu–Mg composite via in-situ mixing TiB_2 and solution treatment, Materials Science and Engineering: A, v. 850, p. 143531, 2022. Doi: 10.1016/j.msea.2022.143531.

[209] Y.R. Fan, R. Chen, D.S. Yan, X.Y. Xue, T. Luo, J.S. Li, M.J. Lai, Discontinuous yielding behavior in the near-α Ti-3Al-2.5V alloy, Materials Science and Engineering: A, v. 923, p. 147701, 2025. Doi: 10.1016/j.msea.2024.147701.

[210] Z. Wang, X. Lin, N. Kang, J. Chen, H. Tan, Z. Feng, Z. Qin, H. Yang, W. Huang, Laser powder bed fusion of high-strength Sc/Zr-modified Al–Mg alloy: phase selection, microstructural/mechanical heterogeneity, and tensile deformation behavior, Journal of Materials Science & Technology, v. 95, p. 40–56, 2021. Doi: 10.1016/j.jmst.2021.03.069.

[211] Q. Jia, C. Lu, Y. Yan, Y. Zhuo, L. Wang, Z. Xia, C. Wang, X. Wu, Tensile deformation behaviors of laser powder bed fusion fabricated Al–Mn-Sc alloy with heterogeneous grain structure, Materials Science and Engineering: A, v. 849, p. 143447, 2022. Doi: 10.1016/j.msea.2022.143447.

[212] Q.Z. Wang, N. Kang, X. Lin, M.E. Mansori, W.D. Huang, High strength Al-Cu-Mg based alloy with synchronous improved tensile properties and hot-cracking resistance suitable for laser powder bed fusion, Journal of Materials Science & Technology, v. 141, p. 155–170, 2023. Doi: 10.1016/j.jmst.2022.09.027.

[213] J. Wang, T. Liu, L. Luo, X. Cai, B. Wang, J. Zhao, Z. Cheng, L. Wang, Y. Su, X. Xue, J. Guo, Selective laser melting of high-strength TiB_2/AlMgScZr composites: microstructure, tensile deformation behavior, and mechanical properties, Journal of Materials Research and Technology, v. 16, p. 786–800, 2022. Doi: 10.1016/j.jmrt.2021.11.150.

[214] M. Avateffazeli, P.E. Carrion, B. Shachi-Amirkhiz, H. Pirgazi, M. Mohammadi, N. Shamsaei, M. Haghshenas, Correlation between tensile properties, microstructure, and processing routes of an Al–Cu–Mg–Ag–TiB2 (A205) alloy: Additive manufacturing and casting, Materials Science and Engineering: A, v. 841, p. 142989, 2022. Doi: 10.1016/j.msea.2022.142989.

[215] P.J. Withers, M.J. Roy, 4.10 Residual Stresses in Metal Matrix Composites, in: Comprehensive Composite Materials II, Elsevier, p. 275–286, 2018. Doi: 10.1016/B978-0-12-803581-8.09963-X.

[216] R.B. Calhoun, D.C. Dunand, Dislocations in Metal Matrix Composites, in: Comprehensive Composite Materials, Elsevier, p. 27–59, 2000. Doi: 10.1016/B0-08-042993-9/00002-4.

[217] T. Ungár, Microstructural parameters from X-ray diffraction peak broadening, Scripta Materialia, v. 51, p. 777–781, 2004. Doi: 10.1016/j.scriptamat.2004.05.007.

[218] G.K. Williamson, R.E. Smallman, III. Dislocation densities in some annealed and cold-worked metals from measurements on the X-ray debye-scherrer spectrum, Philosophical Magazine, v. 1, p. 34–46, 1956. Doi: 10.1080/14786435608238074.

[219] G.K. Williamson, W.H. Hall, X-ray line broadening from filed aluminium and wolfram, Acta Metallurgica, v. 1, p. 22–31, 1953. Doi: 10.1016/0001-6160(53)90006-6.

[220] A. Muiruri, M. Maringa, W. Du Preez, Evaluation of Dislocation Densities in Various Microstructures of Additively Manufactured Ti6Al4V (Eli) by the Method of X-ray Diffraction, Materials, v. 13, p. 5355, 2020. Doi: 10.3390/ma13235355.

[221] V. Mote, Y. Purushotham, B. Dole, Williamson-Hall analysis in estimation of lattice strain in nanometer-sized ZnO particles, J Theor Appl Phys, v. 6, p. 6, 2012. Doi: 10.1186/2251-7235-6-6.

[222] S.A. Hassanzadeh-Tabrizi, Precise calculation of crystallite size of nanomaterials: A review, Journal of Alloys and Compounds, v. 968, p. 171914, 2023. Doi: 10.1016/j.jallcom.2023.171914.

[223] J.A. Muñoz, A. Komissarov, M. Avalos, R.E. Bolmaro, Y. Zhu, J.M. Cabrera, Improving density and strength-to-ductility ratio of a 3D-printed Al–Si alloy by high-pressure torsion, J Mater Sci, v. 59, p. 6024–6047, 2024. Doi: 10.1007/s10853-023-09298-2.

[224] J.J. Sidor, P. Chakravarty, J.Gy. Bátorfi, P. Nagy, Q. Xie, J. Gubicza, Assessment of Dislocation Density by Various Techniques in Cold Rolled

1050 Aluminum Alloy, Metals, v. 11, p. 1571, 2021. Doi: 10.3390/met11101571.

[225] E.O. Hall, The Deformation and Ageing of Mild Steel: III Discussion of Results, Proc. Phys. Soc. B, v. 64, p. 747–753, 1951. Doi: 10.1088/0370-1301/64/9/303.

[226] Ø. Ryen, B. Holmedal, O. Nijs, E. Nes, E. Sjölander, H.-E. Ekström, Strengthening mechanisms in solid solution aluminum alloys, Metall Mater Trans A, v. 37, p. 1999–2006, 2006. Doi: 10.1007/s11661-006-0142-7.

[227] V.C. Nardone, K.M. Prewo, On the strength of discontinuous silicon carbide reinforced aluminum composites, Scripta Metallurgica, v. 20, p. 43–48, 1986. Doi: 10.1016/0036-9748(86)90210-3.

[228] Z. Zhang, D. Chen, Consideration of Orowan strengthening effect in particulate-reinforced metal matrix nanocomposites: A model for predicting their yield strength, Scripta Materialia, v. 54, p. 1321–1326, 2006. Doi: 10.1016/j.scriptamat.2005.12.017.

APPENDIX

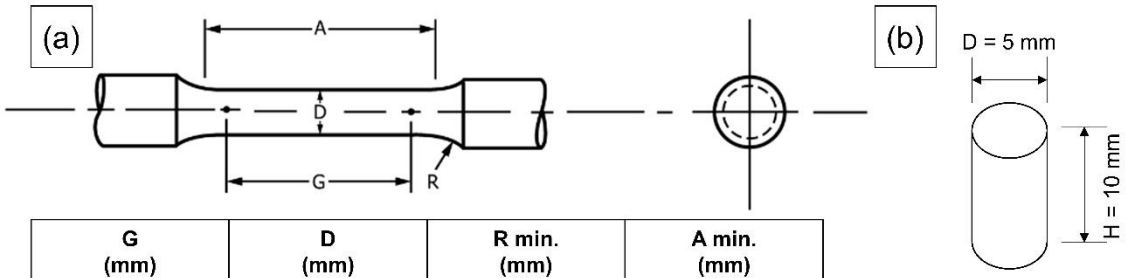

G (mm)	D (mm)	R min. (mm)	A min. (mm)
20.0 ± 0.1	4.0 ± 0.1	4	24

Figure A1 - Dimensions and geometry of the specimens (a) tensile and (b) compression tests according to the ASTM E8M-25 [143] and ASTM E9-19 [142] standards, respectively.

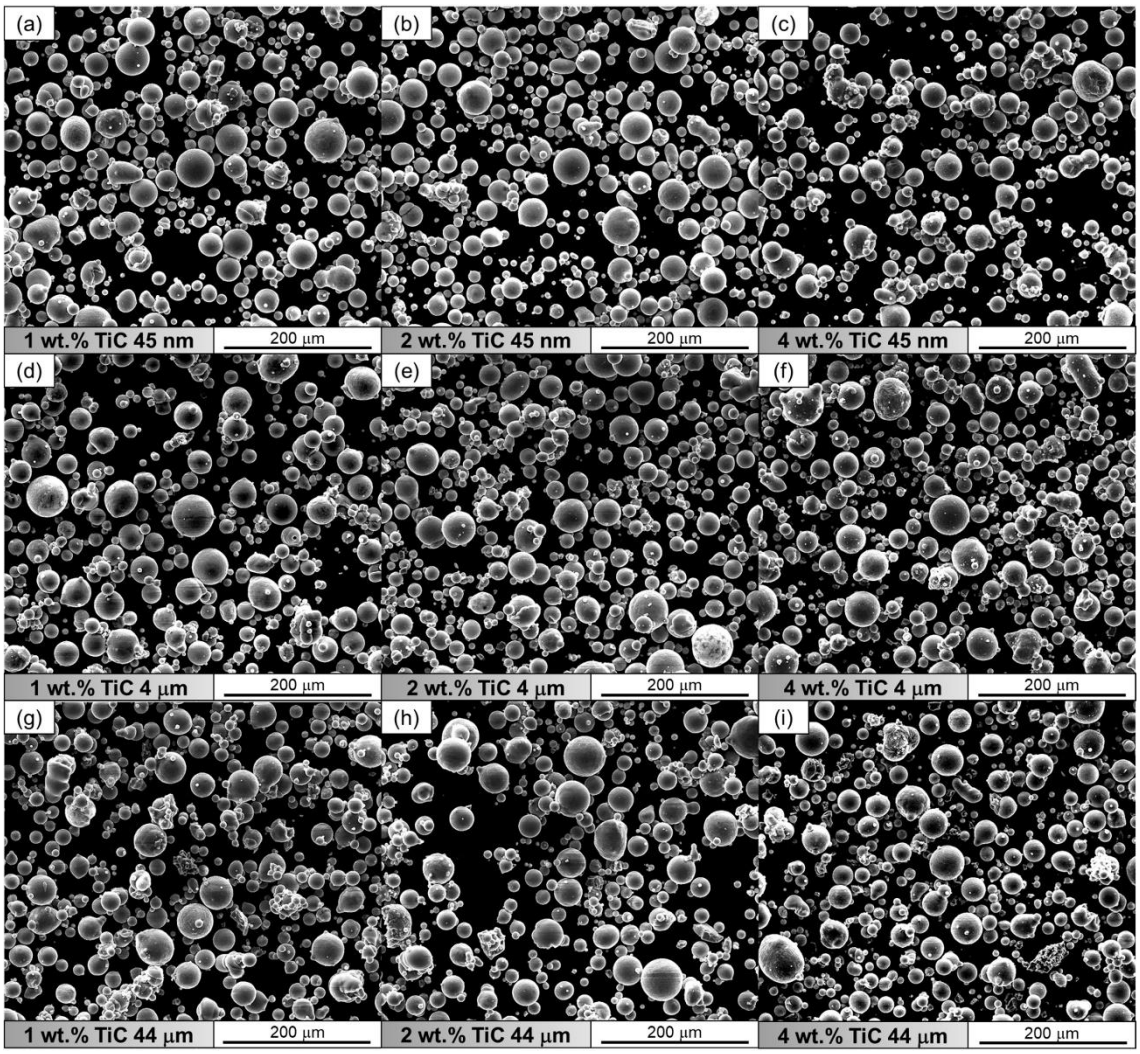

Figure A2 - Overall morphology and distribution of the TiC surface-functionalized AA2017 powders observed by SEM: (a–c) 1 wt.%, 2 wt.%, and 4 wt.% TiC with an average particle size of 45 nm; (d–f) 1 wt.%, 2 wt.%, and 4 wt.% TiC with a particle size <4 µm; and (g–i) 1 wt.%, 2 wt.%, and 4 wt.% TiC with an average particle size of 44 µm.

Table A1 - Experiments applied for the understanding, optimization and validation of the L-PBF process parameters using Box-Behnken design of experiments and resultant porosity and cumulative crack length (CCL) of the AA2017 and TiC/AA2017 alloys.

					AA2017 samples		TiC/AA2017 samples	
Sample	**Laser Power (W)**	**Scanning Speed (mm/s)**	**Hatch Distance (μm)**	**E_v** (J/mm^3)**	**Porosity (%)**	**CCL (mm/mm^2)**	**Porosity (%)**	**CCL (mm/mm^2)**
1	150	100	90	555.56	2.5 ± 1.9	0.8 ± 0.9	1.6 ± 0.4	0.2 ± 0.3
2	250	100	90	925.93	0.3 ± 0.1	0.02 ± 0.10	1.8 ± 0.6	0.005 ± 0.020
3	150	1200	90	46.30	25.8 ± 2.8	3.3 ± 2.0	17.1 ± 2.5	2.8 ± 0.7
4	250	1200	90	77.16	4.2 ± 1.6	6.6 ± 2.4	3.9 ± 0.9	2.8 ± 0.9
5	150	650	60	128.21	13.5 ± 3.6	3.0 ± 0.8	8.4 ± 2.6	2.3 ± 0.6
6	250	650	60	213.68	3.7 ± 2.2	5.1 ± 1.9	3.0 ± 0.8	1.9 ± 1.0
7	150	650	120	64.10	11.2 ± 2.5	4.1 ± 0.9	8.1 ± 1.4	2.7 ± 0.8
8	250	650	120	106.84	2.4 ± 0.9	5.4 ± 1.3	2.6 ± 0.6	2.7 ± 0.9
9	200	100	60	1111.11	0.6 ± 0.8	0.17 ± 0.28	1.6 ± 0.6	Crack-free
10	200	1200	60	92.59	12.6 ± 2.6	3.5 ± 1.3	7.7 ± 2.2	2.0 ± 0.8
11	200	100	120	555.56	0.21 ± 0.08	0.01 ± 0.02	0.6 ± 0.2	Crack-free
12	200	1200	120	46.30	11.5 ± 2.3	3.1 ± 1.5	8.3 ± 1.8	2.3 ± 0.8
13	200	650	90	113.96	5.6 ± 2.8	4.1 ± 1.0	5.0 ± 1.4	2.4 ± 0.7
14	200	650	90	113.96	5.8 ± 1.5	4.6 ± 2.2	4.1 ± 1.2	2.2 ± 0.9
15	200	650	90	113.96	4.0 ± 2.4	3.7 ± 1.6	3.8 ± 1.8	1.9 ± 0.6
16	200	650	90	113.96	3.2 ± 1.3	4.6 ± 2.0	3.5 ± 1.6	2.1 ± 0.8
17	200	650	90	113.96	3.9 ± 1.6	4.6 ± 1.7	3.5 ± 1.3	1.3 ± 0.5
18	200	650	90	113.96	5.1 ± 2.1	5.7 ± 1.9	3.7 ± 1.3	1.0 ± 0.5
19	200	650	90	113.96	4.9 ± 2.1	6.4 ± 2.0	3.6 ± 1.5	1.3 ± 0.6
20	200	650	90	113.96	4.7 ± 2.1	5.6 ± 2.0	3.6 ± 0.9	1.4 ± 0.9
21	200	650	90	113.96	3.8 ± 1.5	5.2 ± 1.6	3.6 ± 1.2	1.4 ± 0.6
22	200	650	90	113.96	4.5 ± 1.7	4.7 ± 1.1	3.7 ± 1.6	1.8 ± 0.7

23*	250	100	120	694.44	1.1 ± 1.2	0.09 ± 0.12	1.6 ± 0.6	Crack-free
24*	200	100	90	740.74	0.4 ± 0.2	0.05 ± 0.18	1.2 ± 0.4	Crack-free
25*	250	100	60	1388.89	1.6 ± 1.8	0.2 ± 0.3	2.1 ± 0.3	Crack-free
26*	150	100	120	416.67	3.8 ± 2.0	1.7 ± 0.9	2.3 ± 0.7	0.3 ± 0.5
27*	200	650	120	85.47	4.1 ± 1.3	4.5 ± 1.3	3.3 ± 1.5	2.1 ± 1.1
28*	250	1200	60	115.74	6.0 ± 2.0	4.1 ± 2.2	3.8 ± 1.7	2.0 ± 1.2
29*	250	650	90	142.45	3.8 ± 3.0	4.0 ± 1.4	3.2 ± 1.0	2.8 ± 1.6
30*	190	100	120	527.78	0.17 ± 0.06	0.01 ± 0.02	0.6 ± 0.2	Crack-free

* Samples used for the validation of the regression models.

** E_v = Volumetric energy density (according to Equation 2.1)

Table A2 - ANOVA test results for the porosity of the as-built AA2017 samples.

Terms	Sum of Squares	Mean of Squares	F-value	p-value
P	226.462	226.462	226.95	0.000
v	319.082	319.082	319.76	0.000
h	3.185	3.185	3.19	0.099
P^2	30.729	30.729	30.79	0.000
v^2	5.432	5.432	5.44	0.038
h^2	1.604	1.604	1.61	0.229
P*v	95.182	95.182	95.39	0.000
P*h	0.254	0.254	0.25	0.623
v*h	0.146	0.146	0.15	0.708
Lack-of-Fit	5.729	1.910	2.75	0.104
Pure error	6.245	0.694		
Total	707.754			

P = Laser Power; v = scanning speed; h = hatch distance

Table A3 - ANOVA test results for the cumulative crack length of the as-built AA2017 samples.

Terms	Sum of Squares	Mean of Squares	F-value	p-value
P	4.4692	4.4692	7.35	0.019
v	29.4903	29.4903	48.51	0.000
h	0.0870	0.0870	0.14	0.712
P^2	0.2425	0.2425	0.40	0.540
v^2	29.2422	29.2422	48.10	0.000
h^2	2.7003	2.7003	4.44	0.057
P*v	4.1305	4.1305	6.79	0.023
P*h	0.1119	0.1119	0.18	0.675
v*h	0.0150	0.0150	0.02	0.878
Lack-of-Fit	1.4918	0.4973	0.77	0.539
Pure error	5.8037	0.6449		
Total	82.9279			

P = Laser Power; v = scanning speed; h = hatch distance

Table A4 - ANOVA test results for the porosity of the as-built 2TiC45nm samples.

Terms	Sum of Squares	Mean of Squares	F-value	p-value
P	71.619	71.619	209.49	0.000
v	123.559	123.559	361.42	0.000
h	0.133	0.133	0.39	0.545
P^2	12.929	12.929	37.82	0.000
v^2	2.066	2.066	6.04	0.030
h^2	0.031	0.031	0.09	0.770
P*v	44.783	44.783	130.99	0.000
P*h	0.002	0.002	0.01	0.941
v*h	0.604	0.604	1.77	0.209
Lack-of-Fit	2.291	0.764	3.79	0.052
Pure error	1.812	0.201		

Total	263.861

P = Laser Power; v = scanning speed; h = hatch distance

Table A5 - ANOVA test results for the cumulative crack length of the as-built 2TiC45nm samples.

Terms	Sum of Squares	Mean of Squares	F-value	p-value
P	0.0423	0.0423	0.23	0.639
v	11.9033	11.9033	65.25	0.000
h	0.2879	0.2879	1.58	0.233
P^2	1.4077	1.4077	7.72	0.017
v^2	2.7898	2.7898	15.29	0.002
h^2	0.1370	0.1370	0.75	0.403
P*v	0.0108	0.0108	0.06	0.812
P*h	0.0336	0.0336	0.18	0.675
v*h	0.0137	0.0137	0.08	0.789
Lack-of-Fit	0.3013	0.1004	0.48	0.705
Pure error	1.8878	0.2098		
Total	18.1680			

P = Laser Power; v = scanning speed; h = hatch distance

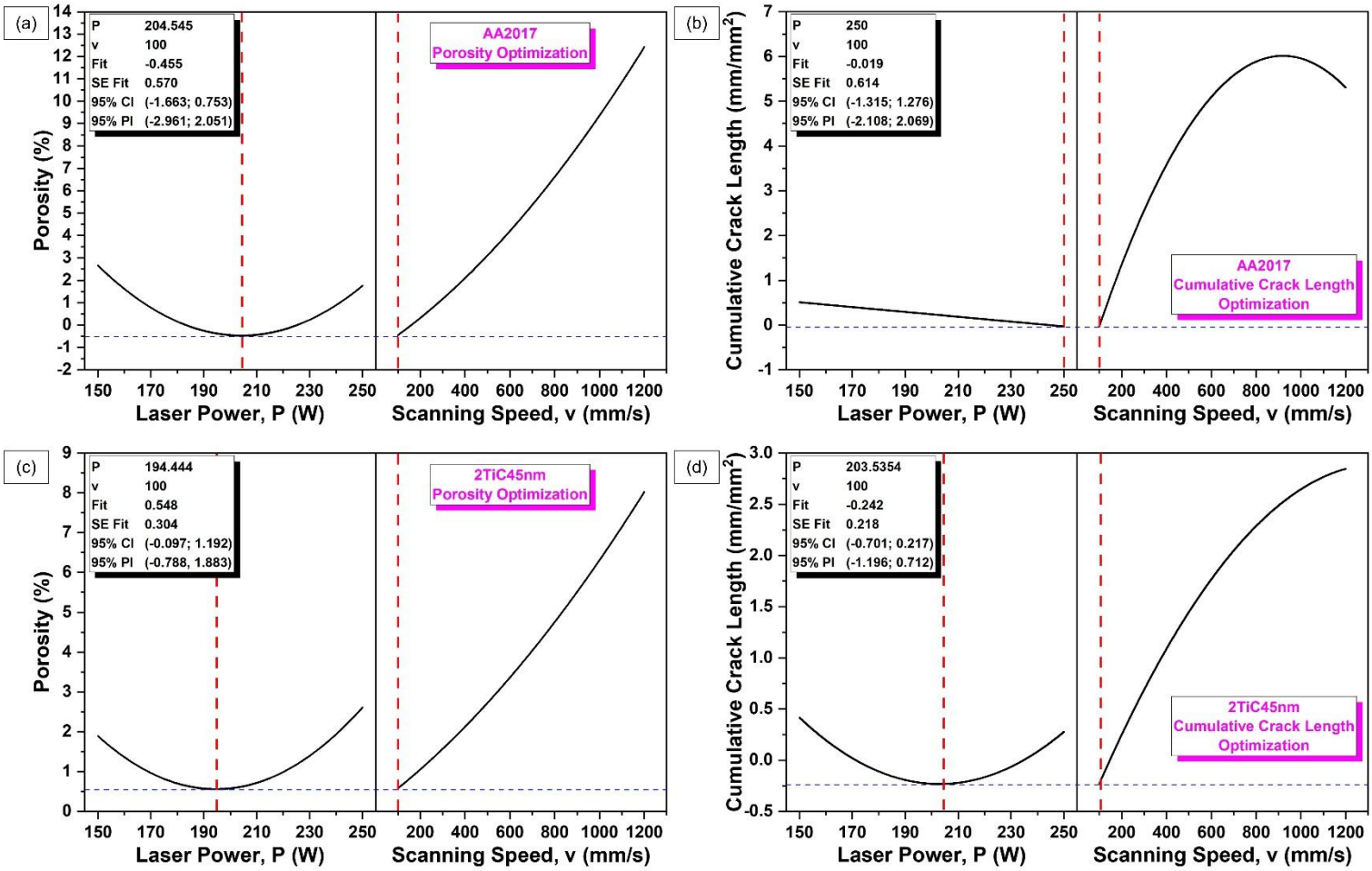

Figure A3 - Response graphs generated using the reduced regression models for the porosity and cumulative crack length of the AA2017 and 2TiC45nm alloys. These plots were used as the basis for identifying optimized L-PBF parameter combinations through desirability-based multi-response optimization.

Table A6 - Comparison of porosity and cumulative crack length of the AA2017 and 2TiC45nm samples produced using the optimized sets of L-PBF process parameters.

L-PBF process parameters				AA2017 samples		TiC/AA2017 samples	
Laser Power (W)	**Scanning Speed (mm/s)**	**Hatch Distance (μm)**	**E_V (J/mm^3)**	**Porosity (%)**	**Cumulative Crack Length (mm/mm^2)**	**Porosity (%)**	**Cumulative Crack Length (mm/mm^2)**
200	100	60	1111.11	0.6 ± 0.8	0.17 ± 0.28	1.6 ± 0.6	Crack-free
200	100	90	740.74	0.4 ± 0.2	0.05 ± 0.18	1.2 ± 0.4	Crack-free
200	100	120	555.56	0.21 ± 0.08	0.01 ± 0.02	0.6 ± 0.2	Crack-free
250	100	60	1388.89	1.6 ± 1.8	0.2 ± 0.3	2.1 ± 0.3	Crack-free
250	100	90	925.93	0.3 ± 0.1	0.02 ± 0.10	1.8 ± 0.6	0.005 ± 0.020
250	100	120	694.44	1.1 ± 1.2	0.09 ± 0.12	1.6 ± 0.6	Crack-free
190	100	120	527.78	0.17 ± 0.06	0.01 ± 0.02	0.6 ± 0.2	Crack-free

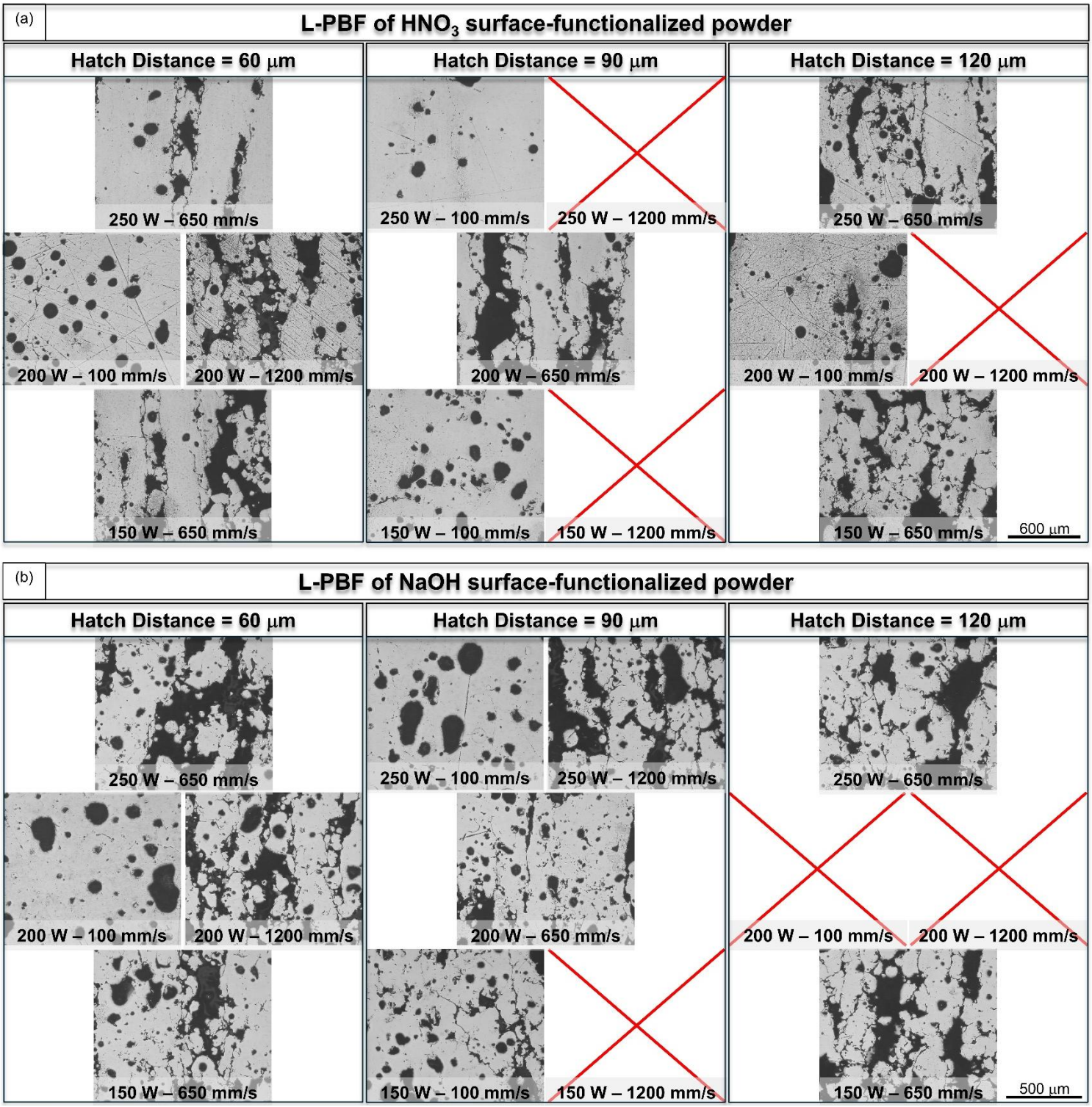

Figure A4 - Optical micrographs showing defects in L-PBF-processed samples using (a) HNO_3 and (b) NaOH surface-functionalized powders, under different processing conditions.

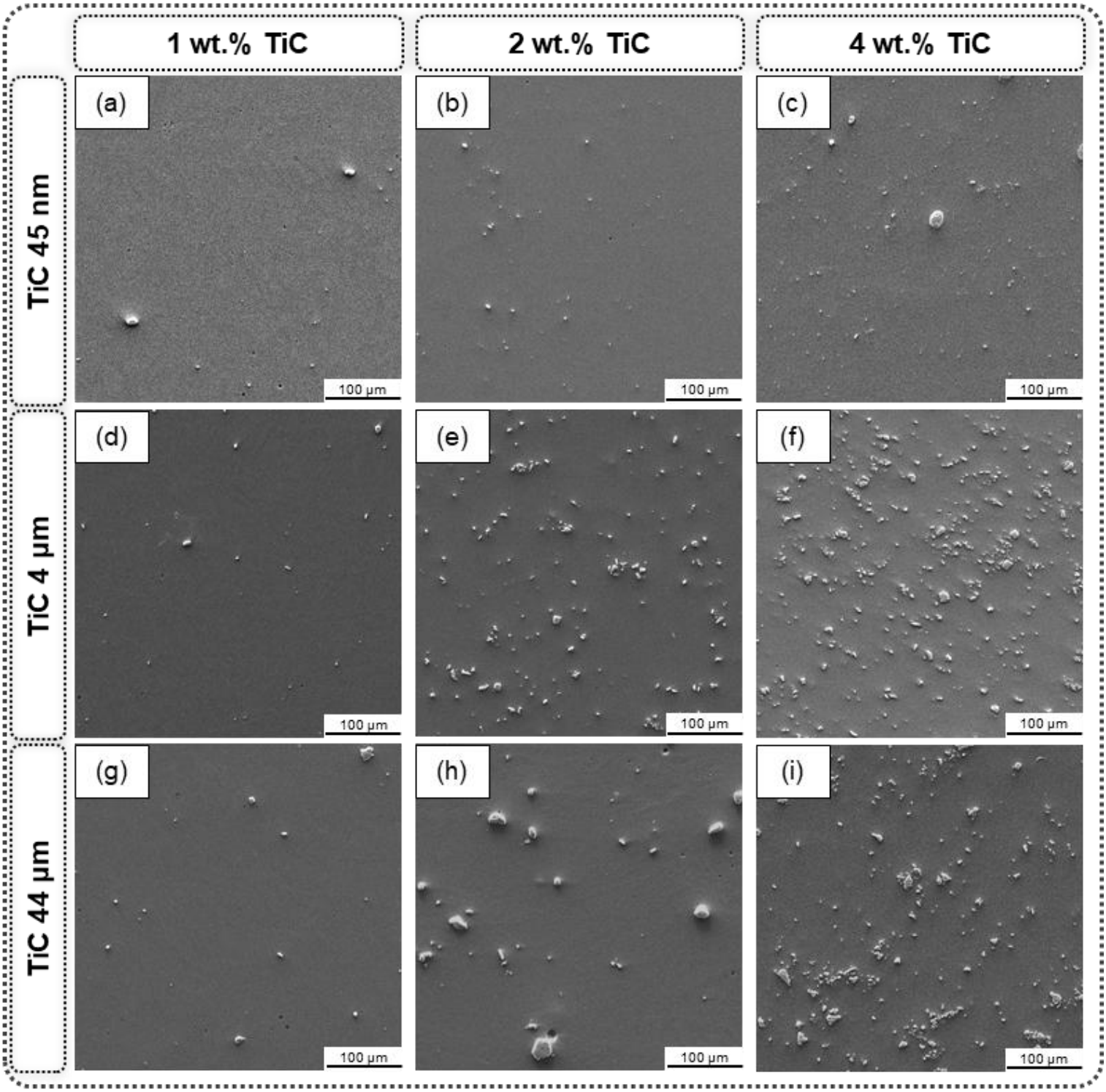

Figure A5 - Secondary electrons (SE-SEM) images from the cross-section parallel to the building direction (BD) of the as-built TiC/AA2017 L-PBF alloys.

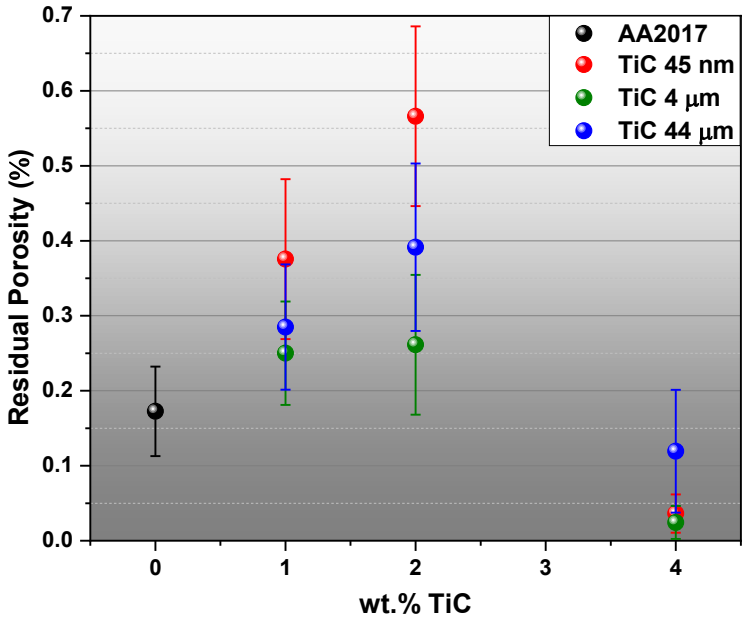

Figure A6 - Residual porosity of the as-built AA2017 and TiC/AA2017 alloys produced by L-PBF with different TiC particle size and concentration.

Table A7 - Position of the (111) and (200) α-Al peaks of the as-built AA2017 and TiC/AA2017 alloys from the XRD diffractograms.

As-built Alloys	α-Al Peak Positions (2θ) (°)	
	(111)	(200)
AA2017	38.59945	44.84432
1TiC45nm	38.57587	44.81997
1TiC4µm	38.61541	44.8593
1TiC44µm	38.59656	44.83922
2TiC45nm	38.61529	44.85868
2TiC4µm	38.61703	44.85878
2TiC44µm	38.63703	44.87928
4TiC45nm	38.56731	44.81185
4TiC4µm	38.5791	44.82423
4TiC44µm	38.56685	44.81195

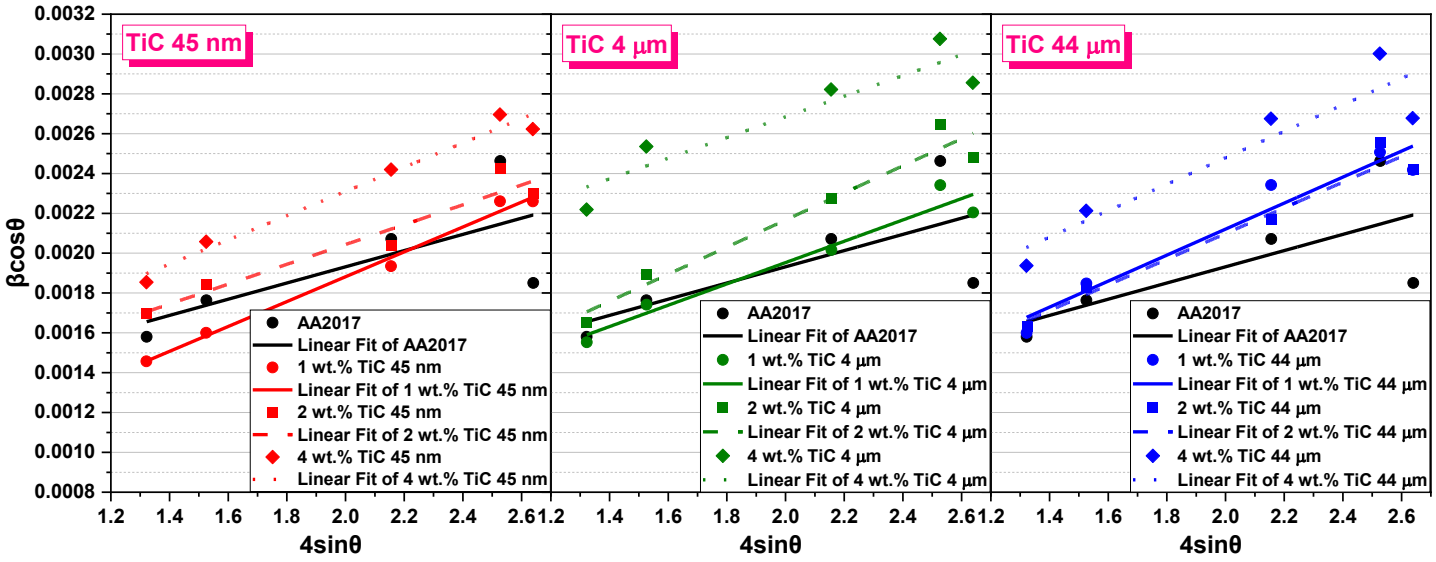

Figure A7 - Williamson-Hall plots for the as-built AA2017 and TiC/AA2017 alloys.

Table A8 - One-way ANOVA test results for the microhardness of the as-built AA2017 and TiC/AA2017 alloys.

Terms	Sum of Squares	Mean of Squares	F-value	p-value
Composition	12360	1373.28	18.47	0.000
Pure error	58736	74.35		
Total	71096			

Table A9 - Results of Tukey's post-hoc test (95% confidence level) for microhardness of the as-built AA2017 and TiC/AA2017 alloys. Compositions that shere at least one letter are statistically similar. Different letters indicate significant differences between groups.

Composition	Replicates	Mean	Grouping		
AA2017	80	85.67		C	D
1TiC45nm	80	89.997	B		
1TiC4µm	80	88.391	B	C	
1TiC44µm	80	83.063			D
2TiC45nm	80	89.40	B	C	
2TiC4µm	80	89.94	B	C	

2TiC44μm	80	88.705		B	C
4TiC45nm	80	94.521	A		
4TiC4μm	80	96.371	A		
4TiC44μm	80	94.694	A		

Table A10 - Ultimate compressive strength (UCS), yield strength, elongation at fracture, and Young's modulus obtained from compression tests of the as-built AA2017 and TiC/AA2017 alloys.

Alloy	Building Orientation	UCS (MPa)	Yield Strength (MPa)	Elongation at Fracture (%)	Young's Modulus (GPa)
AA2017	0°	546 ± 34	175 ± 10	41 ± 6	46 ± 8
	45°	526 ± 27	217 ± 6	32 ± 13	48 ± 20
	90°	557 ± 25	181 ± 11	44 ± 14	67 ± 39
1TiC45nm	0°	531 ± 20	196 ± 12	38 ± 9	51 ± 29
	45°	548 ± 28	203 ± 28	41 ± 4	38 ± 21
	90°	541 ± 72	195 ± 11	42 ± 8	55 ± 20
2TiC45nm	0°	532 ± 45	209 ± 12	46 ± 9	44 ± 8
	45°	533 ± 62	207 ± 9	31 ± 7	59 ± 4
	90°	541 ± 39	206 ± 6	40 ± 8	56 ± 9
4TiC45nm	0°	558 ± 14	244 ± 18	32 ± 5	45 ± 6
	45°	527 ± 46	271 ± 31	30 ± 7	50 ± 24
	90°	550 ± 20	259 ± 8	32 ± 5	43 ± 17
1TiC4μm	0°	574 ± 15	217 ± 9	25 ± 15	44 ± 12
	45°	522 ± 38	202 ± 6	36 ± 9	46 ± 9
	90°	504 ± 51	200 ± 2	35 ± 8	42 ± 1
2TiC4μm	0°	573 ± 43	230 ± 20	50 ± 9	59 ± 15
	45°	521 ± 20	226 ± 22	43 ± 10	51 ± 12
	90°	547 ± 59	224 ± 6	39 ± 5	55 ± 12
4TiC4μm	0°	534 ± 50	243 ± 19	32 ± 9	45 ± 9
	45°	572 ± 17	252 ± 3	35 ± 6	53 ± 16
	90°	574 ± 21	233 ± 15	34 ± 10	86 ± 29

1TiC44µm	0°	546 ± 31	175 ± 5	36 ± 12	60 ± 55
	45°	506 ± 19	206 ± 28	38 ± 15	46 ± 22
	90°	548 ± 11	109 ± 16	42 ± 2	53 ± 20
2TiC44µm	0°	618 ± 28	226 ± 9	35 ± 6	43 ± 7
	45°	528 ± 30	216 ± 13	46 ± 3	52 ± 12
	90°	531 ± 23	220 ± 10	32 ± 6	45 ± 8
4TiC44µm	0°	567 ± 4	246 ± 4	31 ± 9	60 ± 24
	45°	203 ± 110	237 ± 3	49 ± 15	76 ± 8
	90°	472 ± 9	243 ± 14	49 ± 15	43 ± 18

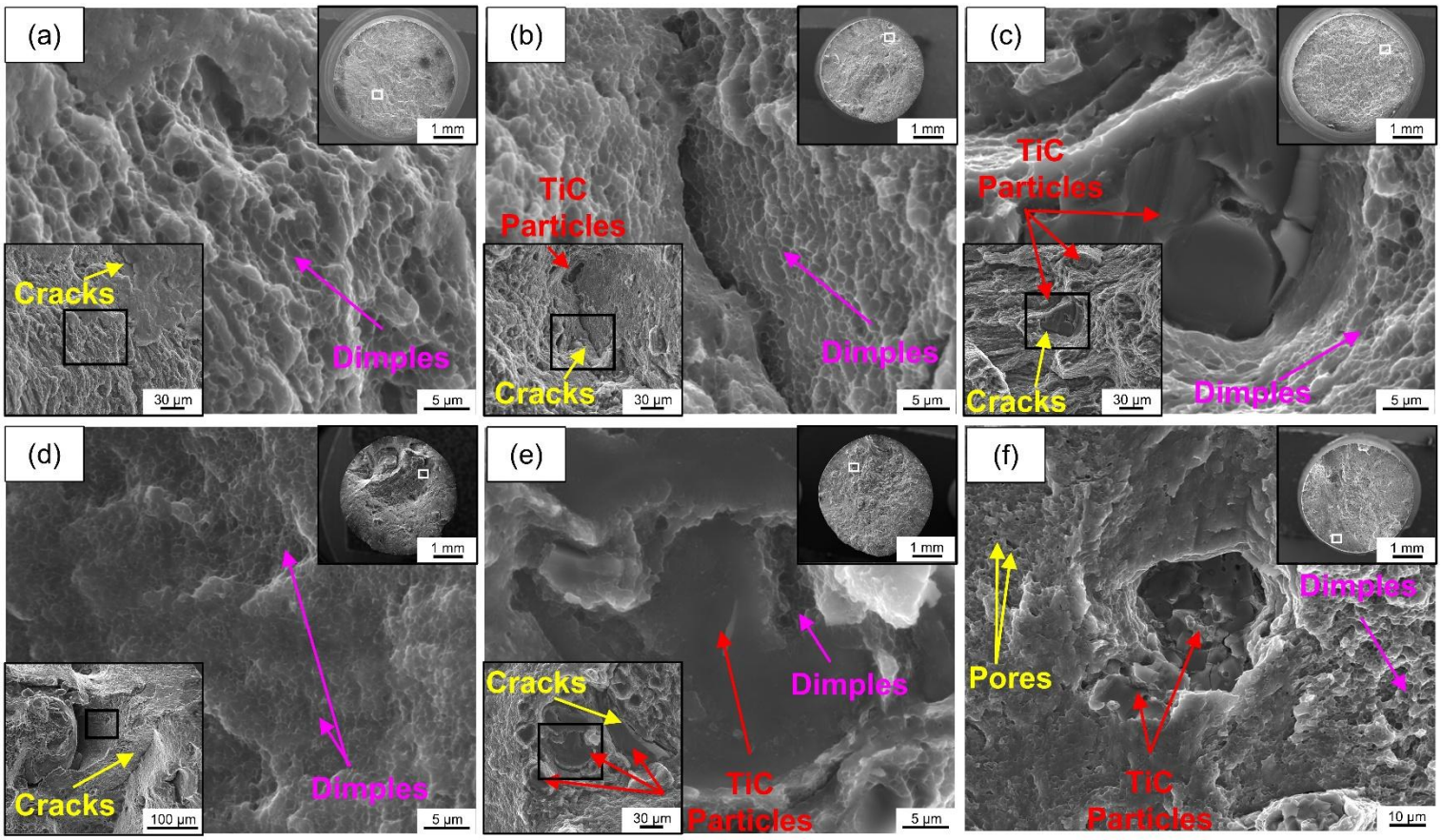

Figure A8 - SEM images of the fracture surface of the as-built (a) 1TiC45nm, (b) 1TiC4µm, (c) 1TiC44µm, (d) 4TiC45nm, (e) 4TiC4µm, and (f) 2TiC44µm alloys.